# 論文 / 著書情報
# Article / Book Information

| | |
|---|---|
| 題目(和文) | 縦型高速双ロール鋳造法により急冷凝固したAl-Mn系合金板材の微細組織 |
| Title(English) | Microstructure of rapidly solidified Al-Mn based alloy strips fabricated by vertical-type high-speed twin-roll casting |
| 著者(和文) | SongRam |
| Author(English) | Ram Song |
| 出典(和文) | 学位:博士(工学),<br>学位授与機関:東京工業大学,<br>報告番号:甲第11084号,<br>授与年月日:2019年3月26日,<br>学位の種別:課程博士,<br>審査員:熊井 真次,村右 信二,中村 吉男,小林 能直,小林 郁夫 |
| Citation(English) | Degree:Doctor (Engineering),<br>Conferring organization: Tokyo Institute of Technology,<br>Report number:甲第11084号,<br>Conferred date:2019/3/26,<br>Degree Type:Course doctor,<br>Examiner:,,,, |
| 学位種別(和文) | 博士論文 |
| Type(English) | Doctoral Thesis |

Tokyo Institute of Technology

# Microstructure of rapidly solidified Al-Mn based alloy strips fabricated by vertical-type high-speed twin-roll casting

Dissertation for Degree of

Doctor of Engineering

Field of Materials Science and Engineering

Ram Song

2018

# Contents

# Chapter 1 General introduction

## 1.1. Background

Since the global warming and resource exhaustion issues, there is a great demand to minimize the impact of human activities on the environmental pollution and to improve energy efficiency for all the manufacturing industrial fields as well as automotive industry. In this regard, weight-reduction and better fuel-efficient in vehicles are desired. In automotive industry, it has been estimated that every 10% weight reduction from total weight of vehicle leads to improve around 7% of fuel efficiency[1)]. Thus, the use of light metals and the application of components made of the light metals have been widely considered. From the point of view, aluminum and its alloys have been received attention as promising light metals for achieving those needs of the industrial applications on the basis of features such as low density, good corrosion resistance, thermal conductivity, moderate strength, workability, and recycling efficiency[2–4)]. In practice, the production of aluminum has been remarkably increased during several decades all over the world as shown in Fig. 1-1[5)].

Generally, there are two major categories of aluminum alloys; cast aluminum alloys and wrought aluminum alloys. The cast aluminum alloys are used for producing the product with final-shape in as-cast condition. Whereas, the wrought aluminum alloys are manufactured as specific standard products such as rods, plates, sheets and foils. Thus, in terms of the wrought aluminum alloys, specific successive processes are applied after the casting *e.g.,* hot- and cold-rolling or extrusion or forging, etc. According to the alloy designation system of Aluminum Association, the wrought aluminum alloys are commonly further classified based on their main alloying elements[2)]. Table 1-1 shows eight-types of wrought alloys labeled with four-digit designation. The present study has been focused on the wrought 3xxx Al-Mn based alloys.

### 1.1.1. Wrought 3xxx Al-Mn based alloys

Wrought 3xxx aluminum alloys have been widely used in diverse applications such as fin of automotive heat exchangers and thin sheets for beverage can body due to their moderate

strength, excellent formability and corrosion resistance[6-10]. The wrought 3xxx aluminum alloys mainly contain Mn as a major alloying element and both Fe and Si as minor alloying elements. Table 1-2 shows the compositions of commercial wrought 3xxx aluminum alloys[11]. Generally, Mn is contained up to 1.5 mass% in the wrought 3xxx aluminum alloys. The Mn can be solid-dissolved in the Al matrix and also form Mn-containing constituent particles. According to the binary Al-Mn phase diagram[12], maximum solubility of Mn in Al matrix is around 1.8 mass% at 657 ℃. The equilibrium secondary phase with Al is the orthorhombic $Al_6Mn$ phase in compositional range of the alloy with 4.1 Mn mass% in the Al-Mn binary system. However, by addition of other alloying elements such as Fe and Si, the Mn solubility in Al matrix is decreased, and the formation of Mn-containing secondary particles is increased during solidification. In general, the Fe prefers forming orthorhombic $Al_6(Mn,Fe)$ phase in wrought 3xxx alloys[13-15]. The $Al_6(Mn,Fe)$ phase is isomorphic to the $Al_6Mn$ and $Al_6Fe$ phase[12]. In contrast, the Si prefers forming cubic α-Al(Mn,Fe)Si phase, instead of $Al_6(Mn,Fe)$ phase[16].

The Mn solid solution and secondary particles have significant roles to determine various metallurgical characteristics in wrought 3xxx aluminum alloys; final mechanical properties and recrystallization behavior. For instance, the Mn supersaturation can contribute to increase solid solution strengthening. Ryen et al.[17] found linear hardening effect in Mn solid solution with increasing Mn supersaturation in Al matrix. They reported that the Mn in solid solution has a strong effect on the initial work hardening rate.

Meanwhile, the high Mn supersaturation can accelerate precipitation of Mn-containing dispersoids during heat treatment (*e.g.,* homogenization and annealing). The dispersoids can contribute to increase the mechanical properties. Muggerud et al.[18] reported increasing Si and Mn contents enhances the precipitation of dispersoids. They obtained as high as 32 MPa of yield stress improvement by the dispersion hardening in Al-0.49Fe-0.48Si-0.99Mn alloy (in mass%). Also, Li et al.[19] reported significant dispersion hardening by fine α-Al(Mn,Fe)Si dispersoids in 3003 aluminum alloy. They found the α-Al(Mn,Fe)Si phase has semi-coherent interface with the Al matrix. It resulted in retarding the coarsening and growth of the dispersoids with high number density during homogenization.

Furthermore, it is well known that the secondary particles strongly affect to recrystallization behavior[20-26]. Well-distributed constituent particles, mainly formed during

solidification, can act as nucleation site of recrystallized grains in annealing process. Karlík et al.[26] studied the influence of secondary particle distribution on recrystallization behavior in Al-Mn-Zr alloy. They revealed the alloy with high-dense of coarse particles (>1.5 μm) recrystallized easily due to particle stimulated nucleation (PSN). Also, fine dispersoids, mainly formed by decomposition of supersaturated Mn in solid solution during heat treatment, can pin the grain boundary movement and thus inhibit recrystallization. Huang et al.[24] reported concurrently precipitated dispersoids mainly retarded grain/sub-grain migration rather than pre-existing dispersoids during recrystallization in Al-Mn-Fe-Si alloy.

In the previous works, the Mn solid solution and secondary particles can be expected to play important roles to determine various metallurgical characteristics in wrought Al-Mn based aluminum alloys. The level of Mn supersaturation in Al matrix, and formation of constituent particles and its distribution are strongly dependent on the overall alloy composition and casting history (*e.g.,* cooling rate). Although the downstream processes are provided to get the wrought 3xxx aluminum alloy products, the initial solidification structure of as-cast products affects the microstructure and physical- and mechanical properties, which are strongly influenced by the cooling rate during solidification.

### 1.1.2. Direct chill casting

Direct chill (DC)-casting has been used extensively for manufacturing aluminum alloy slabs due to its high productivity. Figure 1-2 (a) shows a schematic of the DC-casting process. Firstly, the melt is introduced into the mold. The melt is contacted with the mold wall, and solidified shell is formed. Then, a dummy bar *i.e.,* the bottom part of the mold is gradually moved toward the casting direction. At the same time, the cooling water is directly sprayed to the ingot surface. Consequently, large slabs are fabricated. It is commonly conducted in a range of cooling rates, less than 20 ℃/s[27]. Figure 1-2 (b) shows the schematic of sheets manufacturing process starting by DC-casting. The large aluminum alloy slabs are fabricated by DC-casting. To remove surface imperfections including the metallurgical inhomogeneous portions (*e.g.,* chilled layer, inverse-segregation and cracking), the slab surface is scalped. Then, homogenization treatment is conducted to reduce chemical and structural inhomogeneity. It can be also utilized to control the size and distribution of constituent particles. After the homogenization, subsequent hot- and cold rolling are applied to obtain the

right plate/sheet thickness. At last, annealing process is applied. Depending on the applications, further processes such as temper-rolling and brazing treatment also can be conducted.

In terms of production of aluminum sheets, there are many downstream processes after the DC-casting resulting in high production cost and energy consumption. This is a major problem to the widespread use of aluminum sheets in industrial applications. In addition, due to the relatively low cooling rate of the DC-casting, it is inevitable not only low solute-solubility that unfavorable to the formation of fine dispersoids by the given successive heat treatment, but also forming coarse constituent particles in as-cast condition. The coarse secondary particles are generally brittle, and can act as initiation sites for cracking that lead to a deterioration of mechanical properties in the final rolled sheet or foil. Therefore, alternative manufacturing process combined with economics and metallurgical advantages should be considered.

### 1.1.3. Twin-roll casting

Twin-roll casting (TRC) process is a near-net-shape process for sheet manufacturing. The TRC can be divided into horizontal- and vertical-type by casting direction. Conventional TRC for the aluminum alloy strip manufacturing is horizontal-type[28]. Figure 1-3 (a) shows a schematic of the horizontal-type TRC process. The horizontal-type TRC consists of a pair of rotating water-cooled rolls. At first, melt is introduced between the rolls through a nozzle. The melt is solidified on the rolls, then dragged into the roll gap. At last, a thin metal strip with thickness less than 6 mm is produced. Figure 1-3 (b) shows a schematic of sheets manufacturing process starting by horizontal-type TRC. Since the relatively thin metal strip can be fabricated from the melt directly, subsequent hot rolling process can be eliminated compared to conventional processing route starting by DC-casting. This contributes to reduce the energy consumption and engineering cost. Beside the economic benefits, the horizontal-type TRC is considered to have high cooling rate rather than that of DC-casting. Generally, the horizontal-type TRC is considered to be conducted around $10^2$ ℃/s[29]. Due to relative high cooling rate, the horizontal-type TRC is expected to obtain refined solidification structure, fine constituent particles and high supersaturation of solute elements. However, the application of horizontal-type TRC for the manufacturing of aluminum alloy strip is limited

because of its low productivity; 14 m/min as a casting speed for fabrication around 1.3 mm-thick 1100 aluminum alloy strip[30]. Also, the horizontal-type TRC cannot be applied for alloys with high alloy contents[31-33]. Internal cracking can easily occur for the alloys with wide freezing temperature range. Reduction of casting speed is useful for reducing the internal cracking. However, this approach decreases productivity.

### 1.1.4. Vertical-type high-speed twin-roll casting

Recently, Haga et al.[34,35] developed a laboratory-scale vertical-type high-speed twin-roll caster for aluminum alloy strip casting. Figure 1-4 (a) is an outlook of the vertical-type high-speed twin-roll caster. The caster size is 1700 mm (width) × 1100 mm (depth) × 1800 mm (height). This caster is equipped with a pair of water-cooled copper rolls. Due to a large thermal conductivity of the copper rolls, sticking of the molten alloy during the casting can be prevented[35]. In order to keep the high thermal conductivity, no lubricant is applied on the roll surface. One of the rolls is firmly fixed to the base but, the other roll is fixed to the base via a series of springs to control the roll separating force. Figure 1-4 (b) shows an outlook of the caster equipped with a nozzle and a side-dam plate. The feeding nozzle is set over the rolls to maintain the stable and sufficient height of melt-head. The melt-head introduces a large hydrostatic pressure and contributes to get better heat transfer from the melt to roll. The vertical-type high-speed twin-roll casting (HSTRC) is characterized by high cooling rates. Figure 1-5 shows the temperature profile obtained from direct measurement during the casting. Thin foil-type thermocouples were inserted under the nozzle and melt-head, respectively. First, the thermocouple under the nozzle touched the melt as marked by (a). Following the roll rotation, the thermocouple trapped by the growing solidified shells. When the thermocouple passes through the roll gap, the temperature drastically decreased as marked by (b) due to the very rapid heat transfer from the solid shells to the casting rolls. Another thermocouple submerged into the melt-head inside of the feeding nozzle, showed quite constant temperature as marked by (c). Once the thermocouple was caught by the solidification shells growing from both roll surfaces, the temperature decreases dramatically as marked by (d). From the cooling curve, the estimated cooling rate was over $10^3$ ℃/s even at the strip center. This feature is expected to lead to not only fine solidification structure

including homogeneous distribution of fine secondary particles, but also the enhanced solid solubility of solute atoms in the matrix. This high cooling rate also allows to obtain high casting speed. Using this caster, the strip can be fabricated at speeds of 60-150 m/min with superior surface appearance and fine solidification structure[34-36]. Comparing to the conventional horizontal-type TRC, the present vertical-type high-speed twin-roll caster has around 7-10 times larger productivity.

Various kinds of aluminum alloys were cast by the HSTRC[34-40]. Shimosaka et al.[37] reported refined solidification structure of Al-Mg-Si-Mn alloy strip. The obtained strip showed improved tear toughness resulting from morphological change of $Mg_2Si$ phase from plate-like to globular shape. Suzuki et al.[39] reported the high cooling rates of the HSTRC was effective for manufacturing the aluminum alloy strip containing high Fe impurity; commercial 6063 aluminum alloy sheet containing 3 mass% Fe fabricated by the HSTRC could be bent successfully without cracking for both T4 and T6 conditions. It is also known that the HSTRC is effective for aluminum scrap recycling without drastic deterioration in ductility resulting from its high cooling rates[40].

As above explanations, the HSTRC has a high potential to control the microstructure and final mechanical properties (*e.g.*, yield strength, ductility, etc.) of aluminum alloy sheets resulting from its high cooling rates. In terms of Al-Mn based alloys, high cooling rate of the HSTRC can expand Mn supersaturation. The high Mn supersaturation is important in Al-Mn based alloys because this is essential to not only obtain Mn solid solution strengthening, but also make Mn-containing dispersoids for dispersion strengthening. Improved mechanical properties can expand the application fields of the Al-Mn based alloys, in particular where higher strength is required *e.g.,* application for structural materials. Also, the high cooling rates can promote fine and homogeneous secondary particles distribution. Since the Al-Mn based alloys are applied for the thermo-mechanical process after casting, the recrystallization behavior is also important. The homogeneously distributed secondary particles and fine Mn-containing dispersoids should affect their recrystallization behavior during thermo-mechanical processing steps; softening kinetics, recrystallized grain size, texture evolution, etc.

Most of the previous works concerning Al-Mn based alloys have been focused on the downstream processes to control the microstructure and obtain desired mechanical properties.

The level of Mn supersaturation and the formation of secondary particles as well as their size distribution are determined during solidification. Therefore, understanding of the initial solidification structure characterized by high cooling rate of the HSTRC is important. Without understanding for the initial solidification structure in detail, it is difficult not only to apply suitable downstream thermo-mechanical processes, but also to fully utilize the HSTRC for manufacturing of Al-Mn based alloys in industrial level.

### 1.2. Objective of the present study

The purpose of the present study is to obtain basic information concerning the microstructure of rapidly solidified Al-Mn based alloy strips fabricated by vertical-type high-speed twin-roll casting. Binary Al-Mn, ternary Al-Mn-(Fe,Si), quaternary Al-Mn-Fe-Si and commercial 3003 aluminum alloy were selected for investigation. By comparison with other cast products fabricated under the wide range of cooling rates, influence of cooling rates on the solidified microstructure, characteristics of secondary particles, Mn supersaturation and its decomposition behavior of the HSTRC strip were examined, and how the high cooling rate of HSTRC affects the formation of solidification structure in the Al-Mn based alloy strips was made clear.

### 1.3. Outline of the present thesis

The present thesis is entitled “microstructure of rapidly solidified Al-Mn based alloy strips fabricated by vertical-type high-speed twin-roll casting”. The outline of the present thesis consisting of 7 chapters is shown in Fig. 1-6.

Chapter 1 “General introduction”
Background and purpose of the present study are introduced.

Chapter 2 “Solidification structure and secondary particles in vertical-type high-speed twin-roll cast 3003 aluminum alloy strip”

Commercial 3003 aluminum alloy strip was fabricated by using HSTRC process. Through comparison of the various casting conditions; DC-casting, permanent steel/copper mold

casting and single-roll casting, the aluminum grain size and kinds, size, morphology and composition of secondary phases were characterized to reveal the influence of cooling rate on the solidification structure of the HSTRC processed 3003 aluminum alloy strip.

Chapter 3 “Influence of alloying elements on solidification structure of vertical-type high-speed twin-roll cast Al-Mn based alloy strips”

In order to examine precisely the influence of alloy composition on the solidification structure in the HSTRC processed strips, several kinds of Al-Mn based alloys; binary Al-1.2Mn, ternary Al-1.2Mn-1.0(Fe,Si), quaternary Al-1.2Mn-0.75(Fe,Si)-0.25(Fe,Si) alloy (in mass%) strips were fabricated. Difference in solidification structure, total strip thickness and evolution of secondary particles during the HSTRC were discussed.

Chapter 4 “Influence of cooling rates on formation behavior of secondary particles in vertical-type high-speed twin-roll cast Al-Mn based alloy strips”

Ternary Al-1.2Mn-1.0Fe and Al-1.2Mn-1.0Si alloy (in mass%) strips were focused on this chapter to examine the influence of cooling rate on formation behavior of secondary particles during solidification. The secondary particles were characterized in terms of number density, area fraction and morphology particularly in strip near-surface area. Sorts of secondary phase and their composition ratio were changed in the HSTRC strip due to its high cooling rate.

Chapter 5 “Mn supersaturation and solid solution strengthening in vertical-type high-speed twin-roll cast Al-Mn binary alloy strips”

To investigate the effect of cooling rate on Mn supersaturation, Al-Mn binary alloy strips with hypo-, eutectic and hyper eutectic composition were fabricated by HSTRC. Solidification sequence of the binary Al-Mn alloys and expansion of Mn solubility in HSTRC strip were examined. The effect of Mn solid solution strengthening on their mechanical properties was also discussed.

Chapter 6 “Solute distribution and Mn decomposition behavior in vertical-type high-speed twin-roll cast Al-Mn based alloy strips”

Binary Al-1.2Mn and ternary Al-1.2Mn-1.0Fe and Al-1.2Mn-1.0Si alloy (in mass%) strips were selected in this chapter to investigate solute distribution in as-cast condition and Mn decomposition behavior during homogenization. The high cooling rate of the HSTRC contributed to homogeneous distribution of solute atoms and secondary particles. They had strong influence on following Mn decomposition behavior. The formation of dispersoids free zone in the HSTRC strip was also discussed.

Chapter 7 “General conclusions”

This chapter summarizes overall new experimental findings and conclusions of the present study.

## References


1) E. Ghassemieh: *Materials in Automotive Applications, State of the Art and Prospects*,(2011)
2) J.R. Davies: *Aluminum and Aluminum Alloys*,(2001)
3) S.K. Das, W.J. III Long, H.W. Hayden, J.A.S. Green, and W.H.Jr. Hunt: JOM, **56** (2004) 14–17
4) S.K. Das and W. Yin: JOM, **59** (2007) 57–63
5) The International Aluminium Institute: Retrieved from http://www.world-aluminium.org/statistics/#histogram
6) W.S. Miller, L. Zhuang, J. Bottema, A.J. Wittebrood, P. De Smet, A. Haszler, and A. Vieregge: Mater. Sci. Eng. A, **280** (2000) 37–49
7) J. Lacaze, S. Tierce, M. C. Lafont, Y. Thebault, N. Pébère, G. Mankowski, C. Blanc, H. Robidou, D. Vaumousse, and D. Daloz: Mater. Sci. Eng. A, **413**–**414** (2005) 317–21
8) O. Daaland and E. Nes: Acta Mater., **44** (1996) 1389–1411
9) M. Aghaie-Khafri and R. Mahmudi: Mater. Sci. Eng. A, **399** (2005) 173–80
10) O. Engler: Mater. Sci. Eng. A, **538** (2012) 69–80
11) *ASM Handbook;Properties and Selection:Nonferrous Alloys Amd Special-Purpose Materials*,ASM International, (1991)
12) L.F. Mondolfo: *Aluminum Alloys: Structure and Properties*,Butterworths, (1976)
13) G. Hausch, P. Furrer, and H. Warlimont: Zeitschrift Für Met., **69** (1978) 174–80
14) P Furrer and G Hausch: Met. Sci., **13** (1979) 155–62
15) P.C.M. De Haan, J. Van Rijkom, and J.a.H. Söntgerath: Mater. Sci. Forum, **217**–**222** (1996) 765–70
16) T.J. Pettersen, Y.J. Li, T. Furu, and K. Marthinsen: Mater. Sci. Forum, **558**–**559** (2007) 301–6
17) Ø. Ryen, O. Nijs, E. Sjölander, B. Holmedal, H.E. Ekström, and E. Nes: Metall. Mater. Trans. A, **37** (2006) 1999–2006
18) A. M. F. Muggerud, E. A. Mørtsell, Y. J. Li, and R. Holmestad: Mater. Sci. Eng. A, **567** (2013) 21–28
19) Y. J. Li, A. M. F. Muggerud, A. Olsen, and T. Furu: Acta Mater., **60** (2012) 1004–14
20) F.J. Humphreys and M. Hatherly: *Recrystallization and Related Annealing Phenomena:*

*Second Edition*,(2004)

21) R.D. Doherty, D.A. Hughes, F.J. Humphreys, J.J. Jonas, D. Juul Jensen, M.E. Kassner, W.E. King, T.R. McNelley, H.J. McQueen, and A.D. Rollett: Mater. Sci. Eng. A, **238** (1997) 219–74
22) O. Engler, P. Yang, and X. W. Kong: Acta Mater., **44** (1996) 3349–69
23) F.J. Humphreys: Acta Metall., **25** (1977) 1323–44
24) K. Huang, O. Engler, Y.J. Li, and K. Marthinsen: Mater. Sci. Eng. A, **628** (2015) 216–29
25) K. Huang, R. E. Logé, and K. Marthinsen: J. Mater. Sci., **51** (2016) 1632–43
26) M. Karlík, T. Mánik, and H. Lauschmann: J. Alloys Compd., **515** (2012) 108–13
27) D. G. Eskin, J. Zuidema Jr, V. I. Savran, and L. Katgerman: Mater. Sci. Eng. A, **384** (2004) 232–44
28) Ben Q. Li: JOM, **47** (1995) 29–33
29) E. Robert and Jr. Sanders: JOM, **64** (2012) 291–301
30) 羽賀俊雄: 軽金属, **59** (2009) 509–20
31) R. Cook, P. G. Grocock, P. M. Thomas, D. V. Edmonds, and J. D. Hunt: J. Mater. Process. Tech., **55** (1995) 76–84
32) S. A. Lockyer, M. Yun, J. D. Hunt, and D. V. Edmonds: Mater. Charact., **37** (1996) 301–10
33) M. Yun, S. Lokyer, and J.D. Hunt: Mater. Sci. Eng. A, **280** (2000) 116–23
34) T. Haga and S. Suzuki: J. Mater. Process. Technol., **143**–**144** (2003) 895–900
35) T. Haga, K. Takahashi, M. Ikawa, and H. Watari: J. Mater. Process. Technol., **140** (2003) 610–15
36) T. Haga, K. Tkahashi, M. Ikawaand, and H. Watari: J. Mater. Process. Technol., **153**–**154** (2004) 42–47
37) D. Shimosaka, S. Kumai, F. Casarotto, and S. Watanabe: Mater. Trans., **52** (2011) 920–27
38) K. Suzuki, S. Kumai, Y. Saito, A. Sato, and T. Haga: Mater. Trans., **45** (2004) 403–6
39) K. Suzuki, S. Kumai, Y. Saito, and T. Haga: Mater. Trans., **46** (2005) 2602–8
40) T. Haga, S. Kumai, and H. Watari: Waste and Biomass Valorization, **3** (2012) 419–24

**Table 1-1 Wrought aluminum alloy classification according to their main alloying elements.[2)]**

| Alloy designation | Principal alloying element |
|---|---|
| 1xxx | Pure Al (Min. 99.00%) |
| 2xxx | Cu and Mg |
| 3xxx | Mn |
| 4xxx | Si |
| 5xxx | Mg |
| 6xxx | Mg and Si |
| 7xxx | Zn and Mg |
| 8xxx | Others (Fe and Ni, or Li) |

**Table 1-2 Compositions of commercial wrought 3xxx aluminum alloys[11]. (in mass %)**

| | Si | Fe | Cu | Mn | Mg | Cr | Zn | Ti | Al |
|---|---|---|---|---|---|---|---|---|---|
| 3003 | 0.6 | 0.7 | 0.05~0.2 | 1.0~1.5 | - | - | 0.1 | - | Bal. |
| 3004 | 0.3 | 0.7 | 0.25 | 1.0~1.5 | 0.8~1.3 | - | 0.25 | - | Bal. |
| 3005 | 0.6 | 0.7 | 0.3 | 1.0~1.5 | 0.2~0.6 | 0.1 | 0.25 | 0.1 | Bal. |
| 3103 | 0.5 | 0.7 | 0.1 | 0.9~1.5 | 0.3 | 0.1 | 0.02 | - | Bal. |
| 3104 | 0.6 | 0.8 | 0.05~0.25 | 0.8~1.4 | 0.8~1.3 | 0 | 0.25 | 0.1 | Bal. |
| 3105 | 0.6 | 0.7 | 0.3 | 0.3~0.8 | 0.2~0.8 | 0.2 | 0.4 | 0.1 | Bal. |
| 3203 | 0.6 | 0.7 | 0.05 | 1.0~1.5 | - | - | 0.1 | - | Bal. |
| 3303 | 0.6 | 0.7 | 0.05~0.2 | 1.0~1.5 | - | - | 0.3 | - | Bal. |

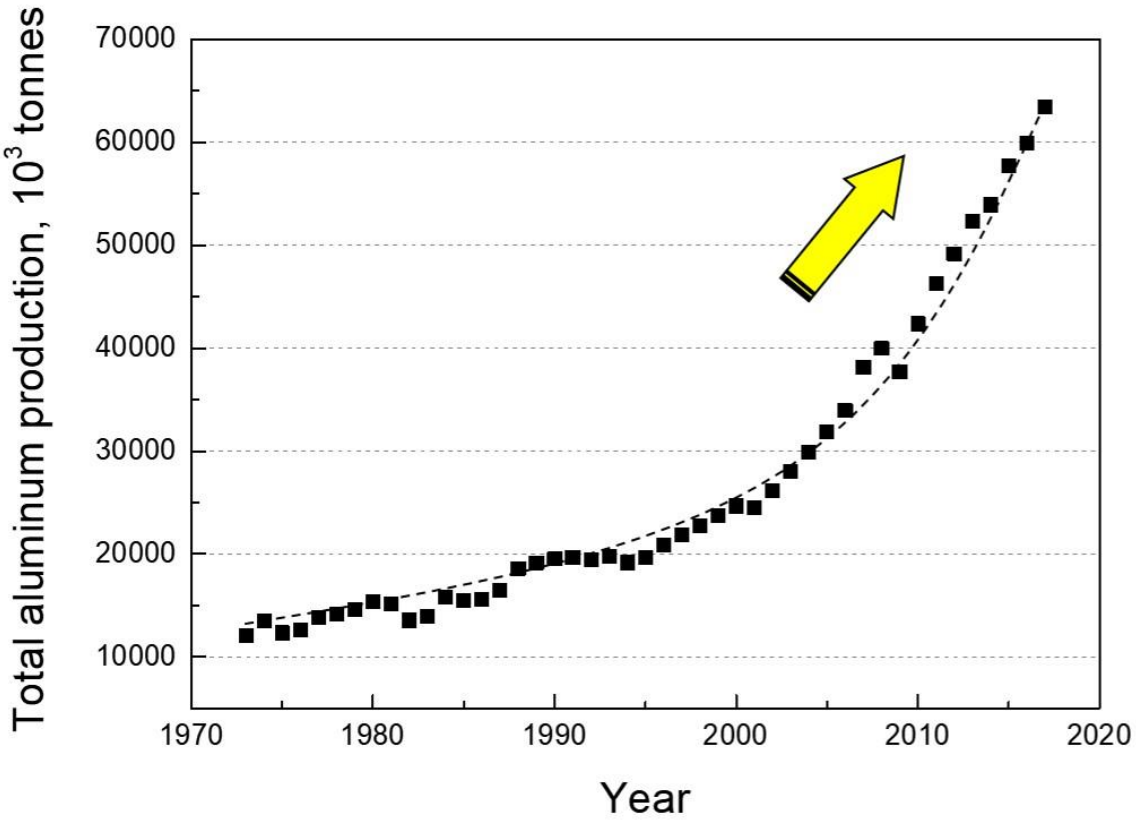


**Fig. 1-1 Histogram of world aluminum production[5].**

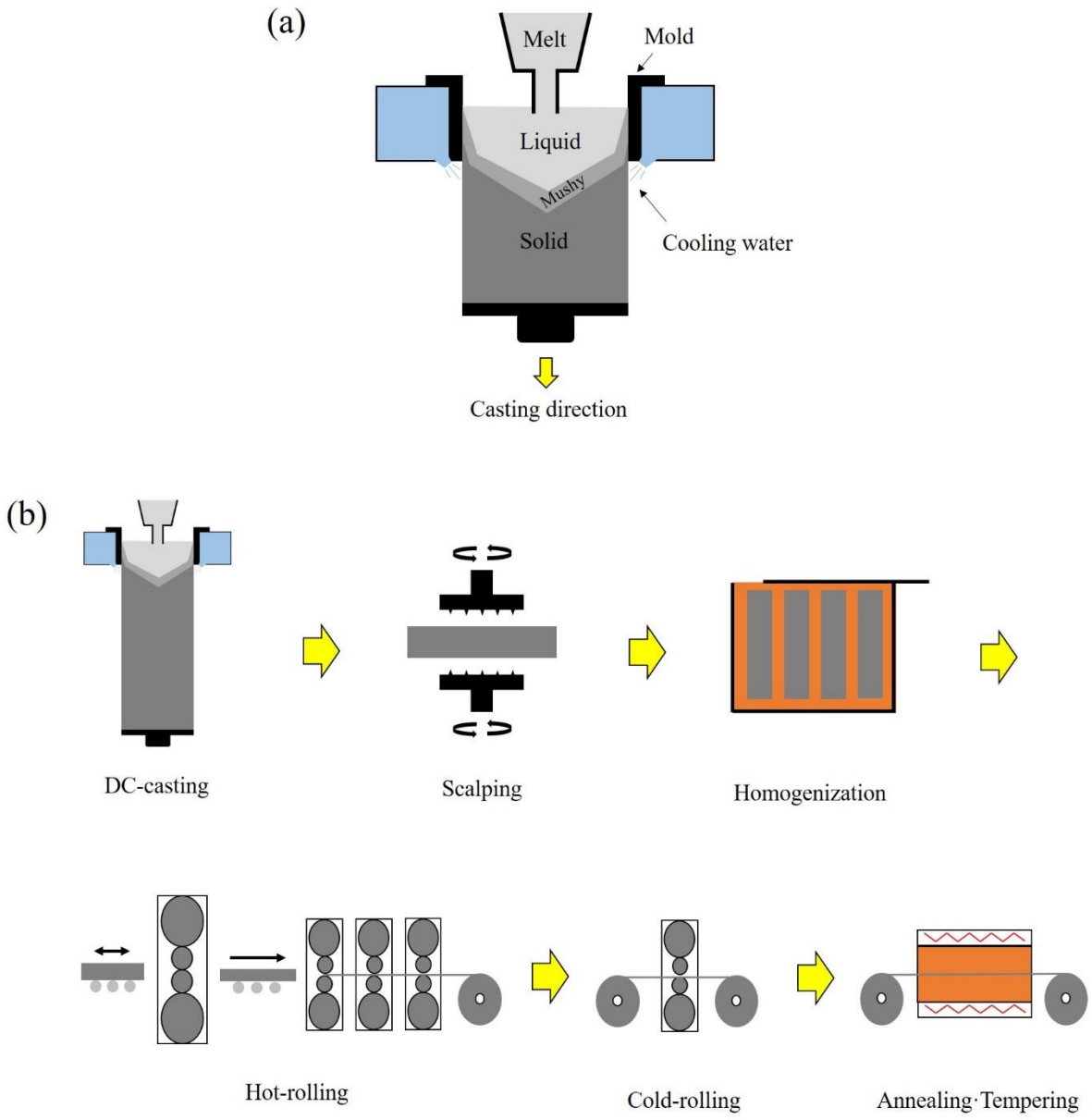


**Fig. 1-2 Schematic of the (a) DC-casting, (b) sheet manufacturing process flow by DC-casting.**

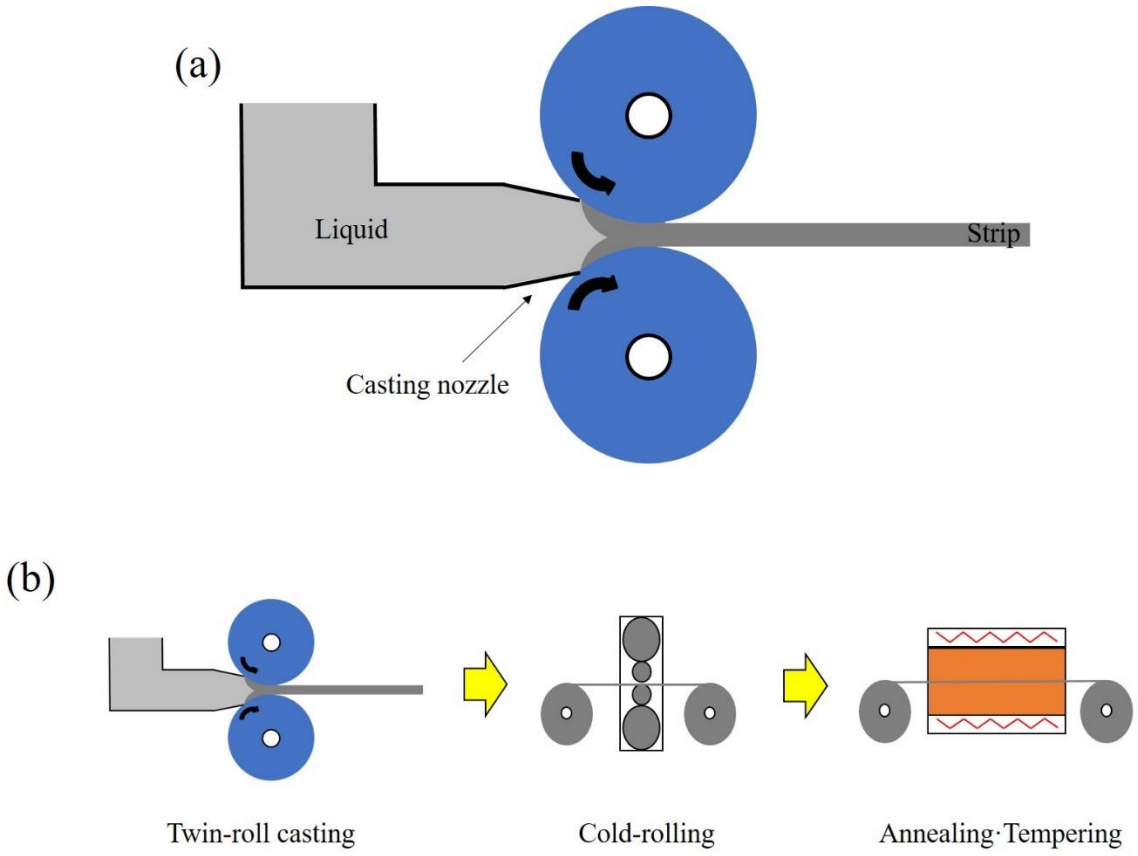


**Fig. 1-3 Schematic of the (a) twin-roll casting, (b) sheet manufacturing process flow by horizontal-type twin-roll casting.**

(a)

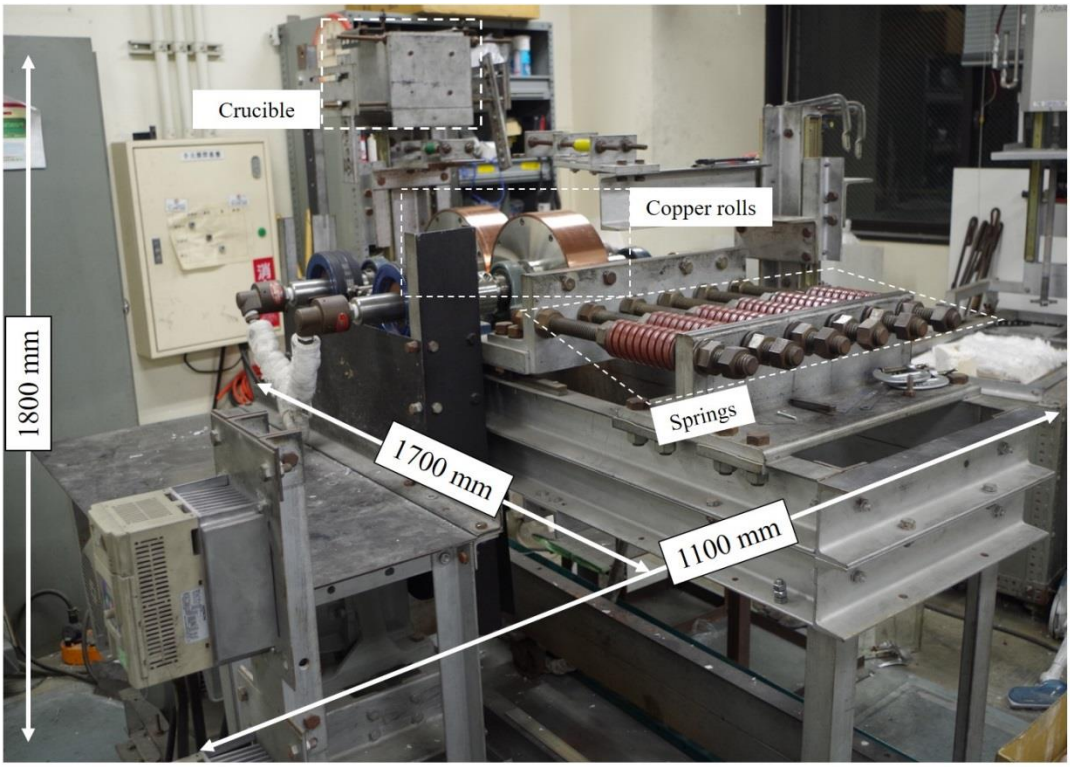


(b)

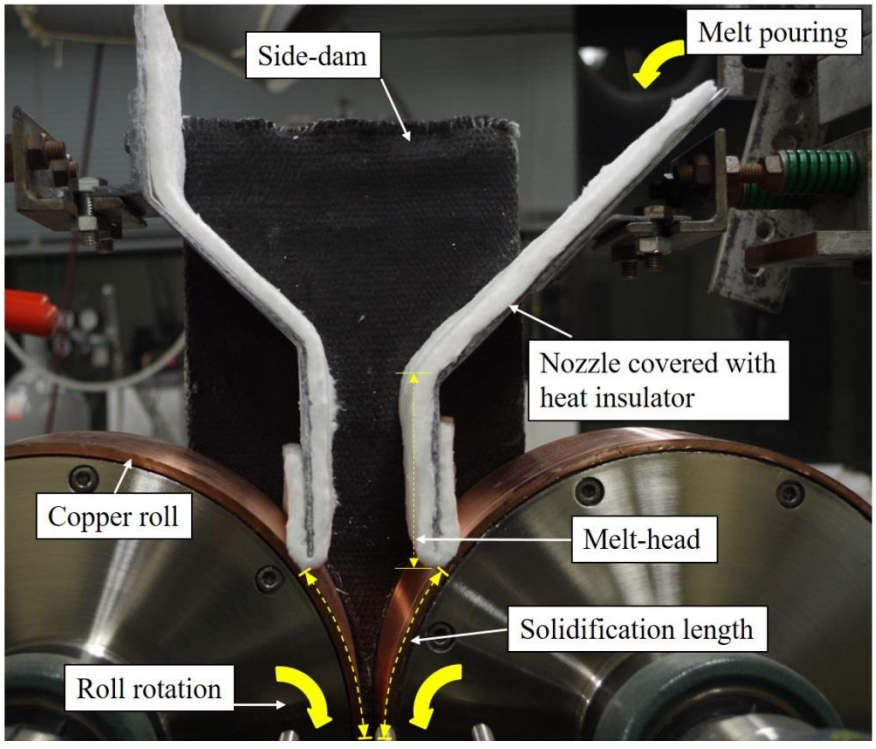


**Fig. 1-4 (a) Appearance of the vertical-type high-speed twin-roll caster, (b) Outlook of the caster equipped with nozzle and side-dam plate.**

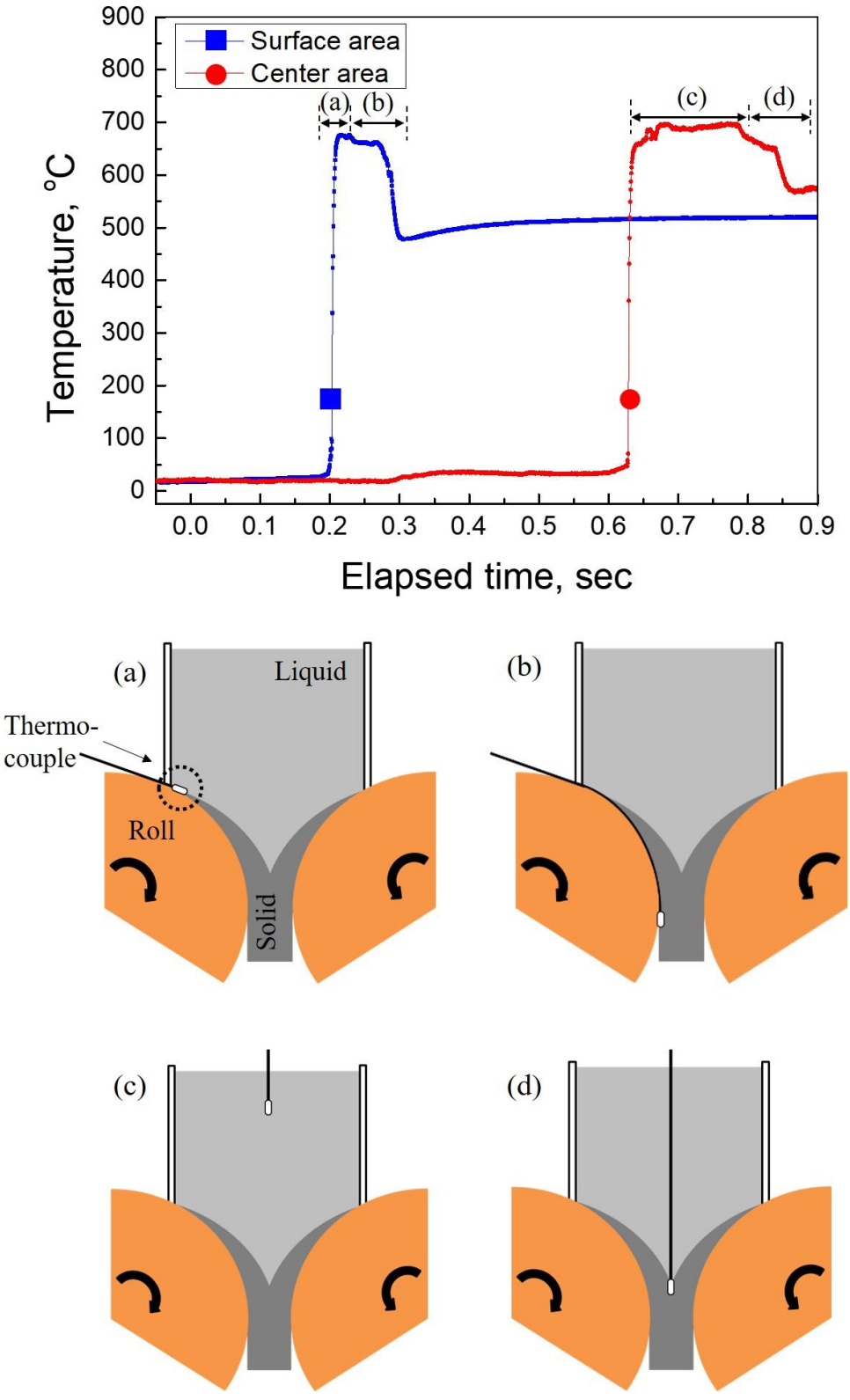


**Fig. 1-5 Temperature profile during vertical-type high-speed twin-roll casting.**

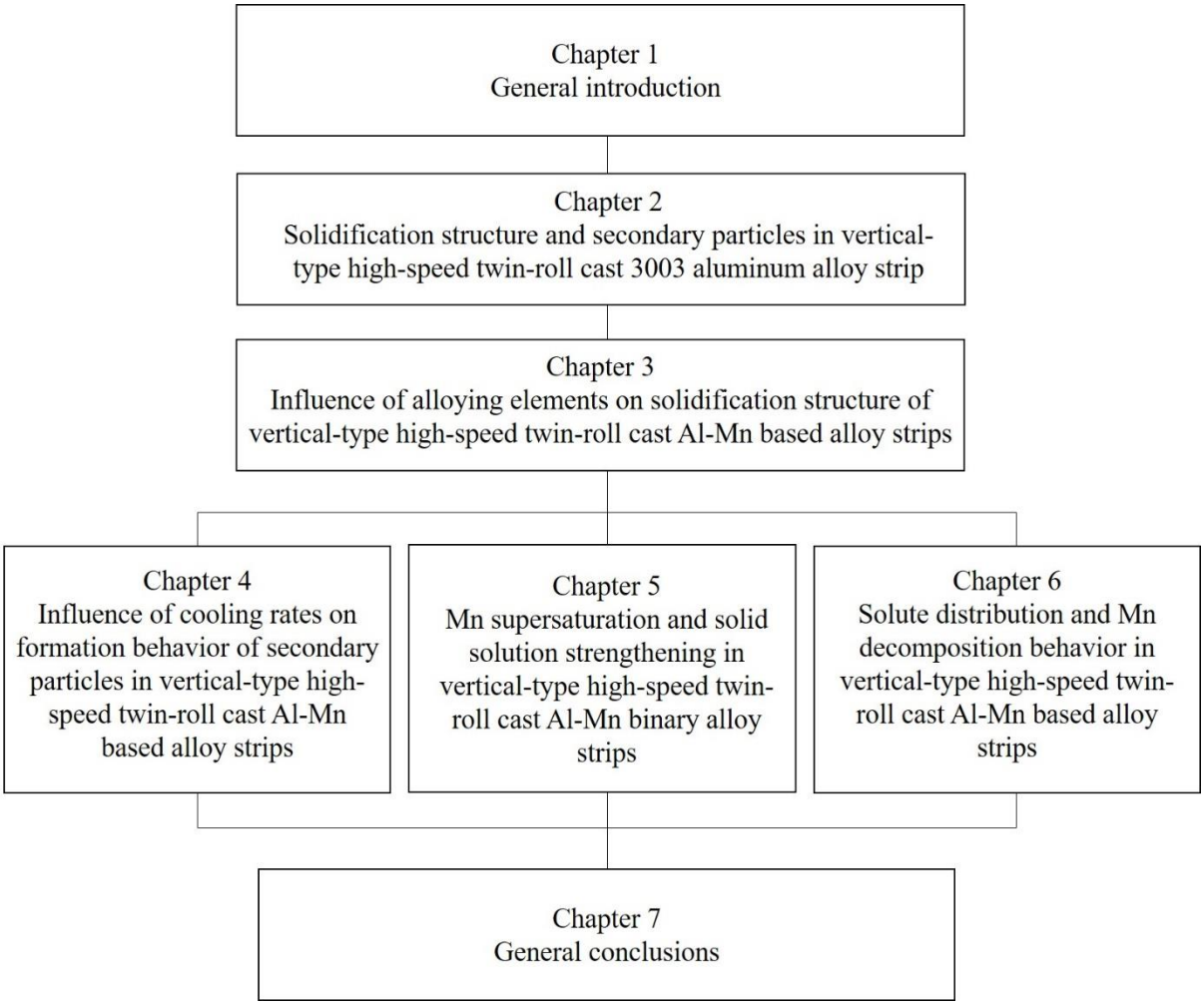


**Fig. 1-6 Outline of the present thesis.**

# Chapter 2 Solidification structure and secondary particles in vertical-type high-speed twin-roll cast 3003 aluminum alloy strip

## 2.1. Introduction

Wrought Al-Mn based 3xxx alloys are mainly used for fin of automotive heat exchangers and thin sheets for beverage can body because of their moderate strength, good ductility and corrosion resistance, etc. For manufacturing process, conventional direct chill (DC)-casting followed by homogenization, hot- and cold rolling has been applied. The DC-casting is commonly conducted in a range of cooling rates, less than 20 °C/s[1)]. Due to the relatively low cooling rate of the DC-casting process, it is inevitable not only low Mn solubility that unfavorable to the formation of fine dispersoids by the given successive heat treatment, but also forming Mn-containing coarse constituent particles in as-cast condition. The coarse secondary particles can act as initiation sites for cracking that lead to a deterioration of mechanical properties in the final rolled sheet or foil. Although the downstream processes are provided to get wrought aluminum alloy products, the initial solidification structure of as-cast products affects the microstructure and physical- and mechanical properties, which are strongly influenced by the cooling rate during solidification.

Recently, vertical-type high-speed twin-roll casting (HSTRC) has been paid attention as a promising manufacturing process to produce a thin aluminum alloy strip directly from the melt with a remarkably high casting speed[2–4)]. Compared with the conventional DC-casting, the HSTRC has numerous advantages; reduction in processing steps, equipment cost, operating cost and energy consumption. The HSTRC is characterized by high cooling rates[5)]. This feature is expected to lead to not only fine solidification structure including homogeneous distribution of fine secondary particles, but also the enhanced solid solubility of solute atoms in the matrix. For dealing with increasing demand for thinner and stronger aluminum alloy sheets, the HSTRC is considered to be applicable to provide an ideal initial microstructure, which is a key to improve the final mechanical properties of Al-Mn based 3xxx alloy sheets.

In the present study, the thin strip of commercial 3003 aluminum alloy composition was fabricated by HSTRC. The present work focused on the solidified structure and secondary

particles in the as-cast condition. The solidification structure was characterized in terms of grain size of the matrix phase and kinds, size, morphology and chemical composition of secondary particles. Through comparison of the various casting conditions; DC-casting, permanent mold casting, HSTRC and single-roll casting showing different range of cooling rate, the effect of high cooling rate of the HSTRC on solidification structure including secondary particles was discussed.

## 2.2. Experimental procedure

### 2.2.1. Materials

A commercial 3003 aluminum alloy was used in the present study. The DC-cast billets of 3003 aluminum alloy were provided from the UACJ Corporation. The chemical composition of the 3003 aluminum alloy is shown in Table 2-1.

### 2.2.2. Casting process

#### 2.2.2.1. Vertical-type high-speed twin-roll casting

Figure 2-1 shows a schematic illustration of the vertical-type high-speed twin-roll caster. The caster was equipped with a pair of copper rolls. A diameter and a width of the rolls were 300 mm and 100 mm, respectively. The rolls were cooled by running water to prevent increasing roll temperature during the casting. One of the rolls was firmly fixed to the base, while the other roll was installed with a series of springs to control the roll separating force. The roll rotation speed was 60 m/min. The initial roll separating force was set to be 20 kN. The minimum roll gap was 1 mm. The contact length between the melt and roll surface was about 100 mm.

The DC-cast billet was melted in the electric furnace (600 mm × 360 mm × 300 mm), and provided for HSTRC. Before the casting, the melt was degassed by injecting Ar gas (0.4 L/min) into the melt for 20 min. In this stage, the electric furnace was set under Ar atmosphere (0.8 L/min). The casting temperature was selected around 15 ℃ over the liquidus temperature. Pouring the melt into the feeding nozzle, solidification shells were formed on the both roll surfaces. A feeding nozzle which was set over the rolls contributed to maintain

the stable melt-height. The stable melt-height was necessary for the stable solidification shell formation on the both roll surfaces. Following the roll rotation, the solidified shells encountered at the roll gap, and were rapidly cooled. At last, a several meters-long thin strip was produced within a few seconds. In the present study, approximately 3~4 m- long and 100 mm- wide strip was obtained from 2.5 kg molten alloy. The constant thickness, which was about 2.4 mm, was obtained in the middle part of the cast strip along the casting direction (around 1 to 2 m-long). It should be noted that the microstructure observation was performed on this part.

#### 2.2.2.2. Permanent mold casting

In order to examine the effect of cooling rates during solidification, the DC-cast billet was melted, and solidified under some different cooling rate conditions using a permanent steel mold (1~10 ℃/s) and a copper mold (10~$10^2$ ℃/s). The permanent steel mold was designed to have a wedge-shape cavity (30 mm × 40 mm as mold bottom surface, 200 mm as mold height) to get different cooling rates depending on the local thickness of the cast ingot[6]. The cavity of copper mold was 100 mm × 100 mm × 2 mm in size. For the permanent steel and pure copper mold casting, 400 g and 170 g of molten alloy were used, respectively. The cooling rate was obtained by the slope of cooling curve at the liquidus temperature.

#### 2.2.2.3. Single-roll casting

A ribbon specimen was also fabricated by single-roll casting (NEV-A05, NISSIN GIKEN), to obtain much higher cooling rate during solidification rather than that of HSTRC. Around 7 g of molten alloy was ejected onto a 250 mm in diameter of copper wheel under Ar atmosphere. The gas pressure for ejecting the melt was 0.01 MPa. The wheel rotation speeds set 1800 rpm (23.5 m/sec). Around 75 μm -thick and 5 mm-wide as-spun ribbon was obtained.

### 2.2.3. Microstructure observation

The metallographic examination was conducted using OM, FE-SEM and TEM.

Optical microscopic observation (BX51M, Olympus) was carried out on transverse cross sections of the cast strip. The polished specimens were etched by the Keller's reagent ($H_2O$:$HNO_3$:HCl:HF = 190:5:3:2 in Vol.%) for 40s. For the observation of as-cast grain structure, Weck's reagent (dissolve 4 g $KMnO_4$ and 1 g NaOH in 100 ml $H_2O$) was applied for 10-15s. The as-cast grain size was measured using linear intercept method based on ASTM-E1382[7].

The number density and area fraction of secondary particles were measured using Image-J software. The measurement was conducted from 10 images for FE-SEM (JEM-7000F, JEOL) observation. Each image was taken randomly from the as-polished sample. In order to observe 3-dimensional morphology of secondary particles, the samples were deep-etched by 5 % NaOH solution. The detailed features were characterized by the FE-SEM.

Secondary particles were observed using TEM (JEM-3010, JEOL). Chemical composition analysis of the secondary particles was also performed by using EDS attached to the TEM.

Phase identification of the secondary particles was performed using X-ray diffractometer (RINT-2100, Rigaku for permanent mold cast sample, DC-cast sample and HSTRC strip, X'Pert-Pro-MRD, Philips (PANalytical) for single-roll cast ribbon) with Cu $K_\alpha$ ($\lambda$ = 1.54 Å) radiation.

## 2.3. Results

### 2.3.1. Solidification structure of 3003 aluminum alloy strip

#### 2.3.1.1. As-cast grain size of 3003 aluminum alloy products

Figure 2-2 (a) to (g) shows the polarized light micrographs of permanent mold cast sample, DC-cast sample and HSTRC strip. It can be seen that the grain size reduced as increasing the cooling rate. The grain size of the products and their corresponding cooling rates are summarized in Table 2-2.

#### 2.3.1.2. Macrostructure of the 3003 aluminum alloy strip

Figure 2-3 shows micrographs of the as-cast 3003 aluminum alloy strip. Columnar grains

grew from both strip surfaces, and they were gradually replaced by the equiaxed grains along the thickness direction as shown in Fig. 2-3 (a). In the mid-thickness region, a band of fine globular grains, so-called a central band, was observed. This is a common microstructural feature of the HSTRC strips of the alloys, which exhibit mushy-type solidification[4]. In the thickness direction, the strip had a clearly different microstructure (Fig. 2-3 (b)). Near the strip surface region, cell structure was observed. Inside of the each cell, fine etch pits were observed as shown in Fig. 2-3 (c). They correspond to the locations of homogeneously dispersed secondary particles. The cell structure gradually changed into the clear dendritic structure along the strip thickness direction as shown in Fig. 2-3 (d). In the mid-thickness area, globular grains and eutectic structure were observed as shown in Fig. 2-3 (e).

Figure 2-4 shows micrographs of the DC-cast sample and near-surface of the HSTRC strip. In DC-cast sample (Fig. 2-4 (a)), secondary particles were mainly located at inter-dendrites. Most of the secondary particles in DC-cast sample were script-like in 2-dimensional morphology with high aspect ratio (Fig. 2-4 (c)). In case of the HSTRC strip, both α-Al cells and secondary particles were much finer than those of DC-cast sample (Fig. 2-4 (b)). The secondary particles were located inside of the cells as well as grain boundaries as shown in Fig. 2-4 (d). Compared with the DC-cast sample, the secondary particles in HSTRC strip exhibited spherical-shape inside of the cells and elongated shape along the boundaries, respectively. Compared with the HSTRC strip, much fine secondary particles were observed in a single-roll cast ribbon as shown in Fig. 2-4 (e). Significant refinement of secondary particles was also detected with increasing cooling rates as shown in Fig. 2-4 (c) to (e). However, due to the distinct shape differences in secondary particles, (*e.g.*, particles between DC-casting and HSTRC, and between grain interiors and boundaries), it was difficult to compare the particle size distribution directly. Figure 2-5 shows the number density and area fraction of the secondary particles in DC-cast sample, HSTRC strip surface and single-roll cast ribbon. In the particle area fraction, the difference among DC-cast sample, HSTRC strip surface and single-roll cast ribbon was relatively small, while the difference in particle number density was large among DC-cast sample, HSTRC strip surface and single-roll cast ribbon that the number density of secondary particles increased with increasing cooling rate during solidification.

### 2.3.2. Secondary particle analysis in 3003 aluminum alloy strip

#### 2.3.2.1. XRD analysis of 3003 aluminum alloy products

Figure 2-6 shows the XRD patterns for each cast product of 3003 aluminum alloy. According to the Al-Mn-Fe-Si phase diagram[8], it is generally expected to the formation of $Al_6$(Mn,Fe) phase and/or α-Al(Mn,Fe)Si phase. The $Al_6$(Mn,Fe) phase and α-Al(Mn,Fe)Si phase with Al matrix phase were detected in the DC-cast sample and permanent mold cast samples. In contrast to that, the α-Al(Mn,Fe)Si phase was dominant in HSTRC strip on both strip surface and central area. Only α-Al(Mn,Fe)Si phase was detected in single-roll cast ribbon sample as secondary particle.

#### 2.3.2.2. Difference in morphology of the secondary particles

Figure 2-7 shows the embossed secondary particles in 3003 aluminum alloy obtained by deep-etching of Al matrix. In DC-cast sample, despite of deep-etching to a depth of around 50 μm from the initial surface, a full view of the particle could not be obtained. These script-like particles as shown in Fig. 2-7 (a) were eutectic particles. In the near-surface region of HSTRC strip, secondary particles were observed along the cell/grain boundaries, as shown in Fig. 2-7 (b) and (c). Homogeneous distribution of fine secondary particles were also observed inside of the cells. The particle exhibited spore-like morphology with a convex surface as show in Fig. 2-7 (d). Similar spore-like morphology of the secondary particles was also observed in single-roll cast ribbon samples as shown in Fig. 2-7 (e).

#### 2.3.2.3. TEM observation of the secondary particles

Figure 2-8 (a) shows a TEM bright-field micrograph of DC-cast sample. A diffraction pattern of the eutectic script-like particle corresponds to the [011] zone of orthorhombic $Al_6$(Mn,Fe) phase (Fig. 2-8 (b)). EDS analysis revealed that the particle contains 86.7 at% Al, 7.2 at% Fe and 5.4 at% Mn, close to $Al_6$(Mn,Fe) as stoichiometric formula. Meanwhile, the α-Al(Mn,Fe)Si phase particles were not observed.

Figure 2-9 shows TEM bright-field micrographs of HSTRC strip. In the strip near-surface,

particles are located along the cell boundaries as well as inside of the cells. The size of particles in HSTRC strip is much finer than that of DC-cast sample. Figure 2-9 (b) shows a representative secondary particle inside of the cell. It is the same as spore-like particles observed by FE-SEM. The small patches with different contrasts in the particle correspond to the convex surface pattern of the spore-like particle observed by FE-SEM (see Fig. 2-7 (d)). From the selected area diffraction pattern of the particles inside of the cell, they are confirmed as body-centered cubic α-Al(Mn,Fe)Si phase. The particles on the grain boundaries are also α-Al(Mn,Fe)Si phase as shown in Fig. 2-9 (c). It is of interest that the particles on the grain boundaries show the same orientation at specific observation condition. The secondary particles located at the grain boundaries are inter-connected along the grain boundaries (see Fig. 2-7 (c)). From the results, it is assumed that these particles grew from a single nucleation event during solidification. In the strip central area, secondary particles are dispersed surrounding the α-Al grains as shown in Fig. 2-9 (d). From the microstructure observation and XRD analysis found that these secondary particles are eutectic α-Al(Mn,Fe)Si phase.

Figure 2-10 shows TEM bright-field micrographs of single-roll cast ribbon. Compared with HSTRC strip, it showed much refined and homogeneously distributed secondary particles (compared Fig. 2-9 (a) and 2-10 (a)). Each particle observed in ribbon sample was also identified as body-centered cubic α-Al(Mn,Fe)Si phase as shown in Fig. 2-10 (b).

Figure 2-11 is the summary the TEM-EDS measurements. As shown on the composition map, secondary particles can be classified into several groups by composition difference. In DC-cast sample with low cooling rate, most of the particles showed a very low Si content that is below 0.5 at% as marked in dotted line. These particles are considered as $Al_6$(Mn,Fe) phase. Some of particles in copper mold cast sample are also regarded as $Al_6$(Mn,Fe) phase. In contrast to that, secondary particles in the HSTRC strip as well as single-roll cast ribbon sample were richer in Si content. The exact identification for each particle is difficult but, the secondary particles can be described by the generic formula α-Al(Mn,Fe)Si phase. This result showed good agreement with the XRD spectrum (see Fig. 2-6).

In terms of the composition ratio in the α-Al(Mn,Fe)Si phase, the (Mn+Fe)/Si ratio was different; in the copper mold cast sample, the composition of the particles lies between the (Mn+Fe)/Si ratio = 1.5~3 as marked in dotted line, and this was in agreement with other

workers' results of 3xxx aluminum alloys in as-cast condition[9-11]. On the other hand, the particles in HSTRC strip near-surface area showed around 1 as the (Mn+Fe)/Si composition ratio. The ratio was much lower in the particles of single-roll cast ribbon. From the result, it is assumed that the (Mn+Fe)/Si ratio decreases with increasing cooling rate during solidification.

## 2.4. Discussion

### 2.4.1. Relationship between cooling rates and solidification structure in as-cast 3003 aluminum alloy

The cooling rates during solidification are often estimated from the solidified microstructure. Suzuki et al.[12] estimated the cooling rate of HSTRC A356 alloy strip using dendrite arm spacing (DAS) of primary α-Al dendrite. Shimosaka et al.[13] estimated the cooling rate of HSTRC Al-Mg-Si-Mn alloy strip by DAS and inter lamellar spacing (ILS) of its eutectic structure. In contrast to that, it is difficult to obtain the DAS or ILS values from the solidified structure of Al-Mn based alloys including 3003 aluminum alloy. Therefore, instead of using DAS or ILS, the relationship between the cooling rates and grain size was examined. In the case of HSTRC strip, the grain size changed along its thickness direction. The near-surface area is considered having higher cooling rate rather than that of the strip central area. Additionally, solidified microstructure of the central area consists of equiaxed and globular grains, and so it is hard to evaluate the average grain size in this area. Thus, in the present study, only the near-surface area was provided for the examination of the effect of cooling rate on the grain size. The relationship between grain size and cooling rates is shown in Fig. 2-12. The relationship between grain size and cooling rates was well approximated on a straight line with a slope of -0.327 in a logarithmic scale. By using the present result, the estimated cooling rate was around 11 ℃/s for DC-casting, $3.1 \times 10^3$ ℃/s for HSTRC strip at near-surface area, respectively. This result showed good agreement with the directly measured cooling rates by using the thermocouples[5].

Since the grain size of HSTRC strip is quite small compared with that of DC-cast sample (see Fig. 2-2 and Table 2-2), the relative amounts of grain boundaries providing the nucleation site of secondary particles are large. In addition, due to the high cooling rate of HSTRC, the residual liquid droplets are trapped at the inter-dendritic regions. This is

considered to result in the homogeneous distribution of refined secondary particles in as-cast HSTRC strip.

### 2.4.2. Characteristic morphology of the secondary particle

Motoi et al.[14] observed similar α-AlFeSi phase nodules in the as-cast structure of commercial pure aluminum containing 0.13 Si and 0.13 Fe in mass% as impurities. They considered the formation behavior of the α-AlFeSi phase nodulus as follows; the hydrogen gas dissolves in liquid of alloy during solidification. The hydrogen gas bubble acts as nucleation site of the α-AlFeSi phase. The α-AlFeSi phase nucleated at the inner-surface of the hydrogen bubble. It grows toward the center. Then, a spherical nodule of α-AlFeSi phase particle with a hollow shell is formed. In contrast to that, the spore-like particles in HSTRC strip in the present study exhibited various morphologies. Furthermore, the size of the particles is quite small; some particles are several hundred nanometers in diameter. These features cannot be explained by the formation mechanism of nodules resulting from the hydrogen bubbles.

In general, morphology of the crystal is controlled by its inherent crystal structure and growth conditions[15]. The crystal structure of α-Al(Mn,Fe)Si is body-centered cubic with {110} planes as the highest reticular density. In fact, it leads to the growth of rhombic dodecahedron. This rhombic dodecahedron morphology of primary α-Al(Mn,Fe)Si phase has been confirmed by other workers[16,17]. However, in the present study, the rhombic dodecahedron α-Al(Mn,Fe)Si phase was not found even in the strip central region. In 3003 aluminum alloy, the α-Al(Mn,Fe)Si phase is hard to be considered as the primary phase during solidification. Instead, the spore-like α-Al(Mn,Fe)Si phase formed from the trapped liquid droplet inside the cells. Thus, the spore-like particle was considered to be one of the eutectic components, not the primary phase. In this case, the cooling rate can strongly influence on the morphology rather than the crystal structure. The same spore-like α-Al(Mn,Fe)Si phase particles were clearly observed in ribbon sample fabricated by single-roll casting with much higher cooling rate than that of the HSTRC (Fig. 2-7 (e)).

### 2.4.3. Change in phase of secondary particles and its composition concentration

Solute elements (Mn, Fe and Si in 3003 aluminum alloy) are considered to segregate at the solid/liquid interface during solidification. Compositions of the solute-rich liquid can be varied depending on the solid solubility of each solute element in Al matrix and the solidification rate. Difference in composition of the liquid determines the sort of secondary-phase. In 3xxx (based on Al-Mn-Fe-Si alloys) alloys, Fe element favors the precipitation of $Al_6$(Mn,Fe) phase, whereas Si element results in the formation of α-Al(Mn,Fe)Si phase. Alexander and Greer[18] reported the compositional change in the liquid during solidification in Al-0.5Fe-1.0Mn-0.2Si (in mass%) alloy using MTDATA thermodynamic modeling software under Scheil approximation (*i.e.*, assuming a uniform solute distribution in the liquid and no diffusion occurs in the solid). As the large undercooling, solute partitioning pushes Fe and Si into the liquid. The undercooling increases with cooling rate during solidification. The HSTRC has much higher cooling rate compared with that of DC-casting. It can lead to substantial partitioning of solute elements including Si into the liquid. As shown in XRD pattern, (see Fig. 2-6), only α-Al(Mn,Fe)Si phase was detected in the HSTRC strip. The enrichment of Si in liquid probably results in the formation of the α-Al(Mn,Fe)Si phase in HSTRC strip rather than $Al_6$(Mn,Fe) phase.

For the α-Al(Mn,Fe)Si particles in the same HSTRC strip, the concentration of solute elements was different between strip surface and strip central area. The concentration of solute Mn, Fe, and Si elements with concentration of Al for the secondary particles in the HSTRC strip is shown in Fig. 2-13. Compared with the particles in the strip surface, the particles in strip central area show higher Fe concentration. In principle, Mn and Fe can substitute each other almost completely in the same α-Al(Mn,Fe)Si phase. However, the partition coefficient of Fe in Al is quite small compared with that of Mn. Also, the solubility of Fe in Al matrix is quite low. Therefore, the segregation of Fe into the liquid is high rather than that of Mn. In HSTRC, strip central area is considered as the final solidification part of the trapped solute-rich liquid. Thus, it can be assumed that relatively Fe-rich α-Al(Mn,Fe)Si phase was formed at HSTRC strip central area.

## 2.5. Conclusions

The solidification structure and secondary particles in the vertical-type high-speed twin-roll cast 3003 aluminum alloy strip were investigated in this chapter. The following results can be drawn.

The refinement of both solidification structure and secondary particles were achieved in HSTRC processed strip. By the relationship between the as-cast grain size and the cooling rate in 3003 aluminum alloy, the cooling rate of HSTRC was estimated around $3.1 \times 10^3$ ℃/s at the strip near-surface.

Significant differences in the formation of secondary particles were found between direct chill (DC)-casting and the vertical-type high-speed twin-roll casting as a result of the different cooling rates; orthorhombic $Al_6(Mn,Fe)$ phase is the main secondary phase in DC-cast sample, whereas only cubic α-Al(Mn,Fe)Si phase is predominant secondary phase in the strip on both strip surface and central area. This results from the increase of solute segregation in liquid phase, especially Si content, during solidification due to the high cooling rate of the HSTRC.

The cubic α-Al(Mn,Fe)Si phase particles mainly observed inside of the cells in the strip near-surface showed spore-like morphology. These particles are considered to be formed as one of the eutectic components from the liquid droplets trapped in the inter-dendrite regions.

There was an obvious difference in the chemical composition concentration of the α-Al(Mn,Fe)Si particles between the strip surface and central area. This is considered to be due to the high Fe segregation into the trapped liquid at the strip central area because of its small partition coefficient in Al.

## References


1) D. G. Eskin, J. Zuidema Jr, V. I. Savran, and L. Katgerman: Mater. Sci. Eng. A, **384** (2004) 232–44
2) T. Haga, K. Tkahashi, M. Ikawaand, and H. Watari: J. Mater. Process. Technol., **153**–**154** (2004) 42–47
3) K. Suzuki, S. Kumai, Y. Saito, and T. Haga: Mater. Trans., **46** (2005) 2602–8
4) M. S. Kim and S. Kumai: Mater. Trans., **52** (2011) 856–61
5) R. Song, Y. Harada, and S. Kumai: Mater. Trans., **59** (2018) 110–16
6) Daisuke Shimosaka: Doctoral Thesis, Tokyo Institute of Technology, (2012)
7) ASTM E1382-97: ASTM Int., **97** (2015) 1–24
8) N. A. Belov, D. G. Eskin, and A. A. Aksenov: *Multicomponent Phase Diagrams: Applications for Commercial Aluminum Alloys*,Elsevier, Oxford, (2005)
9) L.F. Mondolfo: *Aluminum Alloys: Structure and Properties*,Butterworths, (1976)
10) P.N. Anyalabechi, T.N. Rouns, and R.E. Sanders: in *RASELM '91, Conf. Sci. Eng. Light Met.*, K. Hirano, H. Oikawa, and K. Ikeda, eds., The Japan Institute of Light Metals, (1991), 923–28
11) Ch Gras, M. Meredith, and J. D. Hunt: J. Mater. Process. Technol., **167** (2005) 62–72
12) K. Suzuki, S. Kumai, Y. Saito, A. Sato, and T. Haga: Mater. Trans., **45** (2004) 403–6
13) D. Shimosaka, S. Kumai, F. Casarotto, and S. Watanabe: Mater. Trans., **52** (2011) 920–27
14) T. Motoi, K. Fukuoka, and H. Yoshida: J. Japan Inst. Light Met., **48** (1998) 624–28
15) I. Sunagawa: *Crystals: Growth, Morphology, & Perfection*,(2005)
16) T. Gao, Y. Wu, C. Li, and X. Liu: Mater. Lett., **110** (2013) 191–94
17) A. Bjurenstedt, D. Casari, S. Seifeddine, R. H. Mathiesen, and A. K. Dahle: Acta Mater., **130** (2017) 1–9
18) D. T. L. Alexander and A. L. Greer: Acta Mater., **52** (2004) 5853–61

**Table 2-1 Chemical composition of the 3003 aluminum alloy. (in mass %)**

| Alloy | Mn | Fe | Si | Cu | Mg | Cr | Zn | Ti | other | Al |
|---|---|---|---|---|---|---|---|---|---|---|
| 3003 | 1.26 | 0.61 | 0.27 | 0.15 | 0.01 | 0.01 | 0.01 | 0.01 | 0.07 | Bal. |

**Table 2-2 As-cast grain size of each cast products and its corresponding cooling rates.**

| Casting product | Grain size (μm) | Standard deviation | Cooling rate (°C/s) |
|---|---|---|---|
| Wedge-shape steel mold casting (Top) | 155.27 | 28.88 | 5 |
| Wedge-shape steel mold casting (Mid) | 133.02 | 27.07 | 8 |
| DC-casting | 110.19 | 20.07 | * |
| Wedge-shape steel mold casting (Tip) | 91.62 | 15.30 | 31 |
| Copper mold casting | 53.31 | 7.86 | 136 |
| HSTRC strip (surface) | 17.48 | 2.53 | ** |
| Single-roll cast ribbon | 5.78 | 1.03 | *** |

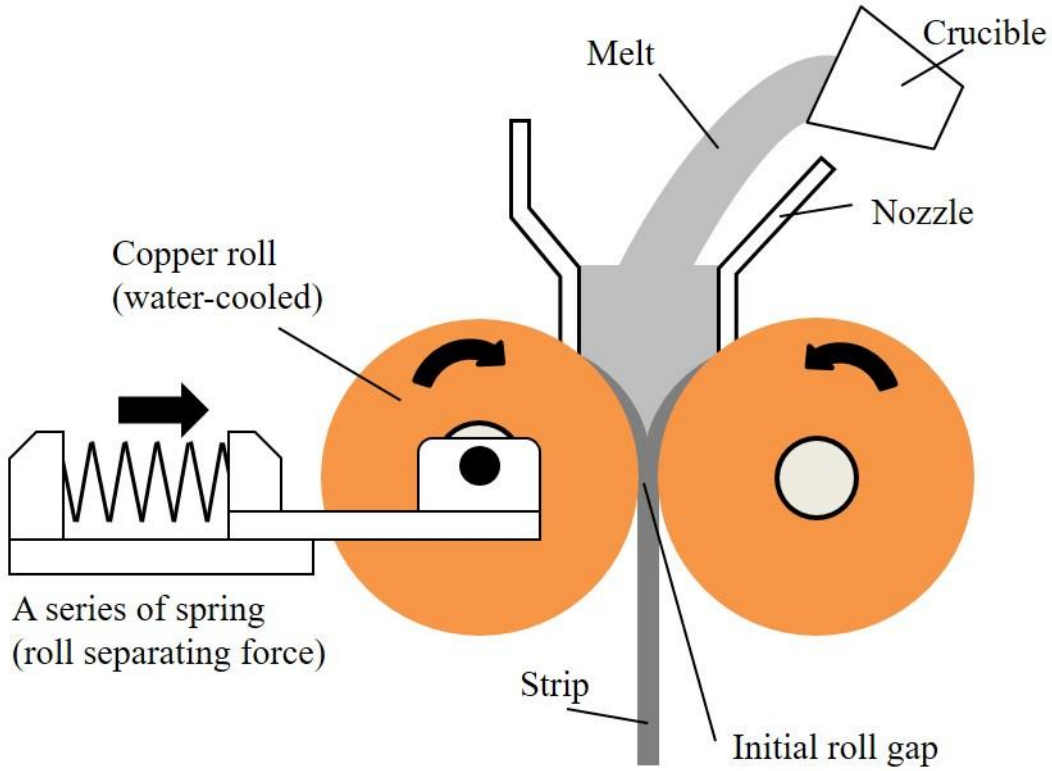


**Fig. 2-1 Schematic illustration of the vertical-type high-speed twin-roll caster.**

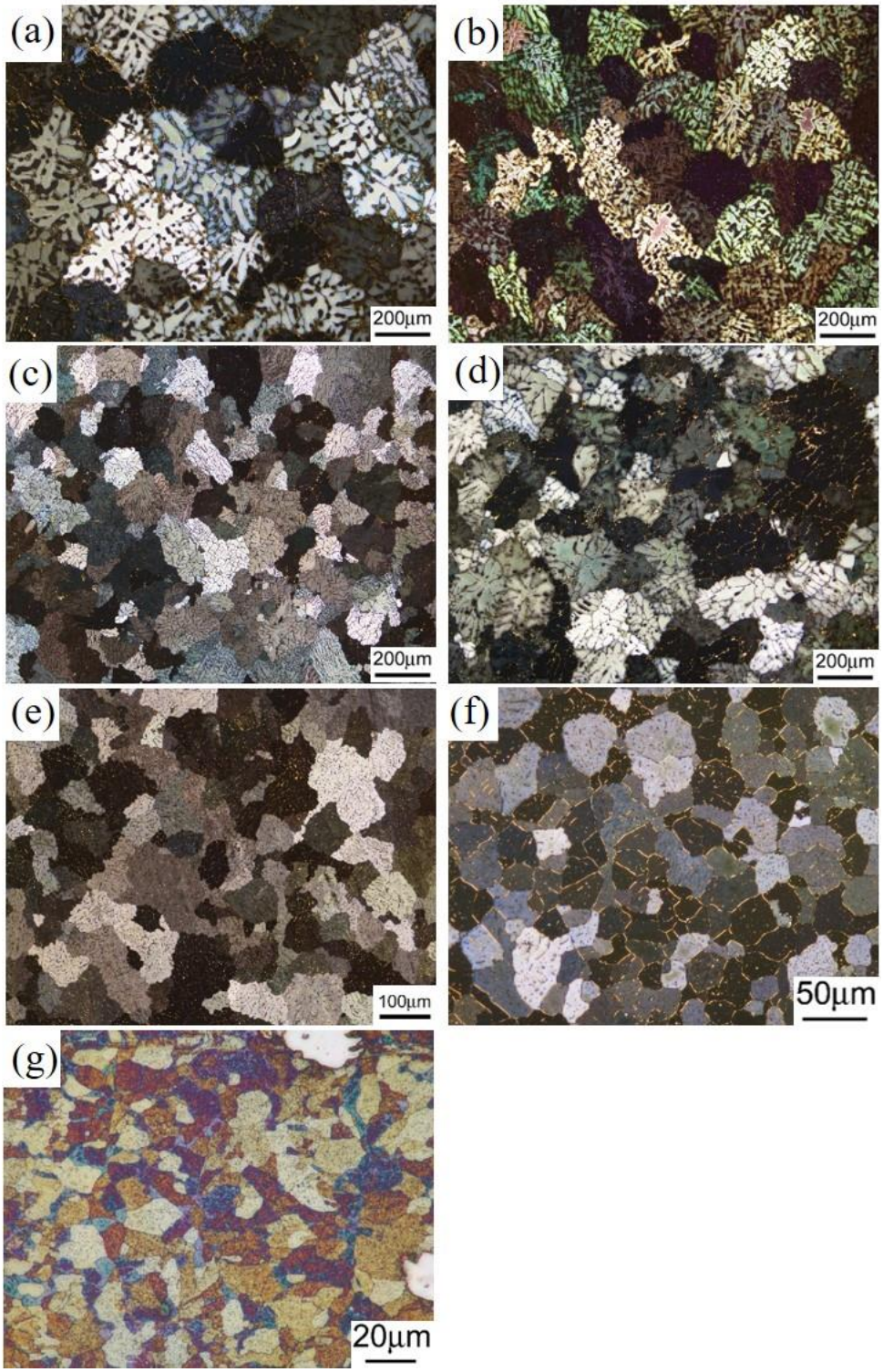


**Fig. 2-2 Polarized light micrographs of the wedge-shape steel mold casting (a) top, (b) middle, (c) tip area, (d) DC-cast sample, (e) copper mold casting, (f) HSTRC strip near-surface, (g) single-roll cast ribbon.**

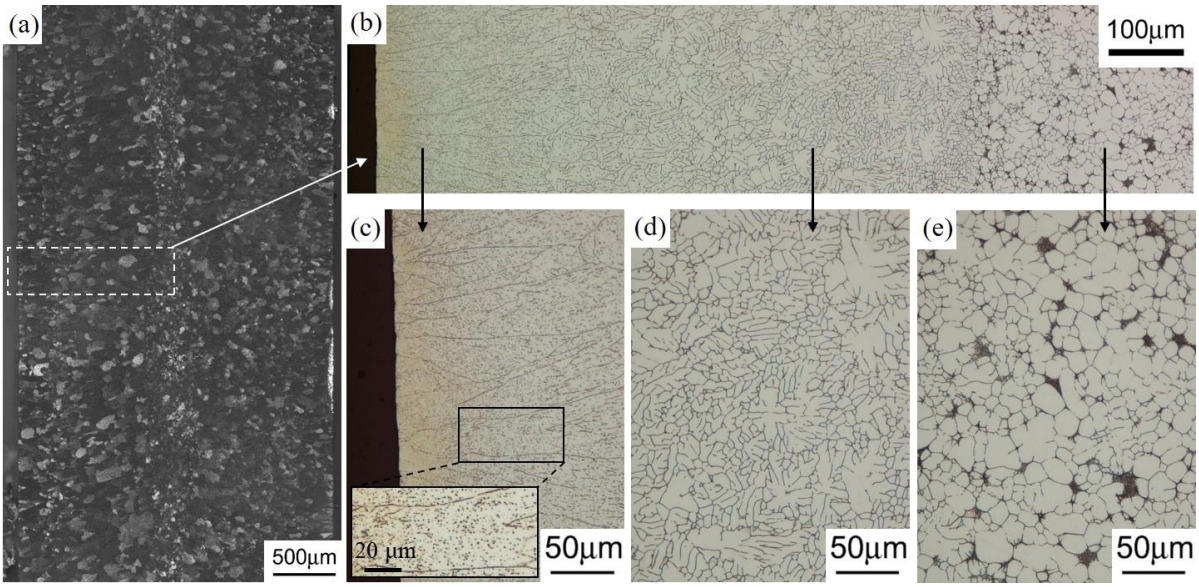


**Fig. 2-3 Optical micrographs of as-cast 3003 aluminum alloy strip. (a) grain structure of the transverse cross section of cast strip, (b) solidified structure of half thickness area, (c) near-surface area, (d) dendrite area, (e) mid-thickness area.**

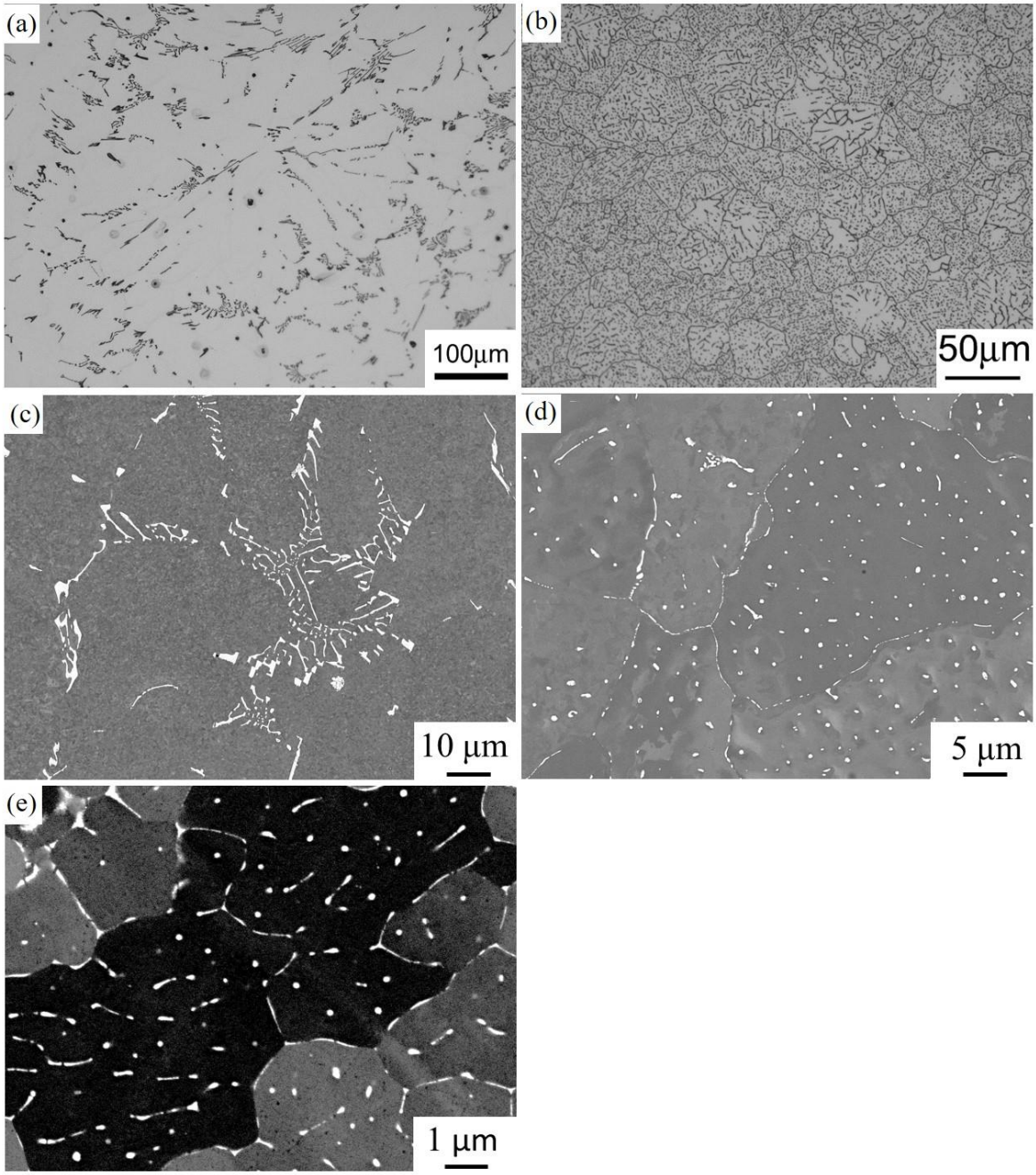


**Fig. 2-4 Secondary particles distribution in DC-cast sample and HSTRC strip. OM images; (a) DC-cast sample, (b) HSTRC strip near-surface. Back-scattered electron images; (c) DC-cast sample, (d) HSTRC strip near-surface, (e) single-roll cast ribbon.**

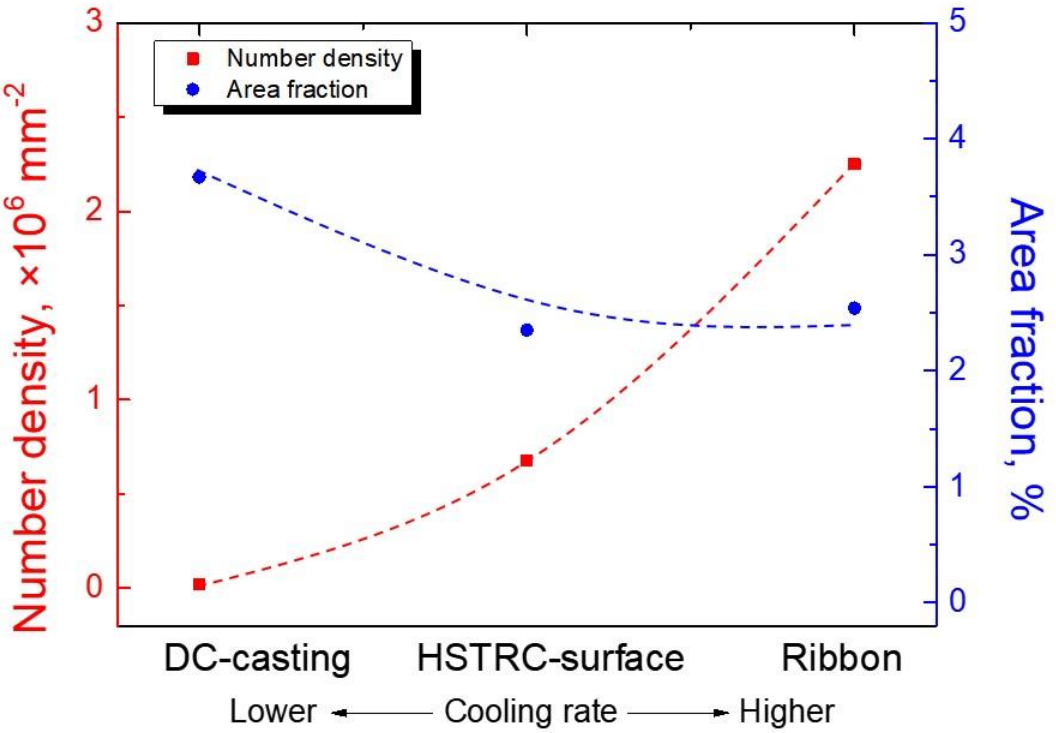


**Fig. 2-5 Comparison of number density and area fraction of secondary particles in each cast products.**

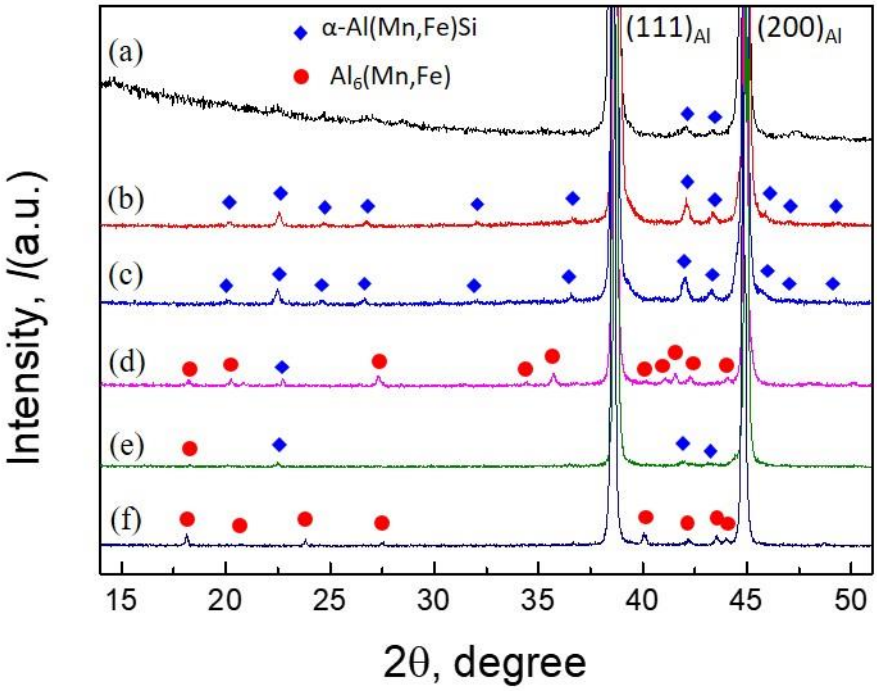


**Fig. 2-6 XRD patterns of 3003 aluminum alloy. (a) single-roll cast ribbon, (b) HSTRC strip surface, (c) HSTRC strip center, (d) DC-casting, (e) copper-mold casting, (f) wedge-shape steel mold casting.**

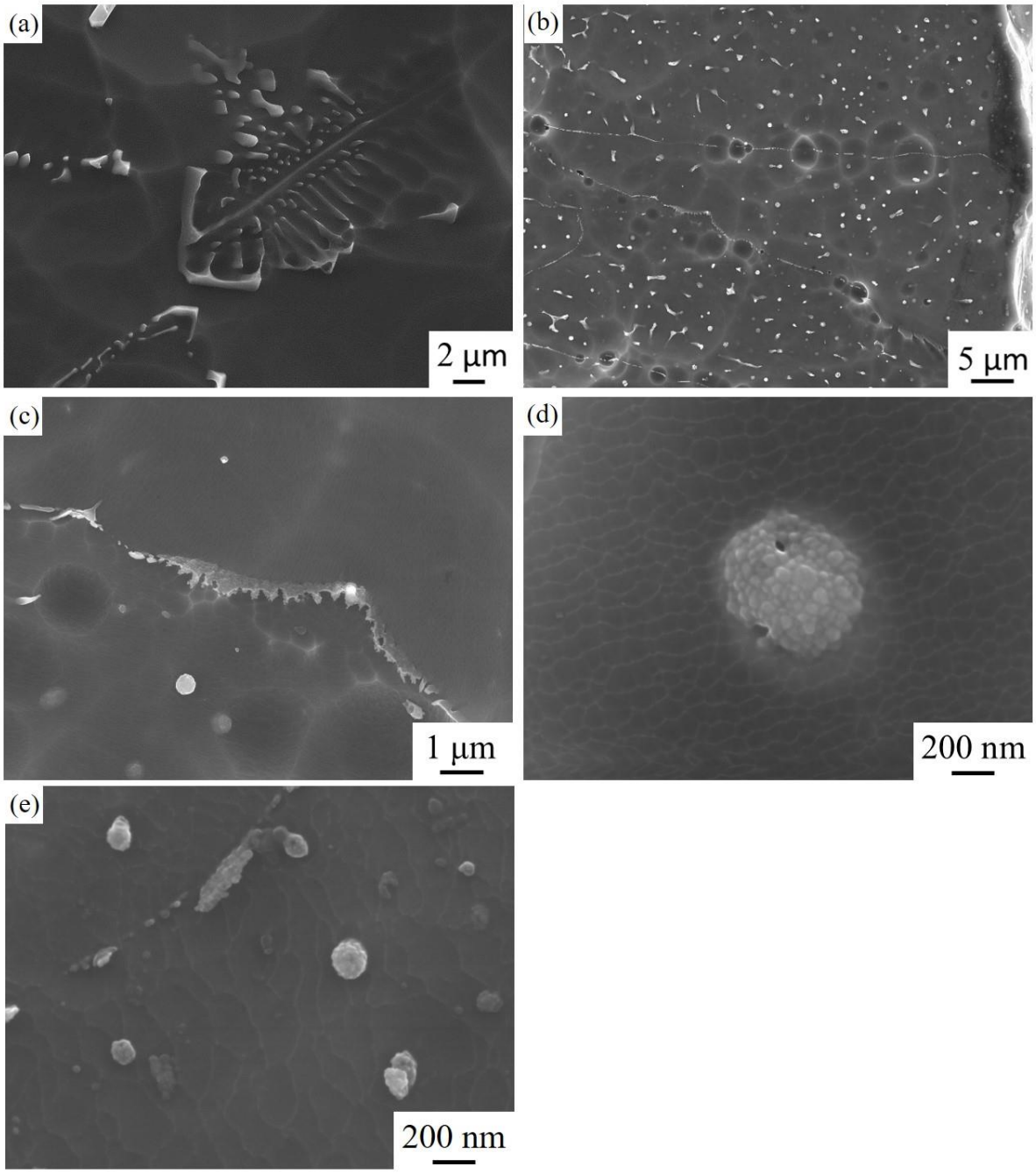


**Fig. 2-7 FE-SEM secondary electron images of deep-etched DC-cast, HSTRC strip surface and single-roll cast ribbon samples (a) script-like eutectic particle in DC-cast sample, (b) HSTRC near-surface area, (c) particles at cell boundary, (d) spore-like inside of cell at near-surface, (e) single-roll cast ribbon.**

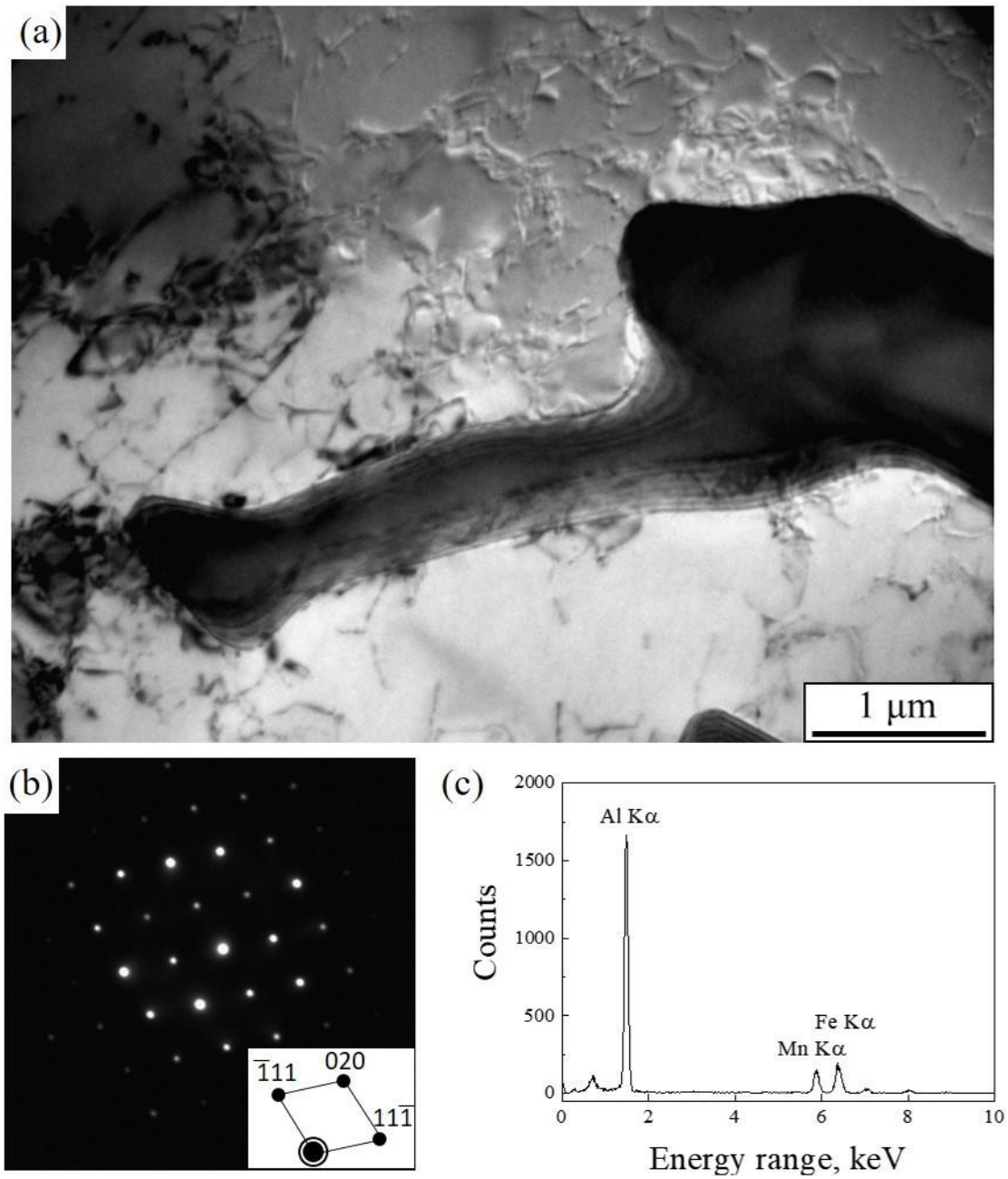


**Fig. 2-8 (a) TEM bright-field image of script-like particle in DC-cast sample, (b) selected area diffraction pattern of the particle in (a) corresponding on a [011] zone axis of $Al_6(Mn,Fe)$, (c) TEM-EDS spectra from the particle in (a).**

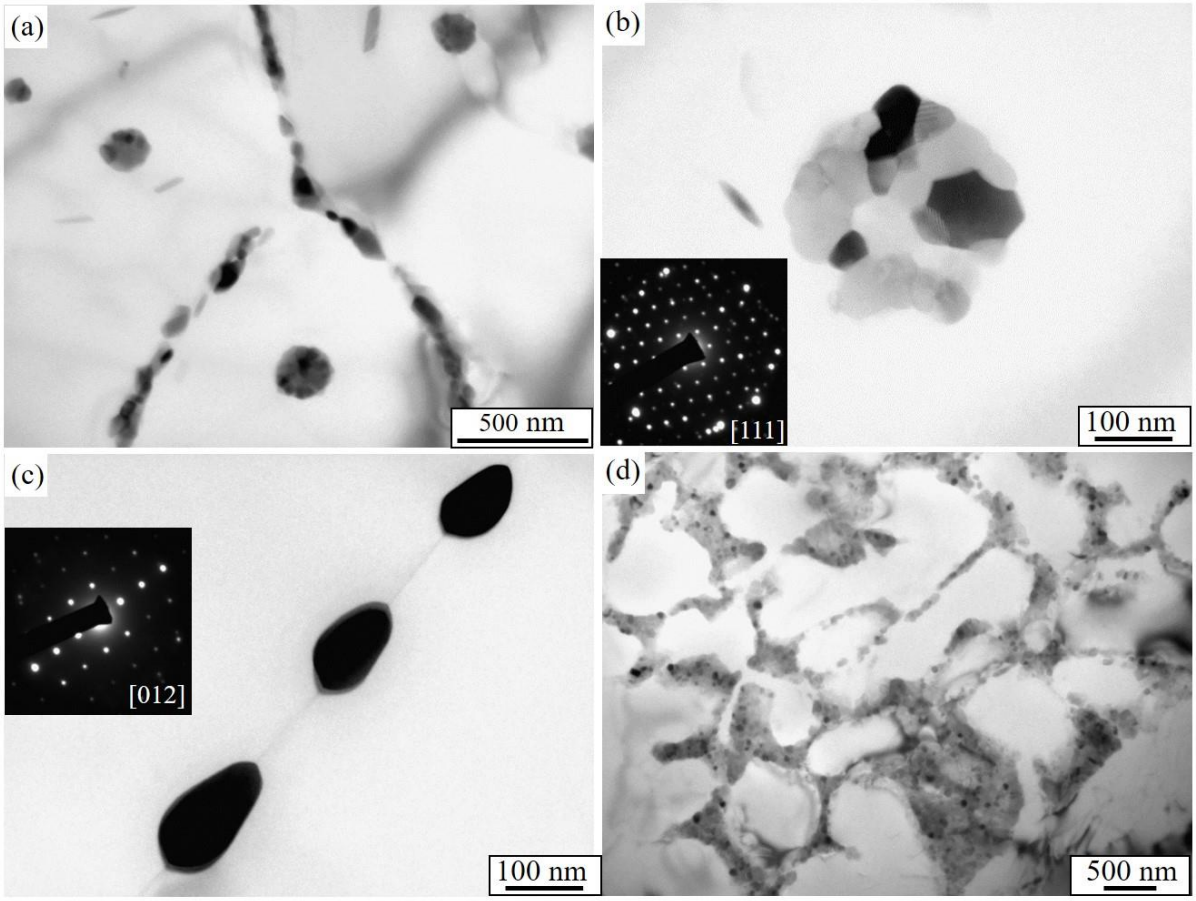


**Fig. 2-9 (a) TEM bright-field image of HSTRC strip near-surface, (b) spore-like α-Al(Mn,Fe)Si particle inside of cell in HSTRC strip near-surface, (c) α-Al(Mn,Fe)Si particles on grain boundary in HSTRC strip near-surface, (d) eutectic constituents in HSTRC strip center area.**

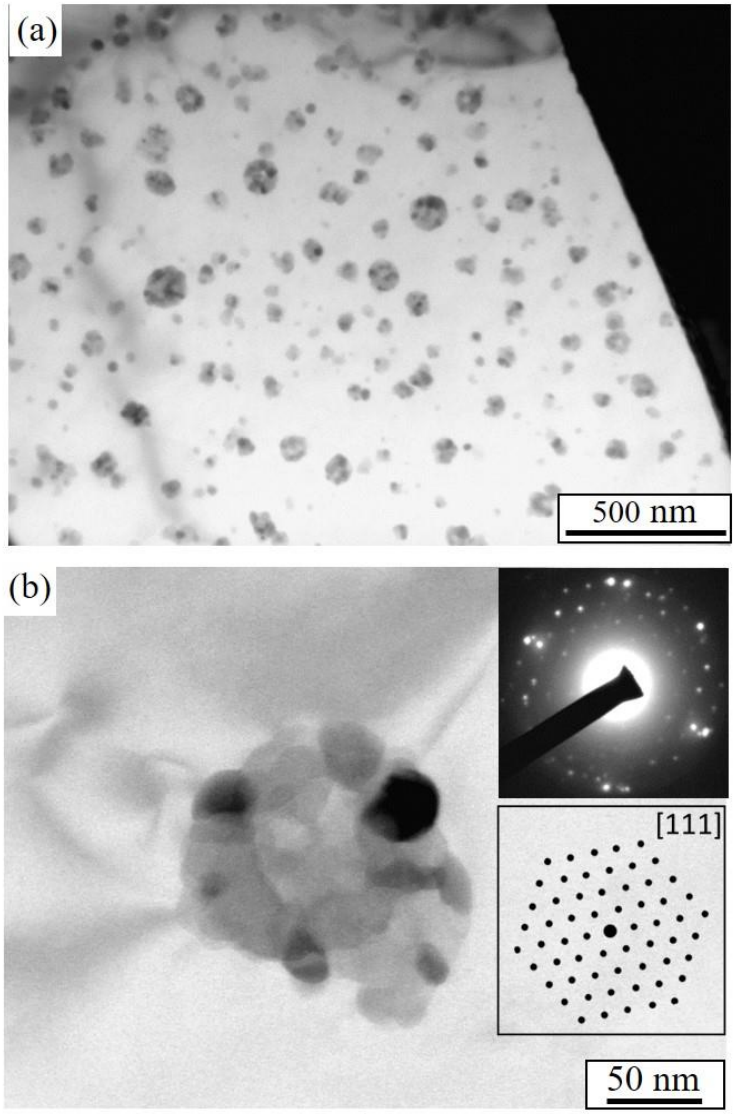


**Fig. 2-10 (a) TEM bright-field image of single-roll cast ribbon, (b) typical spore-like α-Al(Mn,Fe)Si particle in single-roll cast ribbon.**

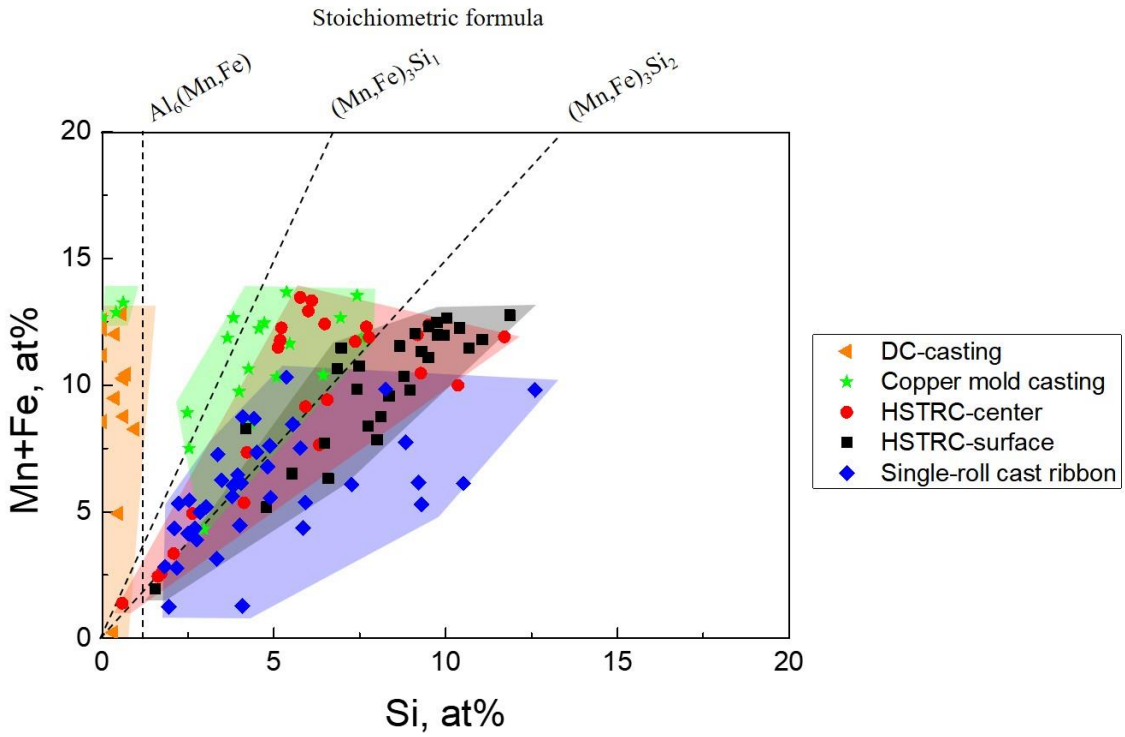


**Fig. 2-11 (Mn+Fe)/Si composition ratio of the secondary particles in each cast products of 3003 aluminum alloy.**

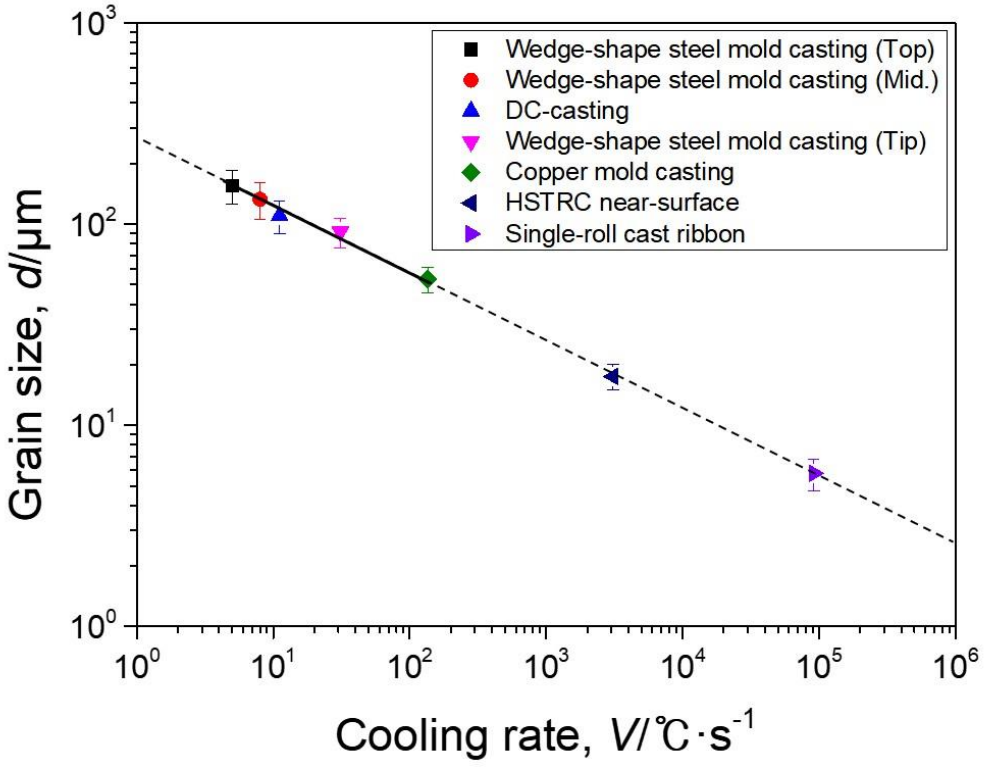


**Fig. 2-12 Correlation between α-Al grain size and cooling rate in 3003 aluminum alloy.**

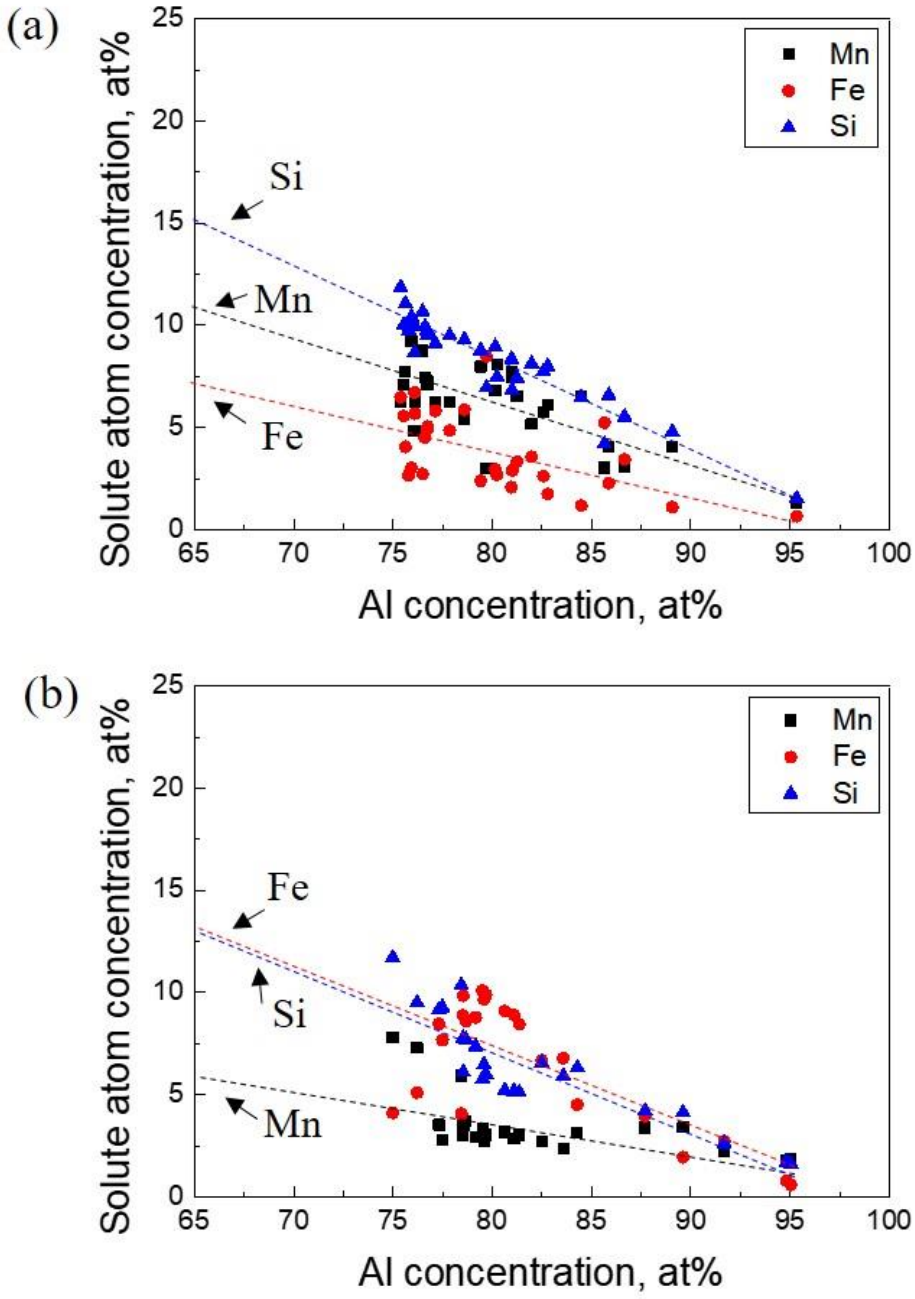


**Fig. 2-13 TEM-EDS results showing relative solute concentration ratio of the secondary particles in HSTRC strip. (a) HSTRC strip surface, (b) HSTRC strip center.**

# Chapter 3 Influence of alloying elements on solidification structure of vertical-type high-speed twin-roll cast Al-Mn based alloy strips

## 3.1. Introduction

In Chapter 2, the effect of cooling rate on solidification structure of 3003 aluminum alloy was investigated. The following experimental results were obtained concerning the microstructural characteristics in 3003 aluminum alloy strip fabricated by vertical-type high-speed twin-roll casting (HSTRC); the 3003 aluminum alloy strip consisted of cell structure, dendritic structure, globular grains and eutectic structure along the strip thickness direction. The kinds, size and morphology of secondary phase and its composition ratio were dependent on the cooling rate during solidification. The cubic α-Al(Mn,Fe)Si was a predominant secondary phase in the vertical-type high-speed twin-roll cast 3003 aluminum alloy strip. The α-Al(Mn,Fe)Si particles showed spore-like morphology, which were considered as one of the eutectic components solidified from the liquid droplets trapped in the inter-dendrite regions. Different (Mn,Fe)/Si composition ratio in the α-Al(Mn,Fe)Si particles was revealed between strip surface and central area due to segregation of solute elements at the strip central area corresponding final solidification part in the strip.

As well as the cooling rate during solidification, the alloy composition also influences on the solidification structure. The solidification type of α-Al *e.g.,* planar-to-dendrite growth, can be varied by its alloy composition. Since the distribution of residual liquid phase is changed by the solidification type of α-Al, distribution of secondary particle can be also changed in the as-cast condition. Furthermore, the kinds, size and morphology of the secondary particles are attributed to the contents of alloying elements. In wrought Al-Mn based alloys, Mn element is a major alloying element, and Fe and/or Si are also commonly included as alloying elements or natural impurities. In practice, as described in Chapter 2, the commercial 3003 aluminum alloy contained several kinds of alloying elements. The alloying elements such as Fe and Si probably change the solidification structure of the commercial 3003 aluminum alloy strip *e.g.,* mushy-type solidification structure, and leading formation of the quaternary α-Al(Mn,Fe)Si phase as secondary particles in the HSTRC strip. However, it is difficult to examine precisely the influence of alloying elements on solidification structure

in vertical-type high-speed twin-roll cast Al-Mn based alloy strip by using the commercial 3003 aluminum alloy.

Influence of alloy composition on solidification structure in Al-Mn based alloy strips fabricated by HSTRC was investigated in this chapter. As major alloying elements, Mn, Fe and Si elements were selected. Binary Al-Mn, ternary Al-Mn-(Fe,Si), and quaternary Al-Mn-Fe,Si alloys were prepared, then grain structure and kinds, distribution of secondary particles in each alloy strip were investigated.

### 3.2. Experimental procedure

Five kinds of Al-Mn based alloy with different of Fe and Si contents were designed. Their chemical compositions are shown in Table 3-1. The Al-Mn binary, Al-Mn-Fe and Al-Mn-Si ternary alloy ingots were produced by Mitsubishi Aluminum Co., Ltd. Two kinds of quaternary alloy were obtained by mixing Al-Mn-Fe and Al-Mn-Si ternary alloy ingots. One is Fe-rich Al-Mn-Fe Si alloy, the other one is Si-rich Al-Mn-Si-Fe alloy. They are referred as AM (Al-Mn), AMF (Al-Mn-Fe), AMS (Al-Mn-Si), AMFS (Al-Mn-Fe-Si) and AMSF (Al-Mn-Si-Fe), respectively.

Figure 3-1 shows a schematic illustration of the vertical-type high-speed twin-roll caster. The casting conditions for each alloy are summarized in Table 3-2. No lubricant was applied on the roll surface. About 2.5 kg of each alloy was melted in the alumina-coated carbon crucible in the electric furnace. Before the pouring, the molten alloy was degassed by Ar gas bubbling of 0.4 L/min for 20 min. After the casting, strip thickness was measured using caliper at the point of 30 mm away from the side-edge of strip.

Optical microscopic observation was carried out on transverse cross sections of the cast strip by using BX51M, Olympus. The polished specimens were etched by the Keller's reagent ($H_2O$:$HNO_3$:HCl:HF = 190:5:3:2 in Vol.%). A NaOH water solution (5%) was used to reveal the morphology of secondary particles. The detailed feature of secondary particles was observed by FE-SEM (JEM-7000F, JEOL). Phase identification of the secondary particles was performed using X-ray diffractometer (RINT-2100, Rigaku) with Cu $K_\alpha$ ($\lambda$ = 1.54 Å) radiation.

## 3.3. Results

### 3.3.1. Solidification microstructure with various alloy composition in vertical-type high-speed twin-roll cast strips

Figure 3-2 shows the cross-section of each alloy strip. The grain structure is roughly divided into two types; The AM alloy strip showed columnar grains in the near-surface region as shown in Fig. 3-2 (a). The columnar grains grew toward the central area. The similar grain structure was exhibited in a pure aluminum strip as shown in Fig. 3-2 (f). On the other hand, for AMF, AMS, AMFS and AMSF alloy strips, columnar grains grew from both near-surfaces, and they were replaced by the equiaxed grains. A central band structure was also observed in the mid-thickness region. The grain structure was similar to 3003 aluminum alloy strip in Chapter 2. The central band structure is commonly observed in other alloys strip fabricated by HSTRC[1-5]. A common feature of the alloys is wide freezing temperature range.

Figure 3-3 shows the stable thickness of each alloy strip. The AMS alloy strip showed the largest thickness. The thickness of other alloy strips was almost the same. Besides the alloy composition, several casting parameters can affect the strip thickness in the HSTRC, such as melt superheating, solidification length, roll rotation speed, etc. In the present study, the casting was conducted under the equivalent conditions. Sufficient melt-head, corresponding hydrostatic pressure by the melt to roll surfaces, was also supplied during the casting. Thus, the effect of casting conditions on the strip is considered to be negligible.

### 3.3.2. Secondary particle distribution in vertical-type high-speed twin-roll cast alloy strips

Figure 3-4 shows the microstructure of the strip near-surface area of the alloy strips. For AM, it is hard to observe any secondary particles at the strip near-surface. For AMF, AMS, AMFS and AMSF, fine etch pits corresponding to the secondary particles were observed. The AMS and AMSF showed cellular structure, whereas AMF and AMFS showed dendrite structure, respectively.

The microstructure of the strip central area is shown in Fig. 3-5. As shown in Fig. 3-2 (a), there is no central band structure of α-Al globular grains in AM. In contrast to that, globular

grains and eutectic structure are observed at the strip central area in AMF, AMS, AMFS and AMSF. There is no specific difference in size of α-Al globular grains. Whereas, AMF and AMFS (Fe-rich) show a relatively large amount of eutectic structure in the strip central area than that of AMS and AMSF (Si-rich).

Figure 3-6 shows the XRD pattern results of the near-surface area HSTRC strips. In the AM, only $Al_6Mn$ phase was detected as a secondary phase. In the AMF, three kinds of secondary phase were detected; $Al_5Fe_2$, $Al_{13}Fe_4$ and $Al_6(Mn,Fe)$. The AMS showed α-AlMnSi, $Al_6Mn$ and Si. In the quaternary alloys strip, α-Al(Mn,Fe)Si phase was predominant in the strip near-surface area. Weak Si peak was also detected in the relatively Si-rich AMSF.

Figure 3-7 shows the XRD pattern results of the central area HSTRC strips. The kinds of secondary phase were different from those of the near-surface. In the central area of AM, peaks of secondary phase were not detected. In AMF, Mn-containing secondary phases of the $Al_6(Mn,Fe)$ and $Al_6Mn$ were detected; $Al_6(Mn,Fe)$ and $Al_6Mn$ are isomorphic, orthorhombic structure. The $Al_5Fe_2$ and $Al_{13}Fe_4$, which were detected in AMF near-surface area, were not observed in the central area. In central area of AMS, α-AlMnSi and Si were detected, whereas the $Al_6Mn$ was not detected. In the quaternary alloys strip, the α-Al(Mn,Fe)Si was predominant in the central area. $Al_6(Mn,Fe)$ and Si were also detected in the strip central area of AMFS (Fe-rich) and AMSF (Si-rich), respectively.

### 3.3.3. Characteristic of secondary particle morphology in vertical-type high-speed twin-roll cast alloy strips

In order to understand the detailed nature of the constituent particles, 3-dimensional morphology was observed using deep-etching technique as shown in Figs. 8 to 10. In the near-surface of AMF, constituent particles are located at cell/inter-dendrite interface, and inter-connected along the strip thickness direction as shown in Fig. 3-8 (a). In the near-surface of AMS, constituent particles with dendritic morphology were mainly observed along to the cell boundaries as shown in Fig. 3-8 (c). Inside of the cells, fine constituent particles, below 1 μm in diameter, were observed as shown in Fig. 3-8 (d). The morphology of the fine particles inside of the cells were irregular; composite agglomerates of spore-like and/or polygonal particles.

Figure 3-9 shows FE-SEM images of the particles in the central area of AMF and AMS. In

AMF, lamella-like eutectic particles are mainly observed in the strip central area as shown in Fig. 3-9 (b). Also, some primary $Al_6$(Mn,Fe) particles are observed as shown in Fig. 3-9 (c). For AMS, dendritic eutectic particles are mainly observed in the strip central area. They are enclosed the α-Al grains as shown in Fig. 3-9 (e). Primary polygonal Si particles are also observed as shown in Fig. 3-9 (f). Their size is around 3 μm in ferret diameter that is much larger than that of the particles inside of cells at the near-surface area (see Fig. 3-8 (d)). Primary α-AlMnSi particles are also observed in central area as shown in Fig. 3-9 (g). They showed hopper-skeletal morphology. Bjurenstedt et al.[6] also reported α-Al(Fe,Mn,Cr)Si particles of similar morphology, hopper rhombic dodecahedron, in Al-Si based alloy (equivalent to A380, a commercial high pressure die casting aluminum alloy). The crystallized primary particles are considered not to be formed at the central area, but formed in the melt-head in advance, then they are gathered at the central area.

Figure 3-10 shows the FE-SEM images of the particles in AMFS and AMSF. In the near-surface area, the particles with spore-like morphology were observed in both AMFS and AMSF as shown in Fig. 3-10 (b) and (f). This morphology of the particles was also observed in 3003 aluminum alloy strip as introduced in Chapter 2. Based on the XRD result, the spore-like particles are considered to be α-Al(Mn,Fe)Si. These particles were located in grain-interiors at inter-dendrite regions. Thus, these particles were also considered as one of the eutectic components. Meanwhile, dendritic particles are observed in AMSF in the near-surface area as shown in Fig. 3-10 (e). In the central area, eutectic particles are observed as shown in Fig. 3-10 (c) and (g). Due to low solubility of Fe element in Al matrix, most of Fe elements are consumed to form constituent particles. Therefore, much amount of eutectic is considered to be observed at the central area of AMFS. The morphology of the eutectic particles was massive-type in AMFS, and skeletal-type in AMSF, respectively.

## 3.4. Discussion

### 3.4.1. Solidification structure and strip thickness

Kim et al.[4] examined the relationship between the total thickness and Si composition of Al-Si binary alloy strip. They showed that the alloy with wider freezing temperature range exhibited larger strip thickness. For AM, the freezing temperature range is less than 5 ℃. In contrast to that, according to the ternary Al-Mn-Si phase diagram, the freezing temperature

range for the composition of the AMS alloy is around 60 ℃[7]. Such a wide freezing temperature range can result in not only the formation of the α-Al grains in the melt-head, but also separation of α-Al dendrite from the solidifying shells. If the free-crystallized primary α-Al grains in the melt-head gather at the strip central area, the central band structure is formed, and the increase of total strip thickness possibly occurs.

The central band structure was also observed in AMF as shown in Fig. 3-2 (b). According to ternary Al-Mn-Fe phase diagram[8], the freezing temperature range for the composition of AMF is less than 5 ℃. Thus, the formation of the α-Al crystals in the melt-head is not considered. Instead, since the low Fe solubility in Al solid, the enrichment of Fe at the solid/liquid interface may occur. This results in the formation of unstable solid/liquid interface, and equiaxed dendritic solidification structure. In this case, fragmentation of α-Al dendrite from the solidifying shells can occur at the kiss point of growing solid shells from the both rolls. The fragmented α-Al dendrite branches can form the central band structure. However, these fragmented α-Al dendrite branches originally come from the broken solidified shells. Therefore, the increase of thickness is balanced to the loss of thickness. So the total thickness change does not occur in AMF.

### 3.4.2. Evolution of secondary particles during HSTRC

During solidification, solute elements segregate at the growth front of solid phase, inter-dendritic regions and grain boundaries. The constituent particles were formed from the solute-rich liquid phase in the last stage of solidification. Thus, it is considered that the kind of the constituent particles is determined by the local composition of the liquid and cooling conditions (*e.g.* cooling rate). According to the phase diagram of Al-Mn-Fe alloy system[9,10], $Al_3Fe$, $Al_{13}Fe_4$ and $Al_6(Mn,Fe)$ phase can be formed in AMF during solidification. The XRD result revealed that the $Al_5Fe_2$ phase was dominant in the near-surface area. As for the HSTRC, the residual liquid droplets are easily trapped at the inter-dendritic regions, due to the high cooling rate. In this stage, compared with Mn, Fe is considered to segregate in the liquid droplets due to its smaller partition coefficient and lower solubility in Al matrix. Thus, Fe-rich constituent particles such as $Al_5Fe_2$ and $Al_{13}Fe_4$ phase are mainly formed rather than Mn-containing $Al_6(Mn,Fe)$ phase. Meanwhile, in the central area, the residual liquid phase may undergo the eutectic reaction, which forms the $Al_6(Mn,Fe)$ phase.

For quaternary alloy strips in both AMFS and AMSF, α-Al(Mn,Fe)Si phase was predominant secondary phase. For strip surface, the residual liquid is mainly trapped at inter-dendrite regions. Since the high cooling rate of the HSTRC, substantial partitioning of solute elements into the residual liquid droplets can occur. Thus, the quaternary α-Al(Mn,Fe)Si phase was formed, though other phases can be formed as well[8]. In contrast to the surface, the central area is the final solidification part of strip. In this case, the composition of residual liquid is dependent on not only cooling rate, but also initial alloy compositions. Thus, the local composition of residual liquid phase should be different between in AMFS and AMSF; Fe-rich residual liquid in AMFS, Si-rich residual liquid in AMSF, respectively. As a result, it is assumed that the formation of secondary phase differs from those of near-surface area that $Al_6$(Mn,Fe) and α-Al(Mn,Fe)Si phase in central area of AMFS and Si and α-Al(Mn,Fe)Si phase in central area of AMSF, respectively.

### 3.5. Conclusions

Al-Mn based alloy strips with various alloying elements were produced by vertical-type high-speed twin-roll casting. Pure Al and Al-Mn binary alloy strip showed skin-type solidification structure, whereas Al-Mn-(Fe,Si) ternary and Al-Mn-Fe-Si quaternary alloys showed mushy-type solidification structure due to the increase a freezing temperature range of the alloy. The crystallized α-Al grains formed in the melt were considered to increase the resultant total thickness of the strip.

Secondary particles were not formed in binary Al-1.2Mn (in mass%) alloy strip. In Al-1.2Mn-1.0Fe and Al-1.2Mn-1.0Si ternary alloy strip, the Fe favored to form $Al_6$(Mn,Fe) phase, whereas Si resulted in formation of α-AlMnSi phase. Some primary constituent particles; $Al_6$(Mn,Fe) particles in Al-1.2Mn-1.0Fe alloy, α-AlMnSi and polygonal Si particles in Al-1.2Mn-1.0Si alloy were observed in the central area. These particles were considered to be formed in the melt-head before the α–Al solidification starts.

In quaternary alloys, the α-Al(Mn,Fe)Si phase was dominant at the near-surface area of the strip. The kinds of secondary phase in the central area was dependent on the alloy compositions; α-Al(Mn,Fe)Si and Si phase in the central area of Si-rich Al-Mn-Si-Fe alloy, α-Al(Mn,Fe)Si and $Al_6$(Mn,Fe) phase in the central area of Fe-rich Al-Mn-Fe-Si alloy. It is considered to be due to difference local composition of residual liquid phase at the final

solidification part.

## References


1) K. Suzuki, S. Kumai, Y. Saito, A. Sato, and T. Haga: Mater. Trans., **45** (2004) 403–6
2) K. Suzuki, S. Kumai, Y. Saito, and T. Haga: Mater. Trans., **46** (2005) 2602–8
3) K. Suzuki, S. Kumai, K. Tokuda, T. Miyazaki, A. Ishihara, Y. Nagata, and T. Haga: Mater. Sci. Forum, **519**–**521** (2006) 1821-26
4) M. S. Kim and S. Kumai: Mater. Trans., **52** (2011) 856–61
5) D. Shimosaka, S. Kumai, F. Casarotto, and S. Watanabe: Mater. Trans., **52** (2011) 920–27
6) A. Bjurenstedt, D. Casari, S. Seifeddine, R. H. Mathiesen, and A. K. Dahle: Acta Mater., **130** (2017) 1–9
7) G. Petzow and G. Effenberg: *Ternary Alloys. A Comprehensiforumve Compendium of Evaluated Constitutional Data and Phase Diagrams.*,VCH Verlagsgesellschaft, Vol. 7 (1993)
8) N. A. Belov, D. G. Eskin, and A. A. Aksenov: *Multicomponent Phase Diagrams: Applications for Commercial Aluminum Alloys*,Elsevier, Oxford, (2005)
9) G. Petzow and G. Effenberg: *Ternary Alloys. A Comprehensive Compendium of Evaluated Constitutional Data and Phase Diagrams.*,VCH Verlagsgesellschaft, Vol. 5 (1992)
10) B.B. Lindahl and M. Selleby: Calphad Comput. Coupling Phase Diagrams Thermochem., **43** (2013) 86–93

**Table 3-1 Chemical compositions of each alloys. (in mass %)**

| Alloy | Mn | Fe | Si | other | Al |
|---|---|---|---|---|---|
| AM | 1.190 | 0.001 | 0.001 | 0.002 | Bal. |
| AMF | 1.190 | 0.970 | 0.002 | 0.001 | Bal. |
| AMS | 1.130 | 0.003 | 0.920 | 0.002 | Bal. |
| AMFS | 1.18 | 0.73 | 0.23 | 0.001 | Bal. |
| AMSF | 1.14 | 0.25 | 0.68 | 0.001 | Bal. |

**Table 3-2 HSTRC conditions for each alloy.**

| Condition | Alloy | | | | |
|---|---|---|---|---|---|
| | AM | AMF | AMS | AMFS | AMSF |
| Melt superheating (℃) | 15 | 15 | 15 | 15 | 15 |
| Roll rotation speed (m/min) | 60 | 60 | 60 | 60 | 60 |
| Solidification length (mm) | 100 | 100 | 100 | 100 | 100 |
| Roll separating force (kN) | 20 | 20 | 60 | 20 | 20 |
| Initial roll gap (mm) | 1.5 | 1 | 1 | 1 | 1 |

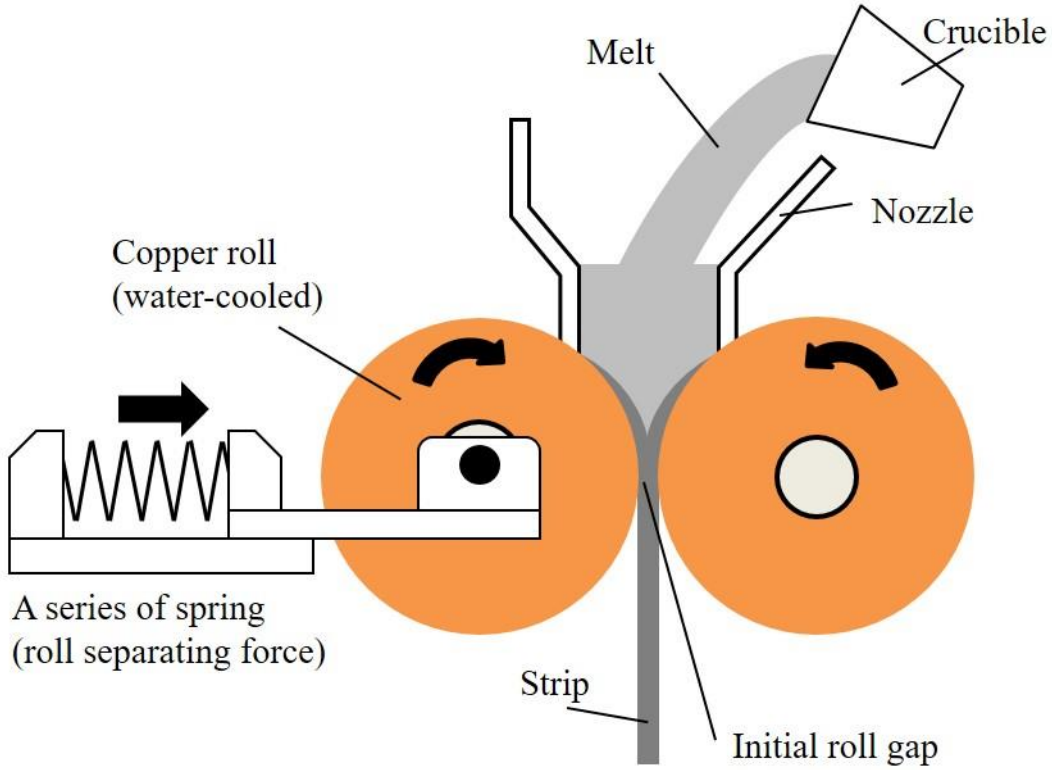


**Fig. 3-1 Schematic illustration of the vertical-type high-speed twin-roll caster.**

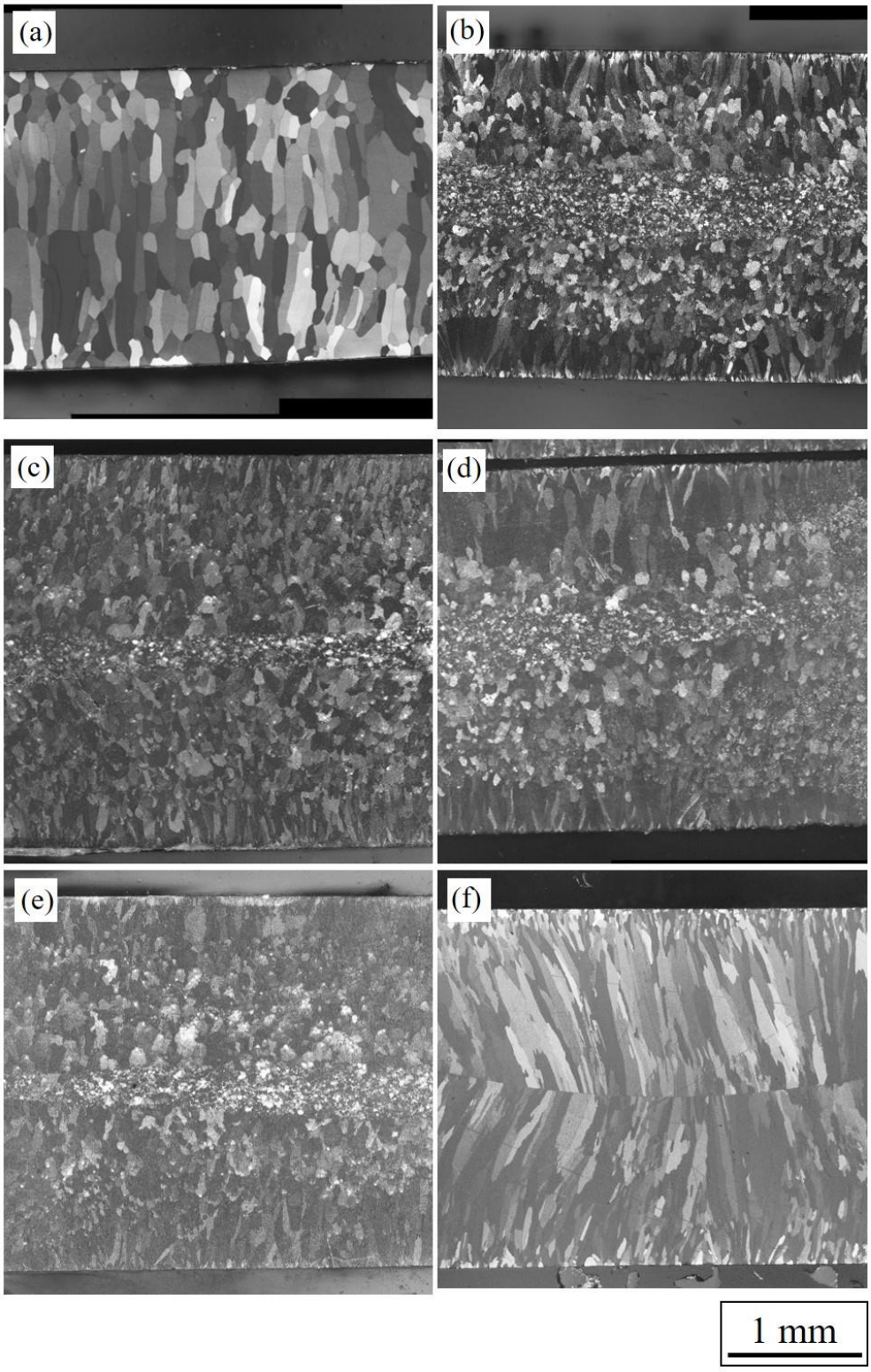


**Fig. 3-2 Grain structure of each Al-Mn based alloy strip. (a) AM, (b) AMF, (c) AMS, (d) AMFS, (e) AMSF, (f) pure Al.**

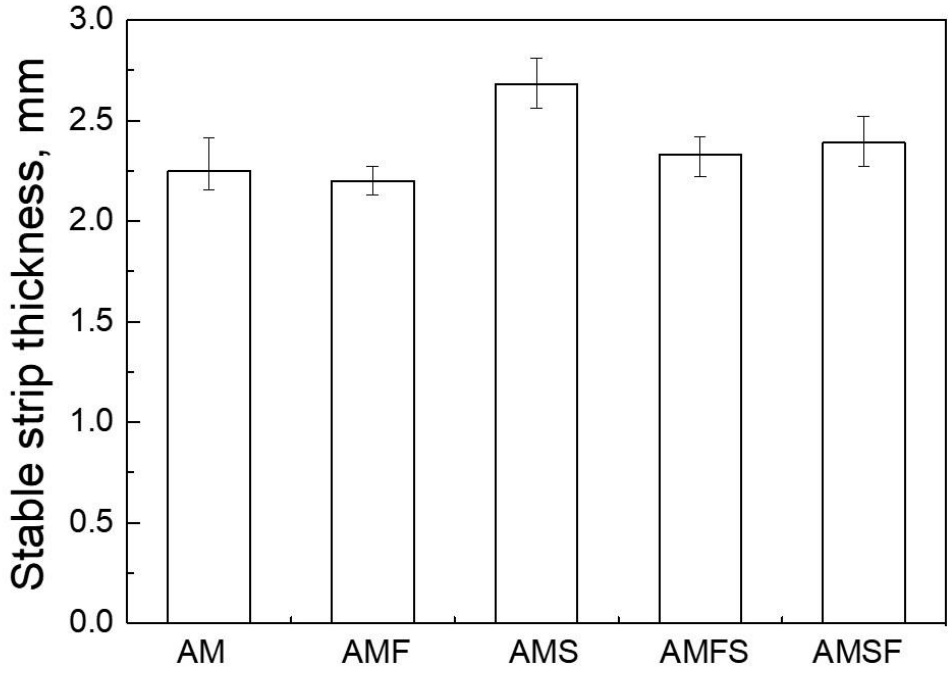


**Fig. 3-3 Stable strip thickness of each alloy strip.**

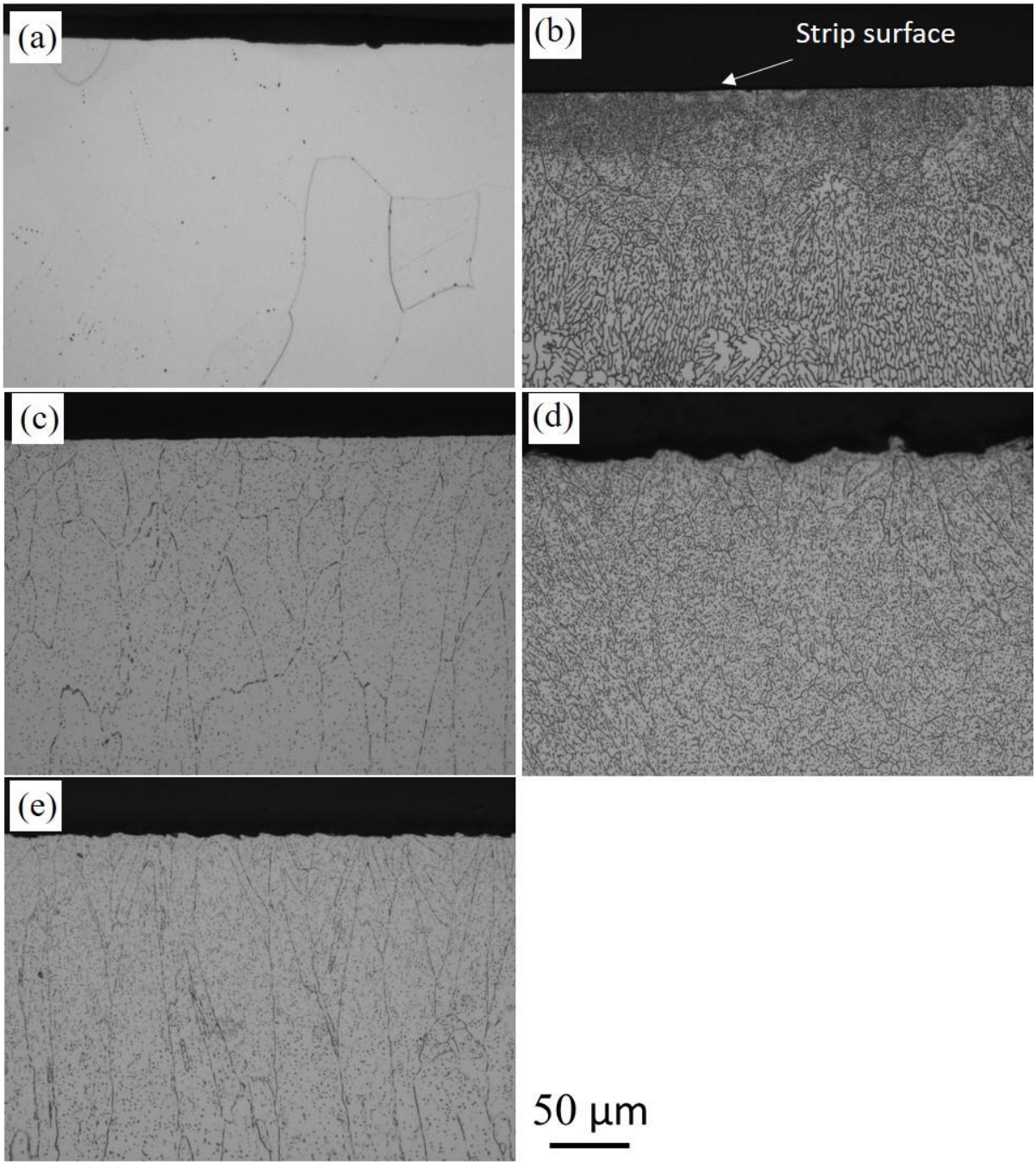


**Fig. 3-4 Microstructure of the HSTRC near-surface area of each strip. (a) AM, (b) AMF, (c) AMS, (d) AMFS, (e) AMSF.**

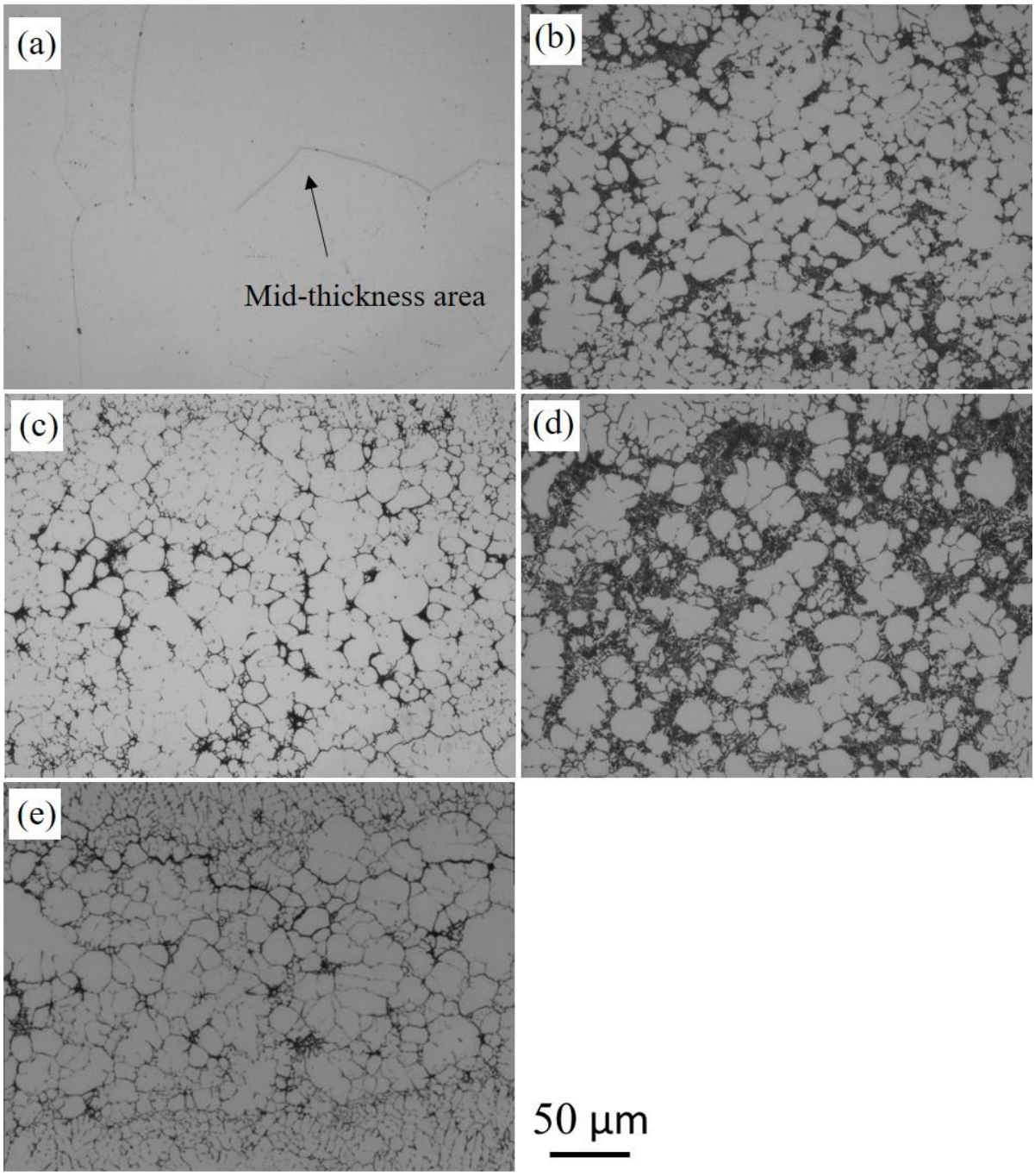


**Fig. 3-5 Microstructure of the HSTRC central area of each strip. (a) AM, (b) AMF (c) AMS, (d) AMFS, (e) AMSF.**

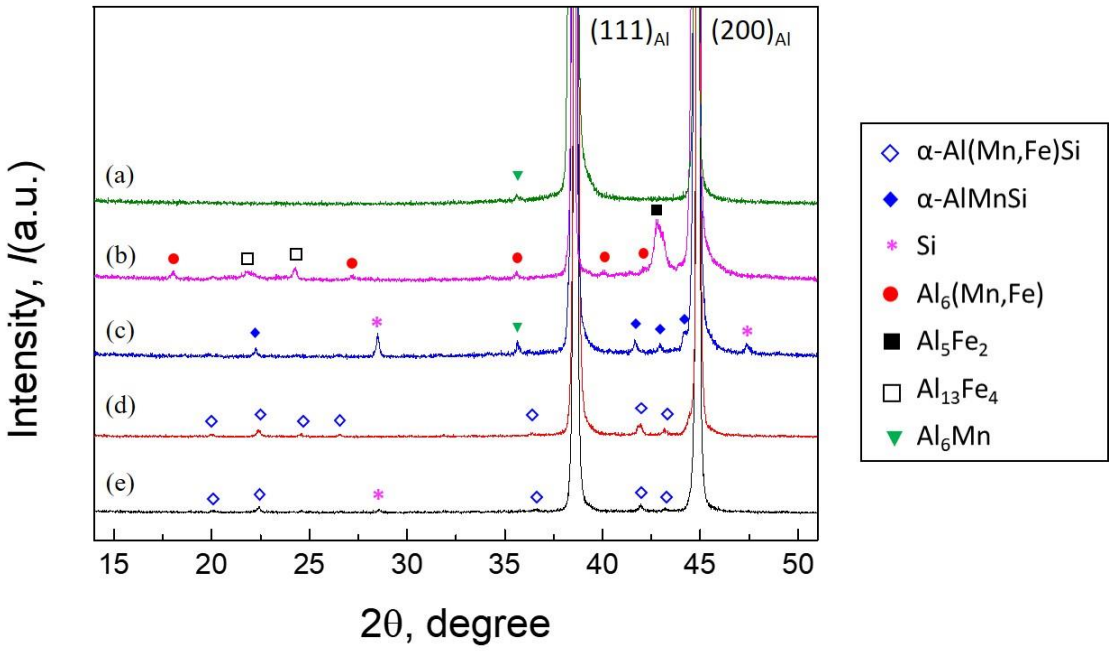


**Fig. 3-6 XRD patterns for strip near-surface. (a) AM, (b) AMF (c) AMS, (d) AMFS, (e) AMSF.**

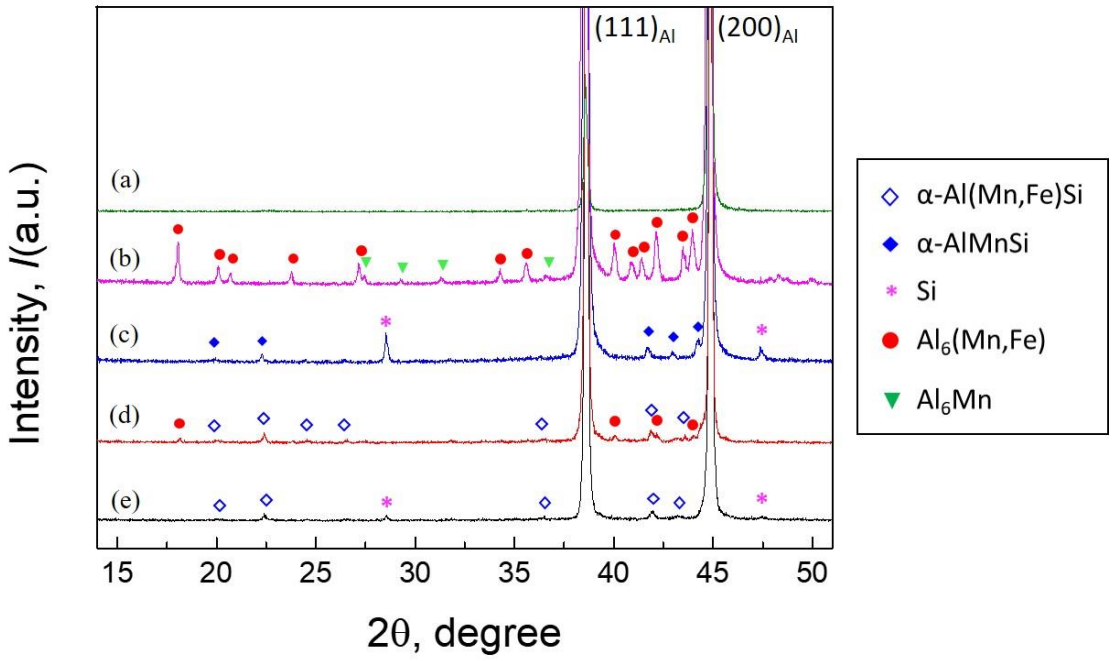


**Fig. 3-7 XRD patterns for strip central area. (a) AM, (b) AMF (c) AMS, (d) AMFS, (e) AMSF.**

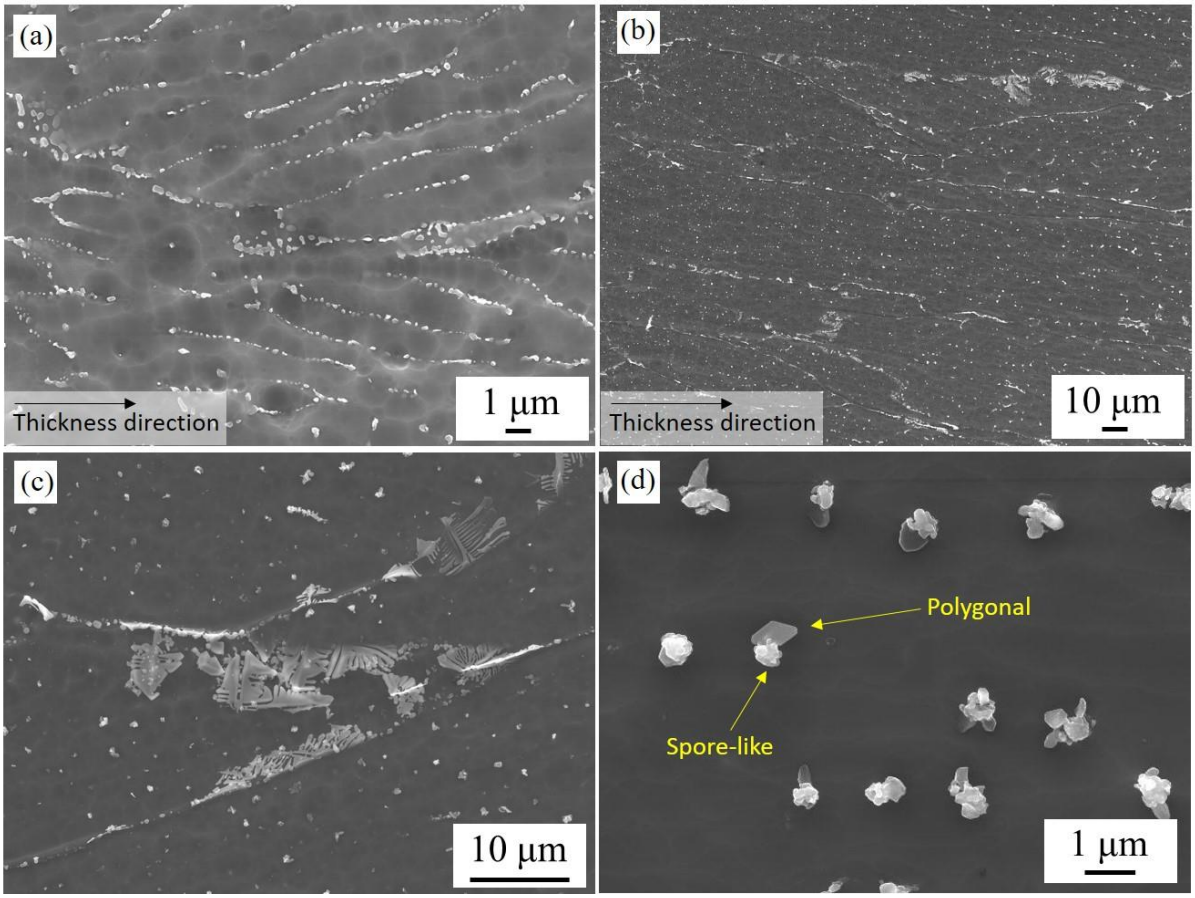


**Fig. 3-8 FE-SEM secondary electron images of deep-etched AMF and AMS strip near-surface area. AMF; (a) near-surface. AMS; (b) near surface, (c) dendritic morphology particle at boundaries, (d) irregular morphology particles inside of cells.**

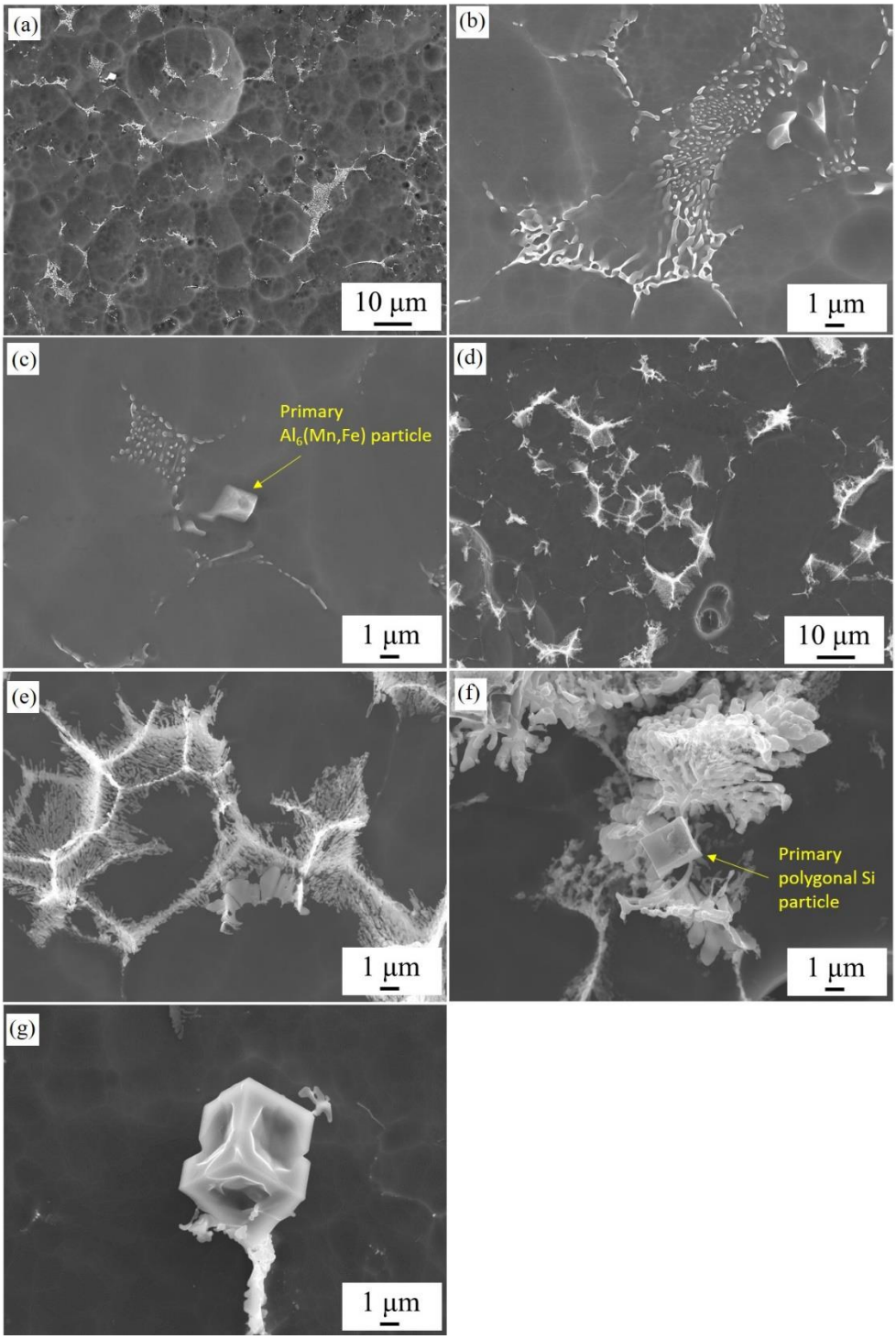


**Fig. 3-9 FE-SEM secondary electron images of deep-etched AMF and AMS strip central area. AMF; (a) central area, (b) eutectic particles, (c) primary $Al_6$(Mn,Fe) particle. AMS; (d) central area, (e) eutectic particle, (f) primary Si particle, (g) primary α-AlMnSi particle.**

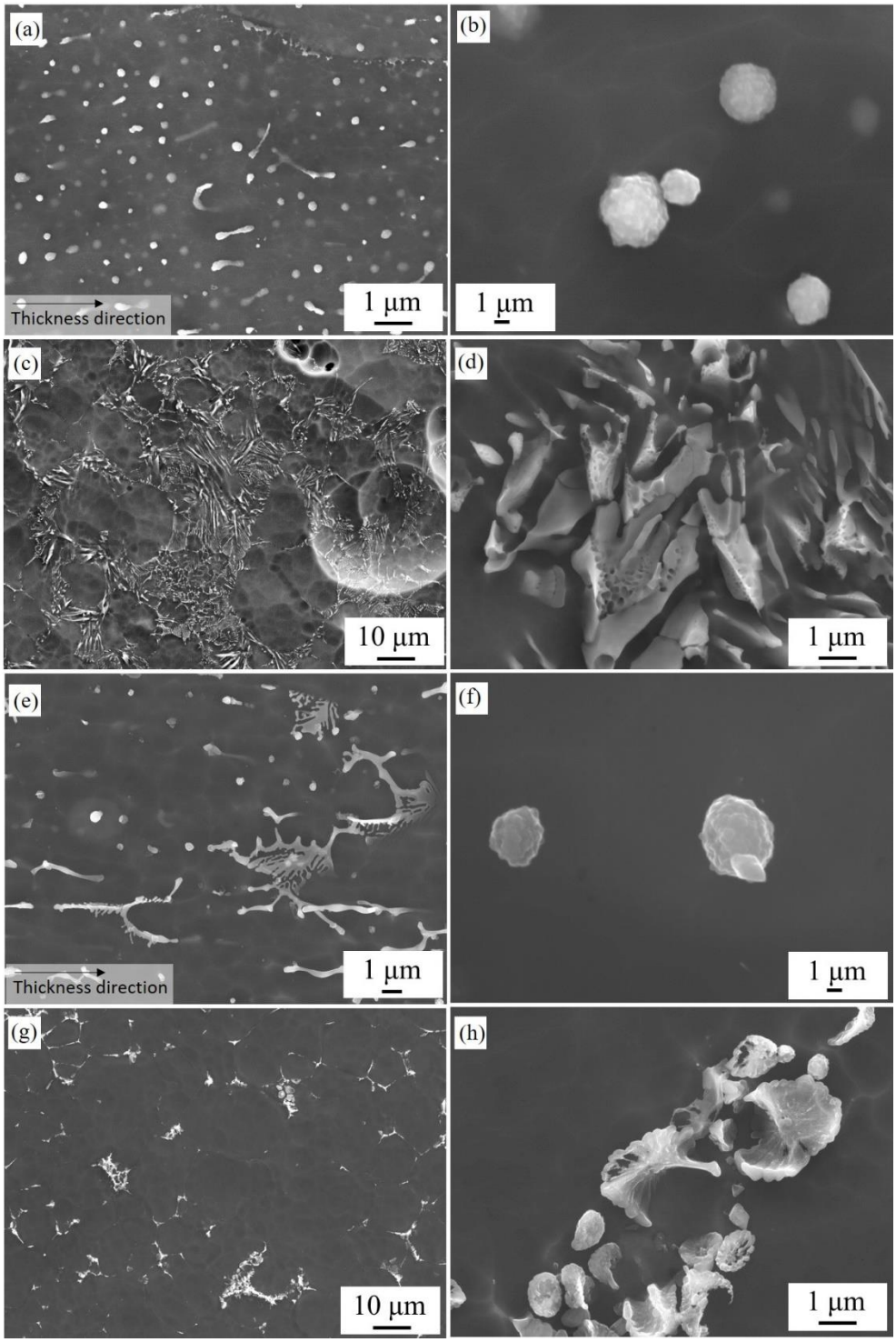


**Fig. 3-10 FE-SEM secondary electron images of deep-etched AMFS and AMSF strip. AMFS; (a) near-surface, (b) spore-like particle inside of cells, (c) central area, (d) typical eutectic particles in central area. AMSF; (e) near surface, (f) spore-like particle inside of cells, (g) central area, (h) typical eutectic particles in central area.**

# Chapter 4 Influence of cooling rates on formation behavior of secondary particles in vertical-type high-speed twin-roll cast Al-Mn based alloy strips

## 4.1. Introduction

In Chapter 3, influence of alloying elements (Mn, Fe and Si) on the solidification structure in vertical-type high-speed twin-roll cast Al-Mn based alloy strips was examined. Microstructure observation found that the strips are characterized by a skin formation-type solidification in pure Al and binary Al-Mn alloy, while mushy-type solidification is dominant in ternary Al-Mn-(Fe,Si) and quaternary Al-Mn-Fe-Si alloy. This is due to the increased freezing temperature range of the alloy, which promotes the instability of solid/liquid interface during solidification. For the formation of secondary particles, Fe favored to form $Al_6$(Mn,Fe) phase, and Si resulted in formation of α-AlMnSi phase.

The kind of secondary particles is controlled by the local composition of the remaining liquid phase during solidification. The composition of the liquid depends on segregation of solute elements, which is controlled by the cooling rates. In this chapter, the formation of secondary particles in the strips was investigated more precisely for ternary Al-1.2Mn-1.0Fe and Al-1.2Mn-1.0Si alloys. Secondary particles in the various casting products fabricated by different cooling rates were compared with respect to number density, area fraction, morphology and composition ratio. Influence of cooling rates on formation behavior of secondary particles in the vertical-type high-speed twin-roll casting (HSTRC) was investigated.

## 4.2. Experimental procedure

Al-1.2Mn-1.0Fe (AMF) and Al-1.2Mn-1.0Si (AMS) ternary alloys were used in this study. Secondary particle formation, several kinds of casting methods providing different cooling rates were selected in order to examine the effect of cooling rates on; furnace cooling, FC ($1.0 \times 10^{-2}$ ℃/s), DC-casting ($1.1 \times 10^{1}$ ℃/s), HSTRC ($3.1 \times 10^{3}$ ℃/s), and single-roll casting (around $10^{5}$ ℃/s).

Figure 4-1 shows a schematic illustration of the vertical-type high-speed twin-roll caster

used in the present study. The specification is identical to the caster in the previous chapter. The details of the casting conditions for each alloy are summarized in Table 4-1. The HSTRC procedure is as follows; about 2.5 kg of DC-cast billet was melted in the electric furnace for each HSTRC. Before casting, the melt was degassed by injecting Ar gas (0.4 L/min) into the melt around 20 min. The casting temperature was selected around 15 ℃ over the liquidus temperature of each alloy. The melt poured into the feeding nozzle was solidified on the both roll surfaces, and so-called solidification shells were formed. The solidified shells encountered at the roll gap by roll rotation, and the overlapped solidified shells was rapidly cooled. At last, it passed through the roll gap and became a thin cast strip. The cast strip was around 3 m-long and 100 mm-wide. The middle part of the resultant strip (around 1 m from the front) exhibited a stable thickness along the casting direction, which was around 2.2 mm for AMF, and around 2.6 mm for AMS, respectively.

A ribbon specimen was fabricated by single-roll casting (NEV-A05, NISSIN GIKEN). Around 7 g of the molten alloy was ejected onto the rotating copper wheel under Ar atmosphere. The diameter of copper roll was 250 mm. The gas pressure for ejecting the melt was 0.01 MPa. The wheel rotation speeds was 1800 rpm (23.5 m/sec). The obtained ribbon was around 71 μm-thick and 5 mm-wide in AMF, 64 μm-thick and 5 mm-wide in AMS.

For optical microscopic observation (BX51M, Olympus), polished specimens were etched by the Keller's reagent ($H_2O$:$HNO_3$:HCl:HF = 190:5:3:2 in Vol.%) for 40s.

EPMA (JXS-8200, JEOL) analysis by wavelength-dispersive spectrometer (WDS) was performed to investigate the chemical composition of secondary particles. The accelerating voltage and beam current were 15 kV and $2 \times 10^{-7}$ A, respectively.

The samples were also deep-etched by 5 % NaOH solution in order to observe 3-dimensional morphology of secondary particles. The detailed feature of the particles was observed by FE-SEM (JEM-7000F, JEOL).

The secondary particles were observed using TEM (JEM-3010, JEOL). Chemical composition analysis of the secondary particles was also performed by using EDS attached to the TEM.

Phase identification of the secondary particles was performed using X-ray diffractometer (RINT-2100, Rigaku for FC, DC-cast sample and HSTRC strip, X'Pert-Pro-MRD, Philips (PANalytical) for ribbon sample) with Cu $K_\alpha$ ($\lambda$ = 1.54 Å) radiation.

## 4.3. Results

### 4.3.1. Phase identification of secondary particles

Figures 4-2 and 4-3 show the XRD patterns for each cast sample of AMF and AMS, respectively. For AMF, the $Al_6$(Mn,Fe) phase was dominant in FC, DC-cast sample and HSTRC strip central area. Fe-rich phases such as $Al_5Fe_2$ and $Al_{13}Fe_4$ were detected mainly in the HSTRC strip near surface and single-roll cast ribbon, corresponding to relatively higher cooling rates during solidification. In the ribbon sample, peak of $Al_6$(Mn,Fe) phase was not detected. For AMS, α-AlMnSi and Si phase were two dominant second-phases. In the ribbon sample, peak of α-AlMnSi phase was not detected.

### 4.3.2. Characterization of secondary particles formed at various cooling rates

#### 4.3.2.1. Distribution of secondary particles

Figure 4-4 shows the optical micrographs of AMF products. Some large rhombus-shaped primary $Al_6$(Mn,Fe) particles were observed in FC sample and DC-cast sample as shown in Fig. 4-4 (a) and (b). For HSTRC strip surface, large primary particles were not observed. Most of the secondary particles were located at the inter-dendrite regions of fine α-Al. In the strip central area, large amount of eutectic particles were observed, which was surrounding the α-Al globular grains. Careful observation found that the rhombus-shaped primary particles were also observed in the strip central area as marked in Fig. 4-4 (d). For the single-roll cast ribbon sample, the rhombus-shaped primary particles were not observed as shown in Fig. 4-4 (e). From the cross-sectional microstructure, two typical regions were observed in the ribbon; the roll-side showed fine cellular microstructure with a small number of secondary particles whereas, the air-side showed dendritic microstructure.

Table 4-2 shows an average feret diameter of the rhombus-shaped primary $Al_6$(Mn,Fe) particles and their aspect ratio in AMF products. It should be mentioned that more than 100 primary $Al_6$(Mn,Fe) particles were examined. The aspect ratio of the primary particles decreased with increasing cooling rates; 4.9 in FC, 2.9 in DC and 2.4 in HSTRC-center, respectively. In the strip near-surface and single-roll cast ribbon, the large primary

$Al_6$(Mn,Fe) particles were not observed.

Figure 4-5 shows the optical micrographs of AMS products. For FC sample, secondary particles were heterogeneously distributed as shown in Fig. 4-5 (a). There are three kinds of secondary particles with different color-contrast and shape as shown in Fig. 4-5 (b). The type I shows script-like morphology. The type II is also script-like morphology, but it has light-gray color contrast in the observation. The type III exhibits sphere-like morphology. The observation in high magnification revealed that the type III was consisting of two different secondary particles. EPMA point analysis confirmed that the chemical composition of the type I was around 72.7 at% Al, 19.6 at% Mn and 7.7 at% Si, close to α-$Al_9Mn_2Si$ as stoichiometric formula. The type II was around 19.3 at% Al, 0.1 at% Mn and 80.6 at% Si. Since the Mn was not detected, and Al could come from the matrix, thus it was considered as crystallized Si particle. For the type III, applying accurate point analysis was hard because two different secondary particles contacted each other closely. Therefore, instead of the point analysis, compositional mapping was applied for the type III as shown in Fig. 4-6. It was the α-AlMnSi phase covered by Si component. Meanwhile, in the DC-cast sample, the secondary particles were located not only at the grain boundaries, but also within α-Al grains, namely inter-dendrite regions as shown in Fig. 4-5 (c). Some secondary particles located at the inter-dendrite regions showed similar morphology to the type III in FC sample as shown in Fig. 4-5 (d). For HSTRC strip, much finer α-Al grains and secondary particle distribution were observed in the strip near-surface area as shown in Fig. 4-5 (e). In the strip central area, large amount of eutectic particles and globular α-Al grains were observed as shown in Fig. 4-5 (f). For the single-roll cast ribbon, secondary particles were hardly observed in the cross-sectional optical microstructure as shown in Fig. 4-5 (g).

Figure 4-7 shows the back-scattered electron images of the secondary particles in AMF and AMS alloy products. Based on the FE-SEM observation result, the number density of secondary particles and their area fraction in AMF and AMS products were examined as shown in Fig. 4-8. It should be noted that the primary $Al_6$(Mn,Fe) particles in AMF were not included. Comparison between AMF and AMS products, since the low Fe solubility within Al matrix, the secondary particles number density and their area fraction in AMF products were higher than that of AMS products. As increasing cooling rates, the number density of secondary particles increased as shown in Fig. 4-8 (a). In contrast to that, the particle area

fraction was equivalent for all the cooling rates conditions as shown in Fig. 4-8 (b).

#### 4.3.2.2. Morphology of secondary particles

Figure 4-9 shows 3D morphology of secondary particles in the deep-etched AMF samples. Rhombus-shaped primary $Al_6$(Mn,Fe) particle with hollows was observed as shown in Fig. 4-9 (a). The hollows were located at the center of the particle. In the eutectic regions, rod-type eutectic $Al_6$(Mn,Fe) particles were observed as shown in Fig. 4-9 (b). For the HSTRC strip, the secondary particles were located at the cell/inter-dendrite regions as shown in Fig. 4-9 (c). The particle morphology was fibrous, and irregular-rod and spherical. Some particles were connected each other along the cell boundaries as shown in Fig. 4-9 (d). For the ribbon sample, much finer secondary particles were observed as shown in Fig. 4-9 (e) and (f). The secondary particles at the roll-side regions showed quite regular spherical-shape. Whereas, the air-side showed fibrous morphology.

Figure 4-10 shows 3D morphology of the secondary particles in the deep-etched AMS samples. For the DC-cast sample, dendritic particles were observed at the grain boundaries and inter-dendrite regions. It was revealed that the particles, which looks distributed separately in optical micrograph (see Fig. 4-5 (c)) were inter-connected mutually. By careful observation, some spherical Si clusters were observed at the tip of dendritic particles as shown in Fig. 4-10 (b). These Si clusters corresponded to the particle type III in FC and DC-cast sample as shown in Fig. 4-5 (b) and (d). For the HSTRC strip, the dendritic particles were observed along to the cell/grain boundaries. At the cell-interiors, fine particles were randomly distributed. They showed irregular morphology consisting of both spore-like and polygonal particles as shown in Fig. 4-10 (e). For the ribbon sample, much finer secondary particles were observed at the roll-side regions. The secondary particles were rarely located at the grain boundaries. At the air-side, petal-like particles were observed as shown in Fig. 4-10 (g).

#### 4.3.2.3. Chemical composition analysis of secondary particles

Figure 4-11 shows the TEM bright-field micrograph of DC-cast AMF sample. Rod-type particles are observed as shown in Fig. 4-11 (a). Cross-section of the rod eutectic particles are also observed as shown in Fig. 4-11 (b) and (c). A diffraction pattern of the eutectic

particle corresponds to the [001] zone of orthorhombic $Al_6$(Mn,Fe) phase (Fig. 4-11 (d)). The rod-type eutectic particles show the equivalent orientation at a specific observation condition. It suggests that these particles grew from a same single nucleation event.

Figure 4-12 shows the TEM bright-field micrograph of HSTRC AMF strip near-surface. The particles were distributed in the matrix randomly as shown in Fig. 4-12 (a). The orthorhombic $Al_6$(Mn,Fe) phase particle was observed on the grain boundary. Most of the secondary particles are smaller than 300 nm in diameter. In contrast to the particles in the DC-cast sample, each particle in HSTRC strip showed different orientations.

Figure 4-13 shows TEM bright-field micrographs of single-roll cast AMF ribbon. Compared with HSTRC strip, much refined and homogeneously distributed secondary particles were observed.

Figure 4-14 is a summary of the TEM-EDS measurement results for the secondary particles in AMF products. The atomic percentages of solute Mn and Fe are plotted against the Al concentration. It should be mentioned that just the relative composition of Al, Mn and Fe was evaluated in the present analysis. The concentration of Fe was higher than that of Mn in the secondary particles in all AMF products. The Fe/(Mn+Fe) ratio of the secondary particles increased with increasing cooling rates as shown in Fig. 4-14 (d).

Figure 4-15 shows TEM bright-field micrograph of DC-cast AMS sample. Some large dendritic secondary particles are observed as shown in Fig. 4-15 (a). They correspond to the particles at the grain boundaries as shown in Fig. 4-10 (a). These particles were identified to be Si phase by electron diffraction pattern. Relatively small particles are also observed as shown in Fig. 4-15 (b). They are identified as α-AlMnSi phase. These α-AlMnSi particles are considered to correspond to the particles located at the grain/cell-interiors.

Figure 4-16 shows the TEM bright-field micrograph of HSTRC AMS strip near-surface. Si phase was detected as shown in Fig. 4-16 (a). It is also observed the particles with irregular-shape consisting of spore-like and polygonal particles as shown in Fig. 4-16 (b). The TEM-EDS analysis results for the irregular-shape particles are shown in Fig. 4-16 (c) and (d) marked in Fig. 4-16 (b). The spore-like particle is considered to be α-AlMnSi phase, while the polygonal particle was considered to be Si phase.

Figure 4-17 shows TEM bright-field micrographs of single-roll cast AMS ribbon. Spherical spore-like particles were randomly distributed. Similar morphology was also

observed in the single-roll cast 3003 aluminum alloy ribbon as described in Chapter 2.

Figure 4-18 is a summary of TEM-EDS measurement results for the secondary particles in AMS products. The atomic percentages of solute Mn and Si are plotted against the Al concentration. It should be noted that the TEM-EDS results for Si particles were not included. It should be also mentioned that just the relative composition of Al, Mn and Si was evaluated in the present analysis. The concentration of Mn was higher than that of Si in the secondary particles in DC-cast sample as shown in Fig. 4-18 (a). For HSTRC strip, the concentration of Mn decreased, while the concentration of Si increased rather than that of DC-cast sample. In the single-roll cast ribbon, the concentration of Si was much higher than that of Mn. Similar to AMF products, the Si/(Mn+Si) ratio of the secondary particles increased with increasing cooling rates as shown in Fig. 4-18 (d).

## 4.4. Discussion

### 4.4.1. Influence of cooling rates on composition ratio in secondary particles

During solidification of Al alloys characterized by $k < 1$ ($k$ is partitioning coefficient of solute elements in alloy), liquid is enriched with solute elements. As the temperature decreases, various secondary particles are formed from the solute-rich liquid by several variant/invariant reactions. In this stage, the high cooling rate makes possible to dissolve more solute elements in α-Al. Thus, an increase in cooling rate basically leads to a decrease in the amounts of solute element in the residual liquid for the secondary particle formation at the final part of the solidification. The compositional change in the liquid caused by normal segregation can be estimated by *Scheil equation*:

$$C_L = C_0 \cdot f_L^{(k-1)}$$

where $C_L$ is the concentration of solute in the liquid at a given temperature, $C_0$ is the initial concentration of solute in the alloy, $f_L$ is the volume fraction of remaining liquid at a given temperature, and $k$ is the partitioning coefficient of solute. According to the Al-Mn, Al-Fe and Al-Si binary phase diagrams as shown in Fig. 4-19[1)], the partitioning coefficient of solute elements in Al is about 0.95 for Mn, 0.03 for Fe and 0.13 for Si, respectively.

According to the phase diagram of Al-Mn-Fe system[1-4)] as shown in Fig. 4-20, $Al_3Fe$ and

$Al_6$(Mn,Fe) phase can be formed during solidification of AMF. Based on the TEM observation and EDS analysis for AMF products, most of the secondary particles are considered as orthorhombic $Al_6$(Mn,Fe) phase which contain around 85.7 at% Al and 14.3 at% (Mn,Fe), or orthorhombic $Al_m(Mn_x,Fe_y)$ phase. According to Malakhov et al.[5], when the melt composition is close to the composition of some possible phases, the precipitation of the particular phase can be facilitated. Thus, the $Al_6$(Mn,Fe) phase can be formed from the remaining liquid with composition of 85.7 at% Al and 14.3 at% (Mn+Fe). By extrapolating at the 85.7 at% Al on the TEM-EDS results (see Fig. 4-14), the composition of Mn and Fe in the $Al_6$(Mn,Fe) particle can be estimated as shown in Table 4-3. In spite of the same $Al_6$(Mn,Fe) phase, different composition ratio between Mn and Fe was estimated; the Fe/(Mn+Fe) composition ratio is increased with increasing cooling rates. In terms of AMF, the segregation of Fe in liquid is higher than that of Mn. It is due to not only the small partitioning coefficient of Fe in Al, but also low solubility of Fe in Al. The Fe concentration may not be changed with increasing cooling rates. In contrast, the segregation of Mn in liquid is limited due to its high partitioning coefficient in Al. Also, with increasing cooling rates, more amounts of the Mn elements are considered to be dissolved in matrix, which decreases the segregation of Mn in liquid. Therefore, the Fe/(Mn+Fe) composition ratio increases with increasing cooling rate in $Al_6$(Mn,Fe) phase of the AMF.

For the AMS, α-AlMnSi and Si phase formed during solidification. The EPMA analysis for FC sample revealed that α-AlMnSi phase contained around 72.7 at% Al, 19.6 at% Mn and 7.7 at% Si. By extrapolating at the 72.7 at% Al on the TEM-EDS results (see Fig. 4-18), the composition of Mn and Si in the α-AlMnSi phase particle was estimated as shown in Table 4-4. The Mn/(Mn+Si) composition ratio also decreased as increasing cooling rates. The Mn segregation in liquid is considered to decrease as increasing cooling rates during solidification. On the other hand, as increasing cooling rates, the solute partitioning of Si into the liquid is considered to be increased[6,7]. Alexander and Greer[6] reported the compositional change in the liquid during solidification in Al-0.5Fe-1.0Mn-0.2Si (in mass%) alloy. According to their result, as the undercooling increases, substantial solute partitioning of Fe and Si into the liquid was dominant compared to that of Mn. Dutta and Rettenmayr[7] also reported the effect of cooling rate on the solidification behavior in Al-0.8Fe-0.8Si (in mass%) alloy that an increase in cooling rates leaded to increase in Si concentration in liquid. This

resulted in the decrease of Fe/Si ratio in eutectic liquid (see Fig. 4-21), consequently α-AlFeSi phase was formed instead of Fe-rich $Al_{13}Fe_4$ phase. In the present study, as increase in the cooling rates, enrichment of Si in liquid occurs, and it is probably the main reason for the increase of the Si/(Mn+Si) composition ratio in α-AlMnSi phase.

### 4.4.2. Formation behavior of secondary particles in vertical-type high-speed twin-roll cast strips

According to phase diagram of ternary Al-Mn-Fe[1)], the $Al_6$(Mn,Fe) phase can be formed by invariant transformation, L + $Al_3Fe$ + $Al_4Mn$ → $Al_6$(Mn,Fe) at 727 ℃, and L → α-Al + $Al_3Fe$ + $Al_6$(Mn,Fe) at 654 ℃. Considering the solidification sequence of AMF, the primary $Al_6$(Mn,Fe) phase crystallizes at 727 ℃. Zhu et al.[8)] reported the $Al_6$(Mn,Fe) phase has a strong faceting tendency so that {110} planes are the close-packed face, and the particle is elongated along the [001] direction. Accordingly, the subsequent growing after nucleation of the primary $Al_6$(Mn,Fe) particle leads to its high aspect ratio (see Table 4-2). In this stage, as the cooling rates increased, the facet growth of the crystallized primary $Al_6$(Mn,Fe) particle was suppressed because time for the growth is limited. Thus, the maximum feret diameter of primary particle and aspect ratio decreased as increasing cooling rates. For the HSTRC strip near-surface as well as the single-roll cast ribbon, the primary $Al_6$(Mn,Fe) particle was not observed. It is due to the melt is rapidly cooled below eutectic temperature before formation of the primary $Al_6$(Mn,Fe) particles due to high cooling rates. On the other hand, the primary $Al_6$(Mn,Fe) particles were located at the strip central area as shown in Fig. 4-4 (d). In the present study, the casting temperature for HSTRC was just 15 ℃ higher than the liquidus temperature, which was lower than 727 ℃. Thus, the formation of primary $Al_6$(Mn,Fe) particle occurs in the melt-head in advance. After pouring the melt, the crystallized particles are gathered at the strip central area. However, the solidification takes place so fast in HSTRC, there is no time for growing the crystallized primary $Al_6$(Mn,Fe) particle.

The Al-Mn-Si phase diagram of Al-rich region is shown in Fig. 4-22, and regarding invariant and variant reactions are summarized in Table 4-5[4,9)]. In the present study, the XRD analysis (see Fig. 4-3), EPMA (see Fig. 4-6) and TEM analysis (see Fig. 4-15 to 4-18) revealed the formation of $Al_6Mn$, Si and α-AlMnSi phase in AMS. The β-AlMnSi phase was not detected in the present study. The absence of the β-AlMnSi phase is possibly due to the

formed β-AlMnSi phase was transformed into $Al_6Mn$ and/or α-AlMnSi by the reaction [4-2], or essentially hard to be formed in the composition range of AMS. For FC sample, there are three kinds of secondary particles, α-AlMnSi (type I), Si (type II) and agglomerates of α-AlMnSi and Si clusters (type III) as shown in Fig. 4-5 (b). In terms of the particles type I and II, considering from the alloy composition and the particles morphology, they were formed by the eutectic reaction [4-6] for α-AlMnSi and [4-7] for Si. The particle type III may be formed either by the reaction [4-4] or combination of reaction [4-6] and [4-7]. The particle type III is also observed in DC-cast sample as shown in Fig. 4-5 (d). In contrast to FC and DC-cast sample, various type of secondary particles was formed in HSTRC strip; agglomerates of spore-like α-AlMnSi and polygonal Si particle as shown in Fig. 4-10 (e) and Fig. 4-16 (b). These spore-like α-AlMnSi and polygonal Si particles were frequently observed at inter-dendrite regions in HSTRC strip.

The formation sequence of the agglomerated particles is considered as follows. At first, α-Al dendrite is formed, and the solute-rich liquid is trapped at the inter-dendritic regions. As further decrease in temperature, secondary particles are formed from the remaining liquid. It is considered that high cooling rates affect the solute segregation at this stage, especially Si content. Let me consider solidification manner of the Al-Si alloy under a large undercooling condition. Under the large undercooling condition, the eutectic composition shifts to a high Si content side and the eutectic temperature decreases. Also, segregation of Si into the liquid is considered to increase due to its small partitioning coefficient. If the Si content exceeds the extended eutectic composition, crystallized polygonal Si as well as Si-rich α-AlMnSi phase can be formed from the remaining liquid.

For the above scenario, formation manner of AMS solidification structure is illustrated in Fig. 4-23. For the lower cooling rate condition, such as DC-casting, Si particles and α-AlMnSi particles are formed at grain boundaries. At the inter-dendrite regions, α-AlMnSi particles and/or composite agglomerates of α-AlMnSi and eutectic Si clusters are formed as shown in Fig. 4-10 (b). For the high cooling rate condition, such as HSTRC, refinement of α-Al dendrite occurs, and the liquid droplets trapped at the inter-dendrite regions increase. Under the large undercooling condition, enrichment of Si in the liquid can occur. The composition in some trapped liquid can be exceeded the extended eutectic composition of AMS. Consequently, polygonal Si and/or Si-rich α-AlMnSi particles are formed at the inter-

dendritic regions.

## 4.5. Conclusions

Ternary Al-1.2Mn-1.0Fe (AMF) and Al-1.2Mn-1.0Si (AMS) in mass % alloy strips were fabricated by HSTRC. Influence of cooling rates on secondary particle formation was studied based on the comparison of various cooling rate conditions; furnace cooling, DC-casting, HSTRC and single-roll casting. Increase in cooling rates resulted in decrease in Mn composition ratio in secondary particles. It was due to not only the decrease in Mn segregation, but also enrichment of Fe and Si in the remaining liquid in the ternary alloy systems.

High cooling rate of HSTRC resulted in reduction in large primary particles, and decrease in the aspect ratio of the primary $Al_6$(Mn,Fe) particles.

For inter-dendrite regions in AMS strip near-surface, high cooling rate increased Si segregation in the remaining liquid trapped at the inter-dendrite regions. The enrichment of Si in the liquid enhanced the formation of secondary particles; spore-like Si-rich eutectic α-AlMnSi and polygonal Si.

## References


1) L.F. Mondolfo: *Aluminum Alloys: Structure and Properties*,Butterworths, (1976)
2) G. Petzow and G. Effenberg: *Ternary Alloys. A Comprehensive Compendium of Evaluated Constitutional Data and Phase Diagrams.*,VCH Verlagsgesellschaft, Vol. 5, (1992)
3) B. B. Lindahl and M. Selleby: Calphad Comput. Coupling Phase Diagrams Thermochem., **43** (2013) 86–93
4) N. A. Belov, D. G. Eskin, and A. A. Aksenov: *Multicomponent Phase Diagrams: Applications for Commercial Aluminum Alloys*,Elsevier, Oxford, (2005)
5) D. V. Malakhov, D. Panahi, and M. Gallerneault: Calphad Comput. Coupling Phase Diagrams Thermochem., **34** (2010) 159–66
6) D. T. L. Alexander and A. L. Greer: Acta Mater., **52** (2004) 5853–61
7) B. Dutta and M. Rettenmayr: Mater. Sci. Eng. A, **283** (2000) 218–24
8) X. Zhu, P. Blake, and S. Ji: CrystEngComm, **20** (2018) 3839–48
9) G. Petzow and G. Effenberg: *Ternary Alloys. A Comprehensive Compendium of Evaluated Constitutional Data and Phase Diagrams.*,VCH Verlagsgesellschaft, Vol.7, (1993)

**Table 4-1 HSTRC conditions for AMF and AMS.**

| Condition | Alloy | |
|---|---|---|
| | AMF | AMS |
| Melt superheating (°C) | 15 | 15 |
| Roll rotation speed (m/min) | 60 | 60 |
| Solidification length (mm) | 100 | 100 |
| Roll separating force (kN) | 20 | 60 |
| Initial roll gap (mm) | 1 | 1 |

**Table 4-2 Feret diameter and aspect ratio of primary $Al_6(Mn,Fe)$ particle in AMF.**

| | Max. feret (μm) | Min. feret (μm) | Aspect ratio |
|---|---|---|---|
| Furnace cooling | 394.9 | 95.9 | 4.9 |
| DC-casting | 55.1 | 22.7 | 2.9 |
| HSTRC central area | 2.9 | 1.3 | 2.4 |
| HSTRC near-surface | - | - | - |
| Single-roll cast ribbon | - | - | - |

**Table 4-3 Composition of Mn and Fe for $Al_6$(Mn,Fe) particle in AMF. (at%)**

| Casting process | Al* | Mn | Fe | Fe/(Mn+Fe) |
|---|---|---|---|---|
| DC-casting | 85.7 | 4.2 | 10.1 | 0.70 |
| HSTRC | 85.7 | 3.3 | 11.0 | 0.77 |
| Single-roll casting | 85.7 | 2.2 | 12.1 | 0.85 |

**Note*: The atomic percentage of Al is extrapolated from the nominal composition of $Al_6$(Mn,Fe) phase.

**Table 4-4 Composition of Mn and Si for α-AlMnSi particle in AMS. (at%)**

| Casting process | Al* | Mn | Si | Si/(Mn+Si) |
|---|---|---|---|---|
| DC-casting | 72.7 | 17.2 | 10.1 | 0.37 |
| HSTRC | 72.7 | 14.0 | 13.3 | 0.49 |
| Single-roll casting | 72.7 | 3.8 | 23.5 | 0.86 |

**Note*: The atomic percentage of Al is extrapolated from the result of EPMA composition analysis for α-AlMnSi particle in FC sample in the present study.

**Table 4-5 Invariant and variant reactions in ternary Al-Mn-Si system[4)].**

| No | Reaction | Location in Fig. 4-22 (a) | Temperature range (°C) |
|---|---|---|---|
| [4-1] | $L + Al_4Mn \rightarrow Al_6Mn + \beta\text{-AlMnSi}$ | $P_3$ | 690 |
| [4-2] | $L + \beta AlMnSi \rightarrow Al_6Mn + \alpha\text{-AlMnSi}$ | $P_2$ | 655-657 |
| [4-3] | $L + Al_6Mn \rightarrow (Al) + \alpha\text{-AlMnSi}$ | $P_1$ | 648-649 |
| [4-4] | $L \rightarrow (Al) + (Si) + \alpha\text{-AlMnSi}$ | E | 573-574 |
| [4-5] | $L \rightarrow (Al) + Al_6Mn$ | $e_1$-$P_1$ | 658-649 |
| [4-6] | $L \rightarrow (Al) + \alpha\text{-AlMnSi}$ | $P_1$-E | 649-574 |
| [4-7] | $L \rightarrow (Al) + (Si)$ | $e_2$-E | 577-574 |

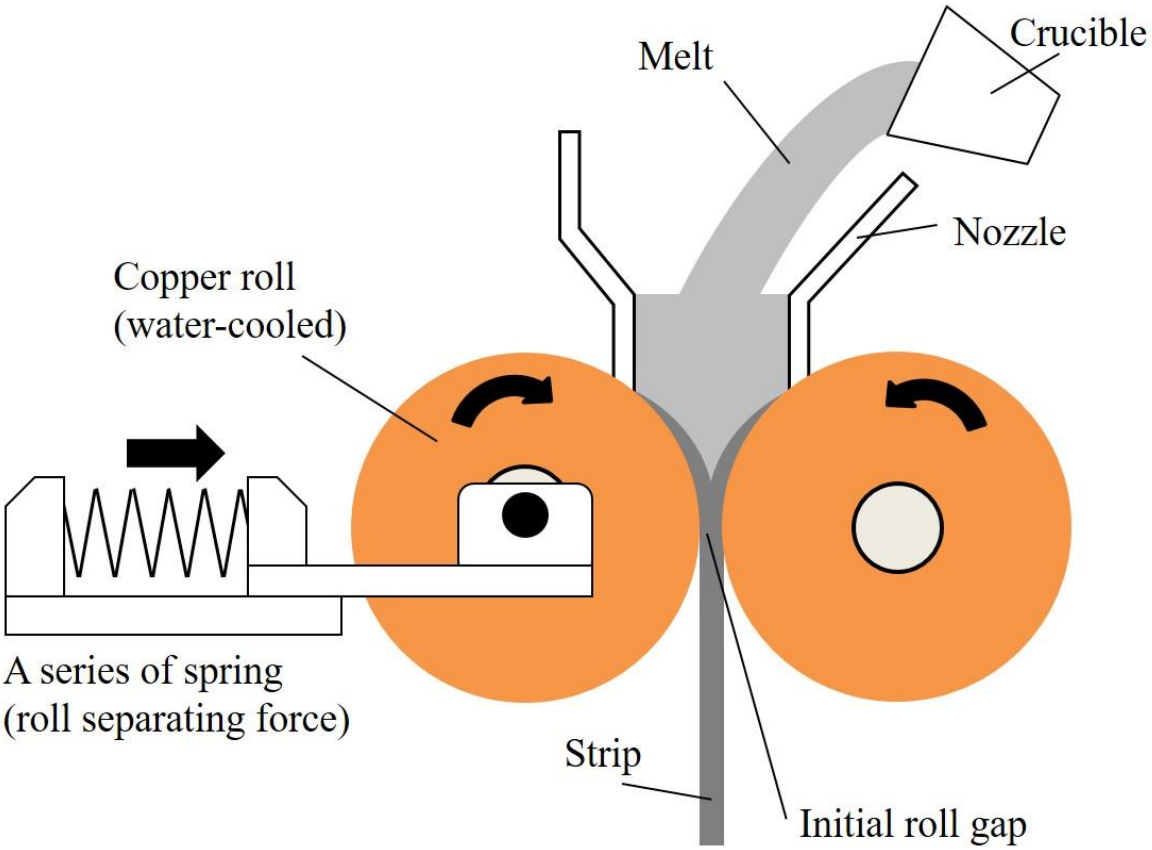


**Fig. 4-1 Schematic illustration of the vertical-type high-speed twin-roll caster.**

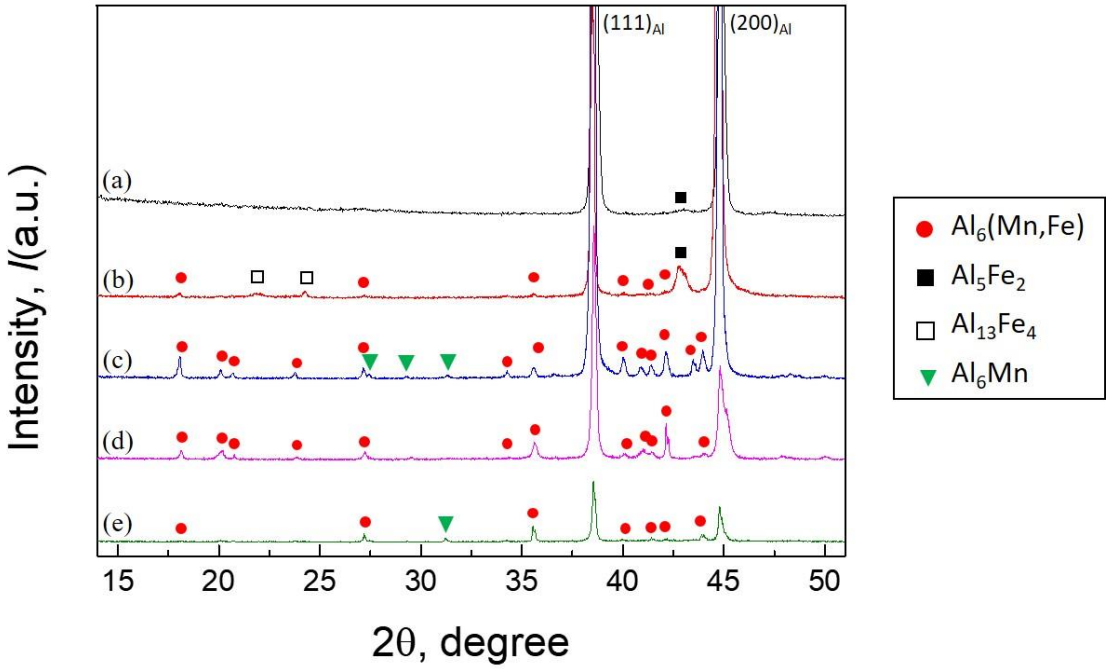


**Fig. 4-2 XRD patterns of AMF cast products. (a) single-roll cast ribbon, (b) strip surface, (c) strip center, (d) DC-cast sample, (e) FC sample.**

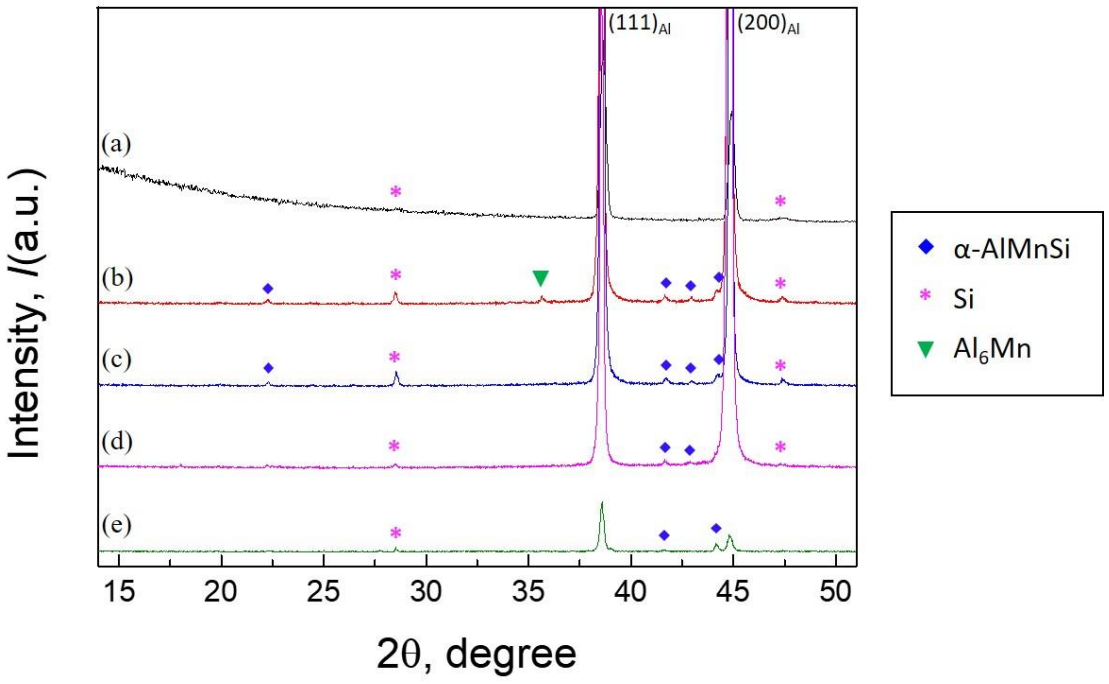


**Fig. 4-3 XRD patterns of AMS cast products. (a) single-roll cast ribbon, (b) strip surface, (c) strip center, (d) DC-cast sample, (e) FC sample.**

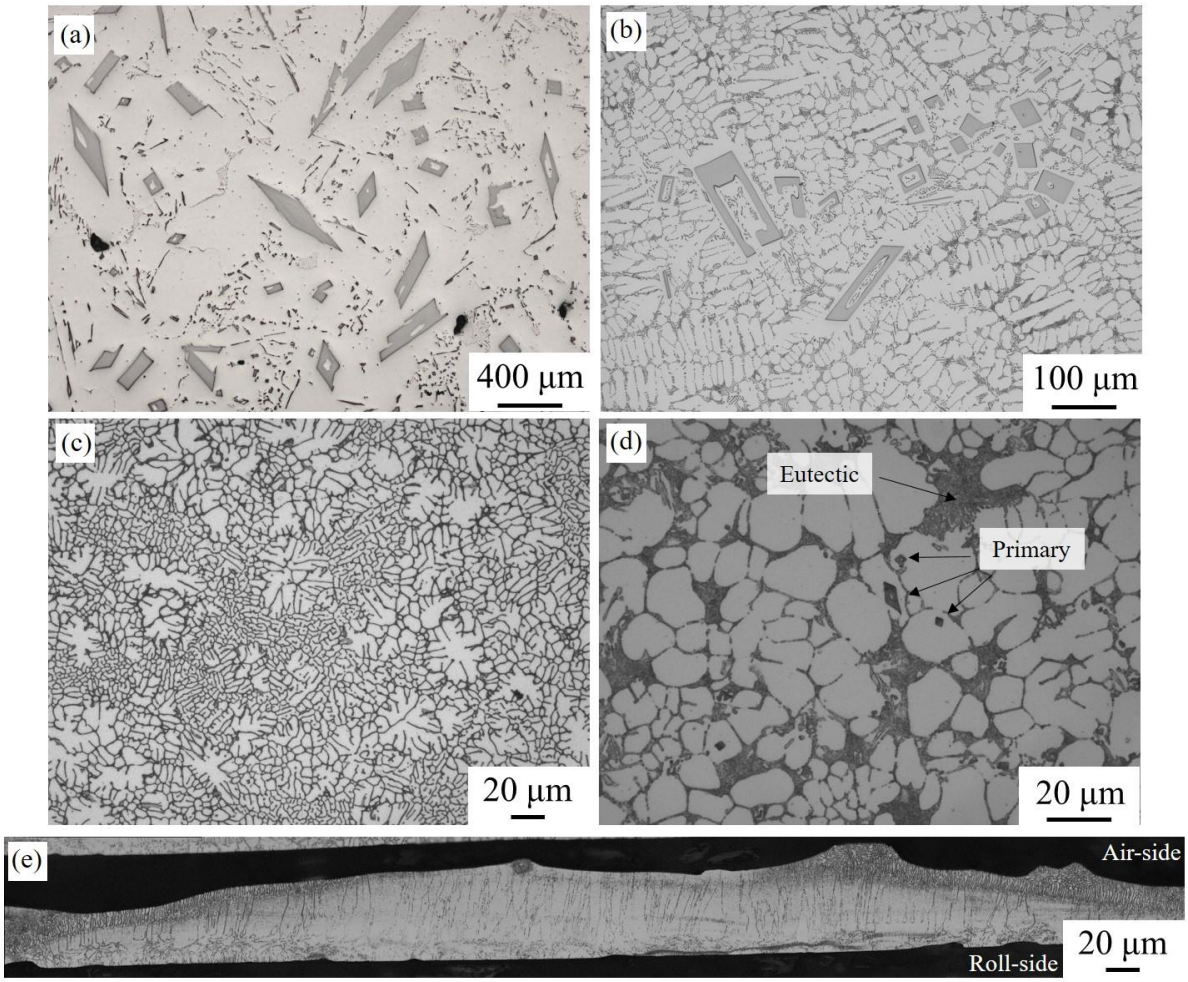


**Fig. 4-4 Microstructure of AMF cast products. (a) FC sample, (b) DC-cast sample, (c) strip surface, (d) strip center, (e) single-roll cast ribbon.**

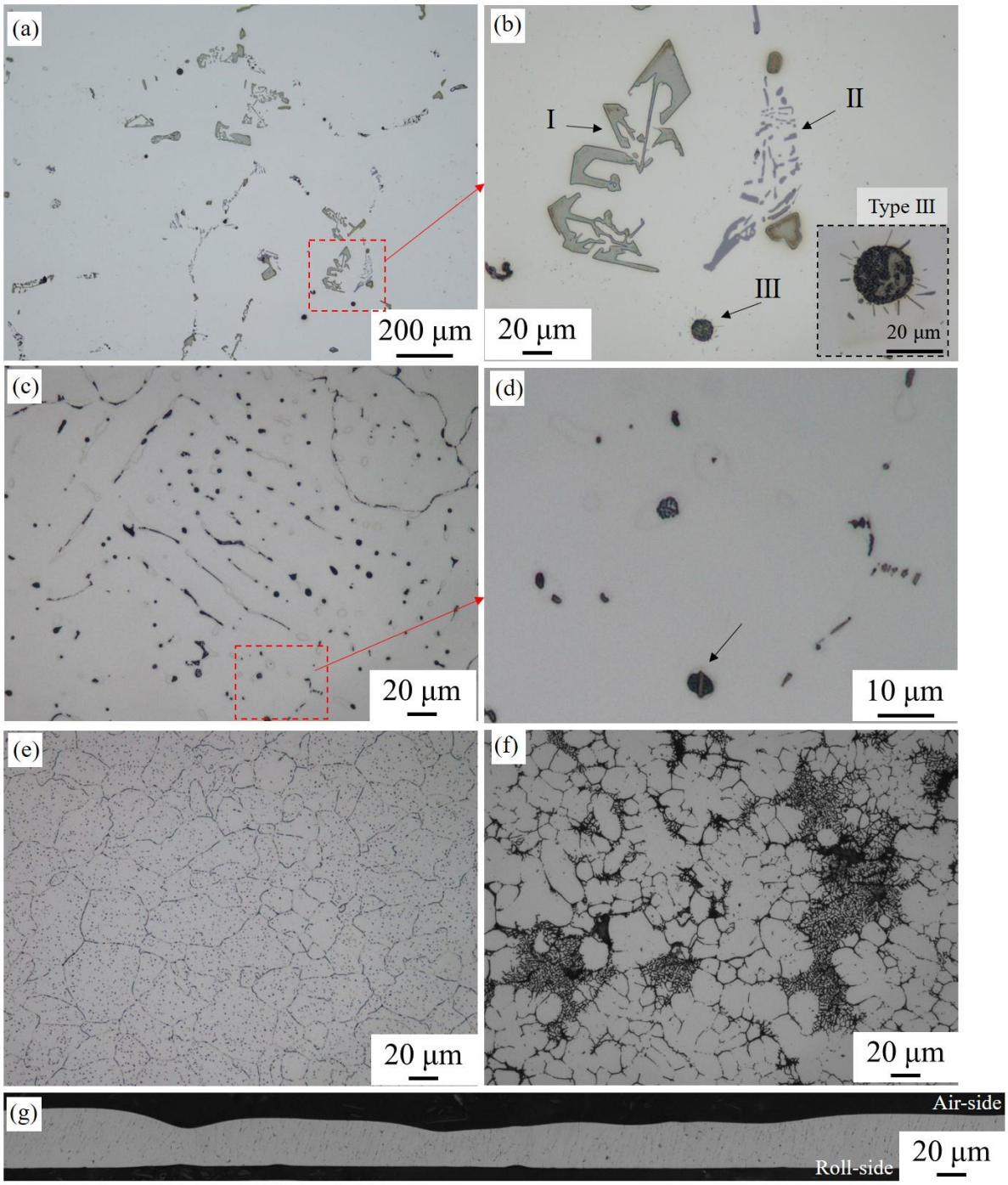


**Fig. 4-5 Microstructure of AMS cast products. (a) FC sample, (b) detail in (a), (c) DC-cast sample, (d) detail in (c), (e) strip surface, (f) strip center, (g) single-roll cast ribbon.**

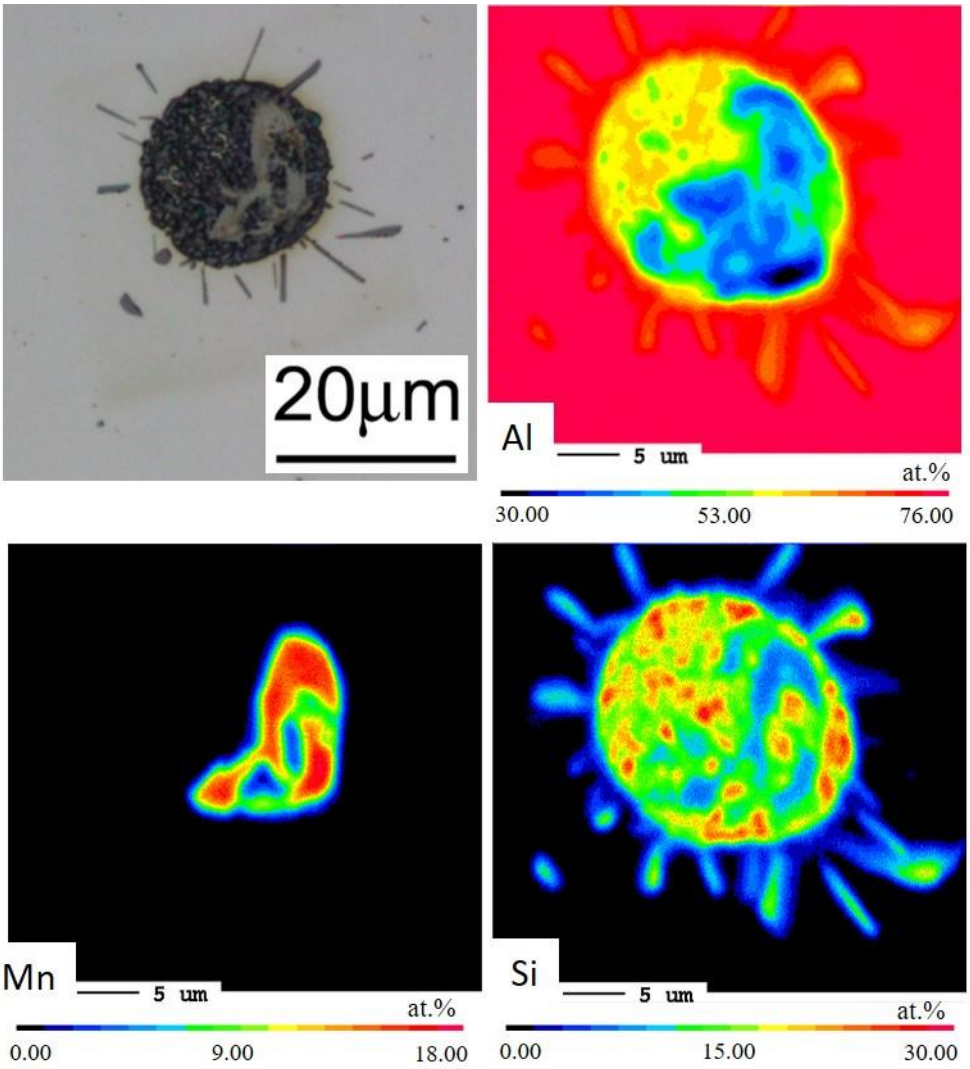


**Fig. 4-6 EPMA element mapping result for the particle type III.**

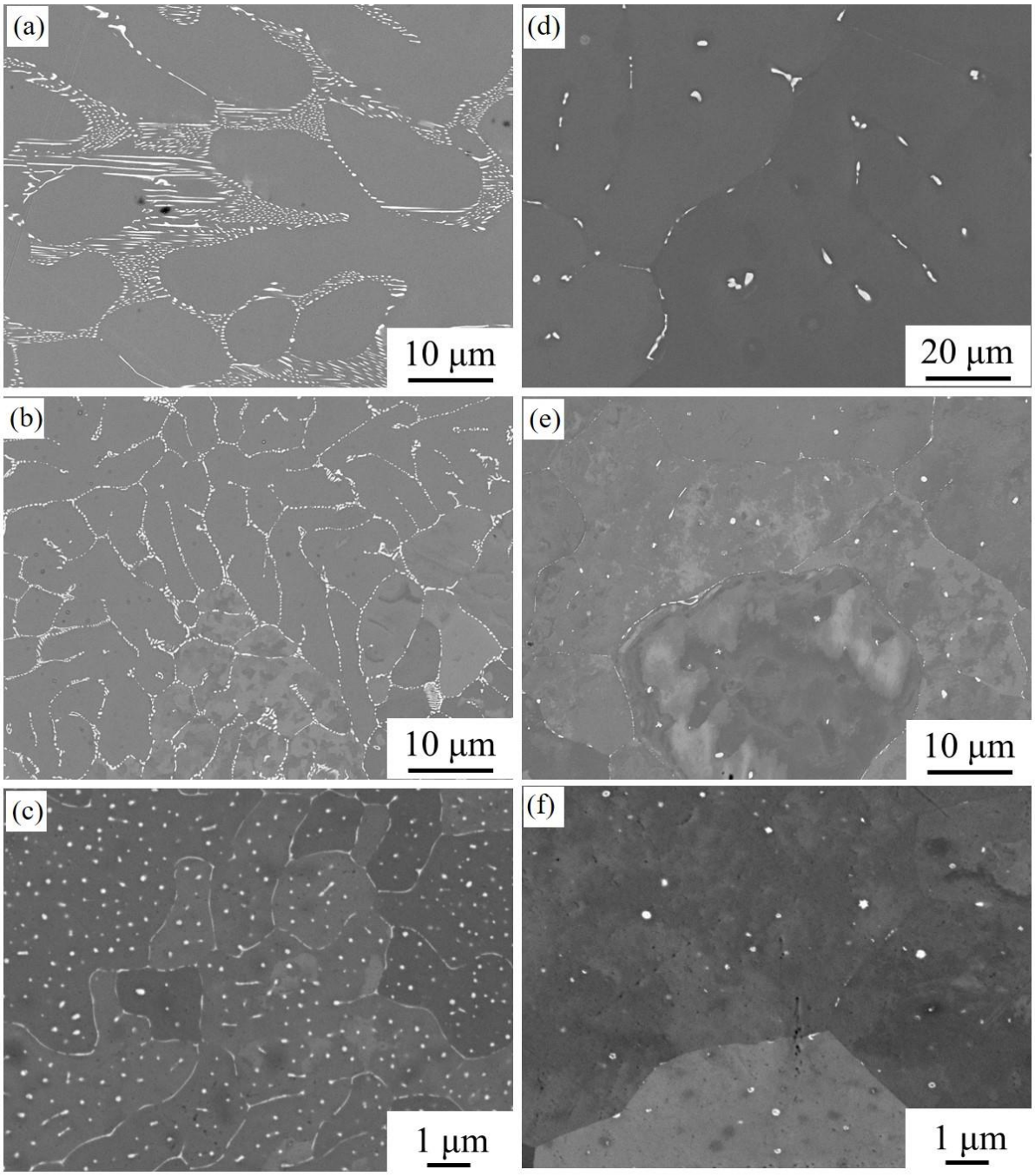


**Fig. 4-7 Back-scattered electron images of AMF and AMS cast products. (a-c) AMF, (d-f) AMS. (a) DC-cast sample, (b) strip surface, (c) single-roll cast ribbon roll-side, (d) DC-cast sample, (e) strip surface, (f) single-roll cast ribbon roll-side.**

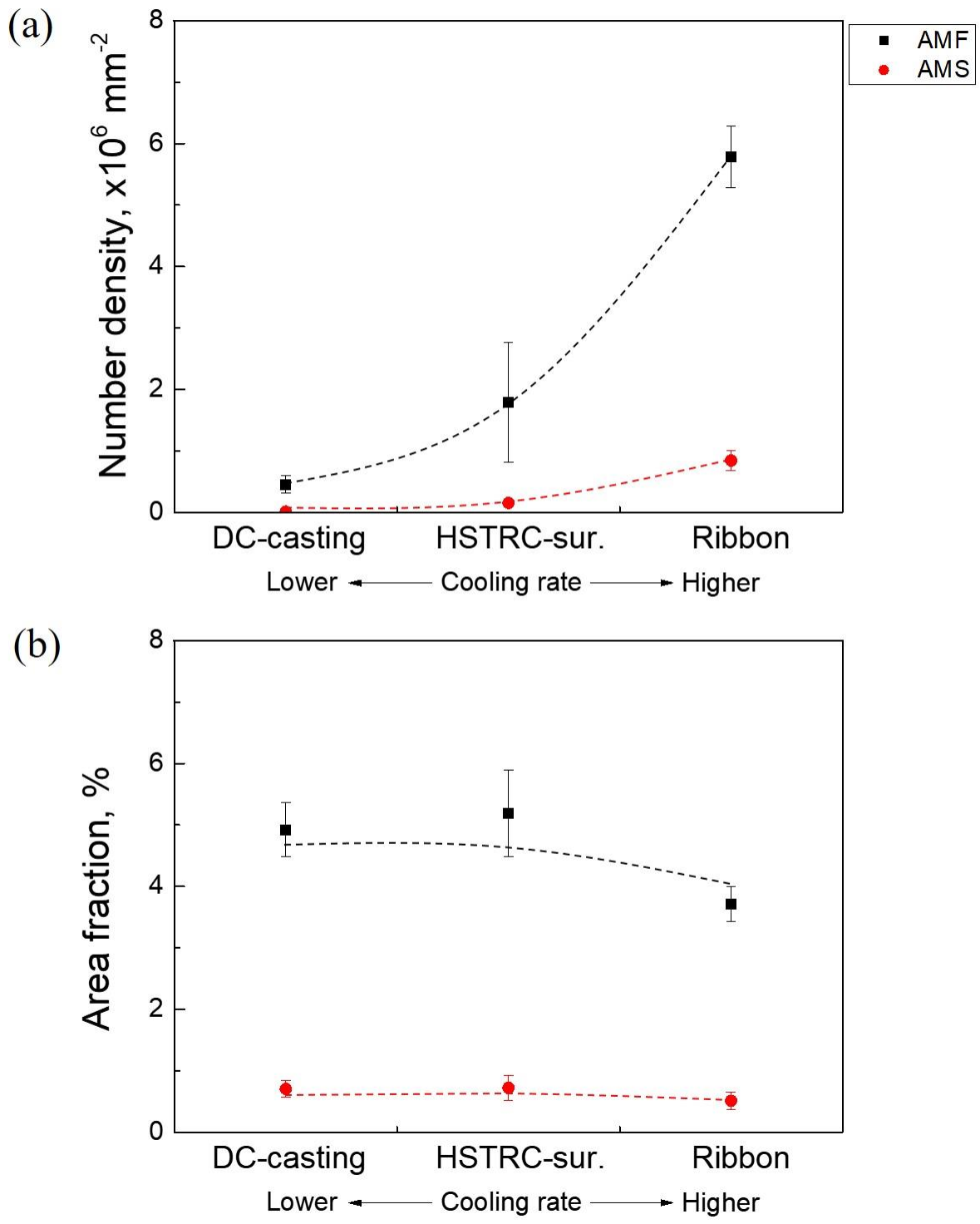


**Fig. 4-8 Comparison of number density and area fraction of secondary particles in each cast products. (a) particle number density, (b) particle area fraction.**

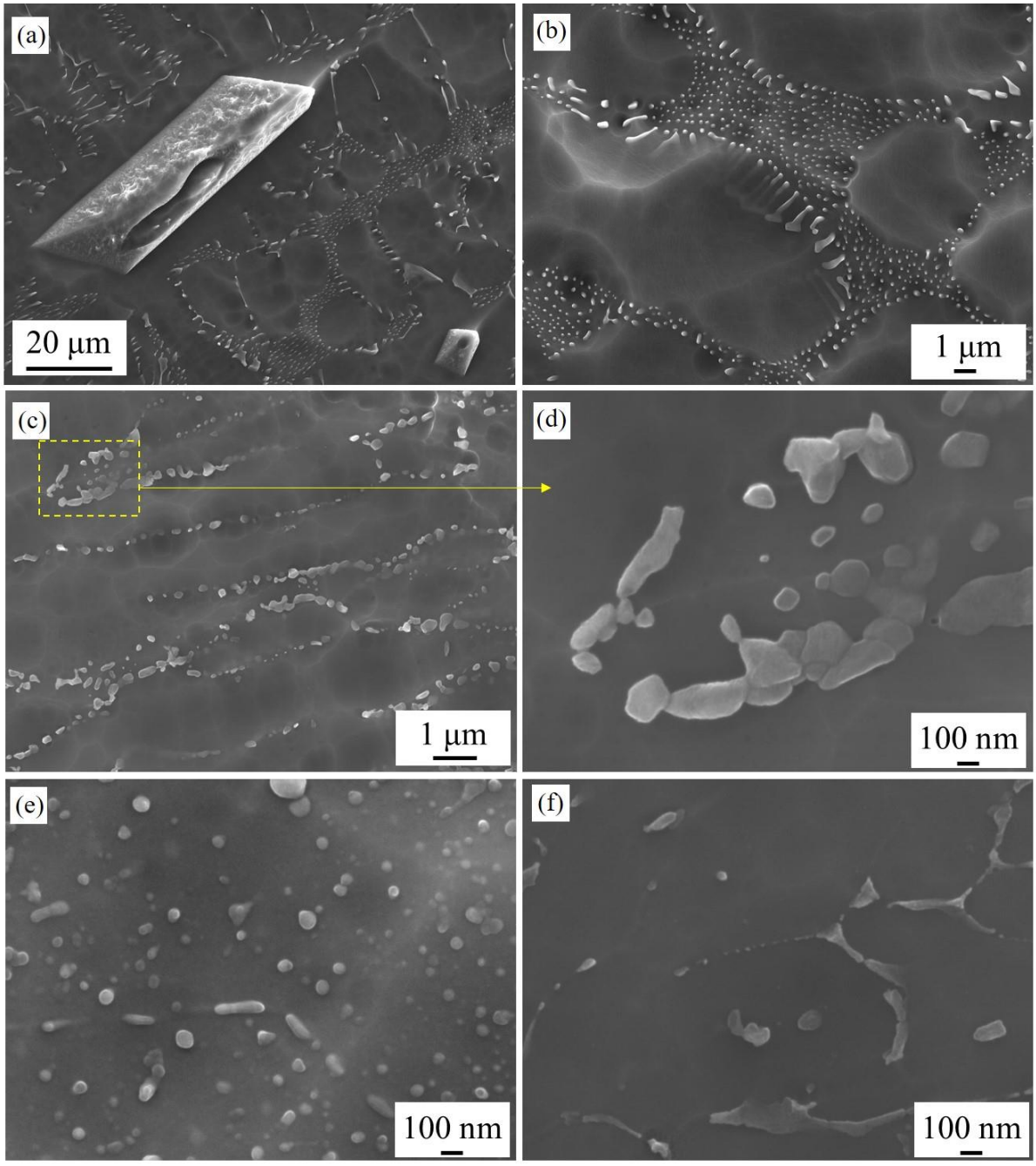


**Fig. 4-9 FE-SEM secondary electron images of deep-etched AMF samples. DC-cast sample; (a) primary particle, (b) eutectic structure, HSTRC strip; (c) near surface, (d) high magnification of typical constituent particle at near surface area, single-roll cast ribbon; (e) roll-side, (f) air-side.**

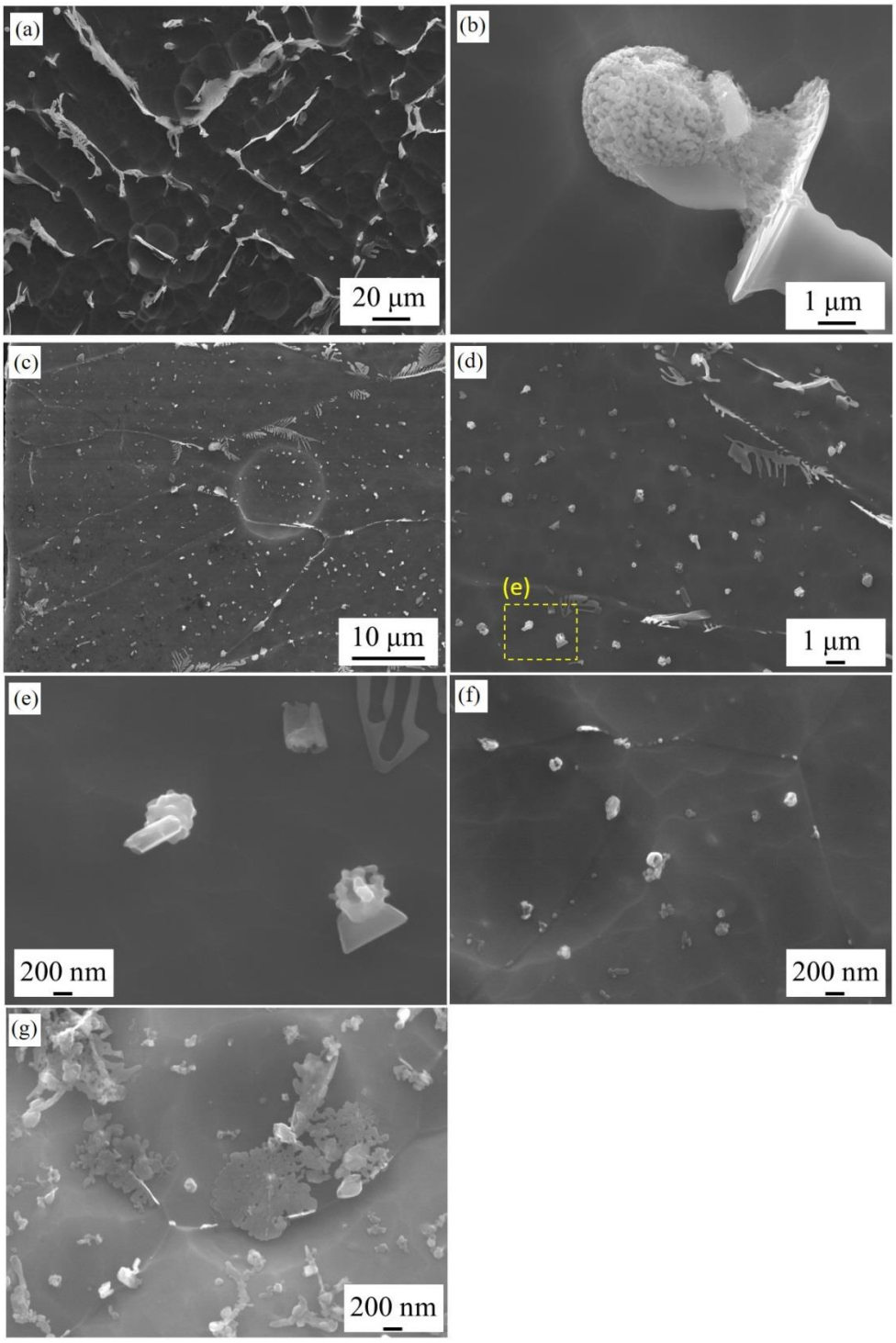


**Fig. 4-10 FE-SEM secondary electron images of deep-etched AMS samples. DC-cast sample; (a) dendritic particle along the boundaries, (b) spherical cluster at inter-dendrite region, HSTRC strip; (c) near surface, (d) particles at cell-interior, (e) high magnification in (d), single-roll cast ribbon; (f) roll-side, (g) air-side.**

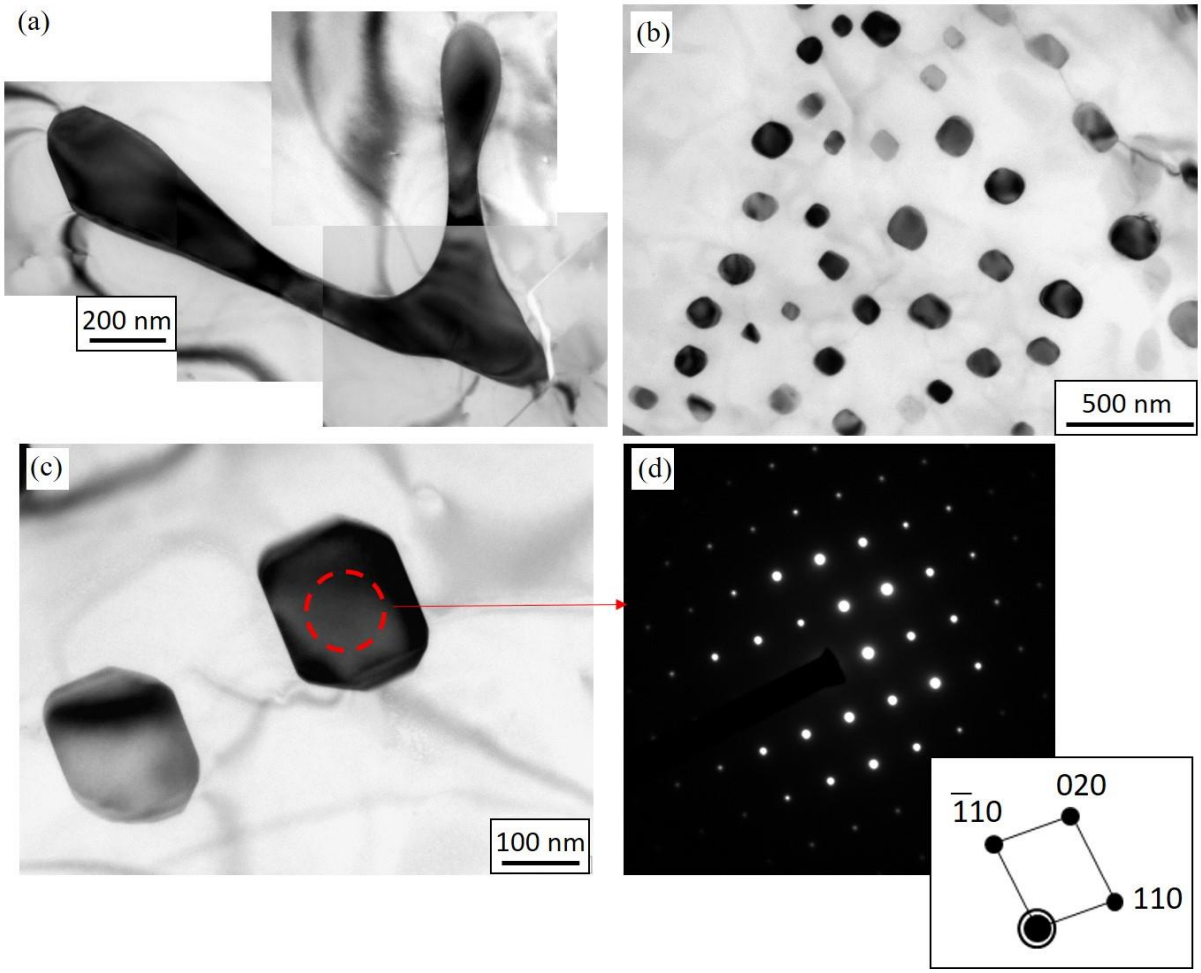


**Fig. 4-11 (a) and (b) TEM bright-field image of rod-type eutectic particles in DC-cast AMF sample, (c) typical rod-type eutectic $Al_6(Mn,Fe)$ particle (d) selected area diffraction pattern of the particle in (c).**

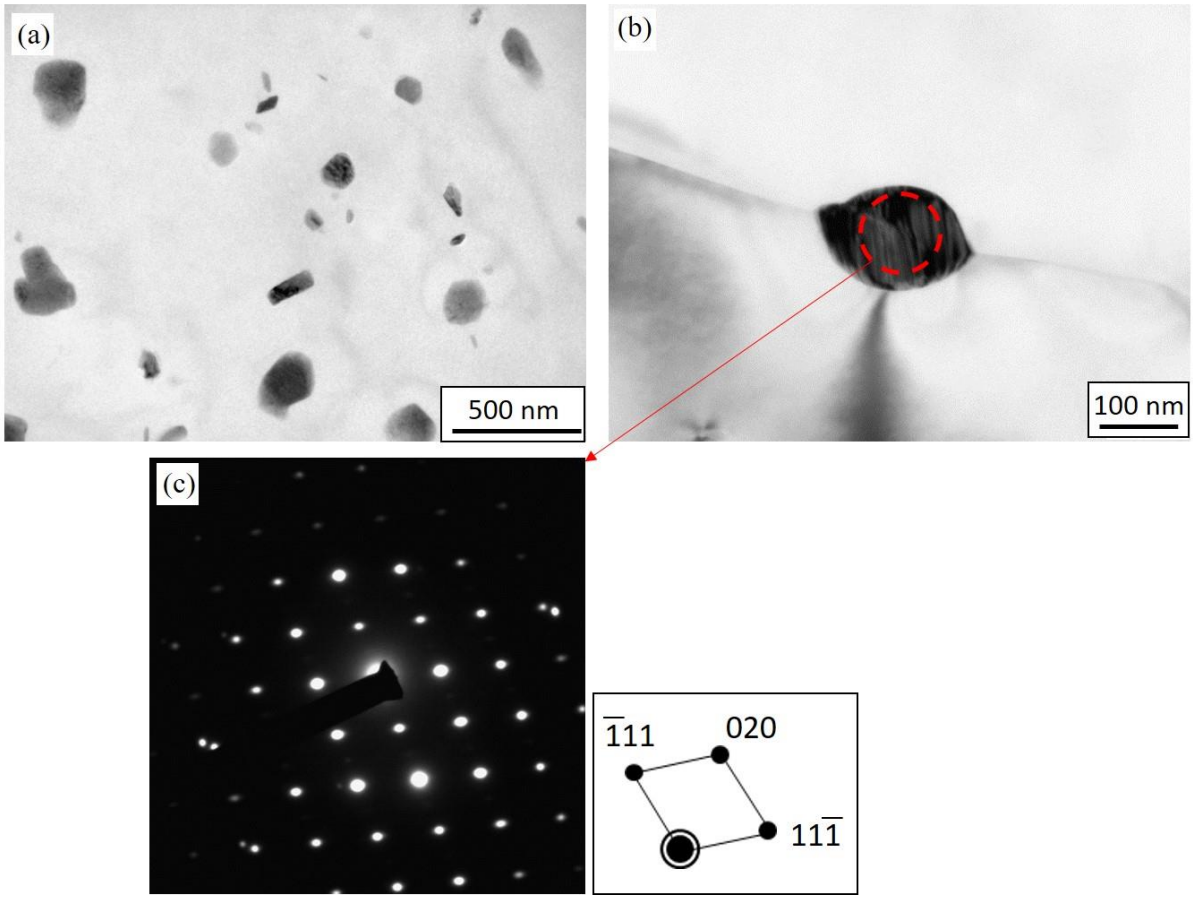


**Fig. 4-12 (a) TEM bright-field image of rod-type eutectic particle in AMF strip near-surface, (b) typical $Al_6(Mn,Fe)$ particle on grain boundary (c) selected area diffraction pattern of the particle in (b).**

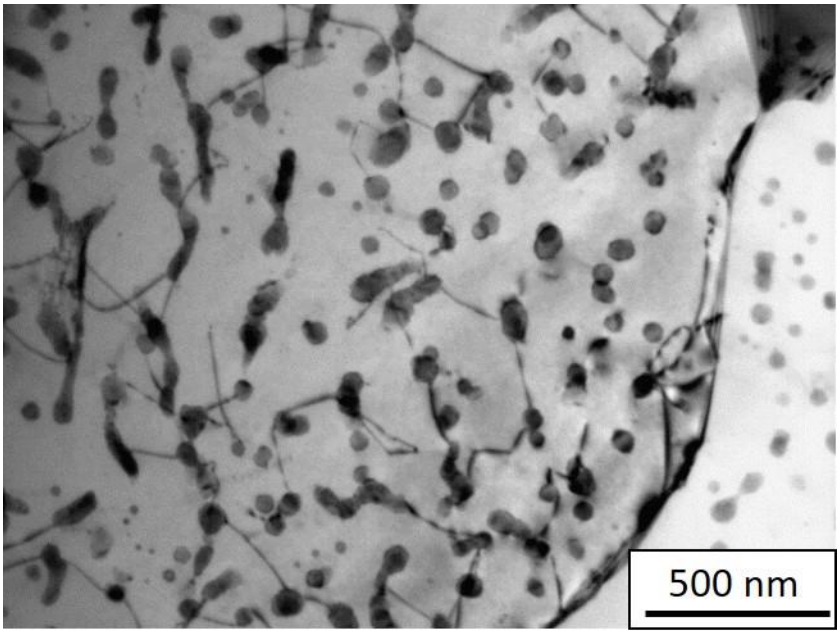


**Fig. 4-13 TEM bright-field image of single-roll cast AMF ribbon. The observed area corresponds to the roll-side.**

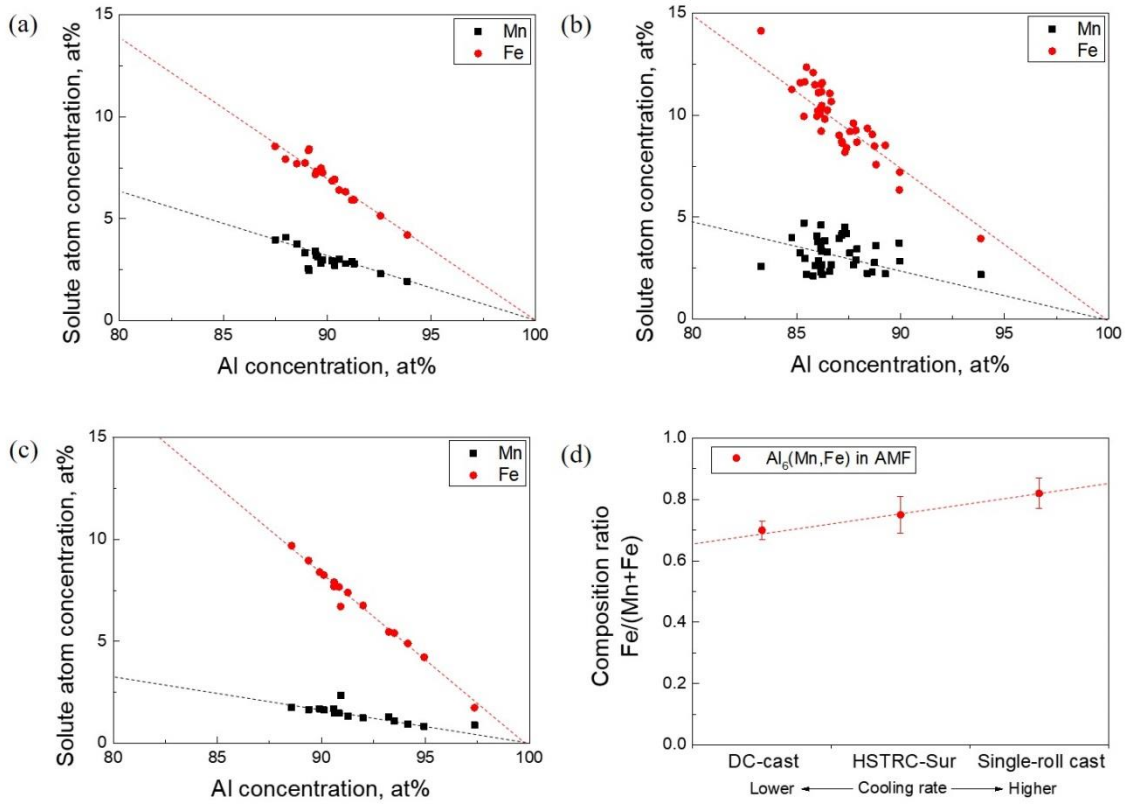


**Fig. 4-14 TEM-EDS results showing relative solute composition ratio of the secondary particles in AMF products. (a) DC-cast sample, (b) strip surface, (c) single-roll cast ribbon, (d) Composition ratio of Fe/(Mn+Fe) for $Al_6$(Mn,Fe) particle in each product.**

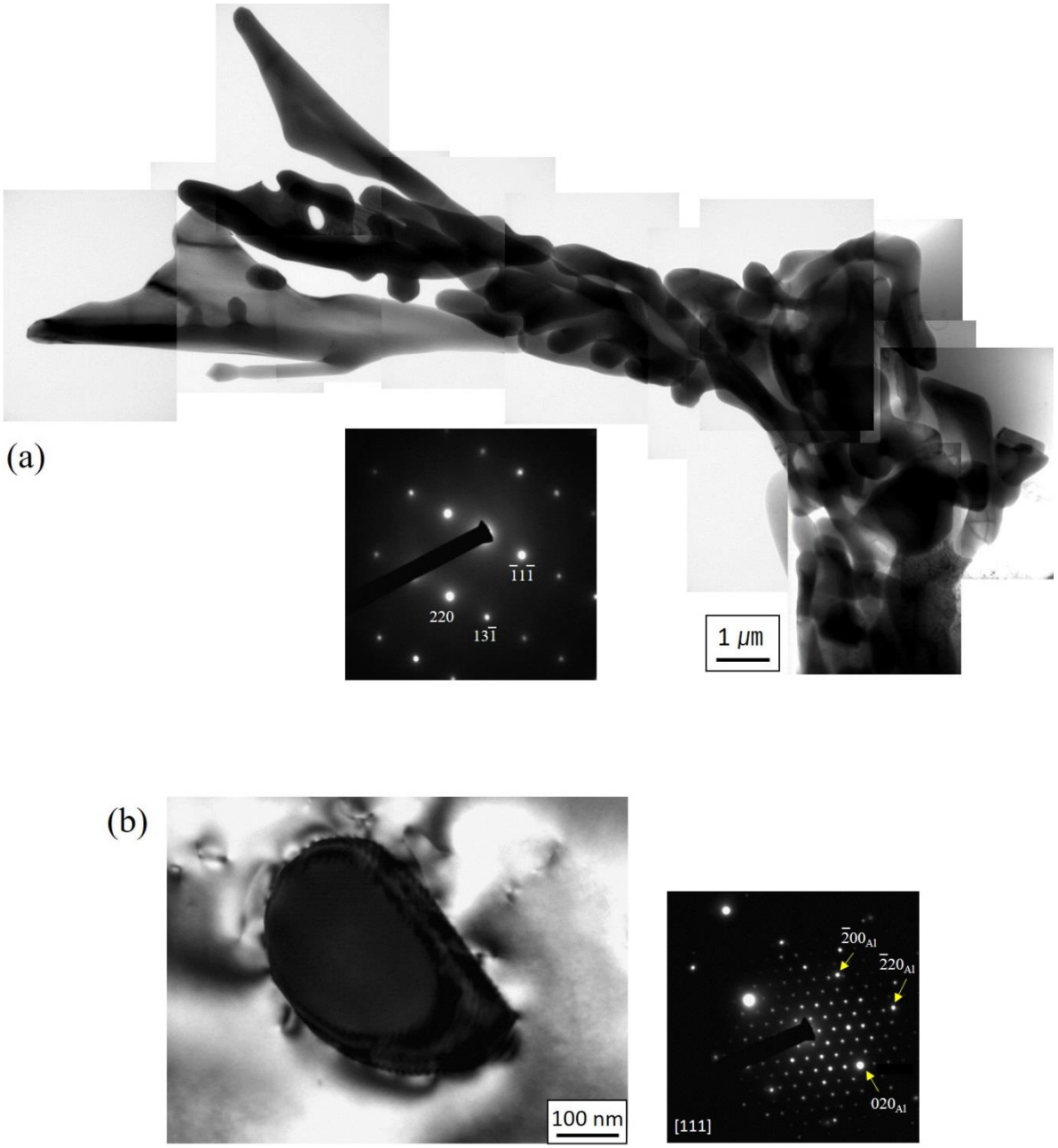


**Fig. 4-15 TEM bright-field images of DC-cast AMS sample. (a) dendritic Si particle, (b) α-AlMnSi particle.**

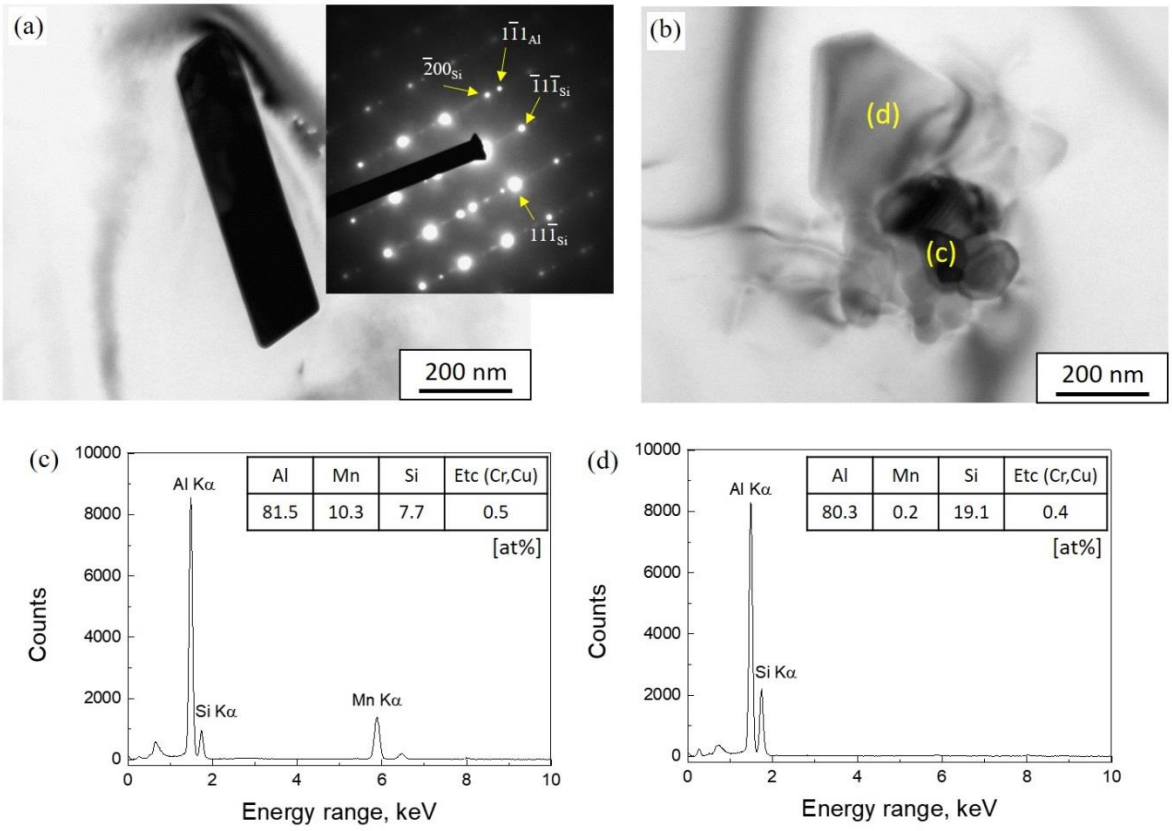


**Fig. 4-16 (a) polygonal Si particle in AMS strip surface, (b) composite agglomerates of spore-like particle and primary-like particle, (c) TEM-EDS spectra from the spore-like particle in (b), (d) TEM-EDS spectra from the primary-like particle in (b).**

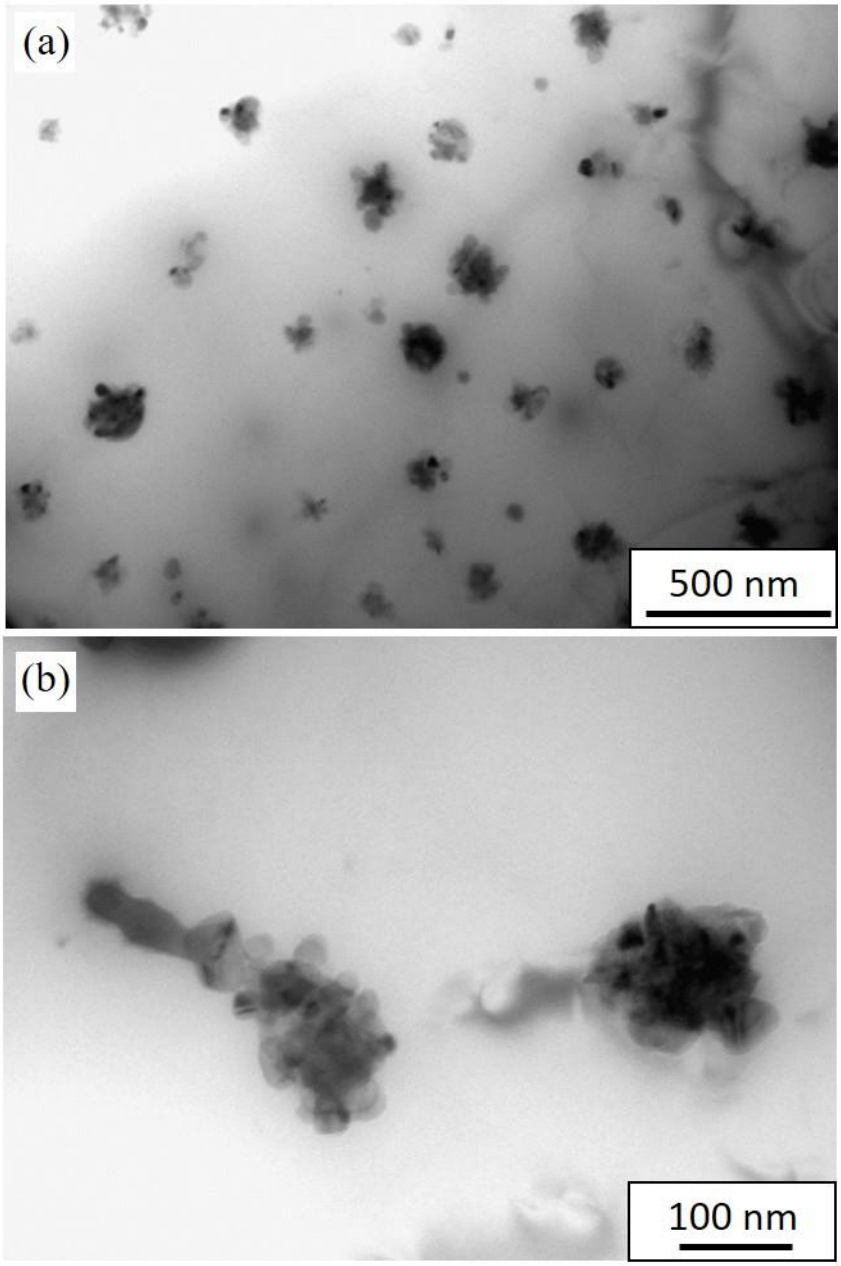


**Fig. 4-17 TEM bright-field image of single-roll cast AMS ribbon. The observed area corresponds to the roll-side.**

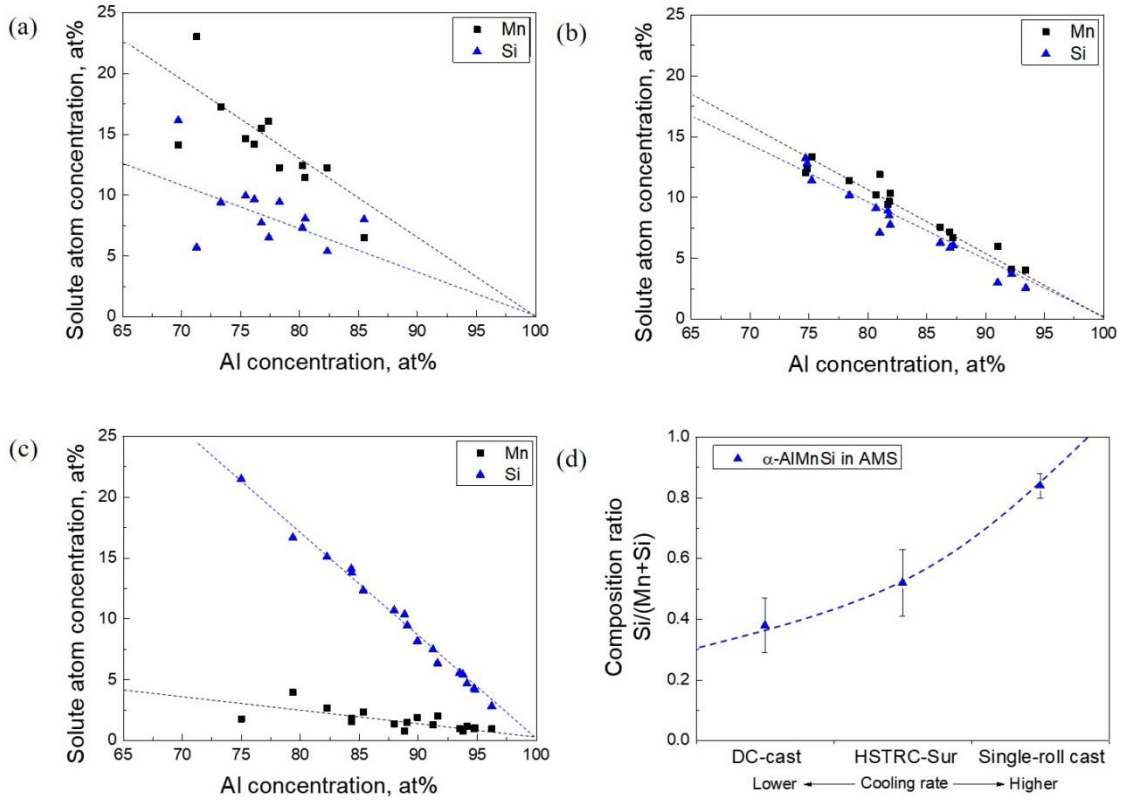


**Fig. 4-18 TEM-EDS results showing relative solute composition ratio of the secondary particles in AMS products. (a) DC-cast sample, (b) strip surface, (c) single-roll cast ribbon, (d) Composition ratio of Si/(Mn+Si) for α-AlMnSi particle in each product.**

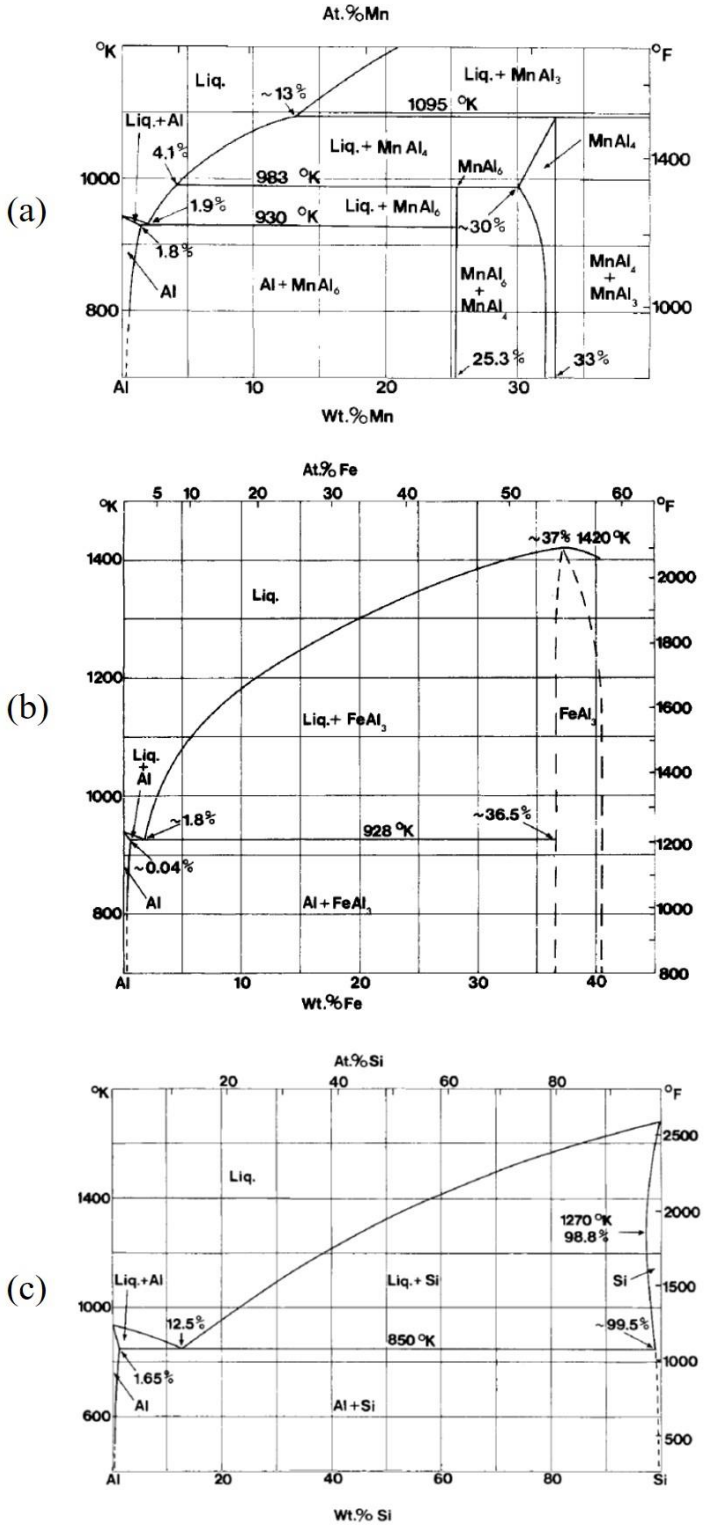


**Fig. 4-19 (a) Binary Al-Mn phase diagram, (b) binary Al-Fe phase diagram, (c) binary Al-Si phase diagram[1)].**

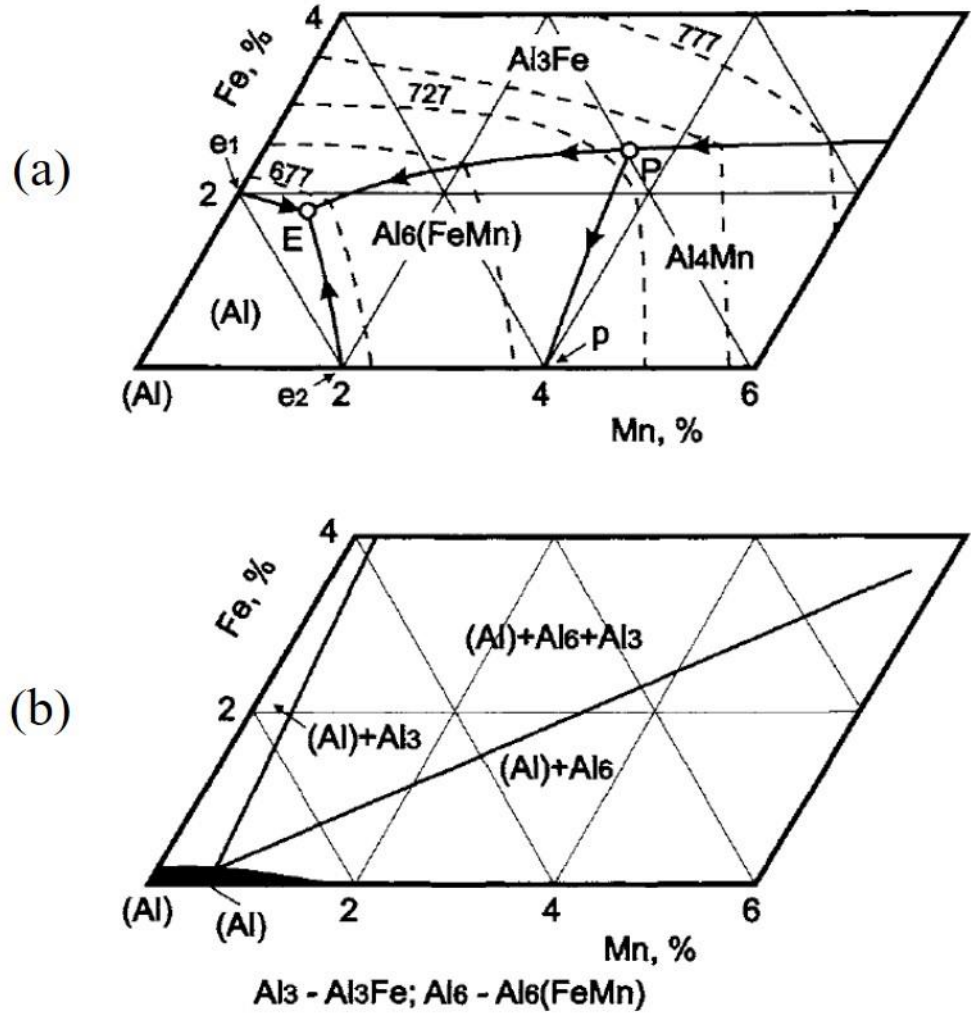


**Fig. 4-20 Phase diagram of Al-Mn-Fe system. (a) liquidus, (b) isothermal section at 627 $^{o}$C[4)].**

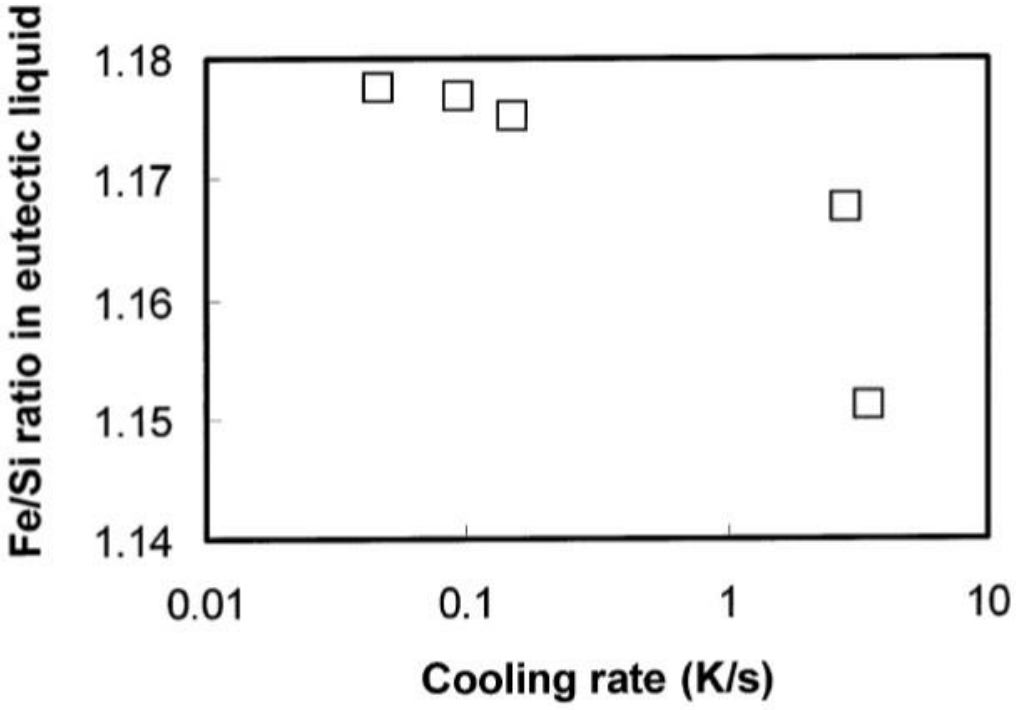


**Fig. 4-21 Relationship between cooling rate and Fe/Si ratio in eutectic liquid of Al-Fe-Si alloy[7].**

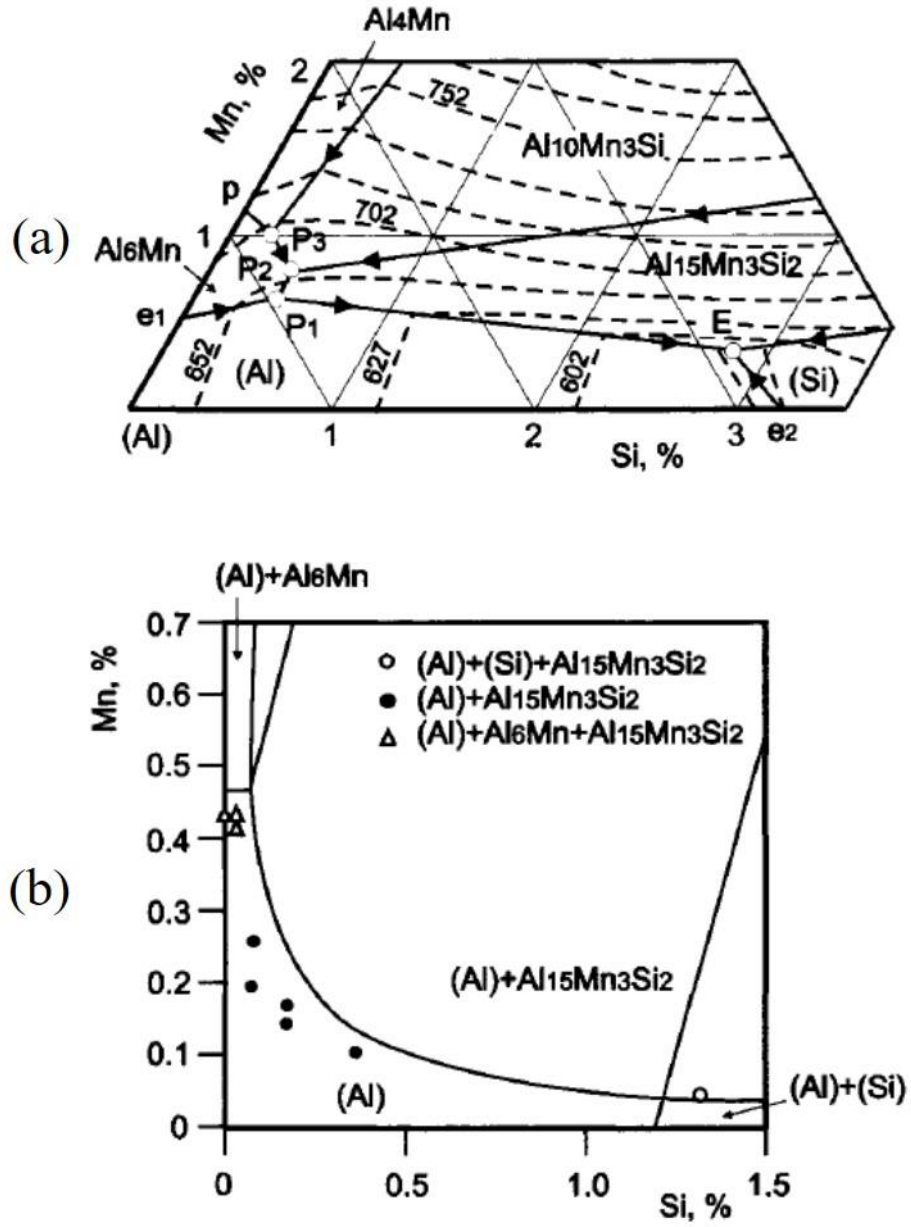


**Fig. 4-22 Phase diagram of Al-Mn-Si system. (a) liquidus, (b) isothermal section at 550 ℃[4].**

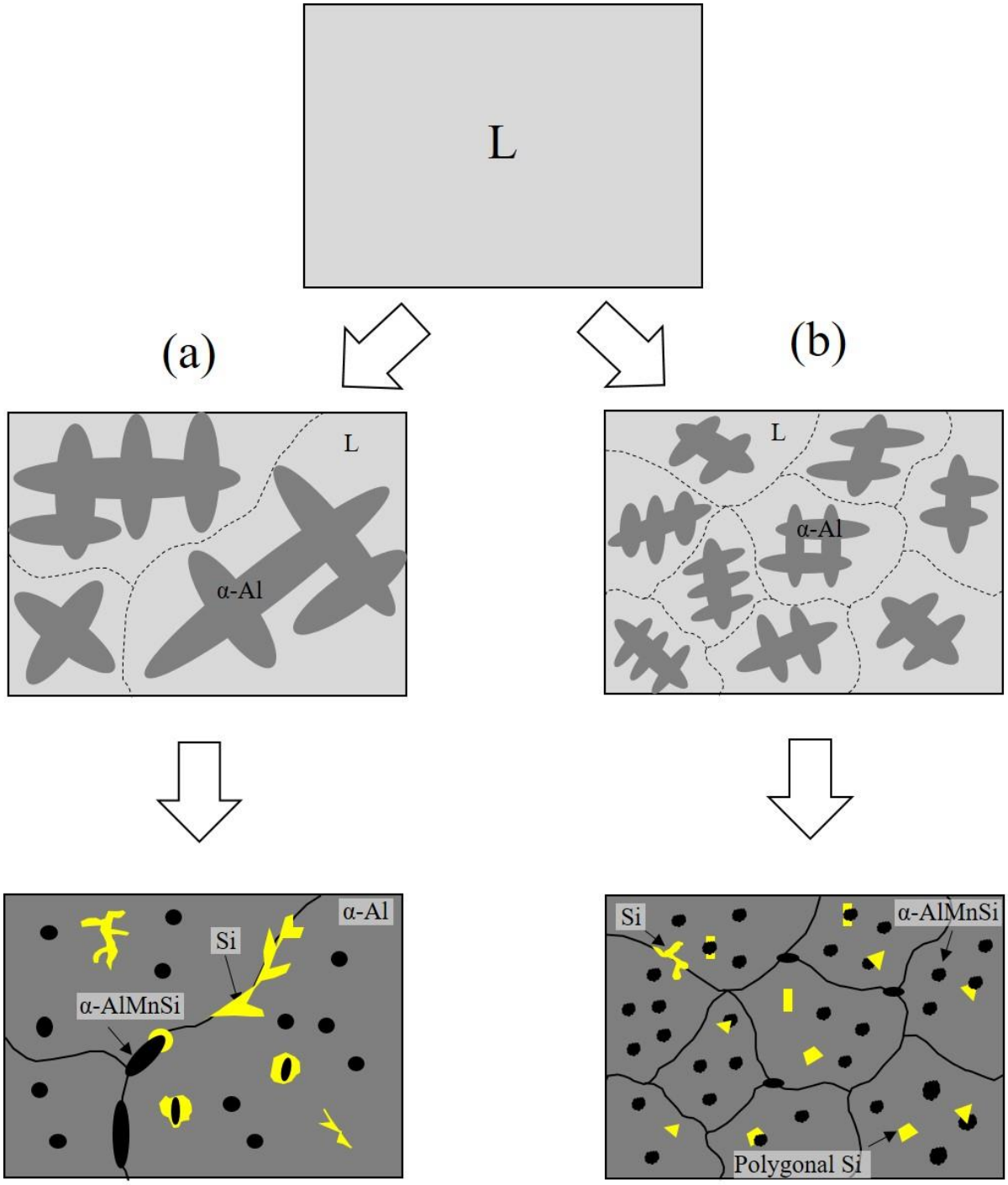


**Fig. 4-23 Illustration for solidification structure of AMS formed at different cooling rates. (a) low cooling rates in DC-casting, (b) high cooling rates in HSTRC.**

# Chapter 5 High Mn supersaturation and solid solution strengthening in vertical-type high-speed twin-roll cast Al-Mn binary alloy strips

## 5.1. Introduction

The Al-Mn binary alloy is a basis of the commercial 3xxx wrought aluminum alloys. The Al-Mn alloy can be classified into the non-heat treatable alloy that can get its strength basically by Mn solid solution strengthening and dispersion strengthening by Mn-bearing dispersoids. Therefore, the level of Mn supersaturation in Al matrix is quite important.

In conventional manufacturing using direct chill (DC)-casting method, high Mn solid solution could not be achieved due to its lower cooling rate. In contrast to that, as described in the previous chapters, vertical-type high-speed twin-roll casting (HSTRC) process shows an extremely high cooling rate during solidification. The rapid cooling of this method can contribute to make high supersaturation of alloying elements in Al matrix. Also, since thin aluminum alloy strips can be fabricated from the molten alloy in a single step, the present process can eliminate some downstream processes in conventional methods (*e.g.,* DC-casting) such as homogenization and/or hot rolling in sheets manufacturing process. Thus, it makes possible to maintain the high supersaturation of alloying elements in Al matrix until the last stage of manufacturing process.

This chapter focused on the Mn supersaturation in vertical-type high-speed twin-roll cast Al-Mn binary alloy strip. Al-Mn binary alloy strips with various Mn compositions were fabricated by using the HSTRC. The extension of Mn solubility in Al matrix was examined, then the effects of Mn solid solution strengthening on their mechanical properties were also discussed.

## 5.2. Experimental procedure

### 5.2.1. Materials

Al-Mn alloys with various Mn composition were prepared by mixing commercially pure aluminum (99.9 mass% Al) and Al-9.91 mass% Mn alloy. Their chemical composition are

shown in Table 5-1. The pure aluminum was melted in an alumina-coated carbon crucible in the electric furnace in advance, then the Al-9.91%Mn master alloy was added to get a series of molten alloys. Figure 5-1 shows an Al-Mn phase diagram[1)]. The Mn composition in each alloy was Al-1, 2 and 4 Mn in mass% (refers to AM1, AM2 and AM4, respectively). Each alloy corresponds to hypo-, eutectic and hyper-eutectic composition, respectively.

### 5.2.2. Casting process

Figure 5-2 shows a schematic illustration of the vertical-type high-speed twin-roll caster used in the present study. The specification was identical to the previous one described in the previous chapters. The details of casting conditions for each alloy are summarized in Table 5-2. In the present study, about 2.5~3 m- long and 100 mm- wide strip was obtained from 2.5 kg molten alloy. The constant thickness, which was about 1.8~2.3 mm, was obtained in the middle part of the cast strip along the casting direction (around 1 to 2 m-long). It should be noted that the microstructure observation was made for the part with the constant thickness.

In order to investigate the effect of cooling rate on the Mn concentration in Al matrix, permanent mold casting was also applied as described in Chapter 2. The permanent steel mold was designed to have a wedge-shape cavity (30 mm × 40 mm as mold bottom surface, 200 mm as mold height) to get different cooling rates depending on the local thickness of the cast plate. The pure copper mold was designed to have a rectangular cavity (100 mm × 100 mm × 2 mm). For the permanent steel and pure copper mold casting, 400 g and 170 g of molten alloys were used, respectively. The casting temperature was the same to HSTRC.

### 5.2.3. Tensile test

The cast strips were cold-rolled for 80 % reduction of the strip thickness. The rolling direction was parallel to the casting direction of the strip. In order to evaluate the influence of Mn supersaturation in as-cast condition on mechanical properties, the cold-rolled sheets were flash-annealed at 600 ℃ for 10 sec by salt-bath. Figure 5-3 shows the geometry and dimensions of the tensile test specimen. The tensile test was conducted using an Instron-type machine (SHIMAZU, AX-10kN) with a strain rate of 0.0017 $s^{-1}$ (1 mm/min as crosshead-speed).

### 5.2.4. Electrical conductivity measurement

The electrical conductivity measurement was performed by eddy current method at room temperature using exclusive 500 kHz probe (Auto Sigma 3000, GE Inspection Technology). For convenience, the electrical conductivity is expressed in terms of %IACS (International Annealed Copper Standard) here. For wedge-shape steel mold cast product, the electrical conductivity was measured at the mid-center of the product. For HSTRC strip, repetitive polishing and conductivity measurement were conducted along its thickness direction until the strip central area. For average electrical conductivity value, it was measured more than 5 times in each specimens.

In the eddy current method for electrical conductivity measurement, the sufficient sample thickness is required to obtain the accurate value. Generally, penetration depth of the eddy current can be defined as[2)]

$$\delta = 1/\sqrt{\pi f \mu \sigma} \qquad (5\text{-}1)$$

where, $\delta$ is penetration depth of eddy current, $f$ is frequency, $\mu$ is magnetic permeability of the sample, $\sigma$ is conductivity value.

In case of the flash-annealed HSTRC strips after cold-rolling, due to the change of strip thickness, it was hard to obtain the accurate electrical conductivity. As replacement, the as-cast strip was heat-treated at the same annealing condition, 600 ℃ for 10 sec by salt-bath, then the electrical conductivity was measured. The value was considered as that of each flash-annealed alloy strips.

### 5.2.5. Microstructure observation

Optical microscopic observation was carried out on transverse cross sections of the cast strip (BX51M, Olympus). The polished specimens were etched by the Keller's reagent ($H_2O$:$HNO_3$:HCl:HF = 190:5:3:2 in Vol%). As-polished cross-sections were also anodized at 40 V voltages using Barker's reagent (3.3% of $HBF_4$ aqueous solution) to reveal the grain structure. Secondary particles were identified using X-ray diffractometer (RINT-2100,

Rigaku) with Cu $K_\alpha$ ($\lambda$ = 1.54 Å) radiation. The size distribution and area fraction of secondary particles were measured using Image-J software based on FE-SEM (JEM-7000F, JEOL) observation.

### 5.2.6. DTA analysis

Differential thermal analysis (DTA) was carried out to investigate the formation of secondary particles during solidification. The DTA analysis was conducted under an Ar gas atmosphere (TG8120, Rigaku). In order to ensure the accuracy of DTA measurements, the data was modified by calibration to remove errors of measurements itself. The $Al_2O_3$ powder of 40 mg in weight was used as a reference material. The Al-Mn binary alloy samples were also made with the same weight as the reference material. For the DTA, the temperature profile was designed so that the temperature increases linearly from room temperature to 800 ℃ for melting. After holding the specimen at 800 ℃ for 30 min, temperature decreased to 300 ℃. Both heating rate and cooling rate were set to 20 ℃/min.

## 5.3. Results

### 5.3.1. Mn solubility estimation by electrical conductivity

Generally, the electrical conductivity has a linear relationship with electrical resistivity[3]. The electrical conductivity can be converted to electrical resistivity value by:

$$1724.1/\%IACS = \rho/n\Omega m \qquad (5\text{-}2)$$

In Al-Mn binary alloy, Mn content in the Al matrix mainly affects its electrical conductivity. According to Komatsu and Fujikawa[4], the Mn content in Al solid solution can be estimated by:

$$Mn\ concentration\ in\ solid\ solution = (\rho_{measure} - \rho_{pure\ Al})/\Delta\rho_{Mn\ in\ Al\ alloy} \qquad (5\text{-}3)$$

where, $\rho_{measure}$ is the electrical resistivity of alloy converted by the measured electrical

conductivity, $\rho_{pure\ Al}$ is the electrical resistivity of pure aluminum, which is 26.5 nΩm at room temperature, and $\Delta\rho_{Mn\ in\ Al\ alloy}$ is the electrical resistivity contribution for Mn solute atom in Al matrix. The value of $\Delta\rho_{Mn\ in\ Al\ alloy}$ is 31 nΩm wt%$^{-1}$ at room temperature.

Table 5-3 shows the Mn concentration in solid solution of each alloy obtained from the measured electrical conductivity. For wedge-shape steel mold casting, the cooling rate changed with the cast product thickness as described in Chapter 2. There is no specific difference of the Mn concentration value in the wedge-shape steel mold cast product regardless of its thickness. For AM1 and AM2, the Mn solubility values were equivalent to their alloy compositions, roughly 1 and 2 in mass%, respectively. For hyper eutectic composition of AM4, the Mn solubility was limited under the eutectic composition, around 2.0~2.1 Mn in mass%. Haan et al.[5] also reported the Mn concentration up to 2.0 mass% in solid solution for the as-cast Al-Mn binary alloy.

In contrast, the copper mold cast product of AM4 showed around 2.9 mass% Mn. This value was larger than that of wedge-shape steel mold cast products. It is considered to be due to higher cooling rate of copper mold casting than that of wedge-shape steel mold casting.

For HSTRC strip, the measured Mn concentration value of the AM1 and AM2 was also equivalent to their alloy compositions for both strip surface and central area. In AM4, over 3.5 mass% Mn was estimated at the strip surface. However, Mn concentration of the strip central area changed depending on the melt superheating conditions. Figure 5-4 shows Mn concentration profile along the strip thickness direction in AM4 for different melt superheating conditions. At the strip surface, no specific Mn concentration difference was observed. While, in the lower melt superheating condition, a decrease in Mn concentration was observed along the strip thickness direction.

Meanwhile, the annealed HSTRC strips at 600 ℃ for 10 sec by salt-bath showed equivalent Mn concentration level to that of as-cast conditions (see Table 5-3). This result suggests that the Mn decomposition does not occur during the flash-annealing.

### 5.3.2. DTA results

Figure 5-5 shows DTA results of AM1, AM2 and AM4 at the cooling rate of 20 ℃/min from 800 ℃ to 300 ℃. Two kinds of exothermic peaks (as marked by peaks (a) and (b)) were observed. The peak (a) was found at 656-652 ℃, and the maximum intensity was observed at

651-648 ℃. The peak (a) represents the solidification of aluminum. The peak (b), only observed in AM4, was confirmed at 689 ℃, and the maximum intensity was observed at 671.6 ℃. The peak (b) corresponds to the formation of primary $Al_6Mn$ phase. The peak for Al-Mn eutectic reaction was not detected.

### 5.3.3. Macrostructure of cast products

Figure 5-6 shows a typical microstructure of the wedge-shape steel mold cast products. In AM1, secondary particles were not observed. In AM2, cellular α-Al and small amount of eutectic phase particles were observed. In AM4, many coarse particles were observed as shown in Fig. 5-6 (c) and (d). From the DTA result, the coarse particles are considered to be a primary $Al_6Mn$ phase. The microstructure of the copper mold cast product is shown in Fig. 5-7. Along the thickness direction, different microstructure was observed. The cell structure was observed near the surface region of the product as shown in Fig. 5-7 (b). Inside of the cell, fine etch pits were observed, which are corresponding to the secondary particles. In contrast to that, the primary particles were observed at the mid-central region. The primary particles were finer than those of the wedge-shape steel mold cast product.

Figure 5-8 shows a grain structure of the transverse cross-section of each alloy strip. Basically, the chilled layers were formed at the near-surface of the all strips by rapid cooling from the roll surfaces. In HSTRC, the freezing temperature range of the alloys has a strong effect on solidification manner of the strip and the resultant microstructure[6]. In Al-Mn binary system, the freezing temperature range is quite narrow (see Fig. 5-1). In this case, skin-formation type solidification is expected; the solidified shells formed at the both roll surfaces grow in the direction of heat flow, resulting in a columnar grain structure. The growth fronts of the columnar grains encounter at the strip central area. There was no specific difference in the grain structure among hypo-, eutectic and hyper eutectic Al-Mn binary alloy strips.

Figure 5-9 shows a microstructure of each alloy strip at the half-thickness regions. Due to the different casting conditions such as melt superheating and roll separating force, the thickness of the stable part in each alloy strip was different. For instance, a relatively large melt superheating is considered to suppress the growth of the shells, resulting in the decrease of strip thickness. Also, Kim et al.[7] reported the decrease of strip thickness by increasing

initial roll separating force due to the squeezing out of the mushy layer from the strip central region when the strip passes through near the minimum roll gap. In the present study, the Al-Mn binary alloy shows skin-formation type solidification, which implies the formation of mushy layer at the solidification growth fronts is limited. The effect of roll separating force on the strip thickness reduction is probably little in this case.

In all cast strips, cell structures were clearly observed near the strip surface. The cell structure extended to the strip central area. A particle distribution along the thickness direction was obviously different depending on the alloy composition; primary particles were not observed in AM1 and AM2. In contrast to that, some amount of primary $Al_6Mn$ phase particles were observed in AM4. The particles were frequently observed at the central area of the AM4 fabricated under the lower melt superheating condition.

### 5.3.4. XRD analysis result

Figure 5-10 shows the XRD pattern results of AM4 with superheating of 70 ℃. The $Al_6Mn$ phase and α-Al phase of matrix peaks were detected in all cast products. Relatively weak intensity for the $Al_6Mn$ phase peak was detected in HSTRC strip and copper mold cast product surface as shown in Fig. 5-10 (a) to (c). Much stronger intensity of $Al_6Mn$ phase peak was observed in the center of copper mold cast product and wedge-shape steel mold cast product as shown in Fig. 5-10 (d) and (e). It is due to both primary and eutectic $Al_6Mn$ phase were detected in the center of copper mold cast product and wedge-shape steel mold cast product with lower cooling rate. This result is well corresponded to the microstructure observation results as shown in Figs. 5-6 to 5-9.

### 5.3.5. Tensile properties of annealed sheet

The representative engineering stress-strain curves of flash-annealed each alloys strip are shown in Fig. 5-11. Table 5-4 shows the 0.2 % strain offset yield stress (YS), ultimate tensile strength (UTS) and elongation of each alloy strip. Significant increases of the YS and UTS were obtained for the AM4. Since the Mn concentration in Al matrix did not change after flash-annealing (see Table 5-3), the improvement of the YS is considered to be mainly due to

Mn solid solution strengthening. Meanwhile, the AM1 showed larger fracture elongation value than those of AM2 and AM4.

## 5.4. Discussion

### 5.4.1. Solidification sequence of Al-Mn binary alloy in HSTRC

According to the equilibrium phase diagram of binary Al-Mn, the following reactions can be considered during solidification as regarding the Al-rich region[1,8,9]:

$$L + Al_4Mn \rightarrow Al_6Mn \quad [5\text{-}1]$$

$$L \rightarrow (Al) + Al_6Mn \quad [5\text{-}2]$$

$$L \rightarrow (Al) \quad [5\text{-}3]$$

The peritectic reaction [5-1] takes place at 706 ± 3 ℃. Also, the eutectic reaction [5-2] occurs at 658 ± 1 ℃. For AM1, it was hard to detect any secondary particle formation from DTA result. The alloy composition of the AM1 was lower than eutectic composition. Thus, AM1 probably underwent only the reaction [5-3]. In contrast to that, AM2 is considered to follow the reaction [5-2]. Consequently, α-Al and/or α-Al + $Al_6Mn$ eutectic structure was observed (see Fig. 5-6 (b)). From the DTA result of AM4, it was confirmed both reactions [5-1] and [5-2] occurred during solidification. It leads to the formation of not only primary, but also eutectic $Al_6Mn$ phases. For the permanent mold cast products, lots of primary $Al_6Mn$ particles were observed as shown in Fig. 5-6 (c), (d) even in the center of copper mold cast product as shown in Fig. 5-7 (c). The XRD results showed the relatively high intensity for $Al_6Mn$ phase in AM4 (see Fig. 5-10 (e)). For the formation of primary $Al_6Mn$ particle, some amounts of Mn element in liquid phase must be consumed before solidification of α-Al. Therefore, the Mn supersaturation in Al matrix was suppressed.

In HSTRC strips, the Mn concentration profile along the strip thickness direction changed with melt superheating conditions (see Fig. 5-4). As shown in Fig. 5-9 (c) and (d), a number of large primary $Al_6Mn$ particles were observed in +15 ℃ superheat cast strip, especially at the strip central area. The direct temperature measurement revealed that the cooling rate of HSTRC was more than $10^3$ ℃/s even at the central area of strip[7,10]. Therefore, it is hard to

consider that the large primary $Al_6Mn$ particles formed at such high cooling rate. Instead, it is reasonable to consider the primary $Al_6Mn$ particles were formed in the melt pool. If the applied casting temperature is not sufficiently high rather than liquidus temperature, primary phase can be formed in the melt pool. On the other hand, in the +70 ℃ superheat cast strip, the primary $Al_6Mn$ particles were not observed on both strip near surface and central area. This result suggests the solidification was conducted through only the eutectic reaction [5-2] and/or the reaction [5-3], rather than the peritectic reaction [5-1]. It was confirmed that the sufficient melt superheating was effective to prevent to form the primary $Al_6Mn$ phase particles in the melt.

Generally, significant level of undercooling of the melt can be achieved by increasing the cooling rate. In the HSTRC, large undercooling can occur due to its high cooling rate during solidification. The 70 ℃ superheat melt of AM4 was rapidly cooled to below its eutectic temperature by large undercooling of the HSTRC. Consequently, high Mn supersaturated Al-Mn binary alloy strip was achieved.

### 5.4.2. Strengthening mechanism of Al-Mn binary alloy strip

For improvement of the yield stress (normally taken as 0.2 % strain offset proof stress) of aluminum alloys, contributions of several kinds of hardening mechanisms are considered; work hardening (or strain hardening), precipitation hardening, dispersion hardening, grain boundary hardening (or Hall-Petch strengthening) and solid solution hardening. Thus, the yield stress, $\sigma_{YS}$, can be expressed by:

$$\sigma_{YS} = \sigma_o + \sigma_{GB} + \sigma_{Disp} + \sigma_{SS} \qquad (5\text{-}4)$$

where $\sigma_o$ is yield stress of pure Al, $\sigma_{GB}$ is strengthening by grain boundaries, $\sigma_{Disp}$ is strengthening by dispersions and $\sigma_{SS}$ is strengthening by solid solution. It should be noted that the Al-Mn based alloy is classified as non-heat treatable aluminum alloys that get their strength by work hardening, solid solution hardening and the hardening by grain refinement and dispersions. In the present study, the strength of fully-annealed specimens was examined. For this reason, the contribution of work hardening is not included. In addition, the Mn decomposition was not observed during the flash-annealing process. Thus, the precipitation

hardening is also considered to be negligible.

Figure 5-12 shows the recrystallized grain structure of the flash-annealed alloy strip. Significant difference in size of recrystallized grains was not detected. The contribution of grain boundaries on the yield stress, $\sigma_{GB,}$ is expressed by Hall-Petch equation:

$$\sigma_{GB} = k \cdot d^{-1/2} \qquad (5\text{-}5)$$

where $k$ is grain boundary strengthening coefficient (84 MPa·μm$^{1/2}$ for Al-Mn based alloy[11]), $d$ is the grain size. The average grain size for AM1, AM2 and AM4 was 43.7 μm, 48.7 μm and 46.8 μm, respectively, and their corresponding calculated $\sigma_{GB}$ was about 12.7 MPa, 12.0 MPa and 12.3 MPa, respectively. It is well known that secondary particles play an important role in recrystallization of deformed aluminum alloys; relatively coarse particles (generally > 2 μm in diameter), mainly formed during solidification, can act as nucleation site of recrystallization. This is called particle stimulated nucleation (PSN), resulting in refined recrystallized grains[12]. Whereas, relatively fine dispersoids, concurrently precipitated during heat treatment, tend to impede the grain boundary movement through a Zener drag effect[13], resulting in slow down recrystallization and growth of recrystallized grains. In the present study, coarse constituent particles were not observed in AM1, AM2 and AM4. Thus, it is hard to consider that PSN works effectively. Also, since the decomposition of supersaturated Mn is quite sluggish in Al-Mn binary alloy because of low diffusivity of Mn in Al solid state[14,15], the concurrent precipitation during the annealing process is scarcely considered. Furthermore, the flash-annealing condition applied in the present study cannot allow the substantial concurrent precipitation due to quite short processing time. As a result, there is no difference in recrystallized grain size of the AM1, AM2 and AM4 after flash-annealing.

Figure 5-13 shows the secondary particle distribution of flash-annealed specimens. Most of secondary particles were considered as the constituent particles formed during solidification. A relatively high-dense secondary particle dispersion was observed in AM4. The size distribution of the secondary particles is shown in Fig. 5-14. With increasing Mn contents in the alloys, quantity of the secondary particles was increased. Most of the secondary particles were less than 1 μm in diameter. It is attributed to high cooling rate of the HSTRC. The contribution of secondary particles to the yield stress can be estimated using Ashby-Orowan

equation[16]:

$$\sigma_{Disp} = \frac{0.8MGb}{2\pi\lambda\sqrt{(1-\nu)}}\ln(\frac{D}{2b}) \qquad (5\text{-}6)$$

where, $M$ is Tayler factor, $G$ is the shear modulus of the Al matrix, $b$ is the Burgers vector of dislocation in Al, $\nu$ is the Poison ratio for Al, $D$ is particle diameter and $\lambda$ is the interspacing of secondary particles. It is considered that the relatively coarse secondary particles have no contribution to the dispersion strengthening. In this study, only fine secondary particles below 200 nm in diameter were used for the calculation. In terms of the $\lambda$, it depends on the particle diameter and its volume fraction. There are a variety of definitions for the interspacing of secondary particles[17]. In this study, the $\lambda$ was replaced by $A^{-1/2}$ ($A$ is particle area fraction)[11]. Note that the particle area fraction, $A$ was also obtained from the particles corresponding to below 200 nm in the particle diameter. Based on the eq. (5-6), the calculated $\sigma_{Disp}$ for AM1, AM2 and AM4 alloy strip was 3.6 MPa, 5.1 MPa and 13.4 MPa, respectively.

The contribution of Mn solid solution to the yield stress was also considered. Ryen et al.[18] reported correlations between the flow stress and the alloying concentration as follow:

$$\sigma_{ss} = \sigma_{pure} + Hc^n \qquad (5\text{-}7)$$

where, $\sigma_{pure}$ is the flow stress of a pure metal, $c$ is the alloy concentration in atomic %, and $H$ and $n$ are constants. At the yield point, $\varepsilon = 0.002$, the $\sigma_{pure}$ is 4.03 MPa, the $n$ is 0.9 and the $H$ is 34.8 MPa/at% in high-purity Al-Mn binary alloy[18]. The calculated $\sigma_{ss}$ for AM1, AM2 and AM4 was 24.8 MPa, 39.5 MPa and 61.3 MPa, respectively.

Based on the above discussion, the contribution of each strengthening mechanism on the yield stress in Al-Mn binary alloy strip is summarized as shown in Fig. 5-15. There is no specific difference of the $\sigma_{GB}$ value among the Al-Mn binary alloy strips. The $\sigma_{Disp}$ of each alloy strip has a relatively small contribution to the total yield stress improvement; 7.9%, 8.4% and 14.7% for AM1, AM2 and AM4 alloy, respectively. The significant improvement of the yield stress is mainly due to the solid solution strengthening by high Mn supersaturation resulting from the high cooling rate of HSTRC, especially in AM4.

Meanwhile, there is a difference in the yield stress between calculated data and

experimentally obtained data only for the AM4; experimentally obtained yield stress was larger than that of calculated data. This difference may be due to the underestimation of the contribution of dispersion strengthening. The evaluation for dispersion strengthening was conducted based on the assumption; a uniform distribution of spherical particles in a regular cubic array. Also, in the present study, the interspacing of secondary particles was replaced by $A^{-1/2}$ because it was obtainable directly from the FE-SEM observation. In practice, however, the secondary particles are dispersed in 3-dimensional. In this case, the interspacing of secondary particles in the volume is probably shorter than that in a 2-dimensional. Thus, it is possible that the overestimated interspacing of secondary particles resulted in the underestimation for the contribution of dispersion strengthening.

### 5.5. Conclusions

Hypo-, eutectic and hyper-eutectic Al-Mn binary alloy strips were produced by using HSTRC. High Mn supersaturation can be achieved by high cooling rate of HSTRC. In the alloy composition of hyper eutectic Al-Mn binary alloy, formation of a number of primary $Al_6Mn$ phase particles in the melt pool were considered to occur during the casting, and it reduced Mn concentration in the Al matrix along the strip thickness direction. Applying the sufficient melt superheating was effective to prevent formation of the primary $Al_6Mn$ phase and to increase the Mn concentration in Al matrix.

Significant increase in 0.2 % strain offset yield stress was obtained for the flash-annealed high Mn supersaturated Al-Mn binary alloy strip. Contribution of several strengthening mechanisms was investigated, and it was concluded that the improvement of yield stress is mainly attributed to the contribution of Mn solid solution strengthening by high Mn supersaturation resulting from high cooling rate of the HSTRC.

## References


1) L.F. Mondolfo: *Aluminum Alloys: Structure and Properties*,Butterworths, (1976)
2) H. Hoshikawa: J. Japan Foundarymen's Soc., **65** (1993) 921–27
3) J.E. Hatch: *Aluminum; Properties and Physical Metallurgy*,(1984)
4) S. Komatsu and S. Fujikawa: JILM, **47** (1997) 170–81
5) P.C.M. de Haan, J. van Rijkom, and J.A.H. Søntgerath: Mater. Sci. Forum, **217**–**222** (1996) 765–70
6) M. S. Kim and S. Kumai: Mater. Trans., **52** (2011) 856–61
7) M. S. Kim, Y. Arai, Y. Hori, and S. Kumai: Mater. Trans., **51** (2010) 1854–60
8) J.L. Murray, A.J. McAlister, R.J. Schaefer, L.A. Bendersky, F.S. Biancaniello, and D.L. Moffat: Metall. Trans. A, **18** (1987) 385–92
9) A. J. McAlister and J. L. Murray: J. Phase Equilibria, **8** (1987) 438–47
10) R. Song, Y. Harada, and S. Kumai: Mater. Trans., **59** (2018) 110–16
11) M. Yoshino, S. Iwao, M. Edo, S. Muraishi, and S. Kumai: JILM, **66** (2016) 652–59
12) F.J. Humphreys and P.N. Kalu: Acta Metall., **35** (1987) 2815–29
13) E. Nes, N. Ryum, and O. Hunderi: Acta Metall., **33** (1985) 11–22
14) Y. Du, Y.A. Chang, B. Huang, W. Gong, Z. Jin, H. Xu, Z. Yuan, Y. Liu, Y. He, and F.Y. Xie: Mater. Sci. Eng. A, **363** (2003) 140–51
15) P. Kolby, C. Sigli, and C.J. Simensen: *Aluminum Alloys: Their Physical and Mechanical Properties*, *ICAA4, Atlanta, USA*,(1994)
16) M. F. Ashby: *Physics of Strength and Plasticity*,MIT press, (1969)
17) C. W. Corti, P. Cotterill, and G. Fitzpatrick: Int. Mater. Rev., **19** (1974) 77–88
18) Ø. Ryen, O. Nijs, E. Sjölander, B. Holmedal, H.E. Ekström, and E. Nes: Metall. Mater. Trans. A, **37** (2006) 1999–2006

**Table 5-1 Chemical compositions of commercially pure aluminum and Al-9.91 Mn alloy ingot. (in mass %)**

| Alloy | Mn | Fe | Si | Al |
|---|---|---|---|---|
| Pure Al | <0.01 | 0.06 | 0.04 | Bal. |
| Al-9.91Mn | 9.91 | <0.1 | <0.1 | Bal. |

**Table 5-2 HSTRC conditions for each alloy.**

| Condition | Alloy* | | | |
|---|---|---|---|---|
| | AM1 | AM2 | AM4-15 | AM4-70 |
| Melt superheating (°C) | 15 | 15 | 15 | 70 |
| Roll rotation speed (m/min) | 60 | 60 | 60 | 60 |
| Solidification length (mm) | 100 | 100 | 100 | 100 |
| Roll separating force (kN) | 20 | 20 | 60 | 60 |
| Initial roll gap (mm) | 1 | 1 | 0.8 | 0.8 |

**Note*: AM1, AM2, AM4-15 and AM4-70 are corresponded to Al-1 mass% Mn, Al-2 mass% Mn, Al-4 mass% Mn with 15 ℃ melt superheat and Al-4 mass% Mn alloy with 70 ℃ melt superheat, respectively.

**Table 5-3 Mn concentration in solid solution of each alloy. (in mass %)**

| Cast product | | | | Alloy | | | |
|---|---|---|---|---|---|---|---|
| | | | | AM1 | AM2 | AM4-15 | AM4-70 |
| As-cast | Permanent mold casting | Steel mold | Top | 1.2 | 2.1 | 2.1 | 2.1 |
| | | | Mid. | 1.2 | 2.2 | 2.1 | 2.1 |
| | | | Tip | 1.2 | 2.2 | 2.1 | 2.0 |
| | | Copper mold | | - | - | - | 2.9 |
| | HSTRC | | Surface | 1.2 | 2.0 | 3.7 | 3.6 |
| | | | Center | 1.1 | 2.0 | 2.7 | 3.8 |
| Flash-annealing (600 ℃, 10s) | HSTRC | | | 1.1 | 2.1 | - | 3.5 |

**Table 5-4 Average values of 0.2 % strain offset proof stress, ultimate tensile stress and fracture elongation for flash-annealed alloy strips.**

| Alloy | 0.2 % strain offset proof stress (MPa) | Ultimate tensile stress (MPa) | Elongation (%) |
|---|---|---|---|
| AM1 | 42.4 ± 1.6 | 95.9 ± 1.2 | 34.7 ± 2.4 |
| AM2 | 61.7 ± 1.2 | 126.6± 0.7 | 26.6 ± 3.6 |
| AM4-70 | 105.5 ± 2.5 | 189.2 ± 1.4 | 26.9 ± 0.8 |

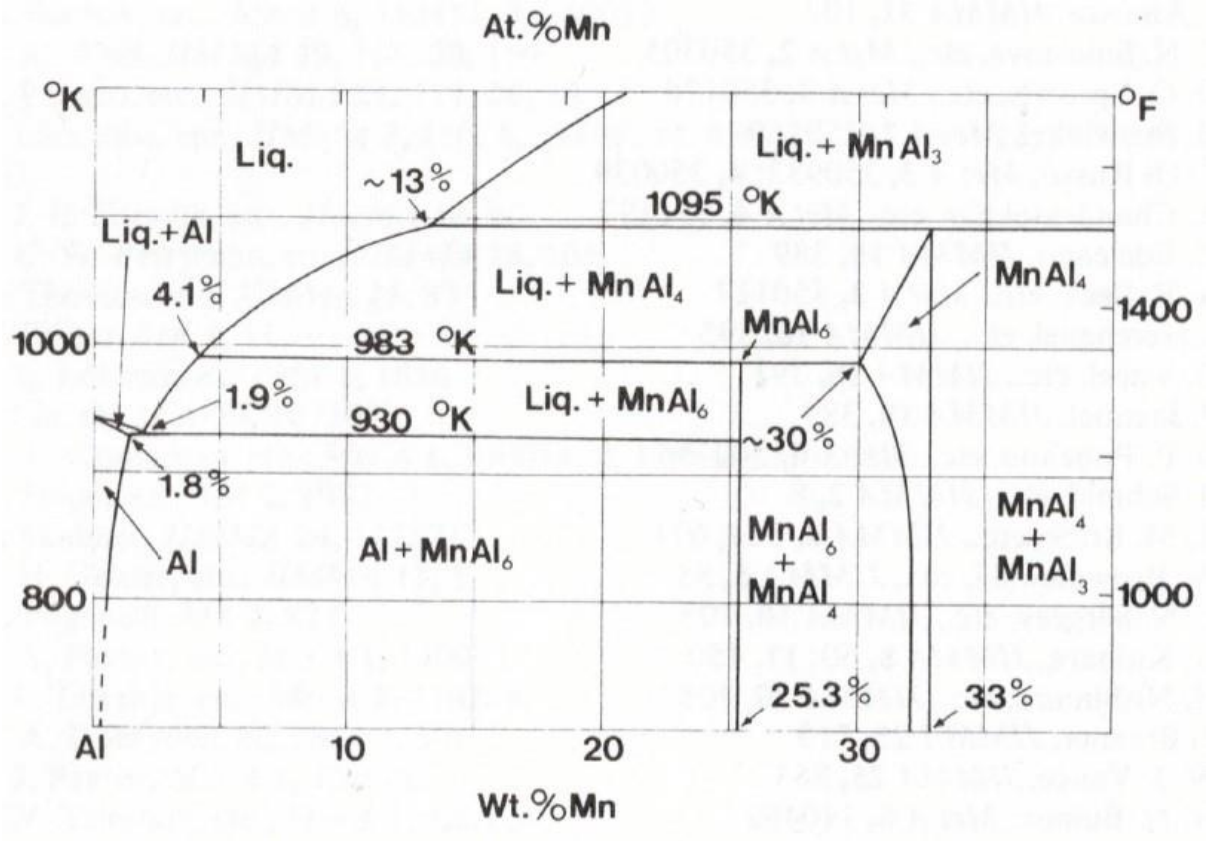


**Fig. 5-1 Al-corner part in Al-Mn binary phase diagram[1)].**

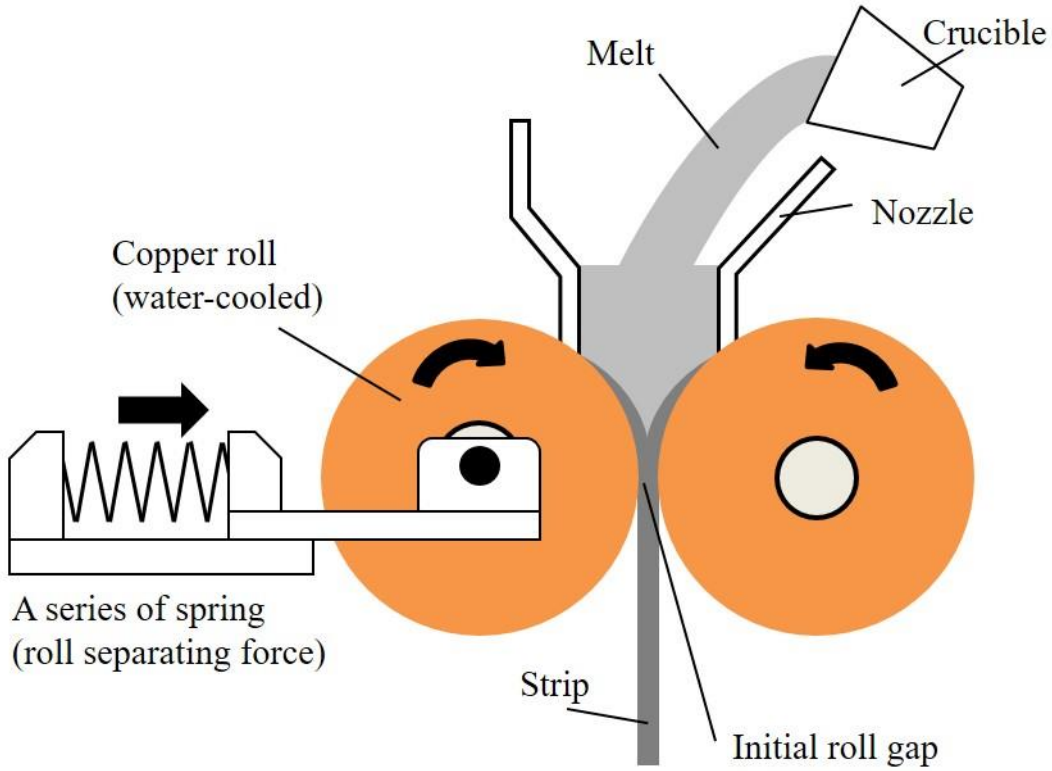


**Fig. 5-2 Schematic illustration of the vertical-type high-speed twin-roll caster.**

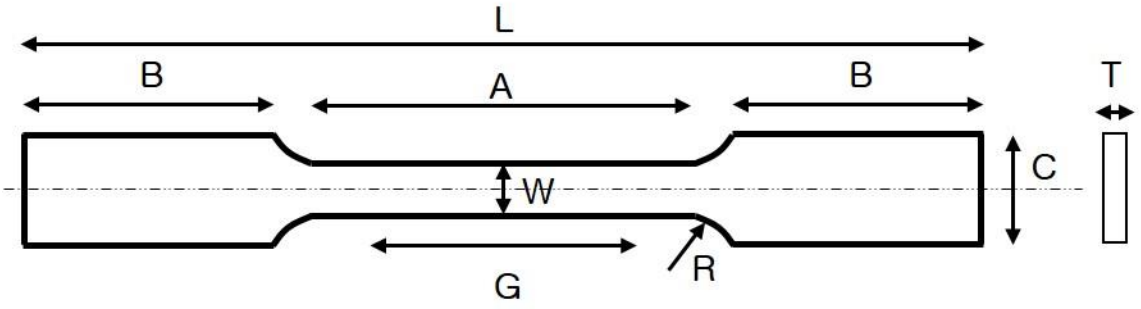


| Specifications | |
|---|---|
| Gauge length (G) | 10 mm |
| Width (W) | 5 mm |
| Thickness (T) | As-rolled<br>(AM1: 0.49, AM2: 0.50, AM4: 0.37 in mm) |
| Length of reduced section (A) | 14 mm |
| Length of grip section (B) | 10 mm |
| Width of grip section (C) | 12 mm |
| Radius of fillet (R) | R= 10.893 |
| Total length (L) | 50 mm |

**Fig. 5-3 Geometry and dimensions of tensile test specimen.**

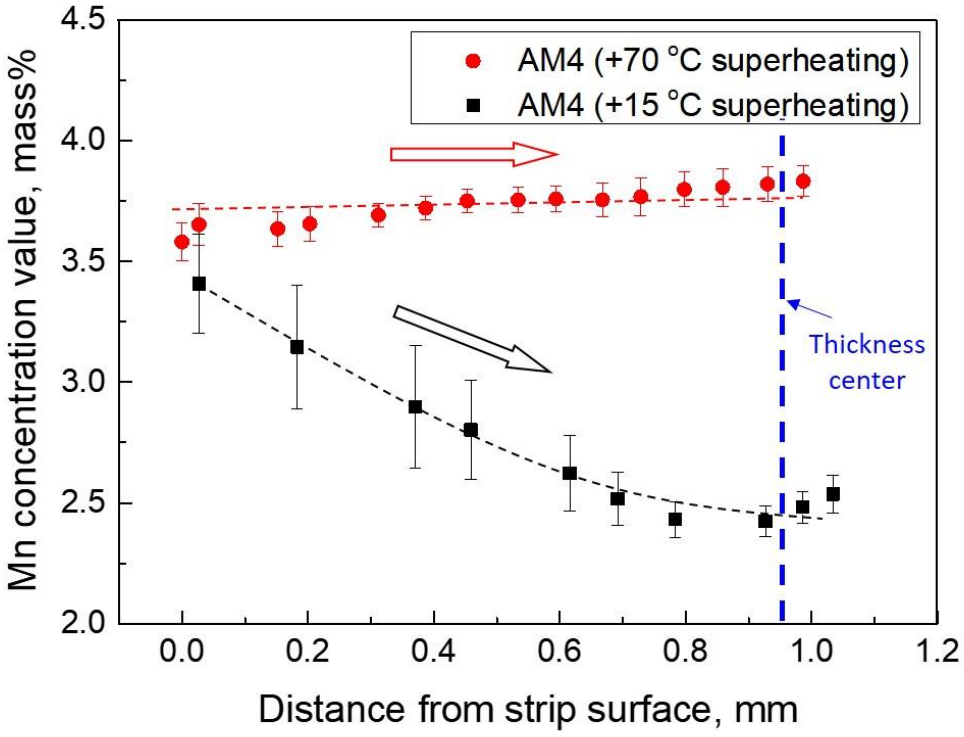


**Fig. 5-4 Mn concentration profile of different melt superheat AM4 from near-surface to central area.**

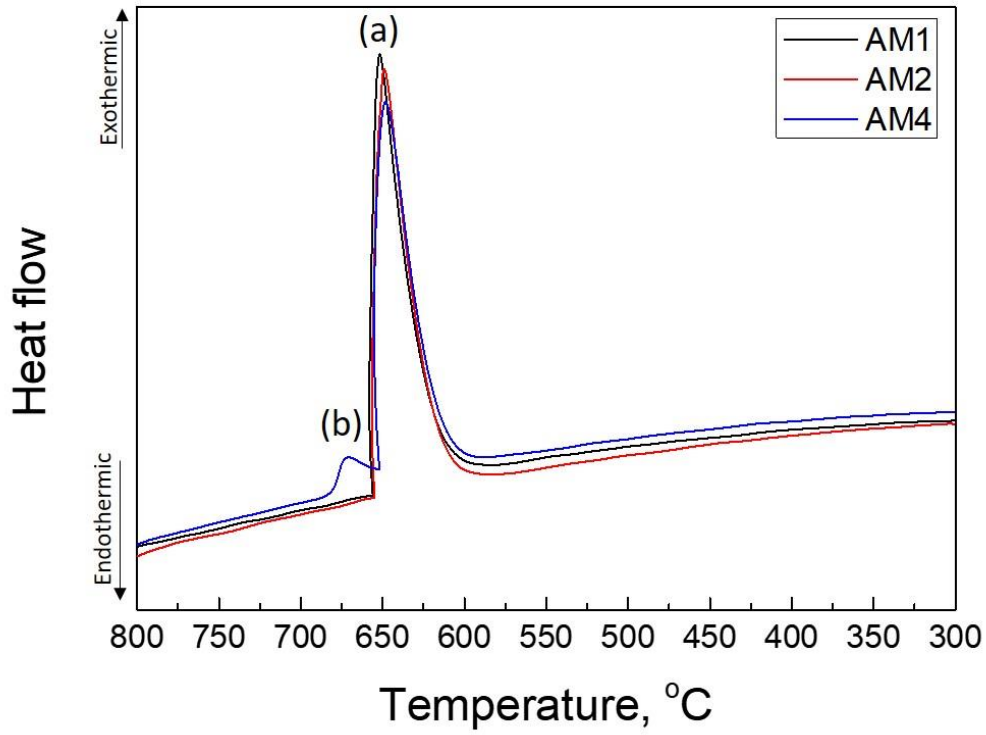


**Fig. 5-5 DTA analysis results of AM1, AM2 and AM4 at a cooling rate of 20 ℃/min. Peak (a) and (b) indicate solidification of aluminum and formation of $Al_6Mn$ phase, respectively.**

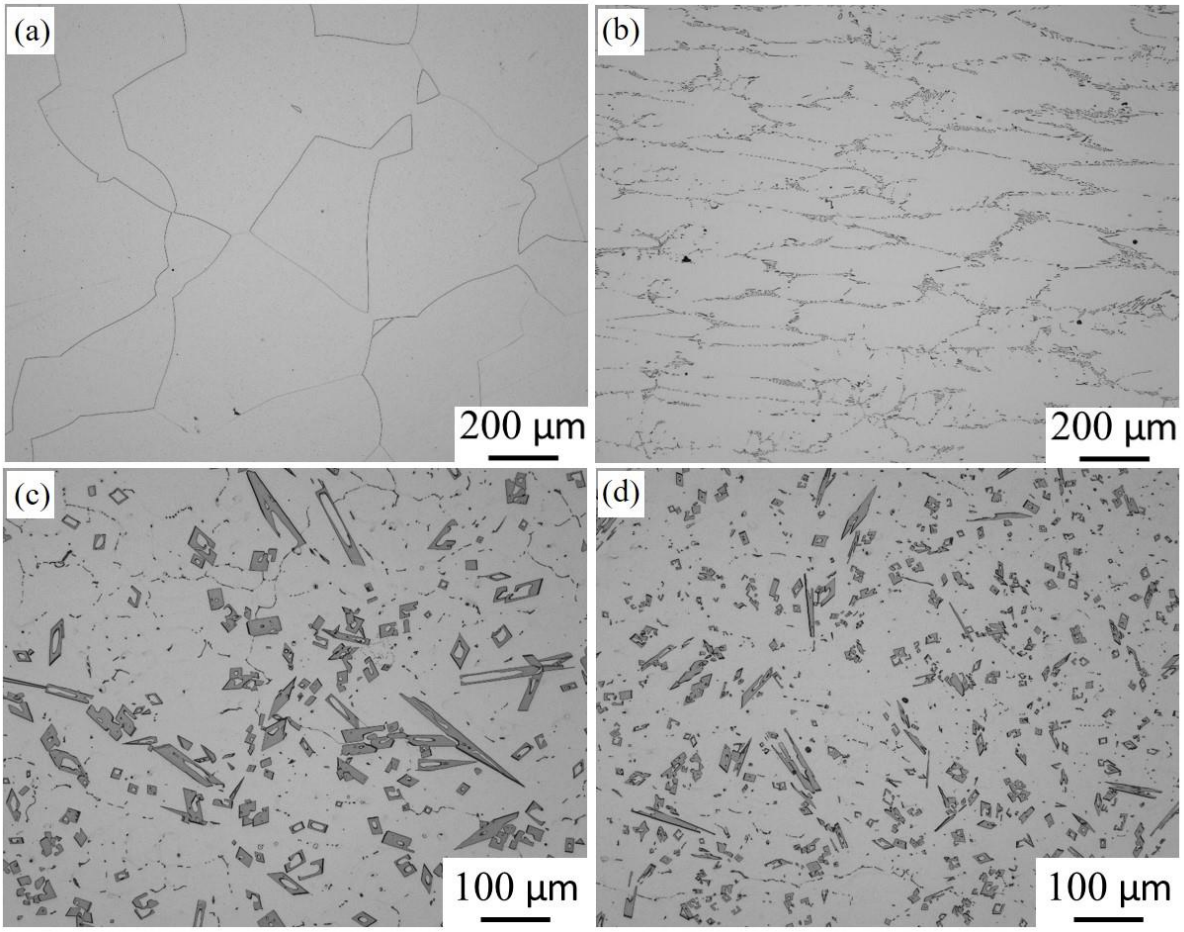


**Fig. 5-6 Microstructure of wedge-shape steel mold cast products. (a) AM1, (b) AM2, (c) AM4-15, (d) AM4-70.**

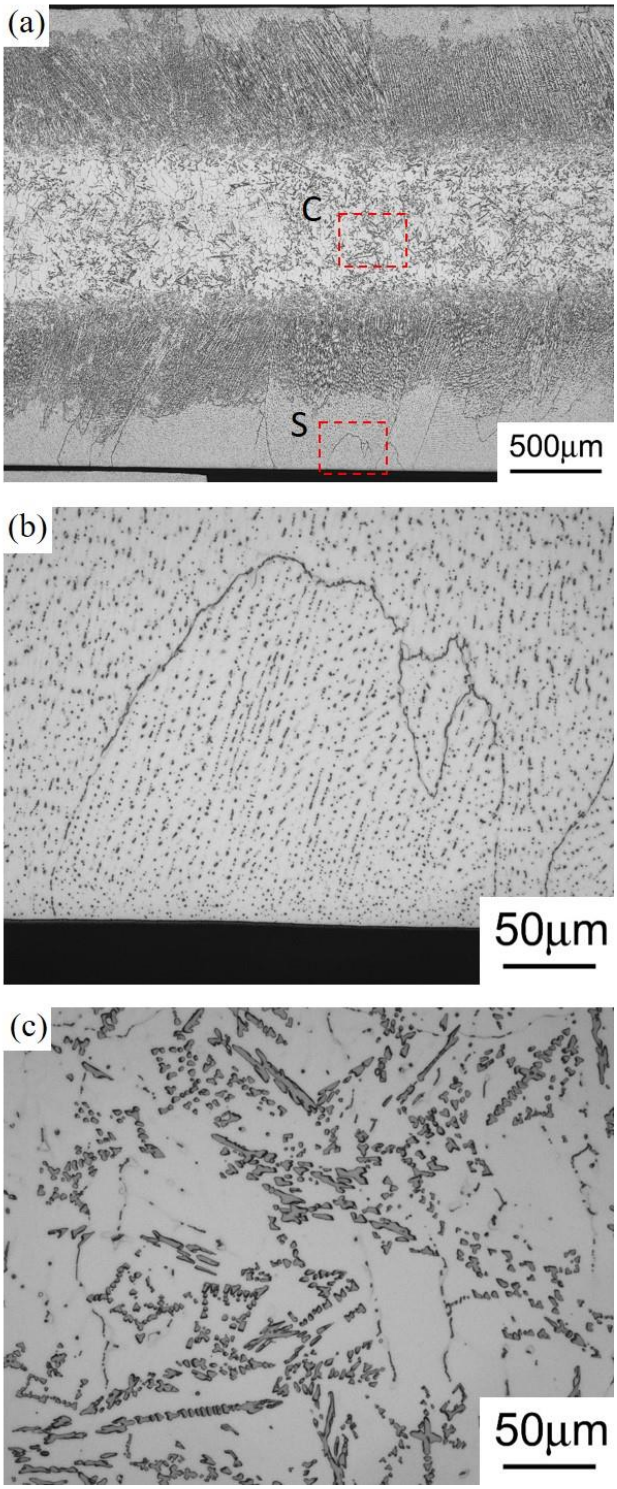


**Fig. 5-7 Microstructure of copper mold cast product. (a) macrostructure (b) high magnification of the part marked "S" in (a), (c) high magnification of the part marked "C" in (a).**

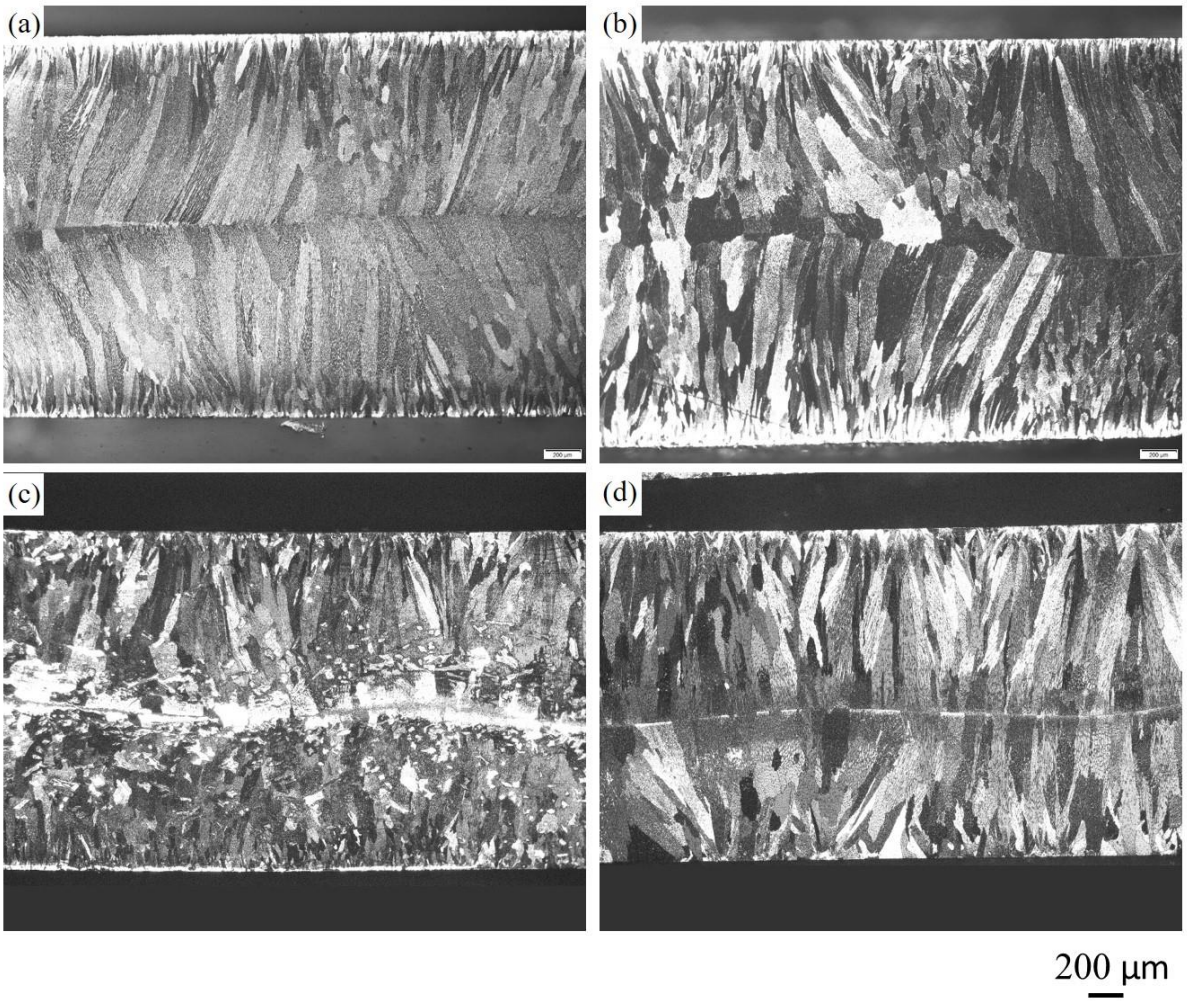


**Fig. 5-8 Grain structure of Al-Mn binary alloy strips. (a) AM1, (b) AM2, (c) AM4-15, (d) AM4-70.**

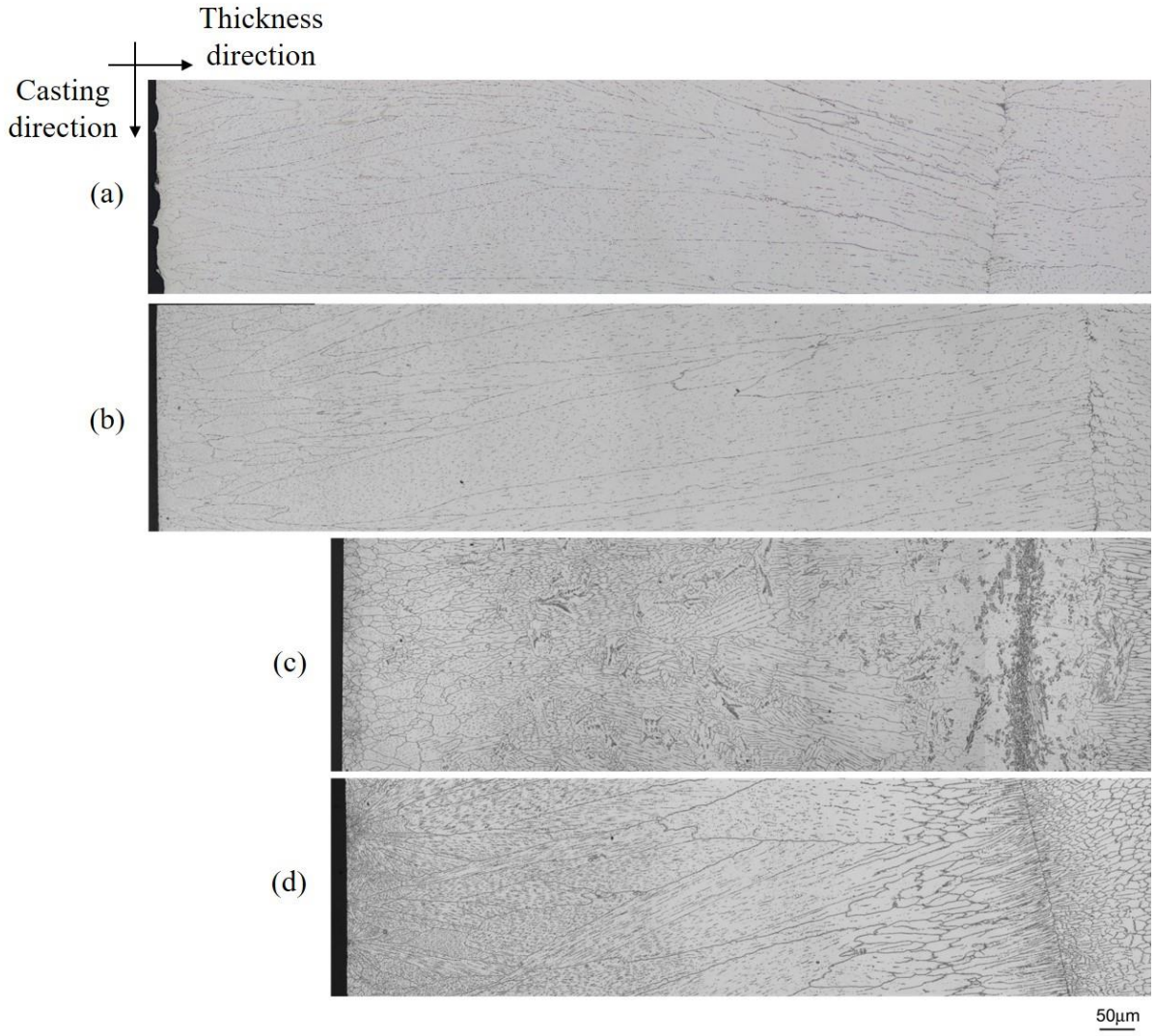


**Fig. 5-9 Macrostructure of the transverse cross section of alloy strips. (a) AM1, (b) AM2, (c) AM4-15, (d) AM4-70.**

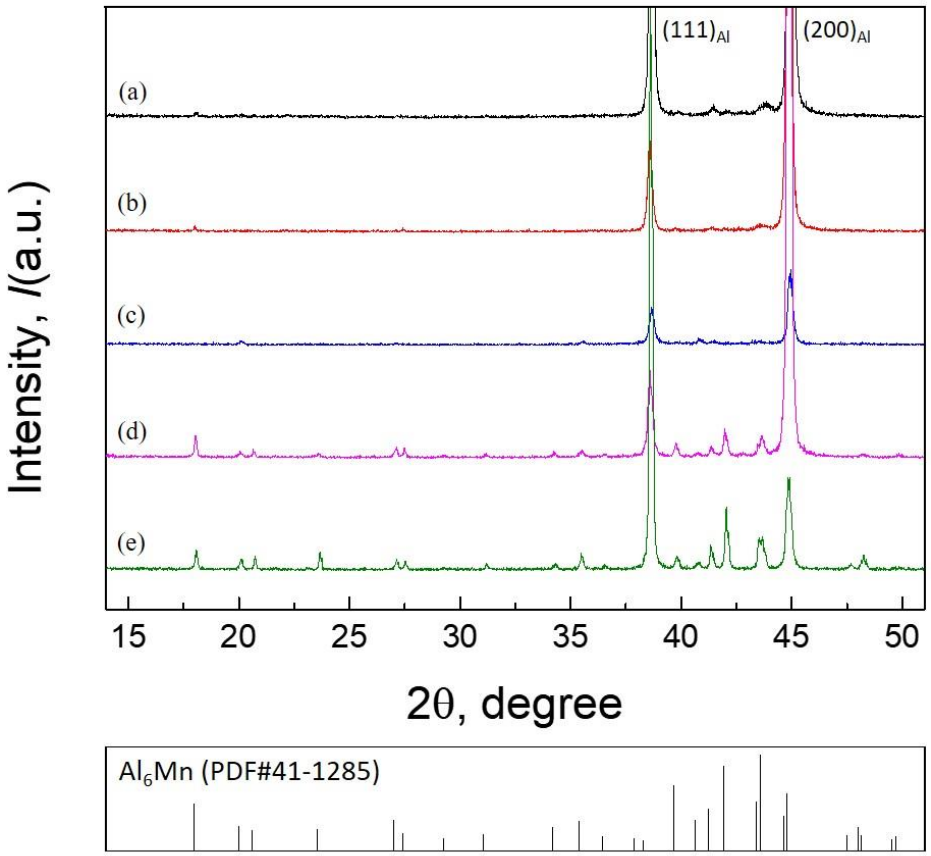


**Fig. 5-10 XRD patterns of AM4-70 cast products. (a) HSTRC strip surface, (b) HSTRC strip center, (c) copper mold cast product surface, (d) copper mold cast product center, (e) wedge-shape steel mold cast product.**

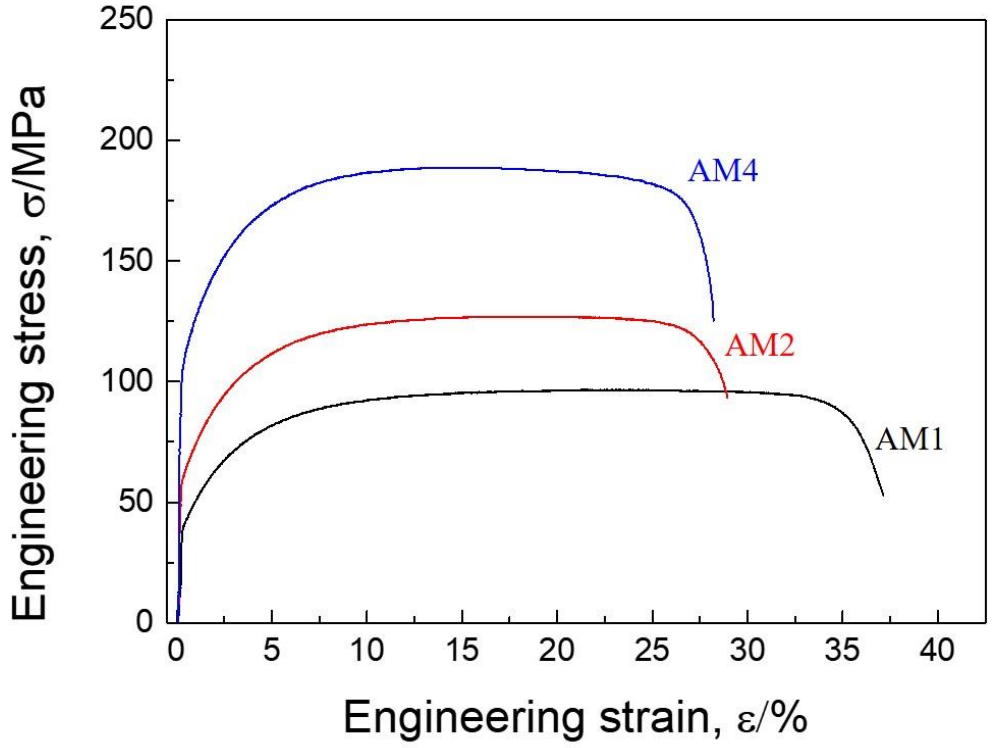


**Fig. 5-11 Representative engineering stress-strain curves of alloy strips.**

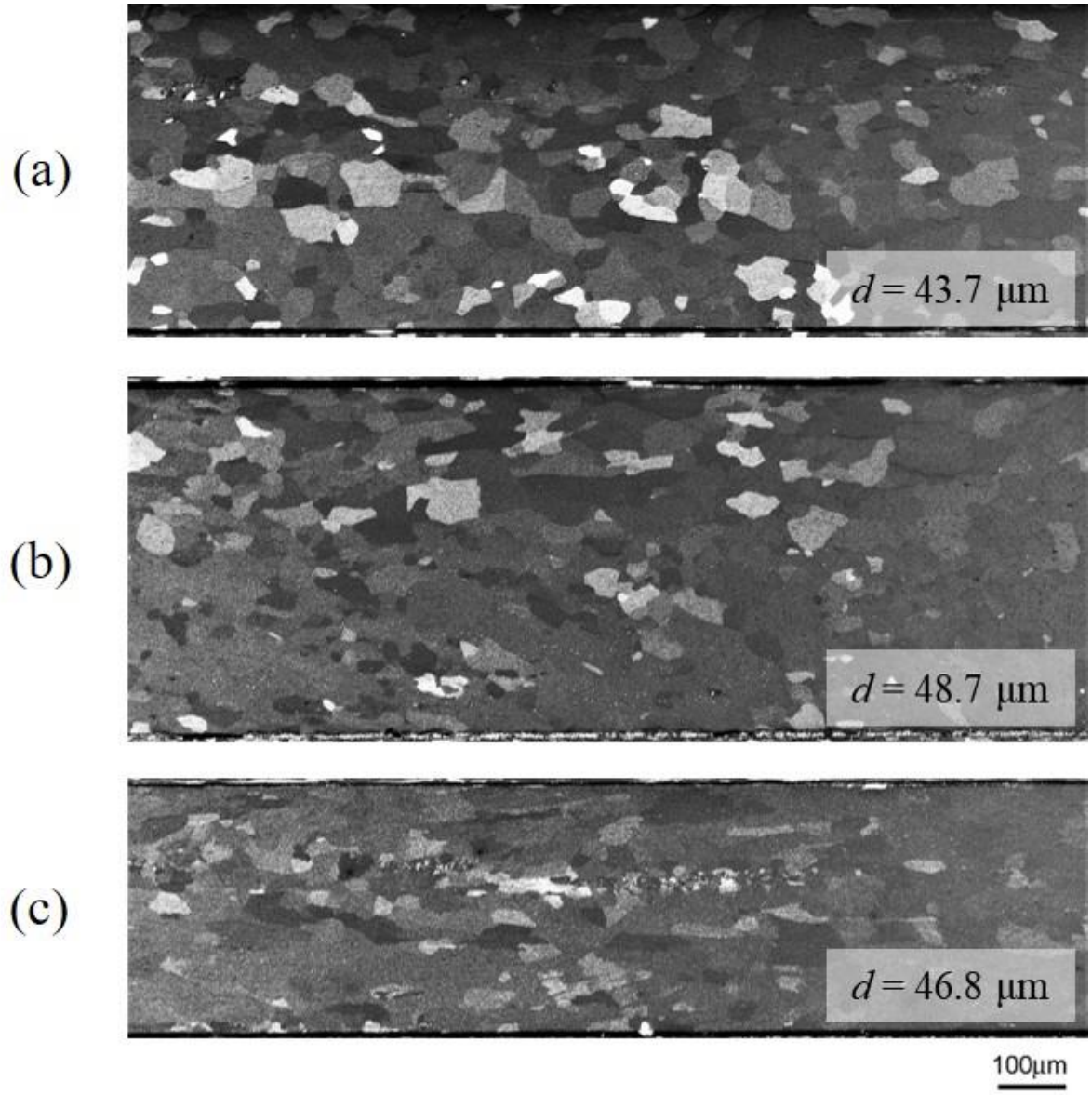


**Fig. 5-12 Grain structure of flash-annealed alloy strips. (a) AM1, (b) AM2, (c) AM4. Average grain size is also shown in the photo.**

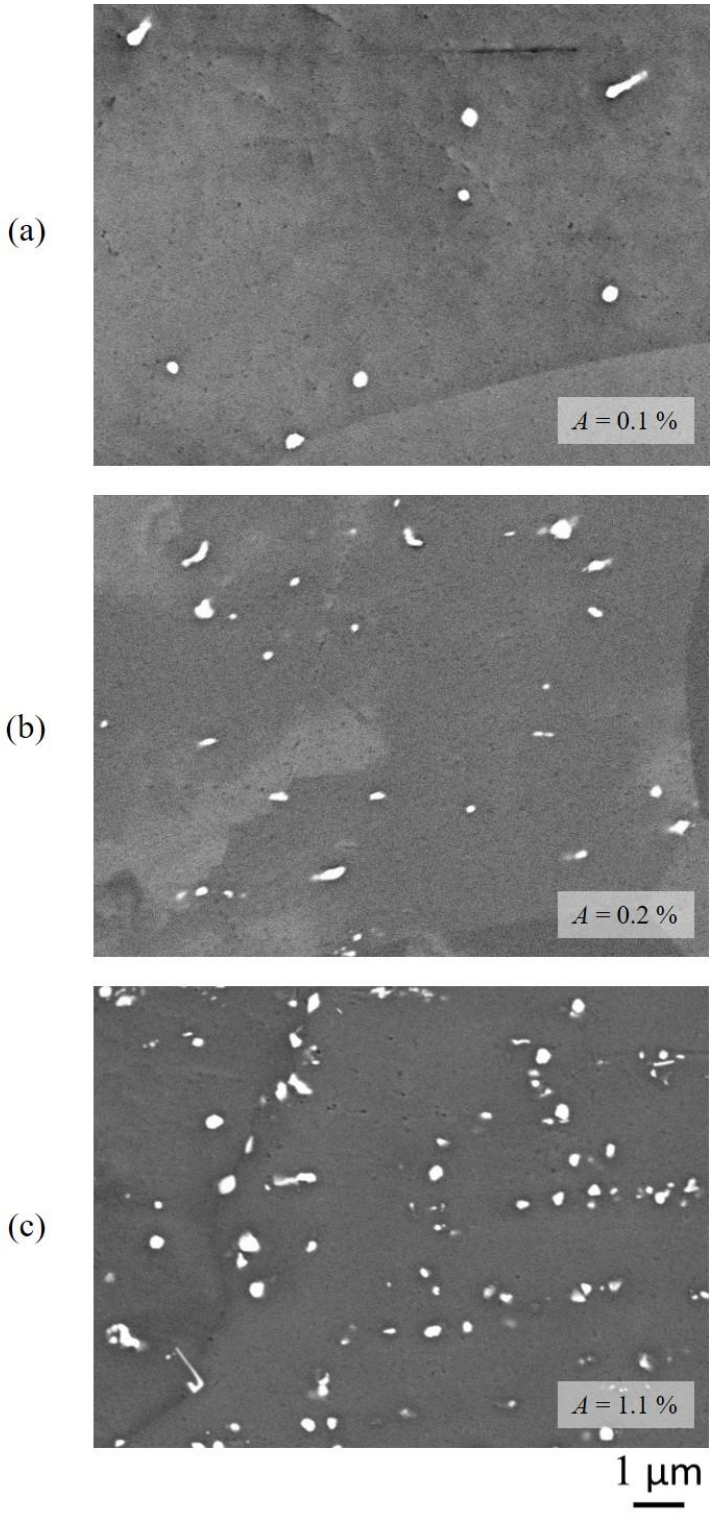


**Fig. 5-13 Secondary particle distribution of flash-annealed alloy strips. (a) AM1, (b) AM2, (c) AM4. The *A* value in the photo is the corresponding area fraction of the secondary particles below 200 nm in diameter.**

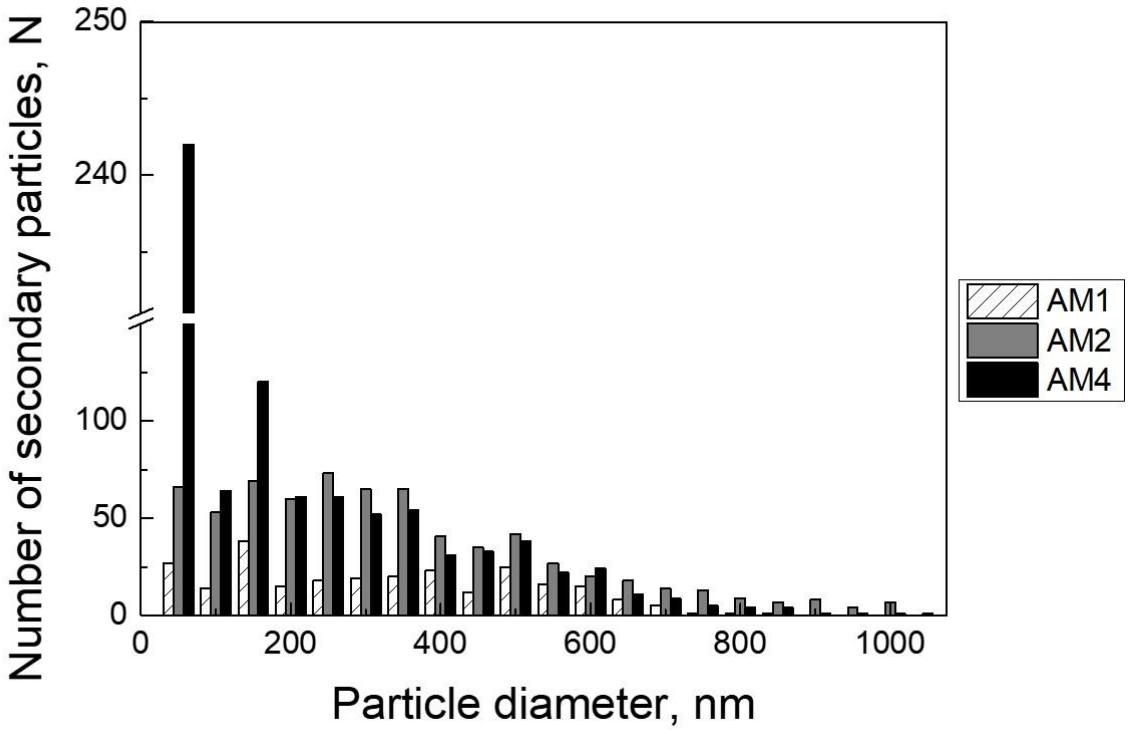


**Fig. 5-14 Secondary particle size distribution of the flash-annealed each alloy strip.**

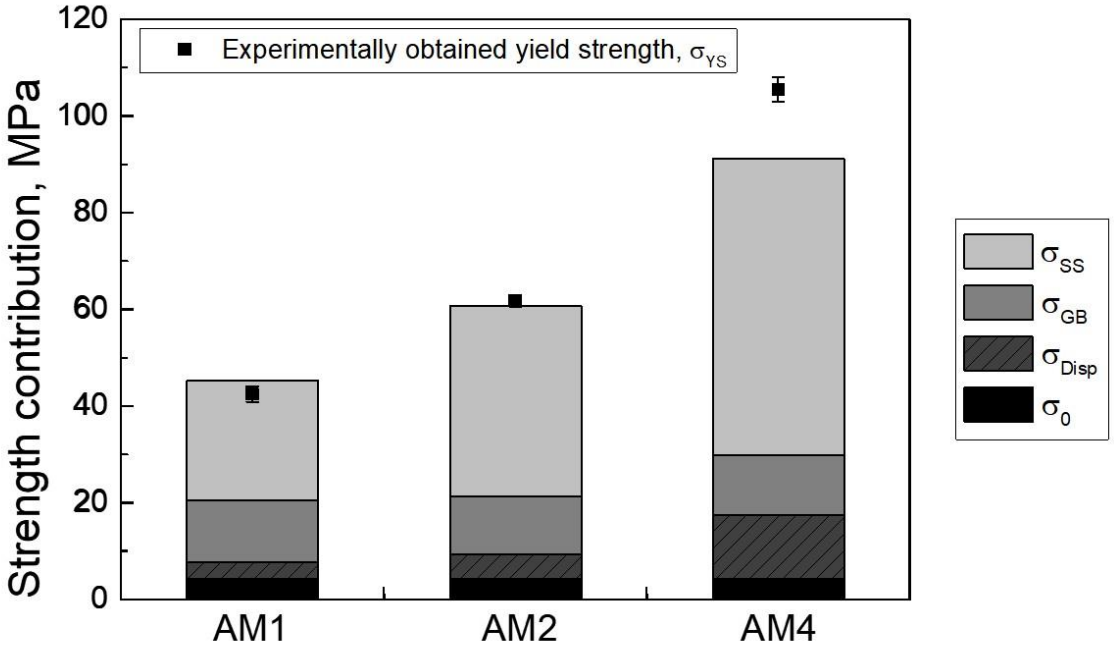


**Fig. 5-15 Contribution of each strengthening mechanism and experimentally obtained yield stress of each alloy strip. $\sigma_{ss}$ is strengthening by solid solution, $\sigma_{GB}$ is strengthening by grain boundaries and $\sigma_{Disp}$ is strengthening by dispersions, $\sigma_0$ is yield stress of pure Al.**

# Chapter 6 Solute distribution and Mn decomposition behavior in vertical-type high-speed twin-roll cast Al-Mn based alloy strips

## 6.1. Introduction

In Chapter 5, hypo-, eutectic and hyper eutectic Al-Mn binary alloy strip were fabricated by vertical-type high-speed twin-roll casting (HSTRC). The formation of primary $Al_6Mn$ phase particle inhibited the Mn supersaturation in Al matrix. Sufficient melt superheating was effective to decrease the formation of primary $Al_6Mn$ phase particles during solidification. As a result, high Mn supersaturated Al-Mn binary alloy strip was obtained. Significant increase in 0.2 % strain offset proof stress in the high Mn supersaturated Al-Mn alloy strips was mainly due to the contribution of Mn solid solution strengthening.

In wrought Al-Mn based alloys, other alloying elements such as Si and Fe are also important. It is because, with Mn element, they form not only constituent particles during solidification, but also fine dispersoids during heat treatment (*e.g.*, homogenization, annealing). The secondary particles have significant roles to determine various metallurgical characteristics in the wrought Al-Mn based alloys; recrystallization behavior and final mechanical properties[1-8]. For instance, well distributed constituent particles, mainly formed during solidification, can act as nucleation sites of recrystallized grains in annealing process[3,4]. Also, fine dispersoids, mainly formed by decomposition of supersaturated Mn in solid solution during heat treatment, can pin the grain boundary movement and thus inhibit recrystallization[5,6]. The fine dispersoids contribute to improve mechanical properties of the alloys by dispersion strengthening[7,8].

This chapter focused on the solute distribution and Mn decomposition behavior, which have a strong influence on secondary particles formation in vertical-type high-speed twin-roll cast Al-Mn based alloys strip. Binary Al-Mn, ternary Al-Mn-Fe and Al-Mn-Si alloys were prepared. In order to demonstrate the effect of cooling rate on solute distribution, HSTRC strip was compared to conventional direct chill (DC)-cast samples. Constituent particle distribution and solute concentration in Al matrix were investigated. The decomposition behavior of supersaturated Mn in vertical-type high-speed twin-roll cast alloys was also discussed.

## 6.2. Experimental procedure

Three kinds of Al-Mn based alloys were prepared. They were binary Al-Mn, ternary Al-Mn-Fe and Al-Mn-Si alloys, which are referred as AM (Al-Mn), AMF (Al-Mn-Fe) and AMS (Al-Mn-Si), respectively. Their chemical compositions are shown in Table 6-1. DC-cast billets (60 mm wide × 190 mm long) were produced by Mitsubishi Aluminum Co., Ltd. Some of them were re-melted, then cast by HSTRC.

Figure 6-1 illustrates a schematic of vertical-type high-speed twin-roll caster. The specification was identical to the caster described in previous chapters. One of the rolls was fixed firmly on the base, while the other roll was installed with a series of springs for controlling the initial roll separating force. It was 20 kN for AM and AMF, and 60 kN for AMS. The roll rotating speed was 60 m/min. The contact length between the melt and roll surface was about 100 mm. The initial roll gap was set as 1 mm.

The HSTRC procedure is as follows; about 2.5 kg of DC-cast billet was melted in the electric furnace for each HSTRC. Before the casting, the melt was degassed by injecting Ar gas bubbling of 0.4 L/min for 20 min. The casting temperature was selected around 15 ℃ over the liquidus temperature of each alloy. Pouring the melt into the feeding nozzle, the melt was solidified on the both roll surface, and formed so-called solidification shells. The shells encountered at the roll gap by roll rotation. At last, the solidifying alloy passed through the roll gap to produce a thin strip. The cast strip was around 3 m-long and 100 mm-wide. The middle part of the resultant strip around 1 m long exhibited a stable thickness along the casting direction, which is around 2.2 mm for AM and AMF, and around 2.6 mm for AMS, respectively.

In order to investigate the Mn decomposition behavior, two homogenization conditions were selected; one is isothermal condition (ISO), the other is corresponding to industrial condition (IND). The ISO homogenization was conducted in a salt bath at 450 ℃ for 8 h. The samples were quenched into water after the ISO homogenization. The IND homogenization consisted of three steps including (i) heating the sample at 50 ℃/h, (ii) holding at 450 ℃ for 8 h, and then (iii) cooling at 30 ℃/h to room temperature. A schematic drawing of homogenization conditions is shown in Fig. 6-2.

As described in Chapter 5, the electrical conductivity was measured at room temperature

by using SIGMA tester with 500 kHz probe (Auto Sigma 3000, GE Inspection Technology) to estimate not only supersaturated Mn content in solid solution, but also an amount of Mn decomposition after homogenization. From the electrical conductivity, electrical resistivity was converted by:

$$1724.1/\%IACS = \rho/n\Omega m \qquad (6\text{-}1)$$

From the converted electrical resistivity, the Mn concentration in solid solution was estimated by:

$$Mn\ (mass\%) = (\rho_{measure} - \rho_{pure\ Al})/\Delta\rho_{Mn\ in\ Al\ alloy} \qquad (6\text{-}2)$$

where, $\rho_{measure}$ is the electrical resistivity of alloy converted by the measured electrical conductivity, $\rho_{pure\ Al}$ is the electrical resistivity of pure aluminum, which is 26.5 nΩm at room temperature[9], and $\Delta\rho_{Mn\ in\ Al\ alloy}$ is the electrical resistivity contribution for Mn solute atom in Al matrix. The value of $\Delta\rho_{Mn\ in\ Al\ alloy}$ is 31 nΩm wt%$^{-1}$ at room temperature[9]. For HSTRC strip, the conductivity measurement was carried out on the normal-direction plane.

For optical microscopic observation (BX51M, Olympus), the polished specimens were etched by the Keller's reagent ($H_2O$:$HNO_3$:HCl:HF = 190:5:3:2 in Vol.%) for 40s. FE-SEM (JEM-3010, JEOL) was used for the secondary particle observation.

EPMA (JXS-8200, JEOL) analysis by wavelength-dispersive spectrometer (WDS) was performed to investigate the chemical composition ratio of secondary particles and the solute distribution in Al matrix. The accelerating voltage and beam current were set to 15 kV and 2 × $10^{-7}$ A, respectively. For HSTRC strip, the EPMA analysis was carried out on the transverse cross sections of the strip near-surface area.

It should be mentioned that specimens for microstructure observation were collected from the HSTRC strip where the thickness was constant. Meanwhile, the DC-cast samples were collected from the mid-central area of the DC-cast billet representing the low cooling rate during solidification.

## 6.3. Results

### 6.3.1. Electrical conductivity change after homogenization

The electrical conductivity change is influenced by the amount of dissolved alloying elements in Al matrix. As increasing the concentration of solute elements in the solid solution, the electrical conductivity decreases. In AM, variation of Mn in solid solution mainly affects its electrical conductivity. In contrast to that, Fe or Si is also included in AMF and AMS, respectively. However, the solubility of Fe in Al matrix is quite low[10]. Also, it is considered that Si in solid solution has much less influence on electrical conductivity than Mn[8]. Therefore, the change of electrical conductivity in AMF and AMS is also considered to be mainly due to the variation of Mn in solid solution in the present study.

Table 6-2 shows the electrical conductivity change and the estimated Mn concentration in solid solution for DC-cast sample and HSTRC strip. The electrical conductivity in as-cast condition showed almost equivalent value in spite of the different cooling rate. It means that the concentration of Mn in solid solution is almost the same for the two samples in as-cast condition. Note that the AMF indicated relatively lower Mn concentration rather than other alloys, AM and AMS. It is considered that Fe favors the formation of constituent particles, mainly $Al_6$(Mn,Fe) phase, during solidification, and this reduces the solid solubility of Mn in Al matrix[11]. A change of the electrical conductivity after homogenization depends on homogenization conditions and casting methods. For AM, no specific change in electrical conductivity was observed regardless of difference in casting methods and homogenization conditions. This indicates the decomposition of supersaturated solid solution hardly occurred during homogenization in AM. Kolby et al.[12] reported the slow kinetics of Mn precipitation in Al-Mn binary alloy. According to their result, the Al-1mass% Mn alloy (including 30 ppm of Fe and less than 50 ppm of Si) has barely reached its equilibrium of Mn solubility in Al matrix at 550 ℃. Haan et al.[13] also reported that the Mn precipitation is sluggish in high-purity Al-Mn binary alloy during isothermal soaking treatment in temperature range from 390 ℃ to 640 ℃. In contrast to AM, AMF and AMS showed the apparent increase of electrical conductivity after homogenization. It is because the addition of Fe or Si in Al-Mn based alloy promotes the decomposition of supersaturated Mn in solid solution during heat treatment by formation of Mn-containing secondary particles such as orthorhombic $Al_6$(Mn,Fe) or cubic α-phase[6,12-14]. Particularly, AMS indicated much larger reduction in Mn

concentration in Al matrix rather than AMF.

Meanwhile, for the ISO condition, the change of electrical conductivity was dependent on difference in cooling rate during solidification. In fact, the HSTRC strip showed a large amount of Mn decomposition in spite of the equivalent value of Mn concentration in as-cast condition. Thus, it is assumed that initial solidified microstructure influences on the Mn decomposition behavior. After IND homogenization, the Mn concentration was equivalent for DC-cast sample and HSTRC strip.

### 6.3.2. Microstructure characterization in the as-cast state and following homogenization treatment

#### 6.3.2.1. Al-Mn binary alloy

The optical micrographs of as-cast and homogenized AM of DC-cast product and HSTRC strip are shown in Fig. 6-3. It should be mentioned that the AM samples were etched by Keller's reagent around 4 min to reveal the microstructure more clearly. This etching time is quite longer than the usual etching condition for Al-Mn based alloys. It was just 40 sec for AMF and AMS. Secondary particles were hardly observed in AM on both DC-cast sample and HSTRC strip in as-cast condition and homogenization conditions. The electrical conductivity was not changed after the homogenization, either (see Table 6-2). This means that Mn decomposition did not occur during the homogenization. In fact, the secondary particles were hardly observed in homogenization conditions even by FE-SEM observation as shown in Fig. 6-4. Only a few secondary particles were observed along the grain boundaries in as-ISO and as-IND condition as shown in Fig. 6-4 (b) and (c).

#### 6.3.2.2. Al-Mn-Fe ternary alloy

Figure 6-5 shows the optical micrographs of as-cast and homogenized AMF of DC-cast product. Some large primary and eutectic particles were observed in DC-cast sample as shown in Fig. 6-5 (a). Since the low Fe solubility in Al matrix, much more secondary particles were observed compared to that of AM. Compared to the as-cast condition, there was no difference in optical microstructural appearance in as-ISO as shown in Fig. 6-5 (b). By careful observation, some fine etch pits were observed inside of the α-Al as marked. In as-

IND condition, lots of fine etch pits corresponding to the fine dispersoids were observed inside of α-Al as shown in Fig. 6-5 (c).

Figure 6-6 shows the optical micrographs of as-cast and homogenized AMF of HSTRC strip. Fine dendrite of α-Al was observed near the strip surface area, as shown in Fig. 6-6 (a). The coarse primary particles, commonly observed in DC-cast product, were hardly observed at HSTRC strip near surface area. In the mid-thickness area, globular grains and eutectic structure were observed as shown in Fig. 6-6 (d). Similar to DC-cast product of as-ISO condition, fine etch pits were observed inside of the α-Al at strip near surface area on both as-ISO and as-IND conditions as shown in Fig. 6-6 (b) and (c). In the central area, the fine etch pits were also observed inside of the α-Al globular grains as shown in Fig. 6-6 (e) and (f).

#### 6.3.2.3. Al-Mn-Si ternary alloy

Figure 6-7 shows the optical micrographs of as-cast and homogenized AMS alloy of DC-cast product and HSTRC strip near surface area. In DC-cast product, the secondary particles were observed at the grain boundaries and within α-Al grains, corresponding inter-dendrite areas as shown in Fig. 6-7 (a). After homogenization, quite different microstructure evolution was observed between as-ISO and as-IND conditions. In as-ISO condition, most of dispersoids were localized at periphery of α-Al dendrite. At the center of the α-Al dendrite, no secondary particles were found at all, so-called dispersoids-free zone (DFZ). Judging from the DFZs, shape of the α-Al dendrite was clearly revealed as shown in Fig. 6-7 (b). In contrast to that, in as-IND condition, it was considered that the dispersoids were mainly distributed inside of the former α-Al dendrites, and not presented in the vicinity of the secondary particles.

For as-cast HSTRC strip, much finer α-Al grains and secondary particle distribution were observed as shown in Fig. 6-8 (a). After the homogenization, specific DFZs were not visible at the HSTRC strip near surface in the optical micrograph on both homogenization conditions as shown in Fig. 6-8 (b) and (c). In contrast to that, some DFZs were observed in the strip central area as shown in Fig. 6-8 (e) and (f). It is of interest that each DFZs corresponded to the center of the α-Al globular grains.

There are several explanations for the formation of DFZ in literatures[14-20]. One acceptable explanation is that the formation of the DFZ is due to the micro-segregation of solute

elements in Al matrix and its decomposition by competition between the coarsening of secondary particles (*i.e.*, constituents) and formation of fine dispersoids (*i.e.*, precipitates) during heat treatment. In other words, the formation of DFZ is dependent on the secondary particles distribution and the solute solubility and its distribution within Al matrix in as-cast condition. Since the DC-cast sample and HSTRC strip show quite different initial as-cast structure due to their different cooling rates, thus this indicates that the Mn decomposition behavior is different in DC-cast sample and HSTRC strip.

### 6.3.3. Distribution of solute elements in Al matrix

Figure 6-9 shows the EPMA results of AMF for DC-cast sample and HSTRC strip as-cast condition. A color bar indicates atomic concentration. The area subjected for EPMA analysis on DC-cast product and HSTRC strip was marked by dotted line as shown in Fig. 6-9 (a) and (d), respectively. Due to the low Fe solubility in Al, the matrix was displayed in black color in Fe mapping as shown in Fig. 6-9 (c). Both Mn-rich and Fe-rich areas are corresponded to the secondary particles, which are $Al_6$(Mn,Fe) phase particles. These secondary particles were much finer and homogeneously distributed in HSTRC strip resulting from the high cooling rate of HSTRC rather than DC-casting. In addition, due to the high cooling rate at HSTRC strip surface, higher Mn concentration in Al matrix was observed (comparing Fig. 6-9 (b) and (e)). Fe was not detected in Al matrix as shown in Fig. 6-9 (f).

Figure 6-10 shows the EPMA results of AMS alloy for DC-cast and HSTRC strip as-cast condition. The area subjected for EPMA analysis on DC-cast product and HSTRC strip was marked by dotted line as shown in Fig. 6-10 (a) and (d), respectively. From the solute distribution state in DC-cast product, it can be seen that the Mn concentration in matrix (Fig. 6-10 (b)) slightly increased from the center to the periphery of α-Al dendrite. In the present study, the Mn element mapping result reflects the influence by not only supersaturated Mn in Al matrix but also the Mn containing constituent particles. The high Mn composition in the inter-dendritic region results from the constituent particles. There are some regions displayed in black at the inter-dendritic region in the Mn element mapping. It is considered that this is the place where the constituent particle detached during sample preparation such as polishing. It is also possible that the constituent particles containing no Mn, indicate the crystallized Si particles. In the Si element mapping, the solute distribution was more clearly revealed. Si

content was low inside of the α-Al dendrite core as shown in Fig. 6-10 (c). Note that this inhomogeneous solute distribution is well corresponded to the dispersoids distribution in as-ISO condition as shown in Fig. 6-7 (b). Meanwhile, higher Mn and Si concentration was detected in HSTRC strip as shown in Fig. 6-10 (e) and (f). Homogeneous solute distribution in Al matrix was also clearly observed. It is due to the high cooling rate of HSTRC.

## 6.4. Discussion

From the microstructure observation (Fig. 6-3 and 6-4) as well as electrical conductivity measurement result (Table 6-2) for AM alloy, it was confirmed that the Mn decomposition did not occur during homogenization in AM. This suggests that the other alloying elements such as Fe and Si have significant role to decompose Mn element in Al solid solution. Although the same alloy system, DC-cast sample and HSTRC strip indicated different amounts of Mn decomposition during homogenization.

### 6.4.1. Mn decomposition behavior in Al-Mn-Fe ternary alloy

In order to examine the evolution of the constituent particles and fine dispersoids after the homogenization in detail, the microstructure, in particular, particles distribution was examined. Figure 6-11 shows the back-scattered electron images of the DC-cast AMF. Fine lamellar eutectic structure is observed as shown in Fig. 6-11 (a). In as-cast condition, any other secondary particles were not observed inside of the α-Al. After homogenization, some fine dispersoids were observed inside of the α-Al for the ISO condition as marked in Fig. 6-11 (b). Moreover, the eutectic structure were spherodized and coarsened. These spheroidization and coarsening of constituent $Al_6$(Mn,Fe) phase particles during homogenization were also observed at similar temperature range of homogenization in other Al-Mn based alloys[21,22]. During the homogenization, decomposition of supersaturated Mn element results in the formation of new dispersoids and coarsening of constituent particles in a temperature range from 300 to 600 ℃. Simultaneously, re-dissolution of fine second-phase particles also occurs. The formation of new dispersoids and coarsening of constituent particles, and dissolution of fine particles are contrary processes for decomposition of the solid solution. In the present study, around 0.27 mass% Mn solute element was decomposed

during the ISO condition in DC-cast sample (see Table 6-2). It is hard to assume that the decomposition of the solid solution is mainly controlled by precipitation because of less amount of new dispersoids formation (as marked in Fig. 6-11 (b)). Also, the applied temperature in the ISO condition, 450 ℃, is lower than the re-dissolution temperature of $Al_6$(Mn,Fe) phase. Thus, it can be considered the decomposition of supersaturated Mn in solid solution mainly occurred by deposition of the supersaturated Mn to constituent particles. Figure 6-12 shows Mn/(Mn+Fe) compositional ratio change in constituent particle for DC-cast sample and HSTRC strip after ISO homogenization. In as-cast condition, constituent particles had relatively lower Mn/(Mn+Fe) ratio, while the Mn/(Mn+Fe) ratio increased after homogenization. This is because the supersaturated Mn diffuses toward the constituent $Al_6$(Mn,Fe) phase. The diffusion of Mn into the particles can lead to particle growth and coarsening. The continuous change in chemical compositions of constituent $Al_6$(Mn,Fe) phase was also reported[21,23]. In the IND condition, spheroidization and coarsening of the constituent particles were also observed. In addition, high-dense fine dispersoids were observed inside of α-Al as shown in Fig. 6-11 (c). The IND condition showed much amount of Mn decomposition compared to that of ISO condition (see Table 6-2). It is considered to be due to the formation of fine dispersoids inside of α-Al. It is assumed that the small quantity of Fe in Al matrix contributes to precipitate Mn-containing dispersoids inside of α-Al during the IND condition.

Figure 6-13 shows the back-scattered electron images of the HSTRC strip of AMF. In as-cast condition, the HSTRC strip indicated much finer primary α-Al dendrite and homogeneously distributed constituent particles due to its high cooling rate (see Fig. 6-11 (a) and Fig. 6-13 (a)). After homogenization, spheroidization and coarsening of the constituent particles were observed in HSTRC strip near surface as shown in Fig. 6-13 (b) and (c). From the electrical conductivity change, much amount of decomposition of supersaturated Mn content is considered to occur after the ISO homogenization in HSTRC strip compared to DC-cast product. In AMF, the Mn decomposition mainly occurs through the diffusion of supersaturated Mn within α-Al dendrite toward the constituent particles. Thus, fine and homogeneously distributed constituent particles lead to reduce relevant length for the diffusion of Mn from matrix to constituent particles. Meanwhile, it was hard to observed fine dispersoids on the both ISO and IND conditions of the HSTRC strip surface. Only a few fine

dispersoids were observed at some local regions, inside of the relatively large α-Al dendrite as shown in Fig. 6-13 (b) and (c). It is attributed to the Mn decomposition occurred by formation of fine dispersoids rather than deposition to the constituent particles due to relatively long diffusion distance at the core of α-Al.

Similar to the strip near surface area, spheroidization and coarsening of the constituent particles, surrounding globular α-Al, were also observed in strip central area during homogenization. Inside of the globular α-Al, fine dispersoids were observed on both ISO and IND conditions as shown in Fig. 6-13 (e) and (f). It is also considered the supersaturated Mn elements prefer to precipitate as fine dispersoids rather than diffusion toward constituent particles surrounding the globular α-Al because of long diffusion distance from the center of the globular α-Al to the constituent particles.

### 6.4.2. Mn decomposition behavior in Al-Mn-Si ternary alloy

Figure 6-14 shows the back-scattered electron images of as-ISO AMS alloy DC-cast product and HSTRC strip near surface, respectively. In DC-cast product, fine dispersoids were observed on the periphery of α-Al dendrite, and DFZ was observed at the core of α-Al dendrite as shown in Fig. 6-14 (a) and (b). It was well corresponded to the solute distribution in Al matrix, particularly Si element as shown in Fig. 6-10 (c). For HSTRC strip, fine dispersoids were homogeneously distributed inside of grains as shown in Fig. 6-14 (c) and (d). It is also well coincided with the solute distribution of Si as well as Mn (see Fig. 6-10 (e) and (f)). In Al-Mn-Si ternary alloy, the formation of new dispersoids mainly controls the decomposition of supersaturated Mn in solid solution, which is correlated with the diffusion of Si element. In ISO homogenization, the temperature increased up to 450 ℃, rapidly. This condition make possible to precipitate the Mn and Si in Al matrix themselves at the solute-enriched regions. As shown in Fig. 6-10 (b) and (c), the solute distribution was inhomogeneous in DC-cast sample, especially Si element. Since the lack of solute Si concentration in the core of the α-Al dendrite in DC-cast sample, formation of dispersoids is hard to occur during ISO homogenization, then the DFZ is formed. In contrast, HSTRC strip near surface showed homogeneous solute distribution of Mn as well as Si elements due to its high cooling rate during solidification. This homogeneous solute distribution can promote the Mn-containing dispersoids precipitation in extensive range. For this reason, homogeneous

solute distribution of Mn as well as Si elements in HSTRC strip results in enhanced decomposition of supersaturated Mn in solid solution.

Figure 6-15 shows the back-scattered electrion images of as-IND AMS alloy DC-cast product and HSTRC strip near surface, respectively. In as-IND AMS alloy DC-cast product, the fine dispersoids were homogeneously distributed inside of α-Al dendrite, whereas the DFZ was formed in the vicinity of the constituent particles as shown in Fig. 6-15 (b). Li and Arnberg[14,21] reported that the supersaturated Mn in solid solution begins to precipitate at around 300 ℃, and to dissolve at over 530 ℃. In the heating stage of the IND homogenization condition, due to the inhomogeneous solute distribution within Al matrix in as-cast condition, the diffusion of solute elements in Al matrix may occur from the solute-rich regions to solute-poor regions before the precipitation of dispersoids. Figure 6-16 shows the OM micrographs of DC-cast AMS during heating in IND homogenization. When the alloy was heated up to 200 ℃, no change in microstructure and electrical conductivity was observed as shown in Fig. 6-16 (b). On the other hand, formation of the fine dispersoids was observed near the constituent particles at 300 ℃. In this stage, dispersoids were not observed inside of α-Al dendrite as shown in Fig. 6-16 (e). At the heating up to 400 ℃, dispersoids were observed inside of α-Al dendrite as shown in Fig. 6-16 (d) and (f). From the EPMA element mapping result, the Mn is dissloved at the center of α-Al dendrite (see Fig. 6-10 (e)). The diffusion coefficient of Mn element in Al matrix is much lower than that of Si element[24] (*i.e.*, the diffusion coefficient of Mn and Si in Al matrix at 300 ℃ is $7.1 \times 10^{-22}\,m^2s^{-1}$ and $2.6 \times 10^{-16}\,m^2s^{-1}$, respectively). Thus, it is considered that the Si elements segregated at periphery of α-Al dendrite diffuse toward the center of α-Al dendrite, where the relatively lower Si concentration regions, during the heating stage. Then, the Mn elements, dissolved in the core of α-Al dendrite, precipitated with Si as α-AlMnSi phase as shown in Fig. 6-15 (b). Since the Mn solubility in Al matrix is low at that temperature, the precipitations continuously occur during the homogenization with less re-dissolution of the dispersoids. Consequently, high-dense dispersoids inside of the α-Al dendrite are formed after IND homogenization in DC-cast product. Meanwhile, although the fine dispersoids were precipitated in the vicinity of the constituent particles during the heating stage (see Fig. 6-16 (c) and (d)), these regions were replaced as the DFZ after IND homogenization. It is considered that the fine dispersoids near the constituent particles re-dissolved for the Ostwald ripening of the constituent particles

during IND homogenization.

For the HSTRC strip surface, significant compositional gradient within the α-Al dendrite were not observed in as-cast condition (see Fig. 6-10 (e) and (f)). Thus, fine dispersoids homogeneously precipitated regardless of the homogenization conditions as shown in Fig. 6-15 (c) and (d). However, in contrast to the HSTRC strip surface area, some DFZs were observed in HSTRC strip central area as shown in Fig. 6-8 (e) and (f) after homogenizations. These DFZs were corresponded to the core of some globular α-Al grains in central band structure. Kim et al.[25] reported the formation of the central band structure, consisting of the globular α-Al grains, in Al-Si alloy strip resulted from the fragmentation of dendrite arms growing on the roll surfaces and/or separation of the nucleated crystals from the roll surfaces. This is due to several possible reasons; rough and unstable melt feeding condition, low pouring temperature and shearing pressure to the growth front of mushy layer by roll separating force. In the present study, AMS also showed mushy-type solidification, which means similar phenomenon can easily occur during the HSTRC. Furthermore, AMS has the wide freezing temperature range (around 60 ℃ according to the Al-Mn-Si phase diagram[26]) considering from its Si content, which may result in the formation of primary α-Al in the melt-head. Thus, the fragmented α-Al dendrite branches from the solidification shells and the crystallized primary α-Al grains in the melt-head can be gathered at the strip central area as schematically illustrated in Fig. 6-17. The fragmented α-Al dendrite branches originated in rapidly solidified shells from roll surface. Thus, Mn as well as Si elements can be contained in that α-Al grains. In this case, dispersiods can be formed in the α-Al grains during homogenization. In contrast to that, the crystallized primary α-Al grains were formed just below the liquidus temperature of the AMS alloy in the melt-head. In this case, the α-Al has low solid solubility. Thus, the crystallized α-Al grains in the melt-head may contain less solute elements, especially core of the α-Al grains. Since the lack of solute elements in the core of the α-Al grains, formation of dispersoids is hard, then the DFZ is formed in the core of the crystallized primary α-Al grains.

## 6.5. Conclusions

Solute distribution and Mn decomposition behavior in vertical-type high-speed twin-roll cast Al-Mn binary, Al-Mn-Fe and Al-Mn-Si ternary alloy strips were investigated. The Fe and

Si enhanced the Mn decomposition during homogenization. In the Al-1.2Mn-1.0Fe (in mass%) ternary alloy strip, constituent particles of $Al_6$(Mn,Fe) phase were homogeneously distributed in the strip due to the high cooling rate. The Mn decomposition mainly occurred by the diffusion of Mn toward the constituent particles resulting in increase of Mn/(Mn+Fe) ratio of the constituent particles and their spheroidizing and coarsening during homogenization. In the Al-1.2Mn-1.0Si (in mass%) ternary alloy strip, formation of fine α-AlMnSi dispersoids was predominant way for the Mn decomposition during homogenization. The distribution of dispersiods was well corresponded to the solute distribution within Al matrix especially Si element. Due to the high cooling rate of vertical-type high-speed twin-roll casting, homogeneous Mn and Si distribution was achieved that leads to formation of high-dense fine α-AlMnSi dispersoids during homogenization. This contributes to enhance decomposition of supersaturated Mn during homogenization in vertical-type high-speed twin-roll cast strip.

## References


1) F.J. Humphreys and M. Hatherly: *Recrystallization and Related Annealing Phenomena: Second Edition*,(2004)

2) R.D. Doherty, D.A. Hughes, F.J. Humphreys, J.J. Jonas, D. Juul Jensen, M.E. Kassner, W.E. King, T.R. McNelley, H.J. McQueen, and A.D. Rollett: Mater. Sci. Eng. A, **238** (1997) 219–74

3) F.J. Humphreys: Acta Metall., **25** (1977) 1323–44

4) F.J. Humphreys and P.N. Kalu: Acta Metall., **35** (1987) 2815–29

5) K. Huang, O. Engler, Y.J. Li, and K. Marthinsen: Mater. Sci. Eng. A, **628** (2015) 216–29

6) M. Karlík, T. Mánik, and H. Lauschmann: J. Alloys Compd., **515** (2012) 108–13

7) Y. J. Li, A. M. F. Muggerud, A. Olsen, and T. Furu: Acta Mater., **60** (2012) 1004–14

8) A. M. F. Muggerud, E. A. Mørtsell, Y. J. Li, and R. Holmestad: Mater. Sci. Eng. A, **567** (2013) 21–28

9) S. Komatsu and S. Fujikawa: JILM, **47** (1997) 170–81

10) L. A. Willey: *Aluminum*,(1967)

11) J.T. Theler and P. Furrer: Aluminium, **50** (1974) 467–72

12) P. Kolby, C. Sigli, and C.J. Simensen: *Aluminum Alloys: Their Physical and Mechanical Properties, ICAA4, Atlanta, USA*,(1994)

13) P.C.M. De Haan, J. Van Rijkom, and J.a.H. Söntgerath: Mater. Sci. Forum, **217**–**222** (1996) 765–70

14) Y. J. Li and L. Arnberg: Acta Mater., **51** (2003) 3415–28

15) K. Nagahama and I. Miki: Trans. Japan Inst. Met., **15** (1974) 185–92

16) P. Furrer and G. Hausch: Met. Sci., **13** (1979) 155–62

17) T.H. Sanders: Metallography, **14** (1981) 177–89

18) R. Maldonado and E. Nembach: Acta Mater., **45** (1997) 213–24

19) Ch A. Gandin and A. Jacot: Acta Mater., **55** (2007) 2539–53

20) Q. Du, W. J. Poole, M. a. Wells, and N. C. Parson: Acta Mater., **61** (2013) 4961–73

21) Y. J. Li and L. Arnberg: Mater. Sci. Eng. A, **347** (2003) 130–35

22) K. Liu and X. G. Chen: Mater. Des., **84** (2015) 340–50

23) M. Dehmas, E. Aeby-Gautier, P. Archambault, and M. Serrière: Metall. Mater. Trans. A, **44** (2013) 1059–73

24) Y. Du, Y.A. Chang, B. Huang, W. Gong, Z. Jin, H. Xu, Z. Yuan, Y. Liu, Y. He, and F.Y. Xie: Mater. Sci. Eng. A, **363** (2003) 140–51

25) M. S. Kim and S. Kumai: Mater. Trans., **52** (2011) 856–61

26) G. Petzow and G. Effenberg: *Ternary Alloys. A Comprehensive Compendium of Evaluated Constitutional Data and Phase Diagrams.*,VCH Verlagsgesellschaft, Vol. 7, (1993)

**Table 6-1 Chemical compositions of the alloys. (in mass %)**

| *Alloy | Mn | Fe | Si | other | Al |
|---|---|---|---|---|---|
| AM | 1.190 | 0.001 | 0.001 | 0.002 | Bal. |
| AMF | 1.190 | 0.970 | 0.002 | 0.001 | Bal. |
| AMS | 1.130 | 0.003 | 0.920 | 0.002 | Bal. |

**Note*: AM, AMF and AMS are corresponded to Al-Mn binary, Al-Mn-Fe and Al-Mn-Si ternary alloy, respectively.

**Table 6-2 Electrical conductivity and its corresponding estimated Mn concentration in solid solution.**

| Alloy | Casting method | Electrical conductivity (% IACS) | | | Estimated Mn concentration in solid solution (mass%) | | |
|---|---|---|---|---|---|---|---|
| | | As-cast | As-ISO | As-IND | As-cast | As-ISO | As-IND |
| AM | DC-casting | 26.96 | 27.00 | 28.1 | 1.21 | 1.21 | 1.12 |
| | HSTRC | 26.78 | 27.35 | 27.7 | 1.22 | 1.18 | 1.15 |
| AMF | DC-casting | 30.82 | 36.35 | 45.3 | 0.95 | 0.68 | 0.37 |
| | HSTRC | 30.58 | 41.48 | 43.9 | 0.96 | 0.49 | 0.41 |
| AMS | DC-casting | 27.51 | 43.26 | 56.2 | 1.17 | 0.43 | 0.13 |
| | HSTRC | 27.68 | 48.29 | 54.8 | 1.15 | 0.30 | 0.16 |

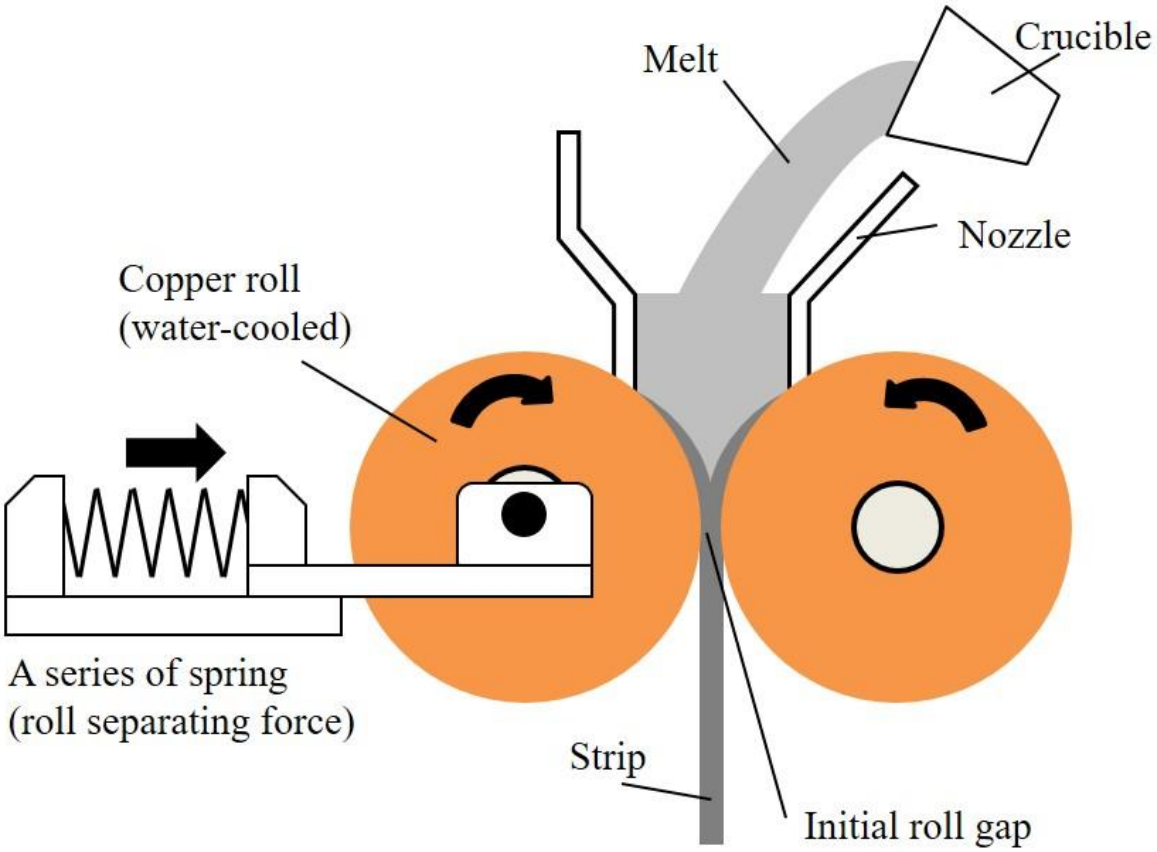


**Fig. 6-1 Schematic illustration of the vertical-type high-speed twin-roll caster.**

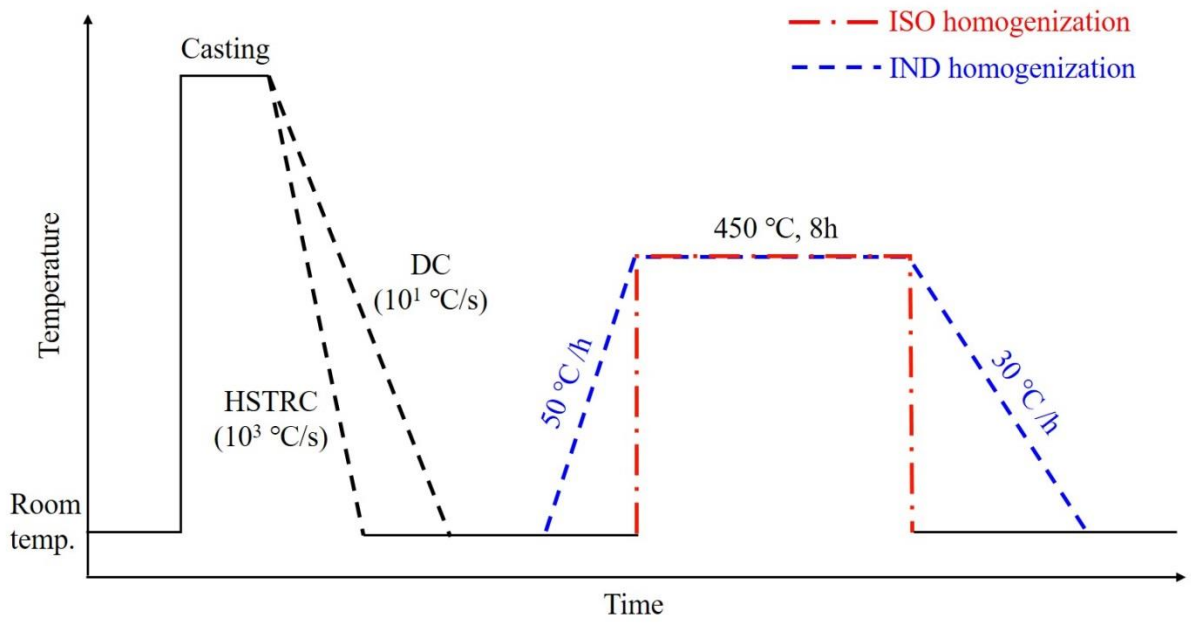


**Fig. 6-2 Schematic drawing of homogenization conditions after the casting.**

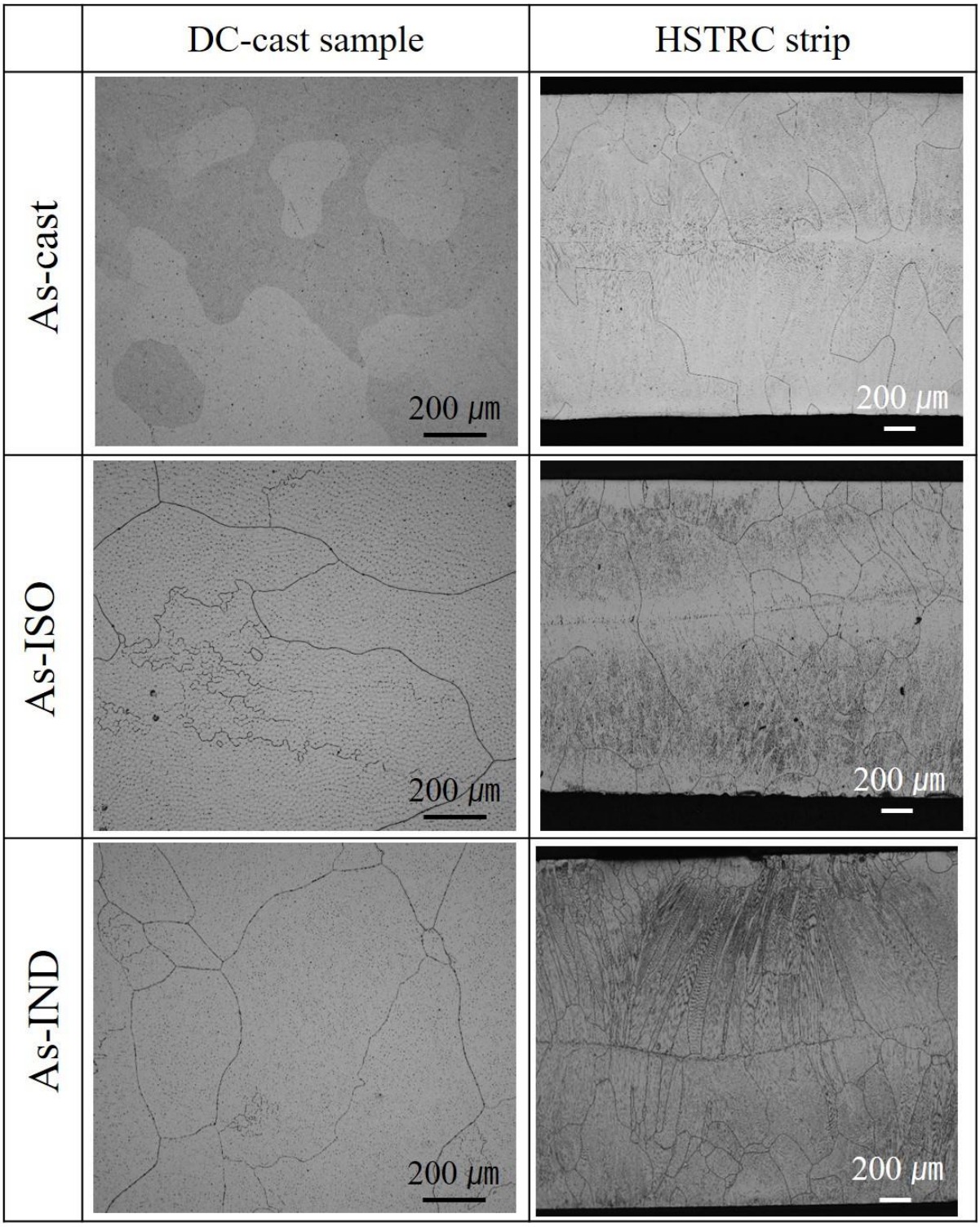


**Fig. 6-3 Microstructure of DC-cast sample and HSTRC strip of AM in as-cast and homogenized conditions.**

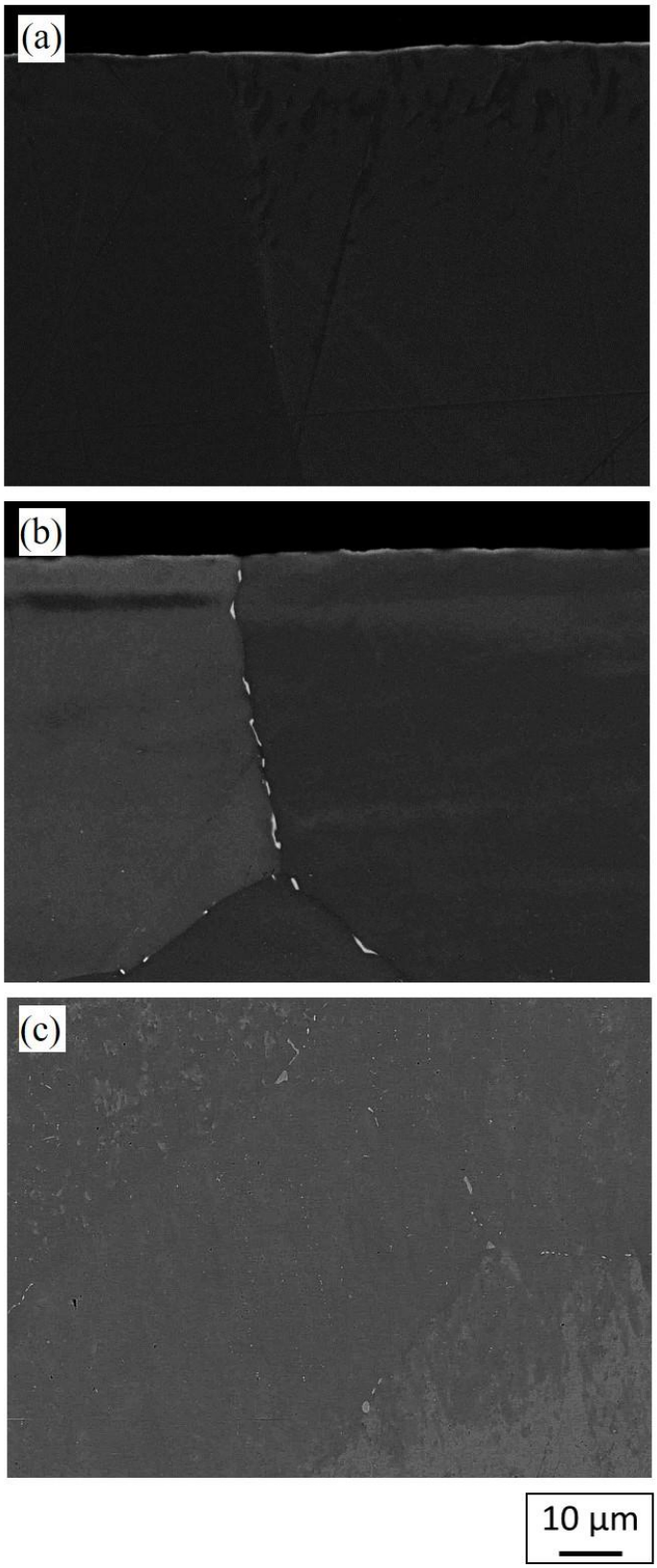


**Fig. 6-4 Back-scattered electron images of HSTRC strip near surface area of AM. (a) as-cast, (b) as-ISO, (C) as-IND.**

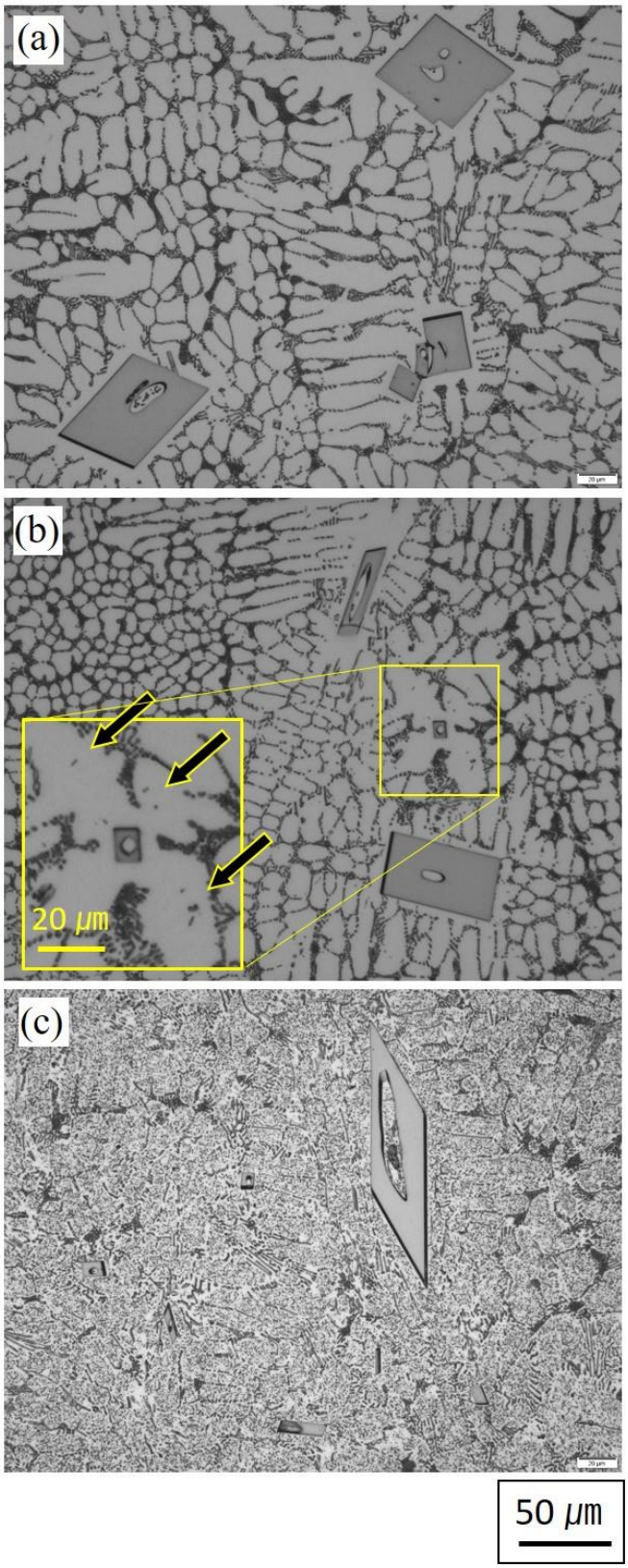


**Fig. 6-5 Microstructure of DC-cast product of AMF. (a) as-cast, (b) as-ISO, (c) as-IND.**

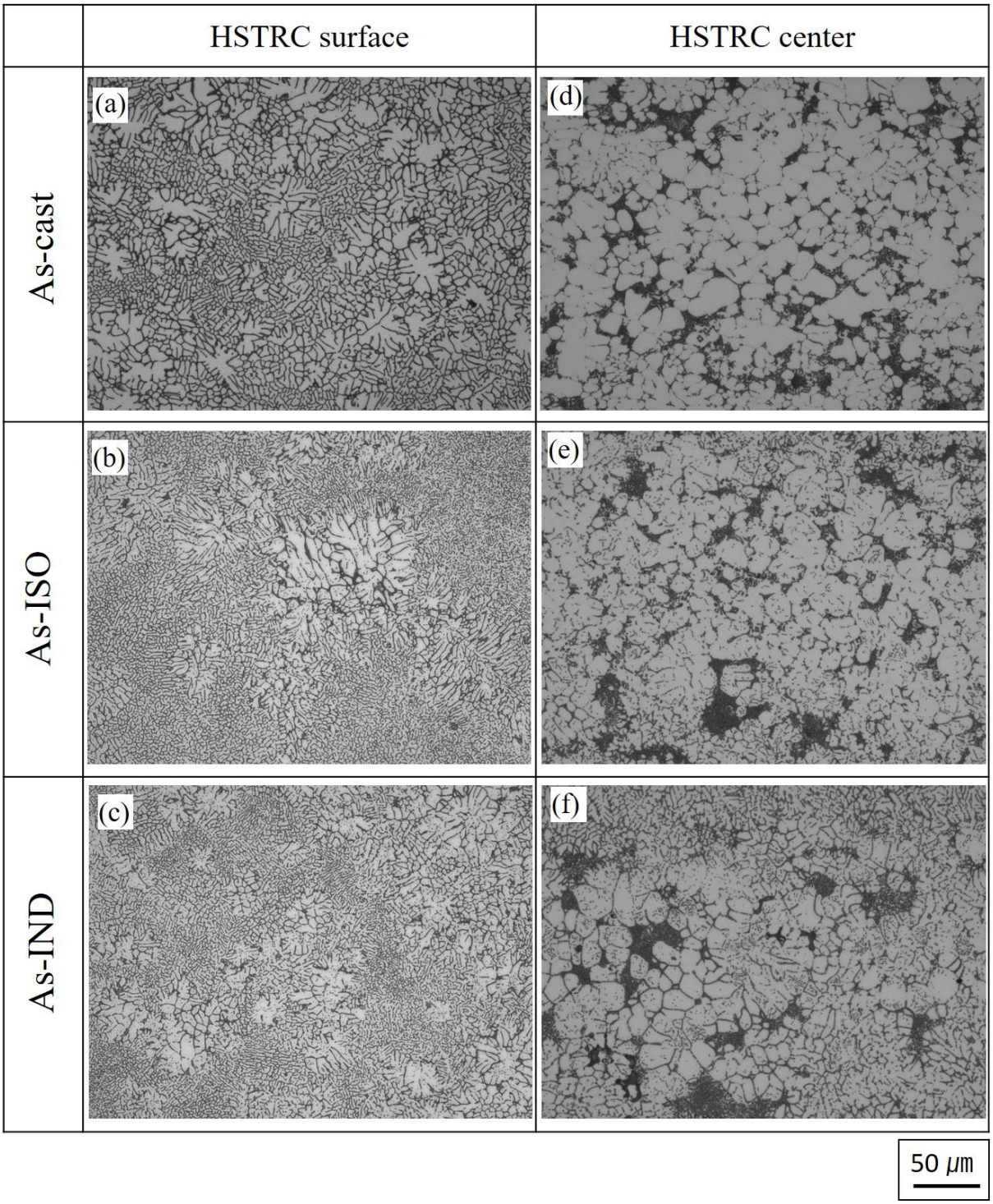


**Fig. 6-6 Microstructure of HSTRC strip of AMF. Strip near surface; (a) as-cast, (b) as-ISO, (c) as-IND. Strip central area; (d) as-cast, (e) as-ISO, (f) as-IND.**

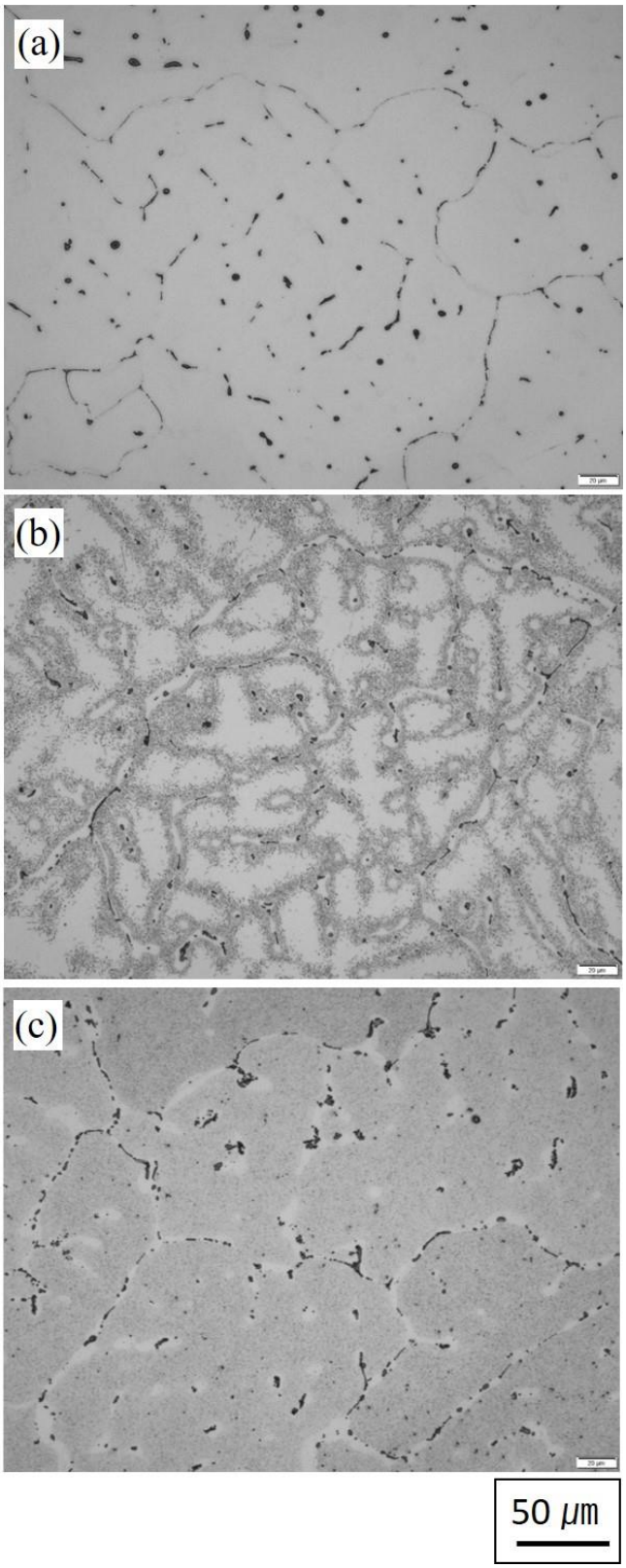


**Fig. 6-7 Microstructure of DC-cast product of AMS. (a) as-cast, (b) as-ISO, (c) as-IND.**

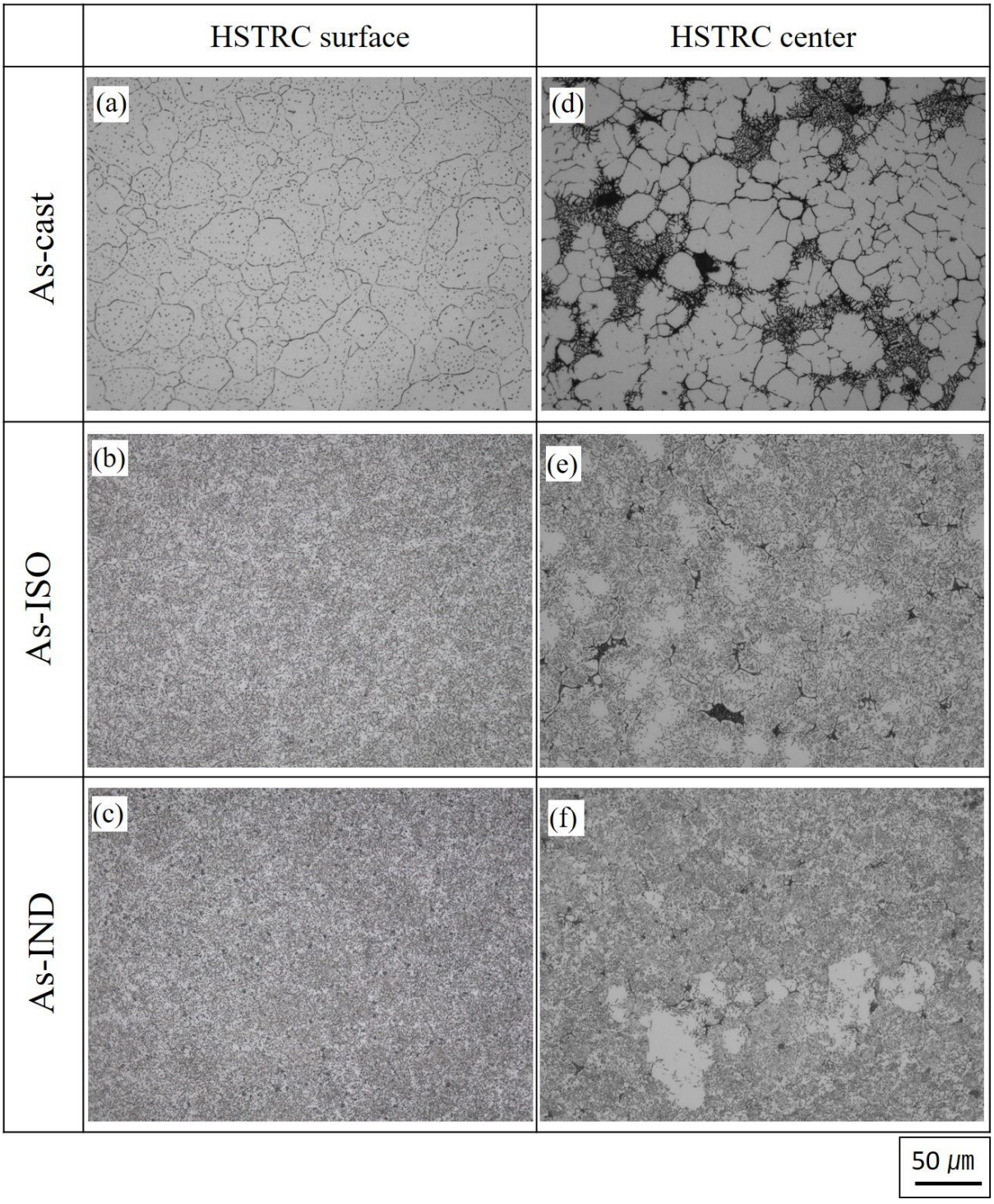


**Fig. 6-8 Microstructure of HSTRC strip of AMS. Strip near surface; (a) as-cast, (b) as-ISO, (c) as-IND. Strip central area; (d) as-cast, (e) as-ISO, (f) as-IND.**

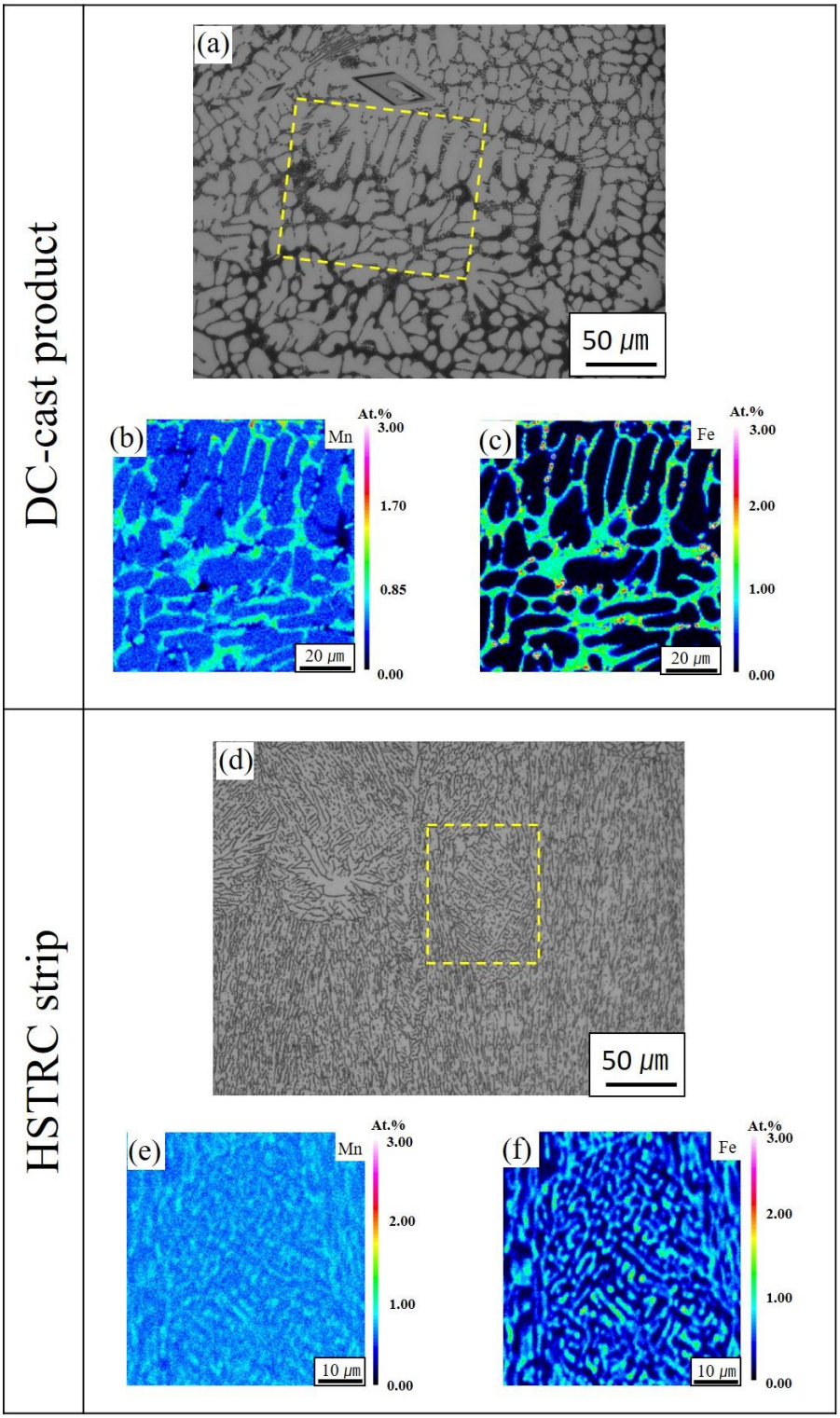


**Fig. 6-9 Solute distribution in AMF. DC-cast product; (a) location where the EPMA analysis was performed, (b) Mn mapping, (c) Fe mapping. HSTRC strip; (d) location where the EPMA analysis was performed, (e) Mn mapping, (f) Fe mapping.**

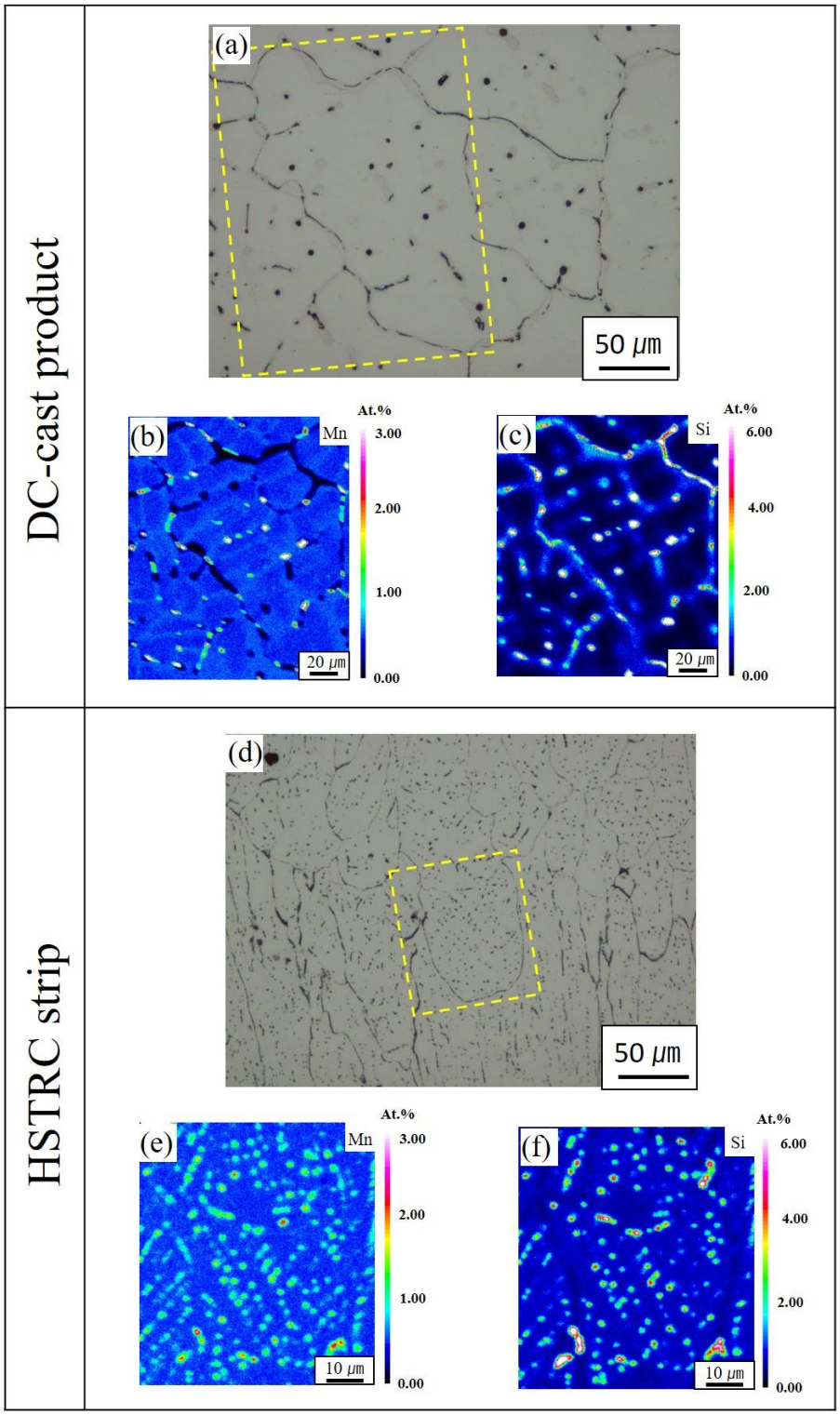


**Fig. 6-10 Solute distribution in AMS. DC-cast product; (a) location where the EPMA analysis was performed, (b) Mn mapping, (c) Si mapping. HSTRC strip; (d) location where the EPMA analysis was performed, (e) Mn mapping, (f) Si mapping.**

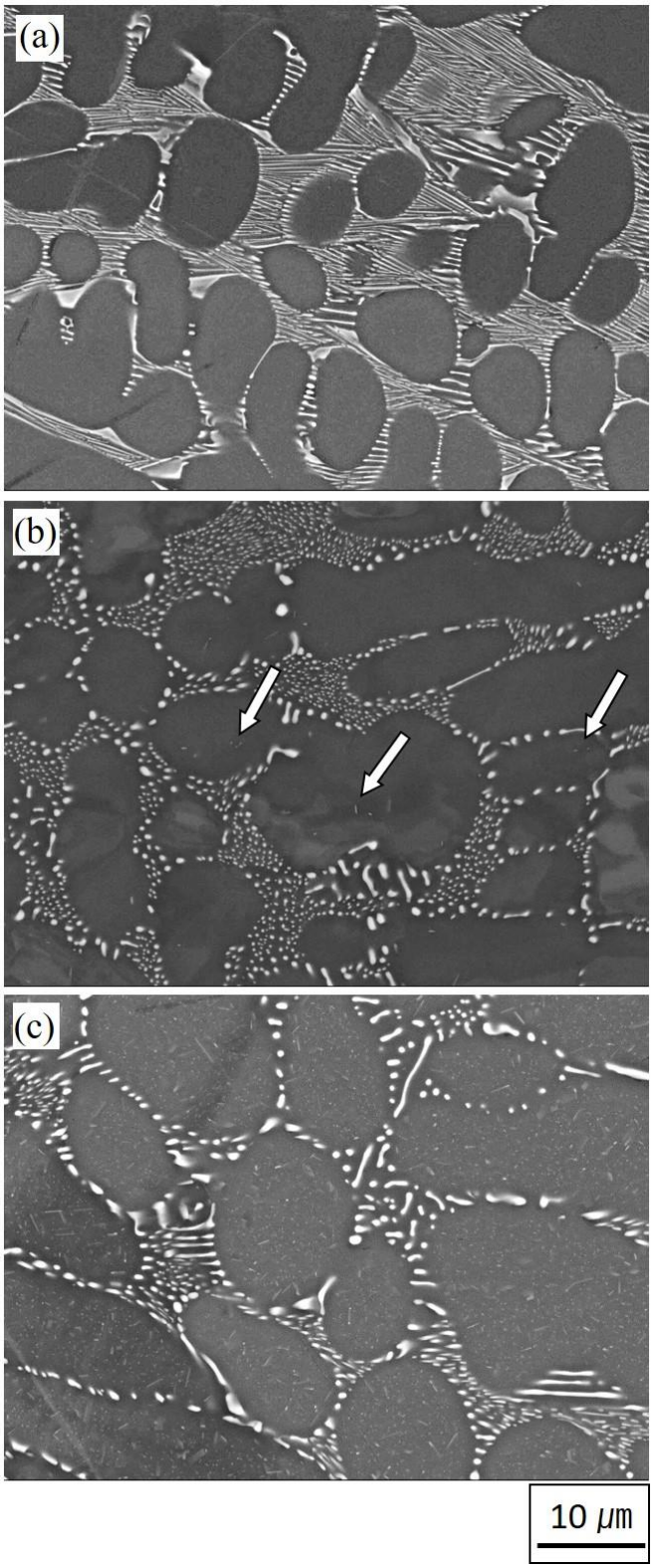


**Fig. 6-11 Back-scattered electron images of DC-cast product of AMF. (a) as-cast, (b) as-ISO, (c) as-IND.**

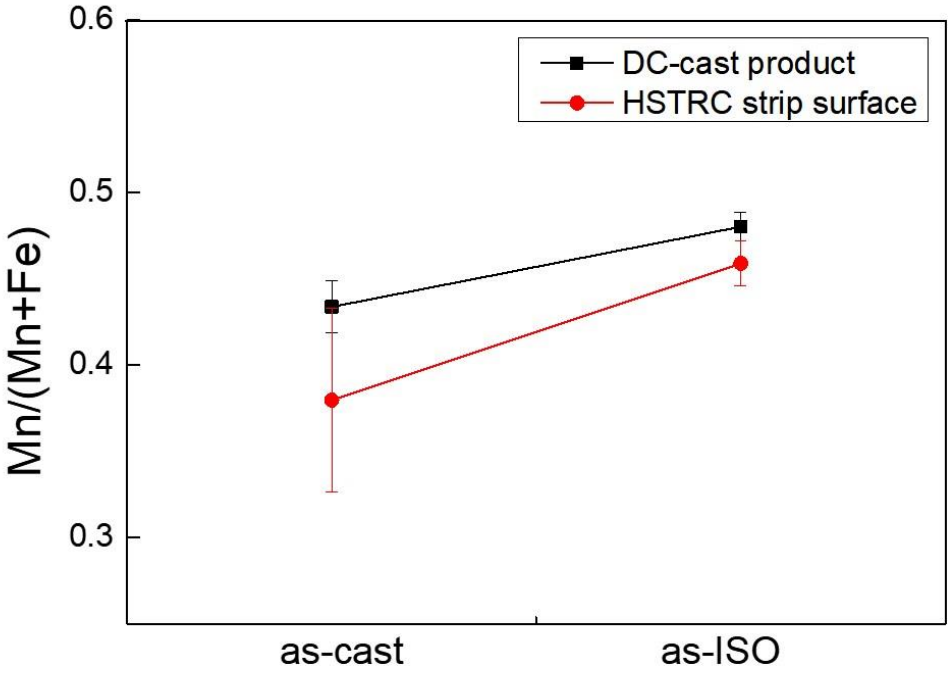


**Fig. 6-12 Mn/(Mn+Fe) composition ratio change of constituent particles in AMF for DC-cast product and HSTRC strip.**

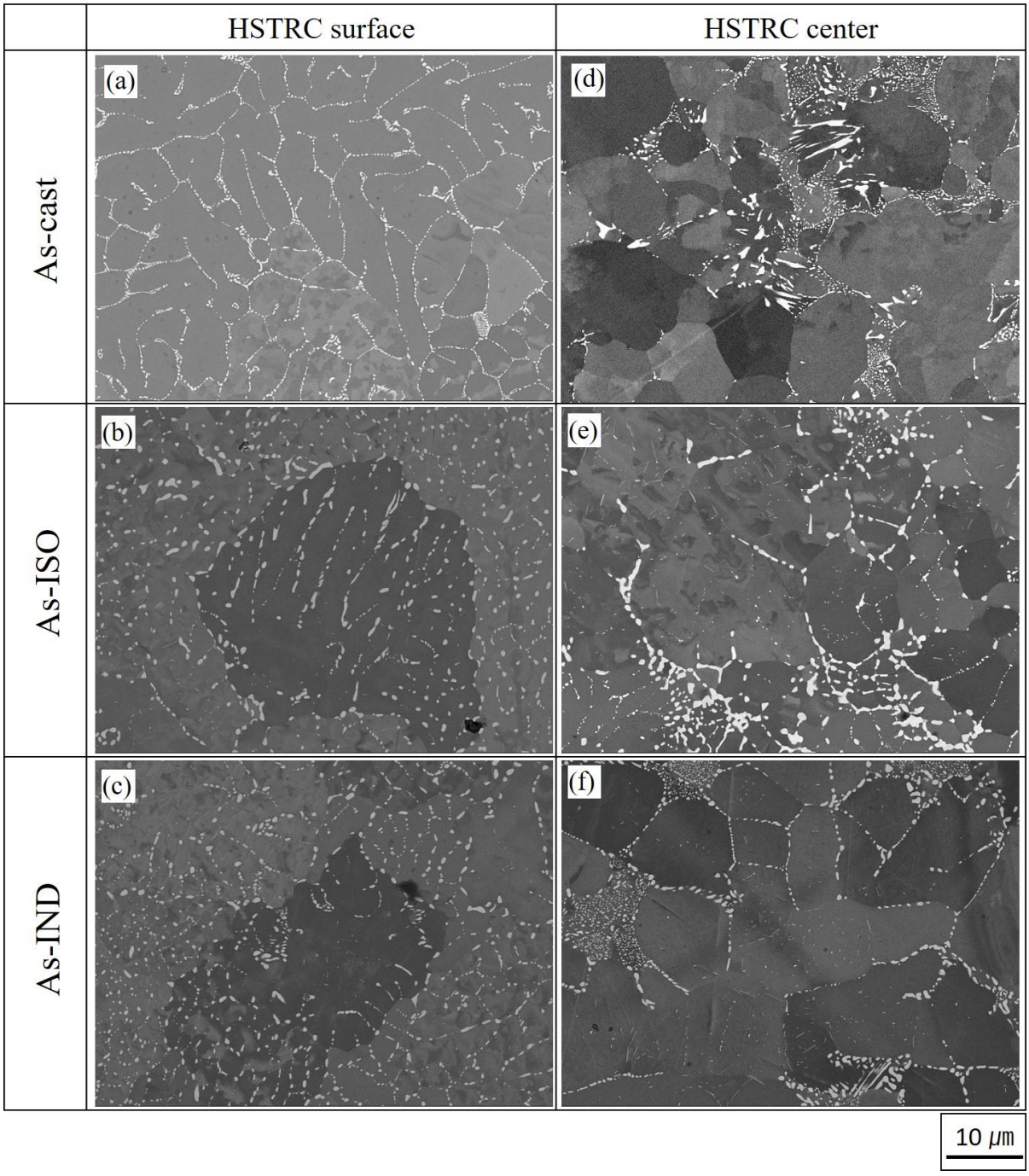


**Fig. 6-13 Back-scattered electron images of AMF HSTRC strip. Strip near surface; (a) as-cast, (b) as-ISO, (c) as-IND. Strip central area; (d) as-cast, (e) as-ISO, (f) as-IND.**

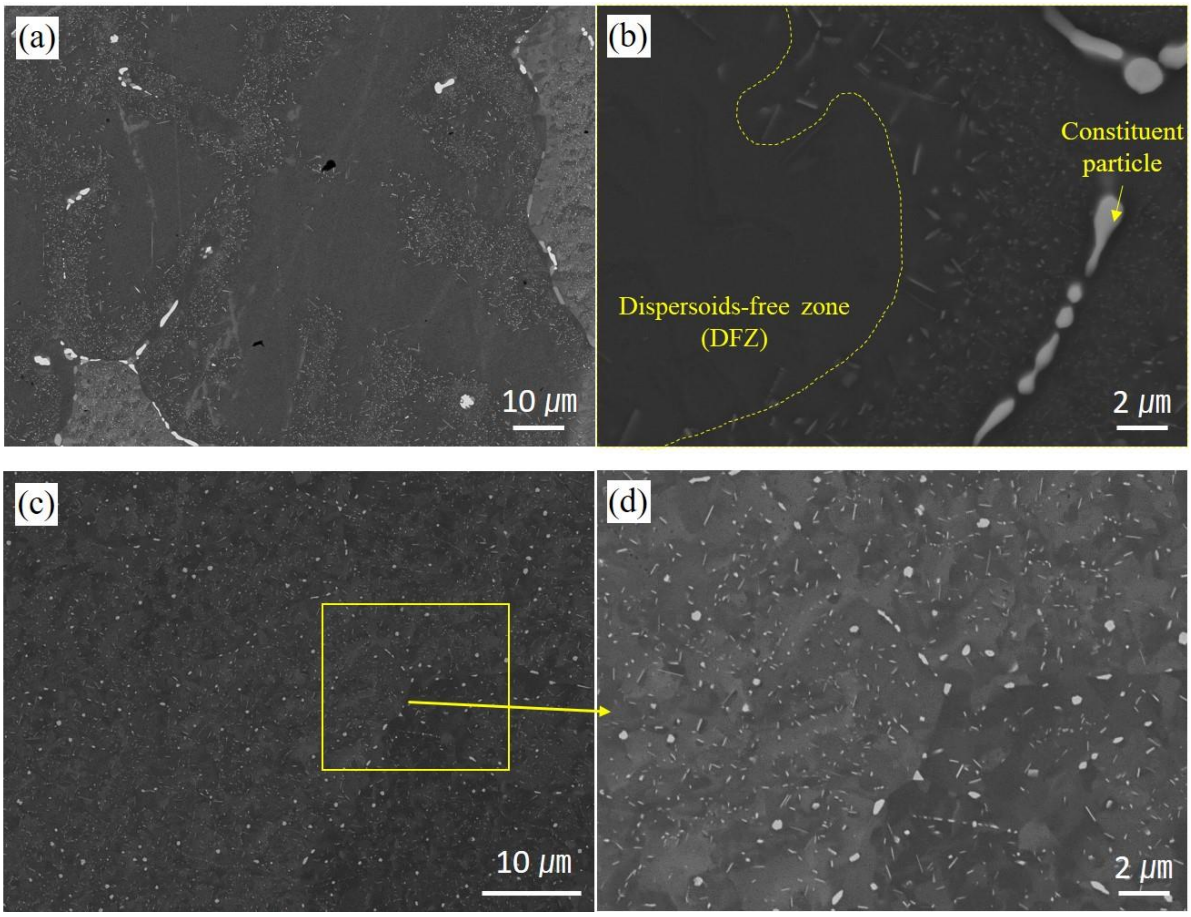


**Fig. 6-14 Back-scattered electron images of DC-cast product and HSTRC alloy strip of AMS in as-ISO condition. (a) DC-cast product (b) dispersoids-free zone (DFZ) inside of core α-Al dendrite, (c) HSTRC strip near surface, (d) detail of specific area in (c).**

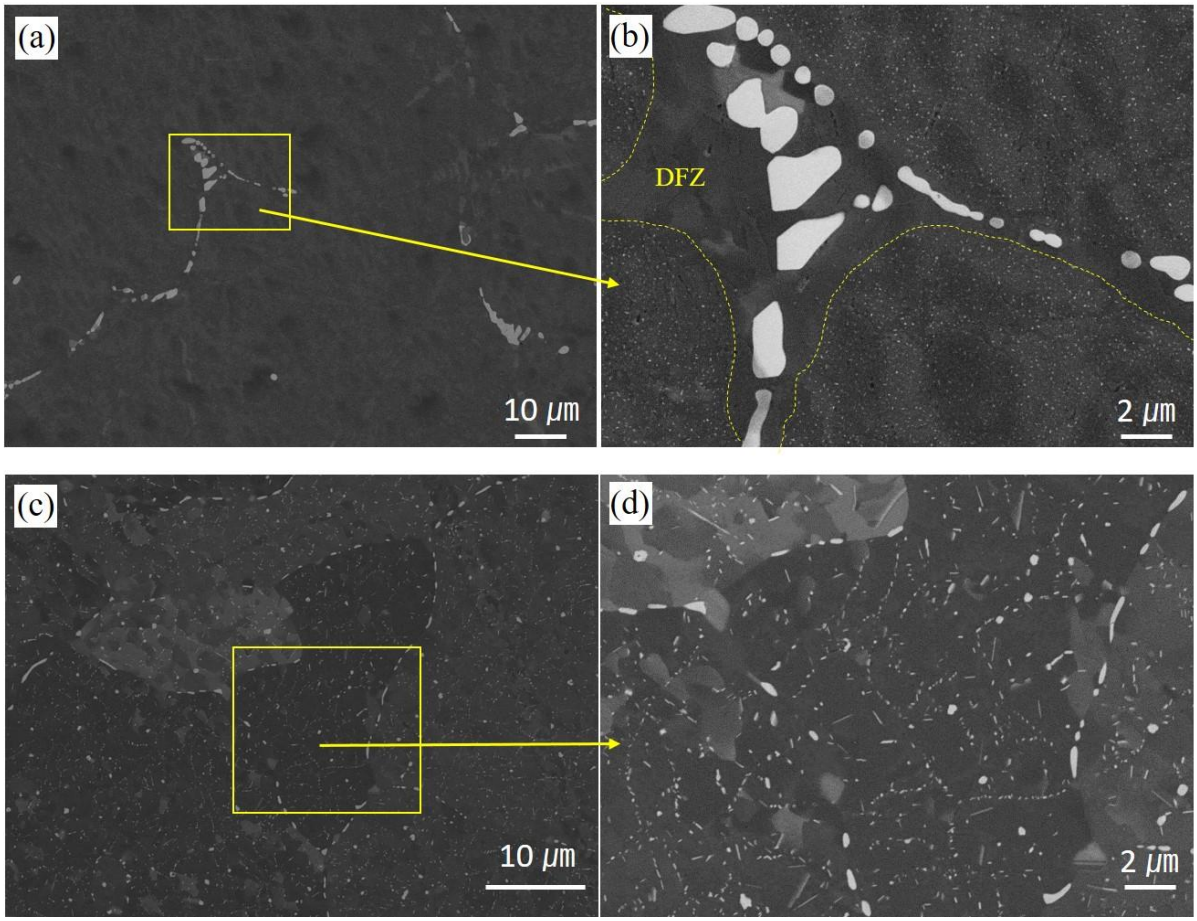


**Fig. 6-15 Back-scattered electron images of DC-cast product and HSTRC alloy strip of AMS in as-IND condition. (a) DC-cast product (b) dispersoids-free zone (DFZ) near the constituent particles, (c) HSTRC strip near surface, (d) detail of specific area in (c).**

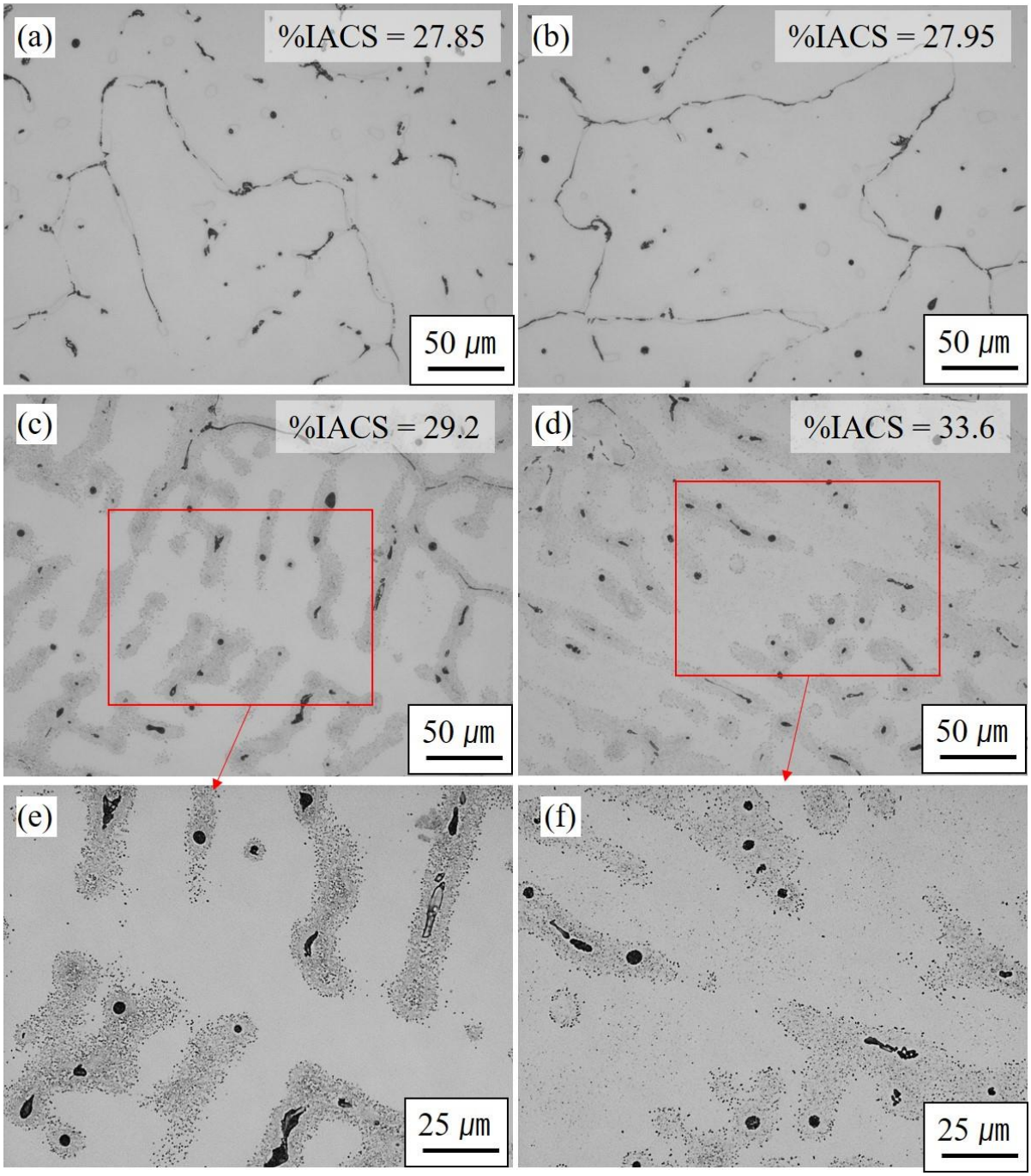


**Fig. 6-16 Microstructure of DC-cast product of AMS during heating in IND homogenization. (a) 100 ℃, (b) 200 ℃, (c) 300 ℃, (d) 400 ℃, (e) detail of specific area in (c), (f) detail of specific area in (d).**

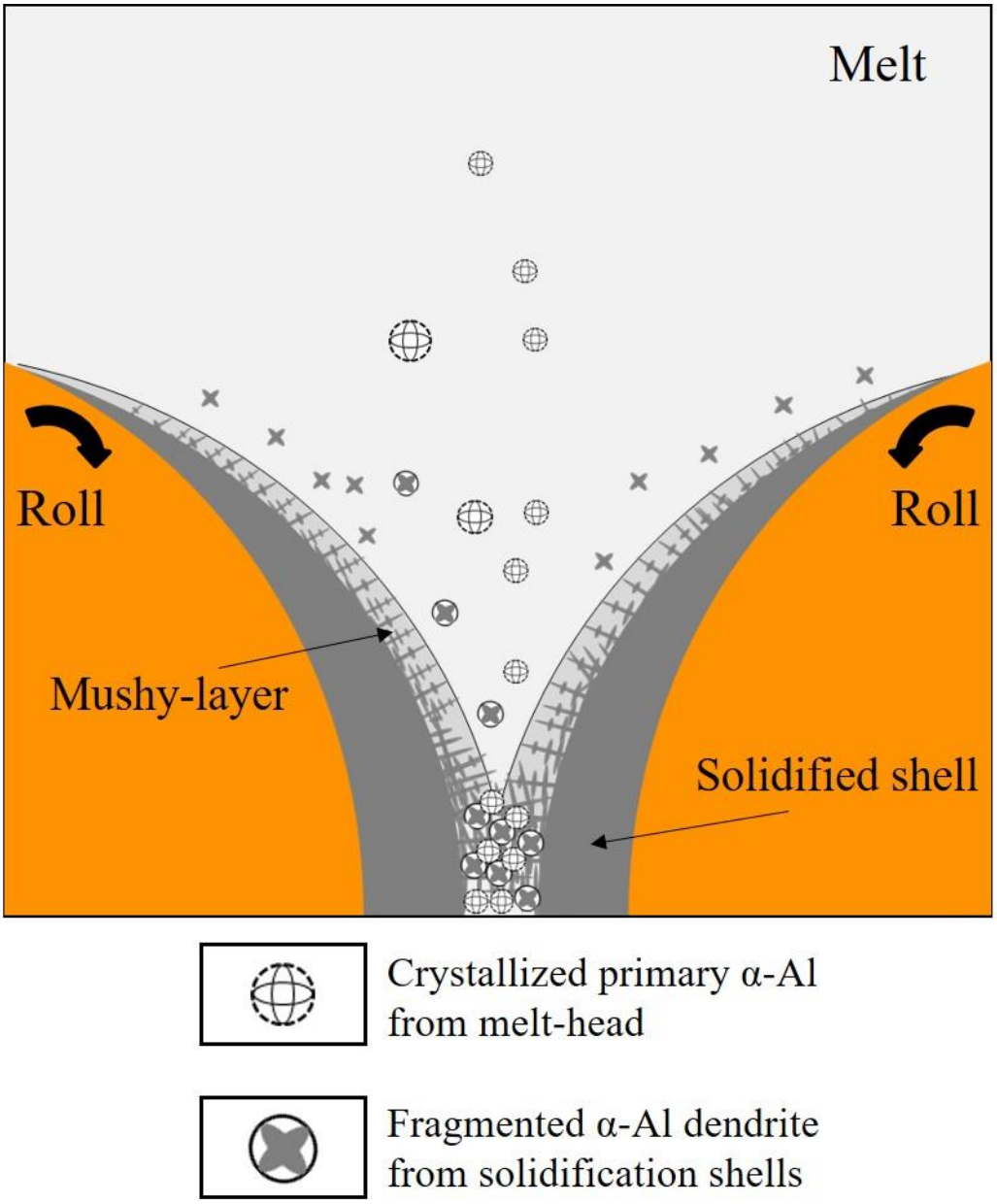


**Fig. 6-17 Schematic diagram of gathering globular grains in the strip central area.**

# Chapter 7 General conclusions

In the present thesis entitled “Microstructure of rapidly solidified Al-Mn based alloy strips fabricated by vertical-type high-speed twin-roll casting”, precise investigation was conducted in order to obtain a basic information for the solidification microstructure of HSTRC processed Al-Mn based alloy strips. Through the microstructure observation and intensive analyses, effects of cooling rates on the solidification structure including formation of secondary particles, Mn supersaturation and segregation behavior of solute elements were made clear. Conclusions of the present thesis are summarized in this chapter based on the overall results and research achievements described in previous chapters.

In Chapter 1, general characteristics and application fields of wrought Al-Mn based alloys were briefly reviewed, and conventional manufacturing processes; direct-chill casting, horizontal-type twin-roll casting, and vertical-type high-speed twin-roll casting were introduced. The objective of the present study and the outline of this thesis were also described.

In Chapter 2, solidification structure and secondary particles of commercial 3003 aluminum alloy strip were investigated, and influence of cooling rates on grain size and kinds, size and morphology of secondary particles was examined. The 3003 aluminum alloy strip consisted of cell structure, dendrite structure, globular grains and eutectic structure along the strip thickness direction. Refinement of both the solidification structure and secondary particles were achieved in 3003 aluminum alloy strip. By the relationship between the grain size and cooling rate, the cooling rate of the HSTRC was estimated around $3.1 \times 10^3$ ℃/s at the strip near-surface. Significant differences in the formation of secondary particles were found between DC-casting and the HSTRC as a result of the different cooling rates; orthorhombic $Al_6(Mn,Fe)$ phase was the main secondary phase in DC-cast sample, whereas only cubic α-Al(Mn,Fe)Si phase was predominant secondary phase in HSTRC processed strip. This resulted in the increase of solute segregation in liquid phase, particularly Si content, during solidification due to the high cooling rate of the HSTRC.

In Chapter 3, to investigate the influence of alloy composition on the solidification structure in the HSTRC, pure Al and several kinds of Al-Mn based alloys; binary Al-1.2Mn, ternary Al-1.2Mn-1.0(Fe,Si), quaternary Al-1.2Mn-0.75(Fe,Si)-0.25(Fe,Si) alloy (in mass%)

strips were fabricated. The solidification structure of the strips was related with their alloy compositions; skin-type solidification structure in pure Al and binary Al-Mn alloy strip, and mushy-type solidification structure in ternary Al-Mn-(Fe,Si) and quaternary Al-Mn-Fe-Si alloy strip, respectively. This is considered to be due to the formation of unstable solid/liquid interface at the growth-front of solidifying shell on the roll surface. Increasing a freezing temperature range of the alloys resulted in the formation of free-crystallized α-Al grains in the melt. The free-crystallized α-Al grains gather at the strip central area that can lead to increase total strip thickness. Secondary particles were not formed in binary Al-Mn alloy strip. In ternary Al-Mn-(Fe,Si) alloy, the Fe favored to form $Al_6$(Mn,Fe) phase, whereas Si resulted in formation of α-AlMnSi phase. In quaternary alloys, α-Al(Mn,Fe)Si phase was dominant at the near-surface area of the strip. The kinds of secondary phase in the central area were dependent on the alloy compositions; α-Al(Mn,Fe)Si and Si phase in the central area of Si-rich Al-Mn-Si-Fe alloy, α-Al(Mn,Fe)Si and $Al_6$(Mn,Fe) phase in the central area of Fe-rich Al-Mn-Fe-Si alloy. It is considered to be due to difference in the local composition of residual liquid phase at the final solidification part.

In Chapter 4, ternary Al-1.2Mn-1.0Fe (AMF) and Al-1.2Mn-1.0Si (AMS) in mass % alloy strips were examined. The influence of cooling rates on secondary particle formation was investigated based on the comparison of various cooling rate conditions; furnace cooling, DC-casting, HSTRC and single-roll casting. Increase in cooling rates resulted in decrease in Mn composition ratio in secondary particles. It was due to not only the decrease in Mn segregation, but also enrichment of Fe and Si in the remaining liquid in the ternary alloy systems. For AMF, high cooling rate of HSTRC resulted in reduction in large primary particles, and decrease in the aspect ratio of the primary $Al_6$(Mn,Fe) particles. For inter-dendrite regions in AMS strip near-surface, high cooling rate of HSTRC increased Si segregation in the remaining liquid trapped at the inter-dendrite regions. The enrichment of Si in the liquid enhanced the formation of secondary particles; spore-like Si-rich eutectic α-AlMnSi and polygonal Si.

In Chapter 5, to examine the effect of cooling rate on Mn supersaturation, Al-Mn binary alloy strips with hypo-, eutectic and hyper eutectic composition were fabricated by HSTRC. Over 3.5 mass% Mn supersaturation was achieved by high cooling rate of HSTRC. In the alloy composition of hyper eutectic Al-Mn binary alloy, formation of a number of primary

$Al_6Mn$ phase particles in the melt pool were considered to occur during the casting. This reduced Mn concentration in the Al matrix along the strip thickness direction. Applying the sufficient melt superheating was effective to prevent formation of the primary $Al_6Mn$ phase and to increase the Mn concentration in Al matrix. The cast strips were cold-rolled, then flash-annealed, and their mechanical properties were investigated. Significant increase in 0.2 % strain offset yield stress was obtained for the flash-annealed high Mn supersaturated Al-Mn binary alloy strip. This is considered to be due to the contribution of Mn solid solution strengthening by high Mn supersaturation resulting from high cooling rate of the HSTRC.

In Chapter 6, solute distribution and Mn decomposition behavior in vertical-type high-speed twin-roll cast binary Al-1.2Mn (AM), ternary Al-1.2Mn-1.0Fe (AMF) and Al-1.2Mn-1.0Si (AMS) in mass% alloy strips were investigated. The high cooling rate of HSTRC resulted in homogeneous distribution of solute atoms and secondary particles. The Fe and Si enhanced the Mn decomposition during homogenization. In the AMF strip, constituent particles of $Al_6(Mn,Fe)$ phase were homogeneously distributed in the strip due to the high cooling rate. The Mn decomposition mainly occurred by the diffusion of Mn toward the constituent particles resulting in increase of Mn/(Mn+Fe) ratio of the constituent particles and their spheroidizing and coarsening during homogenization. In the AMS strip, formation of fine α-AlMnSi dispersoids was predominant way for the Mn decomposition during homogenization. Due to the high cooling rate of HSTRC, homogeneous Mn and Si distribution was achieved that leads to formation of high-dense fine α-AlMnSi dispersoids during homogenization. This contributes to enhance decomposition of supersaturated Mn during homogenization in vertical-type high-speed twin-roll cast strip.

In the present study, the relationship between cooling rates and solidification structure including α-Al grain structure, secondary particles, solute distribution and Mn decomposition in the vertical-type high-speed twin-roll cast Al-Mn based alloy strips was made clear; (I) The cooling rate of HSTRC was estimated by direct/indirect measurement that is considered over $10^3$ ℃/s even at the strip center. (II) The cooling rates, as well as the starting alloy composition can change the kinds, morphology and composition ratio of the secondary particles resulting from change the segregation behavior of solute elements at residual liquid. (III) The HSTRC was able to fabricate the strip of high Mn solid solution. The high cooling rates and sufficient melt superheating are considered to obtain the high Mn supersaturation in

the binary Al-Mn alloy strip. (IV) Homogeneous distribution of fine secondary particles and solute elements was obtained in the cast strips. They enhanced the Mn decomposition of the cast strips during homogenization.

The present study allows us to better understanding for the initial microstructure of vertical-type high-speed twin-roll cast Al-Mn based alloy strips. The present study can contribute to not only the research development for the rapidly solidified Al-Mn based alloys, but also the application of the HSTRC for manufacturing of Al-Mn based alloys in industrial level.